

**MODELING AND DOSE SCHEDULE DESIGN FOR
CYCLE-SPECIFIC CHEMOTHERAPEUTICS**

by

Jeffry Alan Florian Jr.

B.S., Pennsylvania State University, 2002

Submitted to the Graduate Faculty of
the Swanson School of Engineering in partial fulfillment
of the requirements for the degree of

Doctor of Philosophy

University of Pittsburgh

2008

UNIVERSITY OF PITTSBURGH
SWANSON SCHOOL OF ENGINEERING

This dissertation was presented

by

Jeffrey Alan Florian Jr.

It was defended on

March 4th 2008

and approved by

Dr. Robert S. Parker, Associate Professor, Department of Chemical and Petroleum
Engineering

Dr. Joseph McCarthy, Professor, Department of Chemical and Petroleum Engineering

Dr. Steven Little, Assistant Professor, Department of Chemical and Petroleum Engineering

Dr. Merrill Egorin, Professor, Department of Medicine

Dr. Julie Eiseman, Research Associate Professor, Department of Pharmacology

Dissertation Director: Dr. Robert S. Parker, Associate Professor, Department of Chemical
and Petroleum Engineering

Copyright © by Jeffry Alan Florian Jr.

2008

MODELING AND DOSE SCHEDULE DESIGN FOR CYCLE-SPECIFIC CHEMOTHERAPEUTICS

Jeffry Alan Florian Jr., PhD

University of Pittsburgh, 2008

Model-based optimal control has been used to synthesize chemotherapy treatment schedules. Constraints on drug delivery or states are used to maintain drug administration within toxicity limits, and the objective function usually minimizes the tumor volume at a prespecified final time. These solutions predict a characteristic 3-phase treatment profile: maximum initial drug delivery; a non-dosing period; and the remainder of the drug delivered at the end of the treatment window. Ethically, however, a doctor cannot allow a tumor to grow untreated, thereby invalidating the controller formulation. Dose schedule development, therefore, requires an alternative formulation to obtain clinically relevant dosing schedules.

Dose schedule design for the therapeutic tamoxifen (TM) was investigated using nonlinear model predictive control (NMPC) and a tumor regression reference trajectory. Performance was dependent on accurate incorporation of the pharmacodynamic (PD) effect, and the desired trajectory was tracked. The techniques evaluated could be adapted to other therapeutics administered over regular intervals, though alterations to the objective function would be necessary for clinical implementation

More detailed cell-level tumor growth models were investigated using population balance equations. Individual cell cycle states were included within the model, as were saturating growth rates representative of Gompertzian growth seen from solid tumors. Open-loop simulations involving two cycle specific therapeutics (*S*- and *M*-phase active) questioned

the simultaneous administration of therapeutics which predicted the largest final tumor volumes. These results require additional investigation, as does the accuracy of the bilinear PD effect structure.

A physiologically-based pharmacokinetic (PBPK) model for systemic docetaxel (Doc) disposition in SCID mice was developed based on collected plasma, tumor, and tissue concentration data. This model was scaled to humans and compared against patient Doc plasma data from several clinical trials as well as Doc plasma predictions from other models in the literature. A low-order neutrophil model from the literature was tailored to patient neutrophil samples from the clinical study. The human-scaled PBPK Doc and neutrophil PD models were combined and used to evaluate Doc regimens from the literature. Finally, a NMPC was synthesized based on the PBPK and PD models and used to develop clinically-relevant dosing regimens under PD constraints.

TABLE OF CONTENTS

PREFACE	xxxi
1.0 INTRODUCTION	1
1.1 Pharmacokinetic Models	3
1.2 Pharmacodynamic Models	8
1.2.1 Tumor Growth Models	11
1.2.2 Toxicity Models	14
1.3 Controller Algorithms	19
1.4 Dissertation Overview	23
2.0 TAMOXIFEN	25
2.1 Methods	26
2.2 Tamoxifen PK	26
2.3 Tamoxifen Tumor Model and PD	29
2.4 Tamoxifen Controller Synthesis	41
2.5 Clinical Applicability	46
3.0 PBE TUMOR MODELS	49
3.1 PBE Model Development	50
3.2 Mass-Structured Cell Cycle Tumor Growth PBE	53
3.3 Age-Structured Cell Cycle Tumor Growth PBE	54
3.4 Non-saturating PBE Model Results and Discussion	57
3.5 Mass-structured Saturating Cell Cycle PBE	60
3.5.1 Saturating <i>G</i> -Phase Transition Rate	63
3.5.2 Saturating <i>G</i> -Phase Mass Accumulation Rate	64

3.6	Age-Structured Saturating Cell Cycle PBE	70
3.6.1	Three Phase Age-Structured Saturating Cell Cycle PBE	70
3.6.2	Four Phase Age-Structured Saturating Cell Cycle PBE	72
3.6.3	Age-Structured Cell Cycle Model Comparison	72
3.7	Dose Schedule Evaluation and Discussion	74
3.8	Discussion and Summary	96
4.0	MOUSE PBPK MODEL FOR DOC	100
4.1	Materials and Methods	102
4.1.1	Mouse Doc PK Study	102
4.1.2	Sample Processing and LC-MS Analysis	103
4.1.3	Mouse PBPK Model Formulation	103
4.1.4	Model Quality Assessment	107
4.1.5	Parameter Sensitivity Analysis	109
4.2	Results	110
4.3	Discussion	119
5.0	SCALE-UP OF THE MOUSE DOC PBPK TO HUMANS	126
5.1	Materials and Methods	128
5.1.1	Human Doc Clinical Data	128
5.1.2	Human PBPK Model Scale-Up	129
5.1.3	Model Validation	131
5.2	Results	133
5.2.1	Doc Plasma Model Predictions	133
5.2.2	Unbound Doc	139
5.2.3	Simulated Doc Concentration Profiles in Tumors	141
5.3	Discussion and Summary	153
6.0	DOC NEUTROPHIL TOXICITY MODEL	156
6.1	Materials and Methods	159
6.1.1	Patient Data	159
6.1.2	Model Development	159
6.1.3	PK/PD Drug Schedule Simulations	162

6.1.4 PK/PD Drug Schedule Control Algorithm	163
6.2 Results	166
6.2.1 Neutrophil Model Evaluation	166
6.2.2 Coupled PK and PD Predictions	170
6.2.3 Updated Neutrophil Model	171
6.2.4 Human PBPK Model Reduction	182
6.2.5 Dose Schedule Development	184
6.3 Discussion	189
7.0 CONTRIBUTIONS	196
7.1 Conclusions	196
7.1.1 Tamoxifen	196
7.1.2 PBE Models	197
7.1.3 Docetaxel	198
7.2 Future Work	200
7.2.1 Tumor Models	200
7.2.1.1 Untreated Tumor Growth Evaluation	201
7.2.1.2 Inclusion of Natural Apoptosis	201
7.2.1.3 Accurate PD Terms/Kernels	202
7.2.1.4 Bulk Tumor Measurement Errors	203
7.2.2 Neutrophil Toxicity Model	204
7.2.2.1 Low Dose Model Validation	204
7.2.2.2 GCS-F Neutrophil Models	205
7.2.2.3 Objective Function Formulation	205
APPENDIX A. NOMENCLATURE	207
APPENDIX B. PBPK MODEL EQUATIONS	213
APPENDIX C. ACTUAL AND MODEL PREDICTED HUMAN DOC	
PLASMA CONCENTRATION VERSUS TIME PLOTS	216
APPENDIX D. ACTUAL AND MODEL PREDICTED HUMAN DOC	
PLASMA CONCENTRATION VERSUS TIME PLOTS (UNBOUND	
FRACTION)	227

BIBLIOGRAPHY 238

LIST OF TABLES

2.1	PK parameter values for the oral dosing of TM.	28
2.2	Parameter values for the tumor growth models: QCM, SCM, and GM.	34
2.3	Calculated k_D 's from the four TM dose groups using tumor growth models; μ_{1-j} and σ_{1-j} represent the mean and standard deviation, respectively, of the lowest TM dose through the j th lowest TM dose.	34
3.1	Model, transition function, mass allocation, and division function parameters for the mass-structured cell-cycle PBE.	56
3.2	Model, transition function, and division function parameters for the age-structured cell-cycle PBE.	56
3.3	Model, transition function, mass allocation, and division function parameters for the mass-structured saturating cell-cycle PBE with saturating G -phase transition rate.	65
3.4	Model, transition function, mass allocation, and division function parameters for the mass-structured cell-cycle PBE with saturating G -phase mass accumulation rate.	68
3.5	Model, transition function, and division function parameters for the age-structured saturating cell-cycle PBE with three cell phases.	71
3.6	Model, transition function, and division function parameters for the four phase age-structured saturating cell-cycle PBE.	73
3.7	PK and PD parameters used for evaluating the treatment of three age-structured PBEs with S - and M -phase therapeutics.	80

3.8	Day 100 tumor volume predicted for the three models treated with Schedule 1. The first two entries are the final tumor volumes obtained from dosing with only the <i>S</i> -phase or <i>M</i> -phase therapeutic, respectively. The remainder are combination dose schedule regimens with the <i>S</i> -phase treatment started on day 42, and the <i>M</i> -phase treatment initiated the listed number of days prior (-) or after (+).	81
3.9	Day 100 tumor volume predicted for the three models treated with Schedule 2. The first two entries are the final tumor volumes obtained from dosing with only the <i>S</i> -phase or <i>M</i> -phase therapeutic, respectively. The remainder are combination dose schedule regimens with the <i>S</i> -phase treatment started on day 42, and the <i>M</i> -phase treatment initiated the listed number of days prior (-) or after (+).	86
3.10	Day 100 tumor volume predicted for the three models treated with Schedule 3. The first two entries are the final tumor volumes obtained from dosing with only the <i>S</i> -phase or <i>M</i> -phase therapeutic, respectively. The remainder are combination dose schedule regimens with the <i>S</i> -phase treatment started on day 42, and the <i>M</i> -phase treatment initiated the listed number of days prior (-) or after (+).	91
4.1	Parameter values for the mouse PBPK model. Tissue values in bold depict the mean ($\pm\sigma$) tissue volumes from the entire set of mice in the PK study. Total blood flow rate, individual tissue blood flow rates, and vascular fraction were fixed based on literature values [1] while blood volume and tissue volumes for the gut, muscle, and adipose tissue were calculated based on percent of body weight values found in the literature [1]. Finally, the volume of the “other” compartment was calculated using the average weight of mice in the study (22.89 grams) minus the sum of all other tissues.	108
4.2	PBPK model predicted performance for the incorporated tissues. Half-lives ($t_{\frac{1}{2}}$) were calculated using the last four data time points (360, 420, 960, and 1440 minutes).	115

4.3	PBPK model predictive performance comparison at dosing levels of $10 \frac{\text{mg}}{\text{kg}}$ and $20 \frac{\text{mg}}{\text{kg}}$	125
5.1	Patient characteristics from the Phase 1 Doc studies performed at UPCI and MSKCC. Values are reported as the study median and range.	130
5.2	Parameter values from the literature for the human PBPK model (70 kg) [1]. F , V , and f denote tissue blood flow rates, tissue volumes, and tissue vascular fractions, respectively.	132
5.3	Parameter values for the Bruno <i>et al.</i> Doc population PK model [2]. k_{ij} are transition rates from compartment i to compartment j , and V_i is the volume of model compartment i	132
5.4	Doc plasma AUC and clearance mean (standard deviation) values from study data and model predictions.	135
5.5	Model performance mean (standard deviation) values for three Doc studies across multiple Doc dosing levels.	136
5.6	Doc plasma AUC and clearance mean (standard deviation) values from study data and model predictions obtained from estimating the unbound Doc fraction on a per patient basis. ^a were results obtained by including both unbound Doc fraction and liver metabolism as model parameters.	147
5.7	Model performance mean (standard deviation) values for three Doc studies across multiple Doc dosing levels. ^a were results obtained by including both unbound Doc fraction and liver metabolism as model parameters.	148
5.8	Calculated C_{max} and AUC for simulated tumors. AUC for all tumor profiles was calculated over a period of 21 days due to the extended retention times exhibited by the tumor tissue.	150
6.1	Parameter values compared for the neutrophil model from the literature [3] and those estimated using the linear PD effect in Equation (6.7) and patient neutrophil counts from two Phase I clinical trials.	169

6.2 Parameter values for the neutrophil model of Friberg *et al.* [3] and estimated PD model parameters using altered PD effect terms and/or model structures. Neutropenia grade predictions were made using neutrophil model parameters identified for individual patients. 178

LIST OF FIGURES

1.1	a) Open-loop therapeutic delivery as viewed clinically; b) open-loop PK-driven treatment in mathematical block form; c) closed-loop therapeutic delivery managed by a clinician; and d) closed-loop treatment delivery algorithm in mathematical block form.	5
1.2	Representative compartmental PK model structure (solid) with both additional remote compartments (dotted) and tissue-specific compartments (dashed) for representing multiple plasma half-lives and specific tissue distribution, respectively.	7
1.3	Physiologically-based pharmacokinetic (PBPK) model for the distribution of docetaxel (Doc) in plasma, various body tissues, and subcutaneously implanted tumor xenografts.	10
1.4	Cell cycle model showing phases of the cell-cycle, Q , G_1 , S , G_2 , and M . Also shown are experimentally reconcilable phases based on DNA analysis: G ($Q + G_1$), S , and M ($G_2 + M$).	13
1.5	A low-order neutrophil model without feedback (a) and representative circulating neutrophil count progression following treatment with a chemotherapeutic (b).	18
2.1	4-compartment linear model for plasma concentrations of TM and HTM after oral dosing	28
2.2	Actual (circles) vs. simulated (lines) PK for TM (top) and HTM (bottom) after a $200 \frac{\text{mg}}{\text{kg}}$ oral dose of TM. Each data point represents mean plasma concentrations from three mice; error bars are ± 1 standard deviation.	30

2.3	The five phases of the cell-cycle: Q (quiescent), G_1 (growth), S (DNA replication), G_2 (mitotic preparation), M (mitosis). Two cell-cycles models are developed: (i) a three-phase model considering G (lumped Q and G_1), S , and M (lumped G_2 and M) which is resolvable using DNA labeling and flow cytometry; or (ii) a four-phase structure with Q , G_1 , S , and M (lumped G_2 and M) which is resolvable using DNA and RNA labeling and subsequent flow cytometry.	32
2.4	The cell-cycle (a) and typical flow cytometry results from DNA staining alone (b) or combination DNA and RNA staining (c). By staining for DNA it is possible to resolve three groupings of cells (G , S , and M) which can be modeled using three state equations (Equations (2.3)-(2.5)). Simultaneously staining for both DNA and RNA content allows for independent resolution of the Q - and G_1 -phases, and the overall population can be modeled using four state equations (Equations (2.7)-(2.10)). Figures adapted from Shapiro <i>et al.</i> [4]. Identifiable phases of the cell-cycle from combination staining for DNA and RNA content followed by flow cytometry (left) and typical flow cytometry result from DNA staining alone (upper right). The Q/G_1 grouping could be further separated by staining for RNA content.	35
2.5	Measured tumor volumes (circles; mean from 20 untreated mice) for MCF-7 human ER+ breast cancer xenografts growing in athymic nude mice and simulated tumor size (lines) as a function of time for QCM (dash-dot), SCM (solid, overlay on dash-dot), and GM (dashed, overlay on dash-dot) models. Error bars represent a 95% confidence interval (CI) for measured tumor volumes.	36
2.6	Measured MCF-7 tumor xenograft data from tumor-bearing athymic mice (circles with a 95% CI) vs. QCM (dash-dot), SCM (solid, overlay on dash-dot), and GM (dashed, overlay on dash-dot) model predictions. TM doses were administered starting on day 10 (dots, bottom) for five consecutive days, followed by two days off.	40

2.7	<p>NMPC algorithm implementation schematic; as shown, $m = 2$, $p = 6$. Based on a current tumor volume measurement, the controller predicts m dosing alterations to minimize Equation 2.16 over p future days. While NMPC typically employs a continuous input profile with step changes at update intervals (dashed, bottom), many chemotherapeutics are administered as pills, mathematically represented as a bolus (solid, vertical). Doses were scheduled as bolus inputs, but are graphed as steps for easier viewing.</p>	43
2.8	<p>Tumor volume (top), reference volume (dotted, top) and TM dose representation (bottom) as a function of time. Tuning parameters for all three controllers (QCMC, solid; SCMC, dash-dot; GMC, dashed) were $m = 1$ and $p = 8$. . . .</p>	45
2.9	<p>Tumor volume (top), reference volume (dotted, top, 10 mm^3), and TM dose representation (bottom) as a function of time. Tumor volumes are measured biweekly under NMPC and tuning parameters for all three controllers (QCMC, solid; SCMC, dash-dot; GMC, dashed) were $m = 1$ and $p = 21$.</p>	47
3.1	<p>The five phases of the cell-cycle: Q (quiescent), G_1 (growth), S (DNA replication), G_2 (mitotic preparation), M (mitosis). Two cell-cycles models are developed: (i) a three-phase model considering G (lumped Q and G_1), S, and M (lumped G_2 and M) which is resolvable using DNA labeling and flow cytometry; or (ii) a four-phase structure with Q, G_1, S, and M (lumped G_2 and M) which is resolvable using DNA and RNA labeling and subsequent flow cytometry.</p>	51
3.2	<p>Tumor volume versus time. Top: Total volume starting from an initial cell distribution given by Equations (3.15)-(3.17). Bottom: Individual cell-cycle phase volumes for G-phase (N_G, dashed), S-phase (N_S, dash-dot), and M-phase (N_M, dotted) cells.</p>	58
3.3	<p>Cell distribution within G-phase (top), S-phase (middle), and M-phase (bottom) during unperturbed growth.</p>	59

3.4	Tumor volume versus time. Top: Total volume starting from an initial cell distribution given in Equations (3.18)-(3.20) (m is normalized mass). Bottom: Individual cell-cycle phase volumes for G -phase (N_G , dashed), S -phase (N_S , dash-dot), and M -phase (N_M , dotted).	61
3.5	Total cell density distribution for G -phase (dashed), S -phase (dash-dot), and M -phase (dotted) during unperturbed growth. Density progression is shown starting from day 0 until day 7.	62
3.6	Tumor volume (solid) versus time starting from an initial cell distribution given in Equations (3.18)-(3.20) (m is normalized mass). Individual cell-cycle phase volumes are shown for G -phase (dashed), S -phase (dash-dot), and M -phase (dotted).	65
3.7	Total cell density distribution for G -phase (dashed), S -phase (dash-dot), and M -phase (dotted) during unperturbed growth. Cell cycle density plots are shown, starting from the upper left, for days 1, 3, 5, 7, 10, 20, 30, 40, 50, 60, 70, 80, 110, 120, 130, and 140.	66
3.8	Total tumor volume (solid) versus time starting from an initial cell distribution of $N_G(m, 0) = 0.40e^{\frac{-(m-0.49)^2}{0.014}}$ with $N_S(m, 0) = N_M(m, 0) = 0$ (m is normalized mass). Individual cell-cycle phase volumes are shown for G -phase (dashed), S -phase (dash-dot), and M -phase (dotted).	68
3.9	Total cell density distribution for G -phase (dashed), S -phase (dash-dot), and M -phase (dotted) during unperturbed growth. Cell cycle density plots are shown, starting from the upper left, for days 1, 3, 5, 7, 10, 50, 90, 130, 170, 180, 190, 200, 210, 220, 230, and 240.	69
3.10	Total tumor volume progression (solid) starting from an initial cell distribution of $N_G(0) = 1.0$ with $N_S(a, 0) = N_M(a, 0) = 0$, and individual cell-cycle phase volumes for G -phase (dashed), S -phase (dash-dot), and M -phase (dotted).	71
3.11	Total tumor volume progression (solid) starting from an initial cell distribution of $N_Q(0) = 1.0$ with $N_G(a, 0) = N_S(a, 0) = N_M(a, 0) = 0$, and individual cell-cycle phase volumes for the quiescent cells (Q , circles), G -phase (dashed), S -phase (dash-dot), and M -phase (dotted).	73

3.12 Total tumor volume progression for the original age-structured PBE (dash-dot), three-phase saturating age-structured PBE (dashed), and four-phase saturating age-structured PBE (solid).	75
3.13 PK profiles for the <i>S</i> -phase chemotherapeutic for Schedule 1 (solid), Schedule 2 (dashed, overlay on first “hump” of Schedule 3), and Schedule 3 (dash-dot). The <i>M</i> -phase PK profile for all three schedules is the same as the <i>S</i> -phase profile for Schedule 1.	79
3.14 Top: Tumor growth profiles predicted for the three-phase saturating age-structured PBE using the regimen from Schedule 1 with a separation of 0 days (solid) and +4 days (dashed) between D_1 and D_2 therapeutic administration. Bottom: <i>S</i> - (0 days, squares; +4 days, dashed) and <i>M</i> -phase (0 days, diamonds; +4 days, dash-dot) cell cycle progression.	83
3.15 Top: Tumor growth profiles predicted for the four-phase saturating age-structured PBE using the regimen from Schedule 1 with a separation of 0 days (solid) and 4 days (dashed) between D_1 and D_2 therapeutic administration. Bottom: <i>G</i> - (0 days, circles; +4 days, dashed), <i>S</i> - (0 days, squares; +4 days, dash-dot), and <i>M</i> -phase (0 days, diamonds; +4 days, dotted) cell cycle progression.	84
3.16 Top: Tumor growth profiles predicted for the three-phase non-saturating age-structured PBE using the regimen from Schedule 1 with a separation of 0 days (solid) and 4 days (dashed) between D_1 and D_2 therapeutic administration. Bottom: <i>G</i> - (0 days, circles; +4 days, dashed), <i>S</i> - (0 days, squares; +4 days, dash-dot), and <i>M</i> -phase (0 days, diamonds; +4 days, dotted) cell cycle progression.	85
3.17 Top: Tumor growth profiles predicted for the three-phase saturating age-structured PBE using the regimen from Schedule 2 with a separation of 0 days (solid) and +4 days (dashed) between D_1 and D_2 therapeutic administration. Bottom: <i>S</i> - (0 days, squares; +4 days, dashed) and <i>M</i> -phase (0 days, diamonds; +4 days, dash-dot) cell cycle progression.	88

3.18 Top: Tumor growth profiles predicted for the four-phase saturating age-structured PBE using the regimen from Schedule 2 with a separation of 0 days (solid) and +4 days (dashed) between D_1 and D_2 therapeutic administration. Bottom: G - (0 days, circles; +4 days, dashed), S - (0 days, squares; +4 days, dash-dot), and M -phase (0 days, diamonds; +4 days, dotted) cell cycle progression.	89
3.19 Top: Tumor growth profiles predicted for the three-phase non-saturating age-structured PBE using the regimen from Schedule 2 with a separation of 0 days (solid) and +4 days (dashed) between D_1 and D_2 therapeutic administration. Bottom: G - (0 days, circles; +4 days, dashed), S - (0 days, squares; +4 days, dash-dot), and M -phase (0 days, diamonds; +4 days, dotted) cell cycle progression.	90
3.20 Top: Tumor growth profiles predicted for the three-phase saturating age-structured PBE using the regimen from Schedule 3 with a separation of 0 days (solid) and +4 days (dashed) between D_1 and D_2 therapeutic administration. Bottom: S - (0 days, squares; +4 days, dashed) and M -phase (0 days, diamonds; +4 days, dash-dot) cell cycle progression.	93
3.21 Top: Tumor growth profiles predicted for the four-phase saturating age-structured PBE using the regimen from Schedule 3 with a separation of 0 days (solid) and +4 days (dashed) between D_1 and D_2 therapeutic administration. Bottom: G - (0 days, circles; +4 days, dashed), S - (0 days, squares; +4 days, dash-dot), and M -phase (0 days, diamonds; +4 days, dotted) cell cycle progression.	94
3.22 Top: Tumor growth profiles predicted for the three-phase non-saturating age-structured PBE using the regimen from Schedule 3 with a separation of 0 days (solid) and +4 days (dashed) between D_1 and D_2 therapeutic administration. Bottom: G - (0 days, circles; +4 days, dashed), S - (0 days, squares; +4 days, dash-dot), and M -phase (0 days, diamonds; +4 days, dotted) cell cycle progression.	95

4.1	PBPK model for the distribution of Doc in plasma, various mouse tissues, and subcutaneously implanted tumor xenografts.	104
4.2	Measured Doc concentration versus time data from tumor-bearing SCID mice (circles, μ , with $\pm\sigma$ error bars, $n = 3$ mice per point) compared with mouse PBPK model predictions (lines) for plasma, liver, tumor, and red blood cells.	111
4.3	Measured Doc concentration versus time data from tumor-bearing SCID mice (circles, μ , with $\pm\sigma$ error bars, $n = 3$ mice per point) compared with mouse PBPK model predictions (lines) for spleen, lung, kidney, and heart.	112
4.4	Measured Doc concentration versus time data from tumor-bearing SCID mice (circles, μ , with $\pm\sigma$ error bars, $n = 3$ mice per point) compared with mouse PBPK model predictions (lines) for brain, “other”, muscle, and fat compartment.	113
4.5	Relative sensitivity plots for liver, lung, tumor, muscle, spleen, heart, fat, kidney, brain, “other”, plasma, and RBCs. Parameters are arranged in groups: flow rates (1-8); tissue volumes (9-21); vascular fractions (22-31); and tissue transition rates (32-56). Parameter ordering within those subgroups follow the ordering from Table 4.1: liver, lung, tumor, gut, muscle, spleen, heart, fat, kidney, brain, “other”, plasma, RBC binding, and tissue binding.	117
4.6	Predicted percentage of administered dose in plasma, liver, tumor, muscle, red blood cells, or the other compartment as a function of time.	118
4.7	Plasma (top left), liver (top right), and kidney (bottom left) Doc predictions from the model developed in Figure 4.1 (dash-dot) and those predicted by a PBPK model from the literature [5] (solid) compared with actual plasma Doc concentration versus time data from tumor-bearing SCID mice (circles, μ , with $\pm\sigma$ error bars, $n = 3$ mice per point) dosed at $10 \frac{\text{mg}}{\text{kg}}$	120
4.8	Plasma (top left), liver (top right), and kidney (bottom left) Doc predictions from the model developed in Figure 4.1 (dash-dot) and those predicted by a PBPK model from the literature [5] (solid) compared with actual plasma Doc concentration versus time data from BALB/c mice (circles) dosed at $20 \frac{\text{mg}}{\text{kg}}$	121

4.9	Measured Doc concentration versus time data from Pc-3 tumor-bearing SCID mice (circles, μ , with $\pm\sigma$ error bars, $n = 3$ mice per point) compared with mouse PBPK model predictions (lines) for the tumor compartment.	125
5.1	Measured Doc plasma concentration data in humans dosed at 50 (top left), 60 (top right), 75 (bottom left) and 35 (bottom right) $\frac{\text{mg}}{\text{m}^2}$ vs. time. Human PBPK model predictions are from the tissue-intensive PBPK (solid), the Bradshaw-Pierce PBPK (dashed), and the Bruno population PK (dash-dot) models.	134
5.2	Actual versus model predicted human plasma Doc concentrations (tissue-intensive PBPK model - circles; Bradshaw-Pierce PBPK model - squares; Bruno population PK model - diamonds) for all patients (top left), UPCI protocol 01-150 (top right), MSKCC study (bottom left), and the MSKCC study comprised only of elderly patients (bottom right).	138
5.3	Individual patient performance error at sampled time points (circles) and median performance error for a sampled time point (squares) versus time for the three investigated models (tissue-intensive PBPK model, left; Bradshaw-Pierce PBPK model, middle; Bruno population PK model, right) for all 25 patients from UPCI protocol 01-150.	140
5.4	Model predicted performance metrics (MAPE and RMSPE) for all 25 patients from UPCI protocol 01-150. Each patient has 5 associated bars: (1) tissue-intensive PBPK model; (2) Bradshaw-Pierce PBPK model [5]; (3) Bruno population PK model [2]; (4) tissue-intensive PBPK model estimating unbound Doc fraction; and (5) Bradshaw-Pierce PBPK model estimating unbound Doc fraction.	142
5.5	Model predicted performance metrics (MAPE and RMSPE) for patients from the MSKCC clinical trial [6] dosed at either 55, 75, or 35 $\frac{\text{mg}}{\text{m}^2}$. Each patient has 5 associated bars: (1) tissue-intensive PBPK model; (2) Bradshaw-Pierce PBPK model [5]; (3) Bruno population PK model [2]; (4) tissue-intensive PBPK model estimating unbound Doc fraction; and (5) Bradshaw-Pierce PBPK model estimating unbound Doc fraction.	143

5.6	Model predicted performance metrics (MAPE and RMSPE) for patients from the MSKCC clinical trial [6] dosed at $70 \frac{\text{mg}}{\text{m}^2}$. Each patient has 5 associated bars: (1) tissue-intensive PBPK model; (2) Bradshaw-Pierce PBPK model [5]; (3) Bruno population PK model [2]; (4) tissue-intensive PBPK model estimating unbound Doc fraction; and (5) Bradshaw-Pierce PBPK model estimating unbound Doc fraction.	144
5.7	Model predicted performance metrics (MAPE and RMSPE) for patients from the elderly MSKCC clinical trial [7] dosed at $35 \frac{\text{mg}}{\text{m}^2}$. Each patient has 7 associated bars: (1) tissue-intensive PBPK model; (2) Bradshaw-Pierce PBPK model [5]; (3) Bruno population PK model [2]; (4) tissue-intensive PBPK model estimating unbound Doc fraction; (5) Bradshaw-Pierce PBPK model estimating unbound Doc fraction; (6) tissue-intensive PBPK model estimating unbound Doc fraction and liver metabolism; and (7) Bradshaw-Pierce PBPK model estimating unbound Doc fraction and liver metabolism.	145
5.8	Tissue-intensive (square) and Bradshaw-Pierce (circles) PBPK model estimates for unbound fraction versus actual patient AAG concentrations. Linear regressions for the tissue-intensive (dash-dot) and Bradshaw-Pierce (dashed) PBPK models are shown plotted against the linear correlation identified by Baker <i>et al.</i> (solid) [8].	146
5.9	Estimated unbound fraction histograms ($n = 48$) for the tissue-intensive PBPK (left) and Bradshaw-Pierce PBPK (right) models.	146
5.10	Simulated Doc tumor concentration versus time plots using the tissue intensive Doc PBPK model for varying dose levels (left) and body weight (right). Left: Simulated tumor concentrations assuming a 100 g tumor in 70 kg human treated with 30 (solid), 54 (dashed), 72 (dash-dot), or 90 (dotted) $\frac{\text{mg}}{\text{m}^2}$ Doc as a 1-hour infusion. Right: Simulated Doc tumor concentrations assuming a 100 g tumor in 50 (solid), 70 (dashed), 90 (dash-dot), or 110 (dotted) kg human treated with $72 \frac{\text{mg}}{\text{m}^2}$ Doc as a 1-hour infusion.	151

5.11	Simulated Doc tumor concentration versus time plots using the tissue intensive Doc PBPK model for varying tumor volume (left) and dosing schedules (right). Left: Simulated tumor concentrations assuming a 5 (solid), 20 (dashed), 100 (dash-dot), or 500 (dotted) g tumor in 70 kg human treated with $72 \frac{\text{mg}}{\text{m}^2}$ Doc as a 1-hour infusion. Right: Simulated tumor concentrations assuming a 100 g tumor in a 70 kg human treated with either 72 (solid) or 90 (dashed) $\frac{\text{mg}}{\text{m}^2}$ Doc as a 1-hour infusion every three weeks or weekly administration of 30 (dash-dot) or 42 (dotted) $\frac{\text{mg}}{\text{m}^2}$ Doc as a 1-hour infusion.	152
6.1	Neutrophil model structure for coupling human Doc plasma concentration to PD effect [3].	160
6.2	Patient neutrophil counts obtained during the first cycle of q3w Doc treatment at 50 (circle), 60 (triangle), and 75 (square) $\frac{\text{mg}}{\text{m}^2}$. Neutrophil profile predictions are based on the original (dashed) and updated (solid) parameter sets. . . .	167
6.3	Individual (left) and population (right) predicted patient neutrophil counts versus actual patient neutrophil count measurements.	169
6.4	Predicted ANC resulting from administration of Doc at various dose level and schedule combinations (a) q3w at 70, 85, and 100 $\frac{\text{mg}}{\text{m}^2}$ (represented by dash-dot, solid, and dashed lines), (b) “weekly” at 28, 35, and 40 $\frac{\text{mg}}{\text{m}^2}$ (represented by dash-dot, solid, and dashed lines), or (c) every other week at 40, 50, and 60 $\frac{\text{mg}}{\text{m}^2}$ (represented by dash-dot, solid, and dashed lines). Subfigure (d) compares the median delivered dose for each of the three regimens, corresponding to q3w 85 $\frac{\text{mg}}{\text{m}^2}$ (solid), biweekly 50 $\frac{\text{mg}}{\text{m}^2}$ (dashed), and “weekly” 35 $\frac{\text{mg}}{\text{m}^2}$ (dash-dot). . .	172
6.5	Predicted ANC (solid) and representative patient ANC data (circles) versus time. Doc dose was 35 $\frac{\text{mg}}{\text{m}^2}$ “weekly”.	173
6.6	Model predicted progression of each state (P -dashed, T_1 -solid, T_2 -dash-dot; T_3 -dotted; N -circles) from the Friberg <i>et al.</i> neutrophil model following administration of 70 $\frac{\text{mg}}{\text{m}^2}$ Doc over a 1-hour infusion on day 0.	175

6.7	Model predicted effect-site concentration as a function of k_f value versus time for a Doc dose of $70 \frac{\text{mg}}{\text{m}^2}$ over a 1-hour infusion to a typical patient (k_f values of 1, 5, and 20 given by circles, dotted, and dash-dot, respectively). Also shown are the original Doc plasma concentration (dashed) and selected tissue Doc concentrations (solid) predicted by the tissue-intensive PBPK model.	177
6.8	Median (solid), min (dash-dot), and max (dash-dot) model predicted neutrophil count progressions for the population using either the updated Friberg neutrophil model (top) or the Friberg model appended with an effect-compartment having a linear PD effect, and $k_f = 5 \text{ day}^{-1}$ (bottom). Treatment results over a 12 week cycle are shown with Doc administered q3w at $70 \frac{\text{mg}}{\text{m}^2}$ (left) and “weekly” at $30 \frac{\text{mg}}{\text{m}^2}$ (right).	180
6.9	Median (solid), min (dash-dot), and max (dash-dot) model predicted neutrophil count progressions for the population using the Friberg model appended with an effect-compartment, $k_f = 5 \text{ day}^{-1}$, and either a log-linear (top) or sigmoidal (bottom) PD effect term. Treatment results over a 12 week cycle are shown with Doc administered q3w at $70 \frac{\text{mg}}{\text{m}^2}$ (left) and “weekly” at $30 \frac{\text{mg}}{\text{m}^2}$ (right).	181
6.10	HSVs for the full 36 ODE human PBPK model. Inset: HSVs for the first 7 states.	183
6.11	ANC predictions (top) and input profiles (bottom) for three separate Doc dosing regimens: $70 \frac{\text{mg}}{\text{m}^2}$ q3w (dash-dot); $30 \frac{\text{mg}}{\text{m}^2}$ “weekly” (dotted); and dosing constrained to maximize delivered drug subject to Grade 2 and 3 neutropenia constraints (dashed), for a low risk patient modeled using the updated Friberg neutrophil model. Neutropenia toxicity Grade 2, 3, and 4 are represented as horizontal lines (dashed) in the top figure, with toxicity grades corresponding to $2.0 \times 10^9 \frac{\text{cells}}{\text{L}}$, $1.0 \times 10^9 \frac{\text{cells}}{\text{L}}$, and $0.5 \times 10^9 \frac{\text{cells}}{\text{L}}$, respectively.	185

6.12	ANC predictions (top) and input profiles (bottom) for Doc regimen predictions constrained to maximize delivered drug subject to Grade 2 and 3 neutropenia constraints (dashed) for a median (left) and high risk (right) patient with the updated Friberg neutrophil model. Also shown are two standard Doc regimens: $70 \frac{\text{mg}}{\text{m}^2}$ q3w (dash-dot) and $30 \frac{\text{mg}}{\text{m}^2}$ “weekly” (dotted). Neutropenia toxicity Grade 2, 3, and 4 are represented as horizontal lines (dashed) in the top figure, with toxicity grades corresponding to $2.0 \times 10^9 \frac{\text{cells}}{\text{L}}$, $1.0 \times 10^9 \frac{\text{cells}}{\text{L}}$, and $0.5 \times 10^9 \frac{\text{cells}}{\text{L}}$, respectively.	187
6.13	ANC predictions (top) and input profiles (bottom) for Doc regimen predictions constrained to maximize delivered drug subject to Grade 2 and 3 neutropenia constraints (dashed) for a median (left) and high risk (right) patient with a log-linear PD effect and effect-compartment ($k_f = 5 \frac{1}{\text{day}}$). Also shown are two standard Doc regimens: $70 \frac{\text{mg}}{\text{m}^2}$ q3w (dash-dot) and $30 \frac{\text{mg}}{\text{m}^2}$ “weekly” (dotted). Neutropenia toxicity Grade 2, 3, and 4 are represented as horizontal lines (dashed) in the top figure, with toxicity grades corresponding to $2.0 \times 10^9 \frac{\text{cells}}{\text{L}}$, $1.0 \times 10^9 \frac{\text{cells}}{\text{L}}$, and $0.5 \times 10^9 \frac{\text{cells}}{\text{L}}$, respectively.	188
6.14	ANC predictions (top) and input profiles (bottom) for Doc regimen predictions constrained to maximize delivered drug subject to Grade 2 and 3 neutropenia constraints (dashed) for a median (left) and high risk (right) patient with a sigmoidal PD effect and effect-compartment ($k_f = 5 \frac{1}{\text{day}}$). Also shown are two standard Doc regimens: $70 \frac{\text{mg}}{\text{m}^2}$ q3w (dash-dot) and $30 \frac{\text{mg}}{\text{m}^2}$ “weekly” (dotted). Neutropenia toxicity Grade 2, 3, and 4 are represented as horizontal lines (dashed) in the top figure, with toxicity grades corresponding to $2.0 \times 10^9 \frac{\text{cells}}{\text{L}}$, $1.0 \times 10^9 \frac{\text{cells}}{\text{L}}$, and $0.5 \times 10^9 \frac{\text{cells}}{\text{L}}$, respectively.	190
6.15	Median (solid), min (dash-dot), and max (dash-dot) model predicted neutrophil count progressions for the population using the Friberg model appended with an effect-compartment, $k_f = 5 \text{ day}^{-1}$, and either a log-linear (top) or sigmoidal (bottom) PD effect term. Treatment results over a 12 week cycle are shown with Doc administered according to the Doc schedule developed for a median (left) and high risk (right) patient.	191

C1	Measured Doc plasma concentration data in humans from UPCI protocol 01-150 dosed at $50 \frac{\text{mg}}{\text{m}^2}$ vs. human PBPK model predictions from the tissue-intensive PBPK (solid), the Bradshaw-Pierce PBPK (dashed), and the population PK Bruno (dash-dot) model.	216
C2	Measured Doc plasma concentration data in humans from UPCI protocol 01-150 dosed at $60 \frac{\text{mg}}{\text{m}^2}$ vs. human PBPK model predictions from the tissue-intensive PBPK (solid), the Bradshaw-Pierce PBPK (dashed), and the population PK Bruno (dash-dot) model.	217
C3	Measured Doc plasma concentration data in humans from UPCI protocol 01-150 dosed at $60 \frac{\text{mg}}{\text{m}^2}$ vs. human PBPK model predictions from the tissue-intensive PBPK (solid), the Bradshaw-Pierce PBPK (dashed), and the population PK Bruno (dash-dot) model.	218
C4	Measured Doc plasma concentration data in humans from UPCI protocol 01-150 dosed at $75 \frac{\text{mg}}{\text{m}^2}$ vs. human PBPK model predictions from the tissue-intensive PBPK (solid), the Bradshaw-Pierce PBPK (dashed), and the population PK Bruno (dash-dot) model.	219
C5	Measured Doc plasma concentration data in humans from a Phase 1 clinical trial at MSKCC [6] dosed at $55 \frac{\text{mg}}{\text{m}^2}$ vs. human PBPK model predictions from the tissue-intensive PBPK (solid), the Bradshaw-Pierce PBPK (dashed), and the population PK Bruno (dash-dot) model.	220
C6	Measured Doc plasma concentration data in humans from a Phase 1 clinical trial at MSKCC [6] dosed at $70 \frac{\text{mg}}{\text{m}^2}$ vs. human PBPK model predictions from the tissue-intensive PBPK (solid), the Bradshaw-Pierce PBPK (dashed), and the population PK Bruno (dash-dot) model.	221
C7	Measured Doc plasma concentration data in humans from a Phase 1 clinical trial at MSKCC [6] dosed at $70 \frac{\text{mg}}{\text{m}^2}$ vs. human PBPK model predictions from the tissue-intensive PBPK (solid), the Bradshaw-Pierce PBPK (dashed), and the population PK Bruno (dash-dot) model.	222

C8	Measured Doc plasma concentration data in humans from a Phase 1 clinical trial at MSKCC [6] dosed at $70 \frac{\text{mg}}{\text{m}^2}$ vs. human PBPK model predictions from the tissue-intensive PBPK (solid), the Bradshaw-Pierce PBPK (dashed), and the population PK Bruno (dash-dot) model.	223
C9	Measured Doc plasma concentration data in humans from a Phase 1 clinical trial at MSKCC [6] dosed at $75 \frac{\text{mg}}{\text{m}^2}$ vs. human PBPK model predictions from the tissue-intensive PBPK (solid), the Bradshaw-Pierce PBPK (dashed), and the population PK Bruno (dash-dot) model.	224
C10	Measured Doc plasma concentration data in humans from a Phase 1 clinical trial at MSKCC [6] dosed at $35 \frac{\text{mg}}{\text{m}^2}$ vs. human PBPK model predictions from the tissue-intensive PBPK (solid), the Bradshaw-Pierce PBPK (dashed), and the population PK Bruno (dash-dot) model.	225
C11	Measured Doc plasma concentration data in humans from a Phase 1 clinical trial at MSKCC in elderly patients dosed at $35 \frac{\text{mg}}{\text{m}^2}$ vs. human PBPK model predictions from the tissue-intensive PBPK (solid), the Bradshaw-Pierce PBPK (dashed), and the population PK Bruno (dash-dot) model.	226
D1	Measured Doc plasma concentration data in humans from UPCI protocol 01-150 dosed at $50 \frac{\text{mg}}{\text{m}^2}$ vs. human PBPK model predictions from the tissue-intensive PBPK (solid), the Bradshaw-Pierce PBPK (dashed), and the population PK Bruno (dash-dot) model.	227
D2	Measured Doc plasma concentration data in humans from UPCI protocol 01-150 dosed at $60 \frac{\text{mg}}{\text{m}^2}$ vs. human PBPK model predictions from the tissue-intensive PBPK (solid), the Bradshaw-Pierce PBPK (dashed), and the population PK Bruno (dash-dot) model.	228
D3	Measured Doc plasma concentration data in humans from UPCI protocol 01-150 dosed at $60 \frac{\text{mg}}{\text{m}^2}$ vs. human PBPK model predictions from the tissue-intensive PBPK (solid), the Bradshaw-Pierce PBPK (dashed), and the population PK Bruno (dash-dot) model.	229

D4	Measured Doc plasma concentration data in humans from UPCI protocol 01-150 dosed at $75 \frac{\text{mg}}{\text{m}^2}$ vs. human PBPK model predictions from the tissue-intensive PBPK (solid), the Bradshaw-Pierce PBPK (dashed), and the population PK Bruno (dash-dot) model.	230
D5	Measured Doc plasma concentration data in humans from a Phase 1 clinical trial at MSKCC [6] dosed at $55 \frac{\text{mg}}{\text{m}^2}$ vs. human PBPK model predictions from the tissue-intensive PBPK (solid), the Bradshaw-Pierce PBPK (dashed), and the population PK Bruno (dash-dot) model.	231
D6	Measured Doc plasma concentration data in humans from a Phase 1 clinical trial at MSKCC [6] dosed at $70 \frac{\text{mg}}{\text{m}^2}$ vs. human PBPK model predictions from the tissue-intensive PBPK (solid), the Bradshaw-Pierce PBPK (dashed), and the population PK Bruno (dash-dot) model.	232
D7	Measured Doc plasma concentration data in humans from a Phase 1 clinical trial at MSKCC [6] dosed at $70 \frac{\text{mg}}{\text{m}^2}$ vs. human PBPK model predictions from the tissue-intensive PBPK (solid), the Bradshaw-Pierce PBPK (dashed), and the population PK Bruno (dash-dot) model.	233
D8	Measured Doc plasma concentration data in humans from a Phase 1 clinical trial at MSKCC [6] dosed at $70 \frac{\text{mg}}{\text{m}^2}$ vs. human PBPK model predictions from the tissue-intensive PBPK (solid), the Bradshaw-Pierce PBPK (dashed), and the population PK Bruno (dash-dot) model.	234
D9	Measured Doc plasma concentration data in humans from a Phase 1 clinical trial at MSKCC [6] dosed at $75 \frac{\text{mg}}{\text{m}^2}$ vs. human PBPK model predictions from the tissue-intensive PBPK (solid), the Bradshaw-Pierce PBPK (dashed), and the population PK Bruno (dash-dot) model.	235
D10	Measured Doc plasma concentration data in humans from a Phase 1 clinical trial at MSKCC [6] dosed at $35 \frac{\text{mg}}{\text{m}^2}$ vs. human PBPK model predictions from the tissue-intensive PBPK (solid), the Bradshaw-Pierce PBPK (dashed), and the population PK Bruno (dash-dot) model.	236

D11 Measured Doc plasma concentration data in humans from a Phase 1 clinical trial at MSKCC in elderly patients dosed at $35 \frac{\text{mg}}{\text{m}^2}$ vs. human PBPK model predictions from the tissue-intensive PBPK (solid), the Bradshaw-Pierce PBPK (dashed), and the population PK Bruno (dash-dot) model. . . 237

PREFACE

If you are reading this thesis, and yours is not one of the six names on the first two pages, then I can only assume that I have finally completed my doctoral work, i.e., 20th grade. To have made it through so many years of hardships and heartaches, support must have been given often and unconditional. My case is no exception, and I would like to spend a few words thanking those who have helped me reach where I am today.

First and foremost, I'd like to thank my family for their support through the years. While I'm sure that no one envisioned the two decades plus of schooling that would follow my kicking and screaming entrance into this world, I have received the utmost support and encourage from my family in each of my academic endeavors and would not be where I am today without your help. Thank you for everything, and I look forward to the next family holiday where we no longer have to deal with awkward questions like "Are you still in school?" and "When are you supposed to finish?" And to my sister Jordan (not to be confused with brother Jordan), I made it before you finished.

I'd also like to thank the other graduate students who helped shaped me into some facsimile of a researcher and endured my antics on a daily basis. Thank you John Harrold and Abhishek Soni, my first generation lab mates, for helping in the education of a naive undergraduate into a legitimate researcher. Your scientific and political discussions were sorely missed in my finishing year, but the influence you two had on both my critical thinking and character was profound. Thanks to Chad Kanick and Anirban Roy, my second generation lab mates, who likewise provided valuable intellectual musings and extreme patience on my day-to-day behavior. I'm sure there were multiple lab wagers on what random topic I would walk through the door yelling about. Both of you took my distractions and personality quirks in stride, and for that I am thankful. Lastly, thank you Yannick Heintz for your

counsel and for sharing a shady apartment for all these years. You are a gentlemen and a scholar.

As a chemical engineer it is second nature to draw parallels between dose scheduling problems and control problems involving more typical instrumentation from the chemical engineering field. Luckily, I had many opportunities to speak with individuals with preclinical and clinical experience to keep me grounded in the reality that these were living individuals/animals we were dealing with and not simply the inlet valve of a system. I can barely recall the naivete I had when I began cancer research in 2002, but my present understanding and graduation would not have been possible without our collaborators from the Hillman and weekly PK lunch meetings, with special mention to Dr. Julie Eiseman, Dr. Merrill Egorin, Dr. Robert Bies, and Dr. Jan Beumer.

During my time as a graduate student, as I was lucky enough to find a special someone in my life, and I would like to thank Amy for her support and for keeping what may otherwise have been an uncontrollable ego in check. Your perspective on problems was insightful, and your patience was inspiring. A number of people have also said you have been a positive influence on my life. Who am I to argue with the opinion of the masses?

Finally, I would like to thank Robert Parker for being an advisor in the truest sense of the word. One expects an advisor to aid with the course of research, but no one informs a graduate student about the other concerns that will arise throughout their research tenure. It is a tumultuous time in the life of a graduate student as concerns about future careers and life plans are intermingled with daily research. Dr. Parker was always available for advice, and for that I am grateful. He even taught me how to properly swing at a volleyball while I was here.

And in the interest of thoroughness, thank you coffee for being a stimulant, and thank you “bad” action movies for being the ideal blend of entertainment while not distracting me from my work.

Threshold! Take us to the Threshold!

1.0 INTRODUCTION

Cancer is a collection of diseases resulting from a series of genetic mutations that is characterized by an imbalance between cell proliferation and apoptosis, or programmed cell death [9]. Currently, cancer is the leading cause of death in adult Americans under the age of 85 and is expected to claim over 565,650 lives in 2008 [10]. In addition, the total disease burden, including treatment costs and loss of productivity, was estimated at \$219.2 billion in 2007, providing both societal and monetary reasons for improving cancer treatment regimens [10].

Current cancer treatment modalities include surgical excision of the tumor mass whenever possible, site-specific treatments (*i.e.*, radiation or photodynamic therapy) when the tumor is localized but not resectable, and systemic administration of a chemotherapeutic agent (that is commonly cytotoxic). The last modality is commonly employed as a single agent, in combination with additional chemotherapeutics, or in conjunction with one or more of the previously mentioned treatment modalities. Systemic chemotherapeutic treatments have numerous advantages, such as an ability to eliminate undetected metastases and doses that can be taken without hospital visits in the case of oral medication. Systemic treatments also have failings, however, the most notable of which is a lack of selectivity in targeting tumor cells. Chemotherapeutics affect all rapidly proliferating cell types in a patient, including gastrointestinal, epithelial, and hematopoietic stem cells, the destruction of which results in the most common toxicities encountered during treatment with cytotoxic agents. The degree to which these toxicity effects can be tolerated are determined in extensive preclinical and clinical trials, during which pharmacokinetic (plasma drug concentration and metabolites) and pharmacodynamic (tumor regression and toxicity) data are collected.

However, the goal of these trials is not on developing the true optimal dose regimen. Rather, protocols focus on demonstrating efficacy and establishing the maximum tolerated dose of the drug while using the same schedule previously used for drugs with similar mechanisms of action. Due to monetary, time, and ethical restrictions, as well as the combinatorial nature of the problem, all feasible dosing schedules, drug dosing levels, and dosing combinations cannot be evaluated in clinical trials. Simulations, on the other hand, provide a low-cost alternative for evaluating the plethora of possible dosing schedules and determining which, if any, could theoretically increase treatment efficacy and/or patient quality of life if implemented in the clinic. Three components are essential in developing these simulations as shown schematically in Figure 1.1: (i) a pharmacokinetic (PK) model for the delivered drug; (ii) a pharmacodynamic (PD) model for the drug effect (toxicity and/or tumor response); and (iii) a model-based algorithm for calculating candidate treatment regimens based on the constructed models, implemented constraints, and objective function.

Following administration of a therapeutic, concentrations of the drug in the plasma and throughout the system will be observed to increase, then decrease back to homeostatic values (or zero) over time. In turn, drug in the system will result in a number of downstream PD effects, including, but not limited to, tumor regression, reduction in circulating neutrophil count, and decreased body weight. In the context of control systems, this connectivity is considered as an open-loop system, where an administered input results in a downstream system effect. When the resulting effect information is used to alter the input, this is considered a closed-loop system [11]. In a clinical context, the clinician serves this role, evaluating the patient outcome of a treatment and making informed alterations to the dosing level accordingly. Usually, the clinician will only make decisions regarding alterations to the dosing level or continuation of the treatment. Alterations to the dosing schedule are avoided due to FDA regulations, the complexity of the problem, and limited experimental evidence regarding increased efficacy resulting from dose schedule alterations.

Alternatively, decisions on input changes can be established using PK and PD model approximations of the patient, a controller framework, and an objective function that optimizes performance according to model-predicted PD effects and/or actual patient measurements by manipulating available inputs. The state of the system (current patient

measurements) and desired output are both provided to the algorithm; based upon a user-defined objective function, the input alterations which minimize the objective function are found and will either be administered to the patient (true in an absolute close-loop implementation) or, for the case of chemotherapeutic treatment, will be examined off-line and administered to the patient on the following treatment visit if accepted.

1.1 PHARMACOKINETIC MODELS

Pharmacokinetics describes the time course of distribution, absorption, metabolism, and excretion for an administered drug [12, 13]. In addition, PK aids in determining the route of drug administration and dosing level. Finally, it is a necessary precursor to drug approval by the FDA [14]. Three types of PK models, ranging from simplest to most complex, are described in the literature: (i) non-compartmental models; (ii) compartmental models; and (iii) physiologically-based pharmacokinetic (PBPK) models.

The simplest and most commonly employed PK analytical tool is non-compartmental modeling. This modeling technique uses statistically-based methods to calculate patient relevant metrics such as drug clearance and drug exposure based upon an area under the curve (AUC) calculation. This approach provides information regarding individual patient data and may be predictive of population metrics across other studies involving the same compound. However, each altered experimental variable (*e.g.*, dosing schedules, infusion duration, dosing levels, etc.) reduces the likelihood of accurate extrapolation of non-compartmental model results. This type of analysis accompanies a majority of clinical trials in the country and is commonly employed as a means of finding correlations between two measures, such as patient toxicity and clearance or patient survival and AUC [15].

Another type of PK modeling, the compartmental approach, uses ordinary differential equations (ODEs) coupled via a compartmental structure to relate drug input to drug concentration output as a function of time. A generic compartmental PK model with intravenous drug infusion and clearance from the central compartment is shown in Figure 1.2 (solid line). Additional compartments may be added to account for lumped-tissue absorption

and release dynamics which may affect plasma PK (dotted lines and compartments, Figure 1.2). Alternatively, these models can be appended with additional compartments to describe drug deposition in other tissues and/or tumor (dashed-lines and compartments, Figure 1.2) if the necessary drug concentration versus time data for that tissue was obtained. Transfer rates between remote compartments and the central compartment, as well as the elimination rate from the central compartment, are assumed to be linear with respect to drug concentration, though nonlinear relationships, such as Michaelis-Menten kinetics, may also be employed. Finally, central compartment volume scales plasma concentration and can be used to estimate tissue distribution and protein binding for the drug in question.

Compartmental modeling is the second most common PK modeling technique, and the developed models can be fit not only to individual data, but to sampled data from an entire population [16]. Furthermore, these population models may be either representative of the population PK or capable of predicting individual PK based on patient specific measures directly affecting parameters within the population PK model [16]. Population PK models are constructed from multiple individual data sets, with parameter values and distributions capable of describing the intra- and inter-individual PK variability observed from the population [17, 18, 19]. On the other hand, these models can also be predictive of individual PK profiles by including patient covariates, such as age, gender, liver function, etc., within parameter calculations [2, 20, 21, 22, 23, 24, 25, 26, 27, 28]. Many standard analytical programs in the community such as NONMEM, ADAPT II, and WinNonlin have pre-made structures for the generation and analysis of low-order compartmental structures [29, 30]. Finally, these models can also be used for calculating the same clinically important parameters (AUC, clearance, etc.) as non-compartmental models.

Compartmental models have a few disadvantages, however. A key shortcoming is that the model structure represents neither the anatomy nor the physiology of the species in question. Furthermore, the estimated parameters have limited physiological significance, representing a mathematical fit to the data rather than individual absorption and clearance dynamics encountered within the subject. Also, the model structure is dosing route dependent. To account for separate administration routes, not only are additional compartments necessary, but the entire model structure and parameters may need to be reevaluated. Finally,

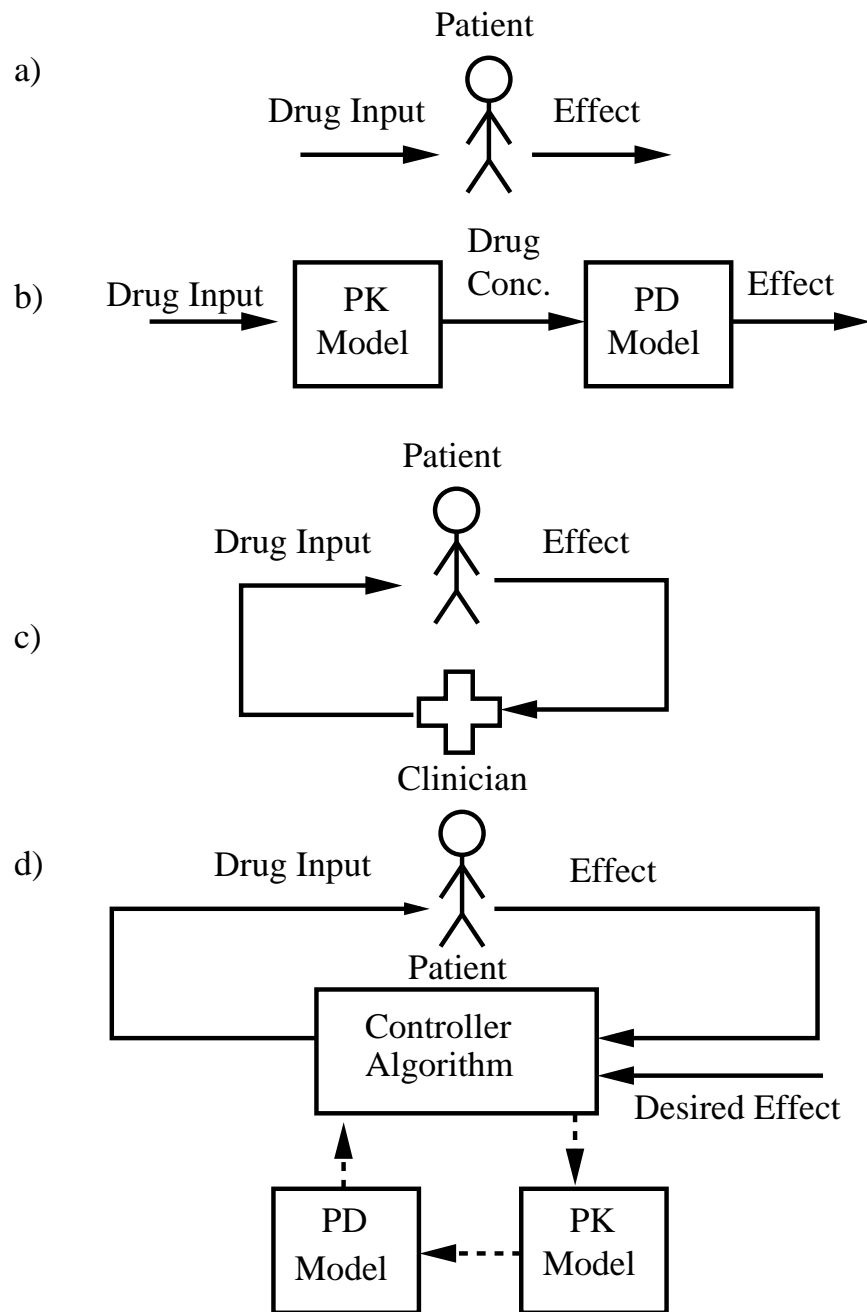


Figure 1.1: a) Open-loop therapeutic delivery as viewed clinically; b) open-loop PK-driven treatment in mathematical block form; c) closed-loop therapeutic delivery managed by a clinician; and d) closed-loop treatment delivery algorithm in mathematical block form.

the allometric scale-up for these models from animals to humans, which is the primary treatment group of interest, may prove unreliable if the modeled drug displays long term tissue retention, is delivered orally, or as additional tissues are incorporated within the compartmental model [31, 32, 33]. These shortcomings can be addressed by developing a PBPK model.

PBPK models use knowledge of the anatomy and physiology of the studied species to develop a PK model that accurately describes plasma, tissue, and, in some cases, tumor concentrations, following drug delivery. These models have found extensive use in toxicology studies [34, 35], delivery of anesthetics [36, 37, 38], treating diabetes [39, 40], and, more recently, in describing chemotherapeutic distribution [5, 41, 42, 43]. An example PBPK structure is shown in Figure 1.3. Individual tissue compartments are represented by ordinary differential equations (ODEs); one equation represents a perfusion-limited tissue, with additional sub-compartments (and equations) included for diffusion-limited tissues. Individual tissues are included based on deposition areas of interest and available data, while the remaining tissues can be lumped together into an “other” compartment (also described as “carcass”, “peripheral”, or “remainder” depending on the investigating group and species in question) as a first step in reducing model complexity and the number of parameters requiring estimation. Drugs are administered via intravenous injection (into the venous compartment), administered orally (into the gut), inhaled (necessitating a pulmonary compartment in addition to the lungs), injected subcutaneously (into a skin compartment), or injected intramuscularly (through the muscle compartment).

For single equation tissue structures, plasma-to-tissue partition relationships are included within these models by introducing partition coefficients that alter the drug concentration in blood flowing out of tissues. Elimination from these tissues, whether metabolic or excretory, is introduced as either linear or nonlinear elimination rates based upon the unbound concentration of drug within the respective tissue. The metabolic rates are often obtained from *in vitro* experiments, while more macroscopic elimination pathways are based on *in vivo* collection of urine and feces. The concentration of drug leaving a tissue may be further altered due to binding kinetics, which introduce additional nonlinearities or dynamics into the PBPK model and are often not fully evaluated during model development (*e.g.*, extrapolated

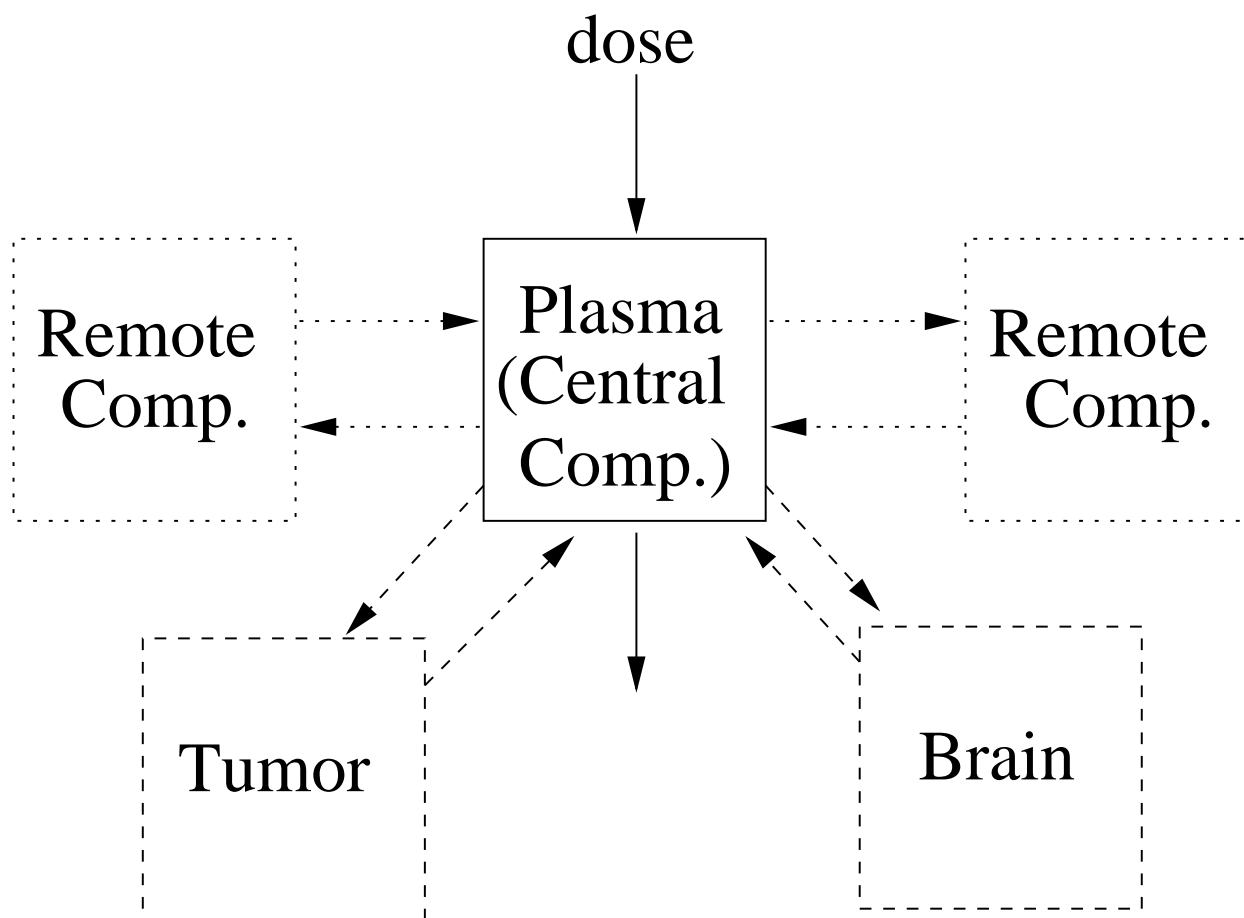


Figure 1.2: Representative compartmental PK model structure (solid) with both additional remote compartments (dotted) and tissue-specific compartments (dashed) for representing multiple plasma half-lives and specific tissue distribution, respectively.

model behavior may predict unrealistic PK results). On the other hand, when tissues are represented as multiple ODEs, the volume of the tissue is divided between all compartments utilizing a vascular fraction parameter obtained from the literature or estimated from experimental data. Transport between compartments can be governed by either a single transfer rate, driven by the concentration gradient between the two compartments, or by unidirectional transport rates between compartments, often necessary when the transport dynamics for a drug within a tissue is governed by non-gradient mechanisms, such as active transport and internal binding. In the latter case, the vascular fraction and exit transit rate may not be estimated independently, requiring prior knowledge or strict bounds on one of those parameters, typically the vascular fraction. Metabolism and excretory dynamics are included within the interstitial compartment of these models, and parameter values can be obtained either from *in vitro* studies or by estimating the parameters to fit experimental data.

Two main disadvantages of PBPK models are the amount of data necessary to estimate parameters and validate the model as well as the complexity of the system compared to more traditional compartmental models. Tissue volumes, blood flow rates, vascular fractions in tissues, intra-tissue exchange rates, and clearance rates for the drug are all required for constructing this type of model. Fortunately, average values for many of these parameters can be obtained from the literature (*i.e.*, blood flow rates and blood volume fractions) [1]; other parameters, such as tissue volumes, are collected during the course of a detailed PK study (lacking this, average values are also obtainable from the literature). The remaining parameters have to be estimated using the study data. Despite the complexity and data-intensive nature of PBPK models, they have proven reliable in predicting plasma profiles following model scale-up to larger species [5, 37, 41, 44, 45].

1.2 PHARMACODYNAMIC MODELS

PD describes the effect that the drug has on the system, where this effect may be desirable (*e.g.*, tumor regression) or harmful (*e.g.*, manifestation of toxicity). Ideally, PD models

would be PK-driven (Figure 1.1b), incorporating drug concentrations within the specific tissue or at the site of action [46]. Currently, such measurements are rarely obtainable in the clinic and can only be estimated using PK models incorporating tissue compartments, though non-invasive imaging techniques may address this limitation in the future. More often, PK-driven PD effect is estimated based on plasma drug concentrations. As the plasma concentration may have different dynamics than the tumor drug concentration, the use of plasma concentration may lead to over- or under-prediction of actual drug effect [47].

For cases involving chemotherapeutic PD effect, realistic PD representations may account for cell surface receptor density and kinetics, internal signaling cascades, or intracellular drug transport following exposure to a therapeutic. Such models, however, require substantial amounts of data to properly describe these biologic pathways and the robust interdependency that exists between them. Due to the complexity of biological systems, mechanistic models for PD effect are often not explored, instead settling for macroscopic relationships capable of describing the observed PD outcomes. Here, a number of simple, causal relationships (*i.e.*, linear, log-linear, Michaelis-Menten, etc.) have been explored in the literature. These typically relate a PK profile to observed PD effects including tumor response [48, 49], neutrophil and leukocyte toxicity [3, 50, 51], diabetes [39, 52, 53, 54], human immunodeficiency virus treatment [55, 56, 57], and depth of anesthesia [58, 59, 60], to name a few.

Common cancer PD models describe anti-tumor effect as being proportional to a bilinear combination of the affected tumor population and the plasma drug concentration [61]. This relationship is also primarily employed in predicting the apoptosis of healthy proliferating cells for toxicity predictions. More complicated functions, such as Michaelis-Menten kinetics, indirect response models, sigmoidal models (*e.g.*, Hill functions), or a necessary threshold plasma drug concentration, can also be employed for modeling PD effects [46, 62, 63, 64]. While the bulk of model-based cancer treatment has focused on tumor models and the subsequent inclusion of drug effect, others have addressed the treatment problem through the incorporation of suitable toxicity models for the delivered drug [65, 66]. Summaries of both approaches are discussed below.

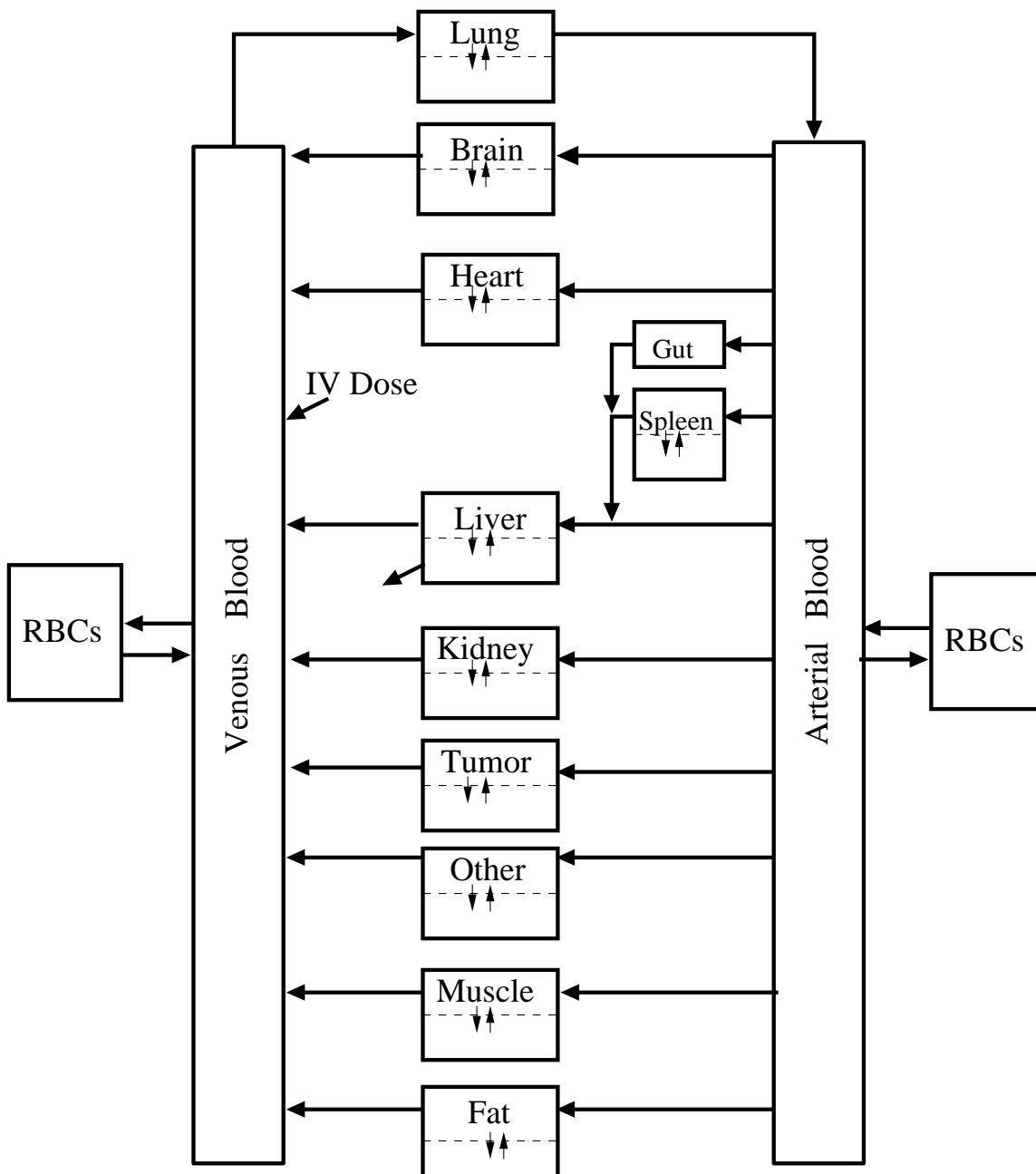


Figure 1.3: Physiologically-based pharmacokinetic (PBPK) model for the distribution of docetaxel (Doc) in plasma, various body tissues, and subcutaneously implanted tumor xenografts.

1.2.1 Tumor Growth Models

Tumor modeling approaches can be grouped into two categories: homogeneous and heterogeneous. The basic homogeneous tumor model is a single, linear ODE characterizing exponential growth with a single parameter governing the doubling time of the tumor. This model accurately describes blood-born cancer progressions (*e.g.*, leukemia), but over predicts the growth progression of solid tumors except over very short windows (*e.g.*, one doubling) [67]. A slightly more complex nonlinear ODE representation is the Gompertz equation, which has been shown to accurately describe clinical data for a wide range of solid tumors [68, 69]. The two parameter Gompertz equation predicts saturating tumor growth as the total tumor volume approaches a preset “plateau” volume. As an approximation to the Gompertz equation, Simeoni *et al.* have constructed models that “switch” growth profiles at a predefined tumor volume [49]. This “switch” alters the growth profile from exponential to linear or continues the exponential progression at a slower doubling time. This model structure is useful for describing tumor growth over multiple doubling times where a single exponential model cannot accurately model the data. The anti-tumor PD effect of administered drugs is incorporated as a bilinear term, that is, a product of drug concentration and the total tumor mass present scaled by an estimated drug effect rate [70]. However, assuming an equal drug effect on the entire tumor population may result in an over-estimate of anti-tumor effect, especially as radiation and most chemotherapeutics are more effective during specific phases of the cell-cycle [71]. Incorporating cell phase information within the model structure, therefore, would allow for a more biologically relevant incorporation of treatment effect and increased model accuracy in response to treatment.

Cell-cycle models seek to describe the biological phase progression of cells. There are five identified cell phases, corresponding to growth (G_1), DNA replication (S), mitotic preparation (G_2), mitosis (M), and quiescence (Q) as shown in Figure 1.4. Actively proliferating cells progress through the cell division loop (G_1 to M and back to G_1), while non-cycling (*i.e.*, the chemotherapy or radiation insensitive population) reside in the quiescent Q -phase [72]. Cell phases are typically resolved by a combination of proliferation, DNA, or RNA staining; however, it is often difficult to resolve individual phase fractions for all five phases

of the cell-cycle [4]. Therefore, constructing a model with explicit representation of all phases would be overparameterized, thereby leading to high parameter sensitivity and uncertainty. Grouping cell phases together reduces the amount of information necessary to model the system in this framework while simultaneously reducing overall model complexity. Smith and Martin have reduced the cell-cycle model to its basic component, namely proliferating and quiescent cells [48, 73]. This two ODE model better incorporates drug effects targeting proliferating cells, however, most chemotherapeutics target proliferation mechanisms specific to certain phases of the cell-cycle. A number of models have been developed [74, 75, 76, 77] to describe either G_1 -, S -, or M -phase (the latter being a combination of G_2 - and M -phase cells, hereafter referred to solely as M -phase within this dissertation) specific drug effects with varying degrees of complexity (*e.g.*, additional equations for All of these models have linear transition rates between phases that can only return exponential tumor volume progression at the macroscopic scale when left untreated. The introduction of saturating phase-transition rates, similar in philosophy to the Gompertz model, or the selective accumulation of cells in a non-cycling compartment, Q , overcomes this limitation. Such models maintain cell-cycle specific information while amassing cells in either Q or a lumped G -phase [78, 79, 80]. These models are often sufficient for describing bulk tumor data observed clinically; however, these models simplify reality by assuming that the tumor is composed of lumped populations of cells. In actuality, these cells have individual transition rates, are exposed to various concentrations of drugs dependent on an erratic vascular network, and may not be actively dividing depending on their overall location within the tumor and nutrient availability.

One class of models that accounts for the heterogeneous properties of tumors is population balance equation (PBE) models. These models incorporate internal cellular properties (*e.g.*, age, mass, or DNA content) and allow for distributed progression through cell phases and drug effect [80, 81, 82, 83, 84, 85, 86]. The discussion of this class of tumor models will be explored in greater depth in Chapter 3. An alternative structure, the cell ensemble model, uses equations to define each cell with parameters fixed from a preset distribution [87]. Such models are simpler for a high number of intracellular properties, but are ill-suited for handling cell division, an essential component of tumor progression. Spatial inhomogeneity of the tumor may also be essential for predicting tumor invasiveness and

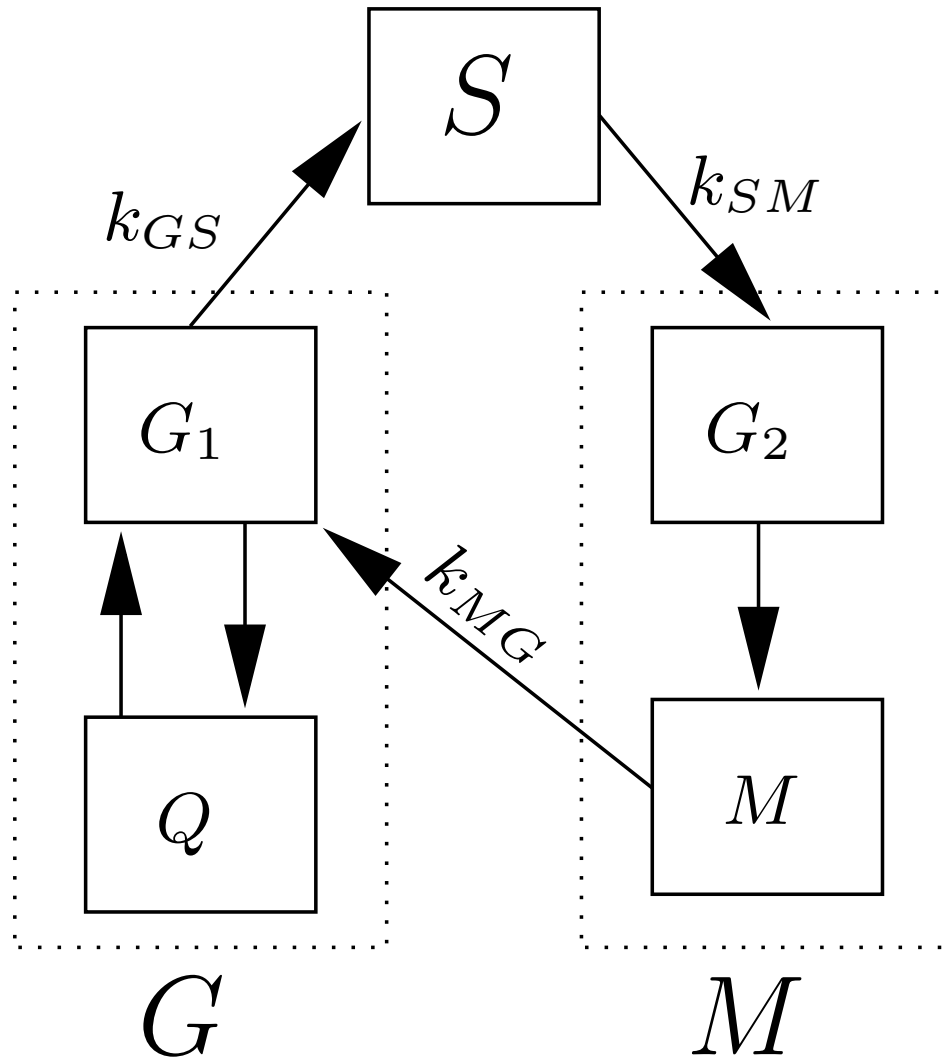


Figure 1.4: Cell cycle model showing phases of the cell-cycle, Q , G_1 , S , G_2 , and M . Also shown are experimentally reconcilable phases based on DNA analysis: G ($Q + G_1$), S , and M ($G_2 + M$).

drug concentration throughout the tumor [88, 89, 90, 91, 92, 93]. Studies have demonstrated that many chemotherapeutics have difficulty traversing the leaky internal vascular networks of tumors, with a majority of exposure occurring in the outer periphery of a tumor mass. While this may be ideal from a treatment perspective, as these cells are actively proliferating, failure to account for internal spatial diffusion limitations of chemotherapeutic compounds (not to mention essential nutrients such as oxygen and glucose) can lead to inaccurate model predictions.

Cell automata models and fractal simulations take the cellular tumor model to its penultimate conclusion, representing each cell individually while accounting for invasive migration, predicting metastases, and constructing an appropriate vascular network for the simulated tumor [94, 95, 96, 97, 98]. Other factors influencing tumor growth, such as external pressure effects, acquired drug resistance, and gene mutations perpetuating tumor growth provide additional information, allowing for a more physiological representation of tumor progression [87, 99, 100, 101, 102, 103]. While all this information would improve model predictions, data on a per patient basis, or a per animal basis in the preclinical setting, would be difficult, at best, to collect. Distributions for phase transitions and drug effects could be obtained from collected data, but the exact tumor geometry with internal necrosis cannot be determined exactly except by destructive biopsy. An important question to consider, then, is whether control based on a less detailed but identifiable model is sufficient for dose scheduling purposes.

1.2.2 Toxicity Models

Eliminating the tumor mass is not the only concern during chemotherapy, as the drugs employed also adversely affect healthy proliferating cells. Common toxicities encountered during the course of chemotherapy include diarrhea, dizziness, bleeding, nausea, vomiting, mucositis, and myelosuppression, with different toxicities manifesting depending on the drug(s) and treatment regimens employed [104]. While maximum dosing limits provide one means of avoiding excessive patient toxicity, patients must still be monitored during a treatment cycle because of inter-patient variability in drug clearance and sensitivity.

Clinicians assess toxicity on a discrete, graded scale from 0-4, with higher grades correlating with worse toxicity [104]. Additional discrete measures, such as discrete events of vomiting and diarrhea introduce another element of complexity in toxicity model development, as well as subjective classification associated with some toxicity measures (such as dizziness or skin irritation).

One approach to toxicity modeling involves identifying those subsets of patients more prone to toxicity and treating them in a less aggressive manner [105, 106]. Others include developing heuristic relationships between a toxicity grade and dose administered, drug plasma concentration area under the curve, or time that plasma drug concentration exceeds a therapeutic value [107, 108, 109]. These relationships provide clinicians with trends and likelihood of toxicity, though the uncertainty on such models precludes them from serving as strict toxicity predictors during treatment. Such models do, however, allow for a continuous formulation of discretely graded variables, facilitating downstream controller design if the toxicity measure is indeed the primary toxicity associated with the drug. Combining both ideas, most toxicity model development has focused on measures that are easily obtainable and already continuous, such as the decrease in platelets, leukocytes, and/or neutrophils following chemotherapeutic treatment [3, 50, 51, 110, 111, 112]. Control algorithms that incorporate models for neutrophil or leukocyte proliferation and drug effect can develop drug schedules that minimize patient toxicity (possibly avoiding other toxicities as well) while simultaneously minimizing overall tumor volume [3, 75, 111, 113]. Secondary toxicities may still manifest in such regimens, but by avoiding the primary toxicity it should be theoretically possible to maintain secondary toxicities within acceptable treatment bounds.

The simplest model for healthy proliferating cells uses the same equations as those used to represent short-term tumor growth or the progression of hematologic cancers. Using either traditional exponential or linear cell-cycle models with adjusted growth rates and appended elimination or apoptotic rates, it is possible to represent leukocyte progression and treatment response over short windows in time. However, these models are either unstable or cannot guarantee convergence back to the original steady state (*i.e.*, will not maintain a steady state cell population in the absence of treatment). Replacing the production rate of cells in the progenitor compartment with a constant (rather than the product of progenitor cells and

a rate) allows for stability of the system and baseline recovery. A typical compartmental neutrophil model without feedback is shown in Figure 1.5a, along with a representative neutrophil time course after administration of a myelosuppressive drug in Figure 1.5b [114, 115]. The structure consists of: (i) a progenitor compartment where drug effect (E_{drug}) occurs; (ii) intermediate compartments between progenitor and circulating cells representing cell maturation, where the cells are unaffected by the drug; and (iii) a circulating neutrophil compartment that has elimination due to natural cell death but is otherwise unaffected by the drug. Figure 1.5b shows a delayed drop in circulating cell count following drug exposure (bolus at $t = 0$) as affected cells progress to the circulation; proliferating cells, and eventually the circulating population, return to baseline following treatment. Models of this type, however, fail to account for the internal biological control loop that regulates circulating hematopoietic cell count and demonstrates baseline cell count overshoot following treatment.

An important compound in regulating neutrophil count is granulocyte colony stimulating factor (GCS-F), which promotes the proliferation of hematopoietic stem cells by binding to and activating the GCS-F receptor. In addition, GCS-F binds to circulating neutrophils, which has no effect on neutrophil production. This interaction between circulating neutrophils and GCS-F results in an equilibrium cell count and systemic GCS-F concentration. If the baseline cell count of circulating neutrophils falls, such as from a chemotherapeutic treatment, the concentration of unbound GCS-F will increase resulting in an upregulation of hematopoietic stem cell division. Similarly, neutrophil counts above baseline decrease the concentration of bound GCS-F and subsequently downregulate hematopoietic stem cell division. As GCS-F plasma concentrations are not often obtained during treatment, many groups have developed neutrophil feedback models based on the circulating neutrophil count. A low-order model developed by Karlsson and coauthors [3] has model states as described above in addition to a nonlinear feedback mechanism dependent on circulating neutrophil deviation from the homeostatic value. Similar neutrophil models have been developed by Zamboni *et al.* [50] and Minami *et al.* [109], though the model output in these cases was percentage decrease in neutrophil count rather than the absolute neutrophil count. More complicated model structures depicting the entire process of human granulopoiesis

incorporate multiple feedback loops, including the effects of granulocyte macrophage colony stimulating factor (GMCS-F), individual drug effects on each subpopulation of precursor cells, and nonlinear transition rates dependent on circulating GCS-F and GMCS-F concentration [51, 66]. Such models are able to capture more rapid alterations in circulating neutrophil counts and are useful for describing population or subpopulation behavior during a chemotherapeutic trial; however, these models require more parameters than less complex neutrophil models and are difficult to tailor to individual patients.

A final item is the location of chemotherapeutic effect relative to the measurement of the effect. As previously mentioned, chemotherapeutics target cellular machinery which is upregulated during cell growth and cell division. This allows for preferential selection of tumor cells versus the majority of other cells in the body (under the assumption that tumor cells proliferate more rapidly than healthy cells), though other rapidly proliferating cells, such as hematopoietic stem cells, are simultaneously affected by the treatment. Circulating neutrophils and post-mitotic neutrophils undergoing differentiation, however, do not proceed through the cell-cycle and are not affected by the administration of chemotherapeutics. Rather, the upstream precursors will undergo apoptosis or growth inhibition which will, in turn, reduce circulating neutrophil count after a period of 3-5 days (the approximate maturation time for neutrophils). Observed fluctuations in circulating neutrophil count, therefore, are a delayed observation of the actual drug effect. More thorough model structures accounting for differentiation states of hematopoietic cells and cell phase can also be found in the literature [51, 66], although the large number of model parameters would hinder the ability to adapt such models for individual patient treatment based on sparse data collection.

Neutrophil toxicity models have been developed for a number of therapeutics including pemetrexed, docetaxel (Doc), paclitaxel, etoposide, vinflunine, irinotecan, 2'-deoxy 2'-methylidenecytidine, topotecan, epirubicin, and 5-fluorouracil [3, 50, 110, 111, 116]. Typically, these models were developed based on individual neutrophil counts and were used to construct representative population models of neutrophil progression following treatment. Karlsson and coauthors have updated the model parameters to include patient-specific measures such as α -1 acid glycoprotein (AAG), body surface area (BSA), patient weight, and albumin levels, in order to develop prospective individual neutrophil progression

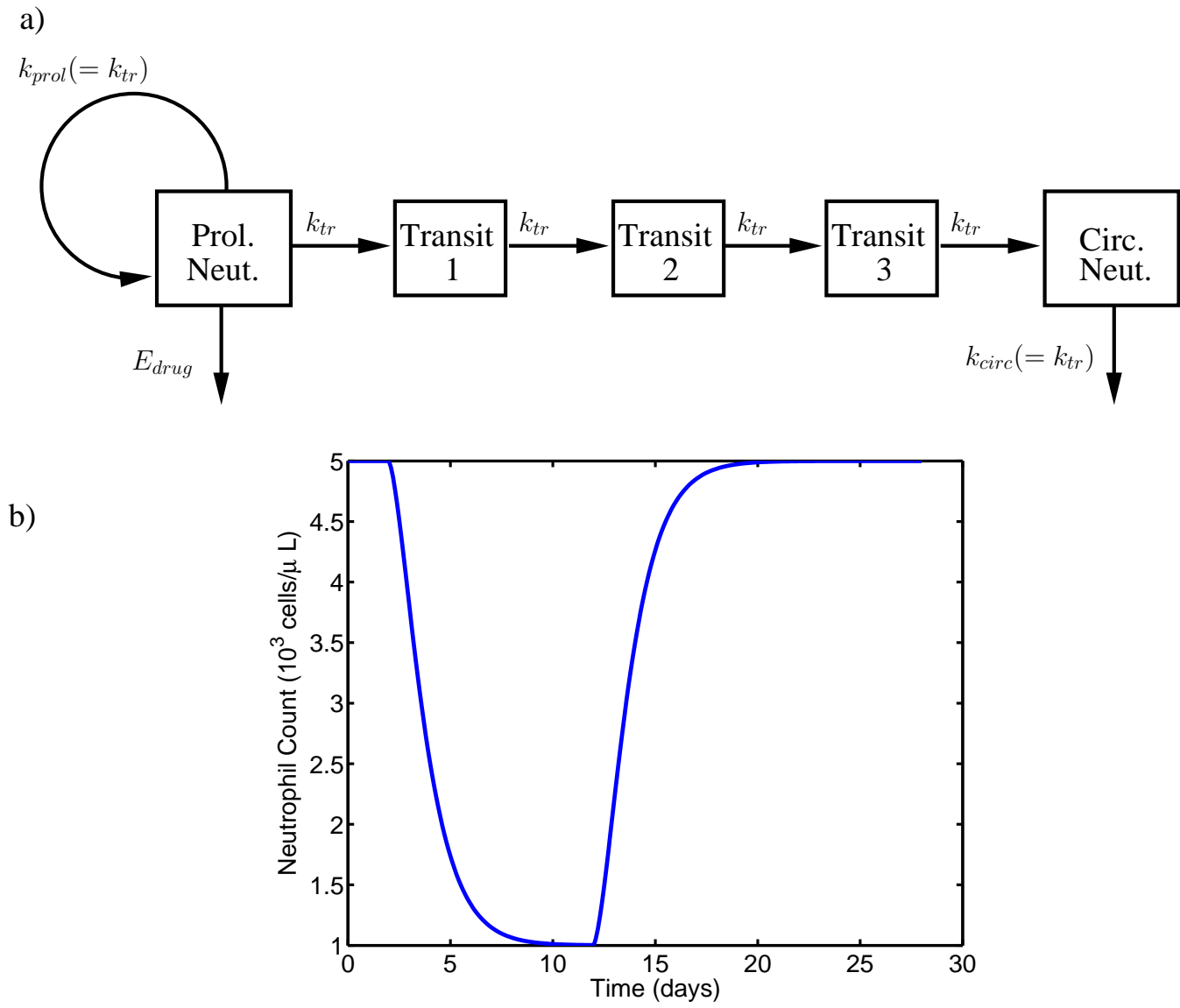


Figure 1.5: A low-order neutrophil model without feedback (a) and representative circulating neutrophil count progression following treatment with a chemotherapeutic (b).

predictions for patients [106]. Results applied to Doc demonstrated that the most important patient parameters included AAG, BSA, and CYP3A enzyme level [106]. Scholz and coauthors used a more involved leukocyte model to investigate the treatment outcomes of a cyclophosphamide/doxorubicin/vincristine/prednisone (CHOP) regimen [66]. These studies focused on defining drug PD parameter profiles representative of patients at high (elderly patients), medium, and low risk for neutrophil toxicity following treatment. Using these groups, subgroup leukocyte progression was simulated and necessary regimen alterations to the cyclophosphamide dose to maintain acceptable toxicity levels were evaluated [66]. To our knowledge, prospective evaluation of alternative dosing regimens have not been investigated using these models in the literature.

1.3 CONTROLLER ALGORITHMS

Model-based control is currently considered the state-of-the-art in the field of process control and is the technique focused on solely within this dissertation. A generic representation of this technique is shown in Equations (1.1)-(1.4):

$$\min_{u(t)} \quad F(x(t_f), x(t), u(t)) \quad (1.1)$$

$$\text{s.t.} \quad \dot{x}(t) = g(x(t), u(t)) \quad (1.2)$$

$$A_1 \geq u(t) \geq A_2 \quad (1.3)$$

$$B_1 \geq x(t) \geq B_2 \quad (1.4)$$

This control technique uses an explicit representation of the system as a model (Equations (1.2)) to make decisions on how to change the manipulated variable ($u(t)$) in order to obtain a desired outcome (based upon the formulation of the objective function, $F(x(t_f), x(t), u(t))$). Objective function terms typically include some combination of penalties (weights) on the state values ($x(t)$), input magnitude or energy ($u(t)$), and final time state values ($x(t_f)$) of the system over the optimization horizon. Input changes are accomplished while satisfying both input (Equation (1.3)) and state (Equation (1.4)) constraints, which may be either strict equality or inequality relationships and are specifically

chosen for the system. This technique has been applied across a range of fields, and a comprehensive list of areas where model-based control has been applied is beyond the scope of this dissertation. Instead, discussion will focus on the implementation of this technique specifically for the cancer treatment problem

Cancer treatment design has been investigated using a variety of control techniques, including optimal control theory [65, 75, 117, 118, 119, 120, 121], control vector parameterization [122, 123], nonlinear model predictive control (NMPC) [79, 80], and mixed-integer linear/nonlinear programming (MILP/MINLP) [64]. Lumped tumor models (*i.e.*, the exponential and Gompertz) coupled with a bilinear kill term have been investigated using optimal control theory in order to minimize a tumor volume at a final time allowing for the continuous administration of a therapeutic. Such dose scheduling approaches, however, have failed to account for the constraints commonly encountered in a clinical setting. First, intravenous (IV) chemotherapeutic administration often occurs during clinical hours, and drugs taken orally at home should be scheduled during the day (*e.g.*, the patient will not routinely wake up in the middle of the night to take a pill). Furthermore, many chemotherapeutics administered IV will not be administered continuously for extended periods of time due to drug toxicity. For pills taken on regular intervals (*i.e.*, daily or weekly administration), the model predictive control framework can be used to develop the dosing schedule [79, 80]. Evaluation of drug schedules over non-regular intervals (*i.e.*, stochastic weekday decisions), however, may require more complex controller algorithms such as MILP/MINLP [64].

The implemented objective function must also be chosen carefully to ensure the existence of solutions which are both nontrivial and clinically relevant. For an objective function based on the final-time tumor volume and an underlying exponential or Gompertz tumor growth model with bilinear drug effect, the solutions returned by the controller will be clinically indistinguishable but numerically different (final tumor volume differences of $<1\%$) [124]. Also, for the above listed objective function, the algorithm predicts a characteristic treatment profile: maximum initial drug delivery, followed by a non-dosing period, with the remainder of the drug delivered at the end of the treatment window [63]. Ethically, however, a doctor cannot allow a tumor to grow untreated, thereby invalidating the controller formulation.

In addition, bulk dosing at the end of the cycle, instead of at the beginning, prohibits dosing immediately after the treatment design window due to patient toxicity. Dose schedule development, therefore, requires either an alternative objective function, PD effect, clinical constraints, or model structure to obtain useful scheduling results. A more suitable model structure for dose schedule development would include the cell-cycle [75, 117, 118, 125], which more accurately captures the phase specificity of drug action, and/or a toxicity model [3, 75, 111, 113] to ensure dosing safety and provide an additional measure of treatment efficacy.

Dose schedule development has been investigated using a number of tumor growth model structures, including lumped models [63, 67], cell-cycle models with cycle-specific treatment effects [75, 80, 125], and tumor growth models with subpopulations of susceptible and resistant cells [117, 118]. The inclusion of a toxicity model within the controller formulation, not just input bounds or limits on the total drug administered over a cycle, however, is limited to a few studies from the literature. Fister and Panetta investigated the case of both healthy and cancerous cells proliferating at different growth rates while subjected to a cycle-specific chemotherapeutic [65]. Using an optimal control algorithm with an output objective of maximizing both total drug delivered and the final quantity of healthy cells remaining, the results demonstrated that the therapeutic should be administered preferentially towards the end of the simulation, again neglecting ethical issues and downstream toxicity. Afenya used an optimal control formulation to determine the minimum time necessary to switch between administration of the drug (*e.g.*, drug delivery was either “on” or “off”) in the presence of two concurrent cell populations: (i) healthy; and (ii) cancerous proliferating cells [113]. Results demonstrated that by shortening the time between dose administration, overall cycle time could be reduced by 1-2 weeks without adverse toxicity effects, a result that is termed “dose-dense” therapy currently practiced clinically in breast cancer treatment [70]. Finally, Harrold *et al.* combined a nonlinear PK model for the therapeutic, 9-nitrocamptothecin (9NC), with a switched exponential model for tumor progression and bilinear PD effect on tumor regression [124]. A toxicity model altered the body weight of the mouse in response to 9NC administration, and the resulting objective function was set to minimize the final tumor volume subject to output constraints on the body weight of the mouse throughout

the treatment. The model of body weight response to therapy was inexact, not to mention non-ideal as a toxicity dosing metric (body weight alterations would manifest after intestinal damage had already taken effect), and this dramatically impacted the dosing schedule design, illustrating the importance of accurate toxicity models [124].

The investigation of closed-loop solutions to dose schedule development may often be too specific to the problem being modeled (*i.e.*, highly sensitive to model parameters, narrow dosing windows, etc.). Furthermore, the solutions obtained from such formulations are highly dependent on the objective function and system constraints, and the true “optimal” solution may be numerically indistinguishable from a number of other more clinically implementable solutions. Given all possible degrees of freedom in clinical implementation of a control algorithm, it may be useful to begin dose schedule evaluation in an open-loop framework.

Open-loop studies based on cultured tumor cell dynamics have also been investigated, focusing on the ideal treatment interval to maximize cell death [84, 126], ensure statistical elimination of the tumor [127], or prevent the development of resistance [85]. Using more involved PBE representations for tumor proliferation, all of these models were consistent in predicting drug delivery with increased frequency compared to normal clinical treatment (approximately cycles of 12 hours). Lacking within these studies were evaluations on how uncertainty in parameter mean values may alter treatment, *in vivo* validation of the proposed cell fraction distribution oscillations exploited during treatment, or an accompanying toxicity model to assess whether the increased frequency of doses were clinically acceptable. Other open-loop studies by Dyson *et al.* [84] and Sherer *et al.* [86] used concurrent models for the proliferation of cancerous and healthy proliferating cells exposed to the same drug concentration. Rather than investigating dose level alteration, these studies focused on the delivery intervals of chemotherapeutics to maximize tumor elimination, again, attempting to exploit oscillations in cell-cycle fractions induced following treatment with cycle-specific therapeutics. Results from both of these studies concluded that the window of delivery for improving anti-tumor effect while sparing healthy proliferating cells was too narrow to exploit in a clinical setting, though no validation of the healthy proliferating cells within an *in vivo* setting was provided.

1.4 DISSERTATION OVERVIEW

Dose schedule development, balancing patient quality of life and treatment efficacy, should be feasible by incorporating coupled drug PK and PD effect models within a control algorithm. Chapter 2 focuses on the development of a compartmental PK model for the *G*-phase specific chemotherapeutic, tamoxifen (TM), and its active metabolite, 4-hydroxytamoxifen (HTM). This PK data is used for developing a series of tumor growth models which differ in growth dynamics structure (saturating versus non-saturating growth behavior) and complexity (lumped approximation versus representations of individual cell-cycle phases). These coupled PK/PD models were then incorporated within a nonlinear MPC (NMPC) framework to determine in mice the daily doses of TM necessary to follow a predefined tumor regression trajectory.

Chapter 3 explores the development of more complicated and biologically-relevant tumor growth models using population balance equations (PBEs). Cell cycle models were developed using either age or mass as intrinsic variables; models were then updated to display saturating dynamics commonly observed during solid tumor growth. Theoretical weekly repeating treatment regimens involving an *S*- and *M*-phase therapeutic were investigated, and simulation results are discussed with comparisons to protocols in clinical practice. Furthermore, the ability to induce cell phase oscillations *in vivo* and the need for increased PD model accuracy is addressed.

Chapter 4 focuses on the PBPK model developed for the chemotherapeutic Doc in severe combined immunodeficient (SCID) mice. This PBPK model extended an existing PBPK model in the literature by including additional tissue compartments, providing predictions on Doc PK within implanted SKOV-3 tumor xenografts, and simplifying the original nonlinear structure through the addition of multiple subcompartments with linear transfer rates. Chapter 5 covers the subsequent scale-up of the this model to humans, along with comparisons against an existing PBPK [5] and patient-specific population PK [2] models from the literature. Additional investigations are performed exploring Doc tumor predictions over various treatment schedules, patient body weight, tumor flow rates, and tumor volumes. Chapter 6 updates the neutrophil toxicity model developed by Friberg *et al.* [3] for Doc.

Actual PK profiles for the patients were used in estimating new parameters, while the original model was developed using PK profile predictions from the population PK model developed by Bruno and coauthors [2]. Attempts to fit neutrophil profiles on alternative Doc schedules were unsuccessful, however, necessitating a structural change to the neutrophil toxicity model. Average patient Doc PK and neutrophil progression parameters were combined with an NMPC algorithm and discrete toxicity constraints to evaluate if alternative Doc schedules may allow for the increased delivery of Doc. Alterations to the dosing regimen were investigated for the entire population set to determine those subjects especially susceptible or non-susceptible to toxicity under the new Doc regimen. Separate regimens were developed for these patients, representative of those groups at high and low risk, respectively. Finally, Chapter 7 discusses conclusions drawn from these model development and dose schedule design studies, along with recommendations for future research areas involving tumor and neutrophil response models.

2.0 TAMOXIFEN

This chapter focuses on designing a coupled PK/PD model and a control algorithm for the chemotherapeutic, tamoxifen (TM), which is used in the treatment of estrogen receptor positive (ER+) breast cancer. Both the parent compound and its active metabolite, 4-hydroxytamoxifen (HTM), function through competitive binding to the estrogen receptor preventing receptor activation by estrogen. Inhibition of receptor activation results in an accumulation of the affected cells in G_1 -phase due to growth signal truncation. While neither TM nor HTM directly induce apoptosis, the accumulation of cells in G_1 results in “cellular stress,” and activates intracellular apoptotic pathways [128].

TM was the drug of choice due to extensive clinical implementation, properties of the drug, and characteristics of the dosing regimen. First, TM has been extensively evaluated in preclinical and clinical studies, providing data for the construction of reliable PK and PD models which should, in turn, improve algorithm accuracy. Also, as previously mentioned, TM is classified as a “cycle-specific” chemotherapeutic, and there was interest in evaluating if TM dosing efficacy could be improved with a more mechanistically motivated PD effect. Furthermore, TM has well documented toxicity and can be taken within accepted dosing levels daily for up to 5 years. Dosing constraints could easily be incorporated within a NMPC algorithm which simultaneously handles dosing over regular intervals. A final note is that while other selective estrogen receptor modulators (SERMs) have been developed, TM remains a first-line drug for ER+ breast cancer treatment and combination therapy. As other SERMs become more predominant, however, the same methodology of developing PK and PD models followed by algorithm deployment could be implemented for developing dosing regimens.

2.1 METHODS

Pharmacokinetic data were obtained from Robinson *et al.* [129]. In that study, a single large dose of TM ($200 \frac{\text{mg}}{\text{kg}}$) was administered orally (in 0.1 mL peanut oil) to non-tumor-bearing, ovariectomized, athymic mice, and plasma samples were taken at 0, 3, 6, 12, 24, 48, 72, and 96 hours after dosing. Plasma samples were purified using chromatography; concentrations of TM, HTM, and N-desmethyltamoxifen were determined via comparison to a standard curve and the resulting plasma concentrations represented the averaged values from three mice.

Tumor volume data for PD modeling were obtained from Conley *et al.* [130]. The study protocol involved athymic mice with human ER+ MCF-7 xenografts and estradiol pellets implanted subcutaneously at day 0. Stratified groups were dosed daily via oral gavage with 7.5, 15, 30, or $60 \frac{\text{mg}}{\text{kg}}$ TM dissolved in 0.1 mL of sterile water (vehicle had no significant effect on tumor growth). Doses were given once a day for five consecutive days followed by two days off, beginning on day 12 of the study. This seven-day pattern was repeated three times. Twice each week, tumor volumes were calculated from a digital caliper measurement of tumor length and width, assuming an ellipsoidal tumor of volume $\frac{\ell w^2}{2}$ (ℓ = longest tumor axis, w = shortest tumor axis perpendicular to ℓ).

2.2 TAMOXIFEN PK

The PK of the oral agent TM, and its active metabolite HTM, were modeled using the first-order parent/metabolite with oral dosing compartmental structure in Figure 2.1.

A TM dose is administered orally, and the parent compound is absorbed from the gastro-intestinal tract (dynamics approximated with the two initial compartments). After absorption, circulating TM can be removed from the system (including conversion to metabolites such as tamoxifen N-oxide, N-desmethyltamoxifen, and others) or converted to HTM. Circulating HTM is also removed from the system. Of the metabolites, only HTM and N-desmethyltamoxifen appear in plasma at detectable concentrations [128]. Affinity

studies have shown N-desmethyltamoxifen binds with estrogen receptors at $\frac{1}{50}$ the affinity of TM and $\frac{1}{1250}$ the affinity of HTM [128]. As such, only TM and HTM are postulated to contribute a significant anti-tumor effect.

The following equations describe the TM and HTM PK:

$$\begin{aligned}
 \frac{dX_0}{dt} &= -k_{01}X_0 + u(t) \\
 \frac{dX_1}{dt} &= -k_{12}X_1 + k_{01}X_0 \\
 \frac{dX_2}{dt} &= -k_{cl2}X_2 - k_{23}X_2 + k_{12}X_1 \\
 \frac{dX_3}{dt} &= -k_{cl3}X_3 + k_{23}X_2 \\
 Y_1 &= \frac{X_2}{V} \\
 Y_2 &= \frac{X_3}{V}
 \end{aligned} \tag{2.1}$$

Here X_2 and X_3 correspond to TM and HTM mass in plasma (μg), respectively, while X_0 and X_1 denote TM mass in the two initial compartments. V is the central compartment volume for the parent compound and metabolite (mL), and k_i denote transfer rates ($\frac{1}{\text{hr}}$). Variables Y_1 and Y_2 represent the measured plasma concentrations of TM and HTM ($\frac{\mu\text{g}}{\text{mL}}$).

The parameters in equations (2.1) were fit by minimizing the squared difference between model predictions and data obtained from non-tumor bearing athymic mice [129] and the resulting parameter values are summarized in Table 2.1. Model predictions for both compounds can be seen in Figure 2.2.

The PK model is able to capture the dynamic profile of the data with only a slight over-prediction of TM concentration at $t = 24$ hours. Additional compartments or delays could be incorporated into the TM model to more accurately fit the data at the cost of increased number of parameters, decreased parameter confidence, and increased mathematical complexity.

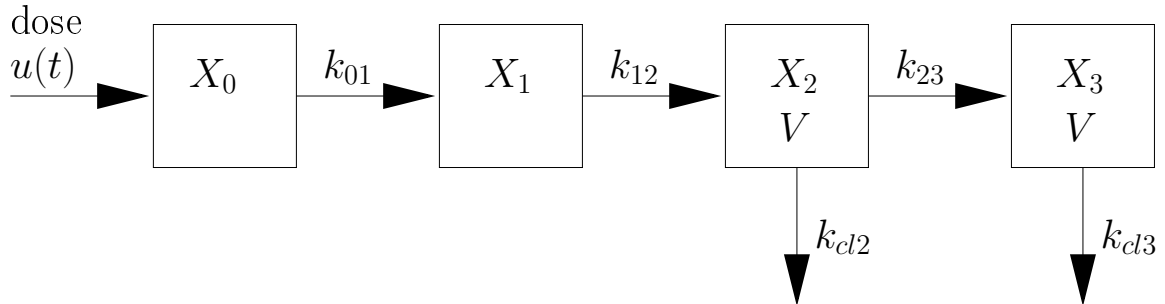


Figure 2.1: 4-compartment linear model for plasma concentrations of TM and HTM after oral dosing

Table 2.1: PK parameter values for the oral dosing of TM.

Parameter	Value
k_{01} ($\frac{1}{\text{hr}}$)	0.048 ± 0.006
k_{12} ($\frac{1}{\text{hr}}$)	0.993 ± 0.062
k_{23} ($\frac{1}{\text{hr}}$)	35.932 ± 0.821
k_{cl2} ($\frac{1}{\text{hr}}$)	1.145 ± 0.214
k_{cl3} ($\frac{1}{\text{hr}}$)	39.525 ± 1.119
V_1 (mL)	8.592 ± 0.723

2.3 TAMOXIFEN TUMOR MODEL AND PD

Tumor growth models which explicitly track the fraction of the cell population in each cell phase are typically referred to as cell-cycle models. In contrast to traditional single state lumped-compartment models (*i.e.*, exponential and Gompertz [63, 69]), these models introduce additional states to represent phases of the cell-cycle. These state and parameter additions allow for direct incorporation of cycle-specific chemotherapeutic effect and typically involve the coupling of two or more linear ordinary differential equations (ODEs). However, linear cell-cycle models cannot simultaneously capture the rapid initial rate of tumor proliferation and the declining rate of growth observed at larger tumor volumes, although they do return predictions accurate over short time intervals. One solution is to model tumor growth with the GM, a structure that lumps cell phases into one homogeneous population, N (with units mm^3). The GM displays saturating growth dynamics as $N \rightarrow \theta$, the plateau population which the tumor asymptotically approaches (mm^3), and is represented by the following ODE:

$$\frac{dN}{dt} = \frac{1}{\tau} N \ln \left(\frac{\theta}{N} \right) \quad (2.2)$$

The parameter τ is the pseudo-doubling time (hr) for the tumor. The GM is capable of describing tumor growth dynamics, but the single-state system does not model cell-phase progression of the lumped population [69]. This loss of information is especially relevant as many anticancer compounds primarily affect cells during specific phases of the cell-cycle (*e.g.* paclitaxel, G_2/M ; topotecan, S ; and tamoxifen, G_1) [48, 74, 131]. Combining cell-cycle data with a saturating growth rate yielded the SCM, which accurately captures saturating tumor growth dynamics while modeling the overall solid tumor as a collection of three cell phases [79]:

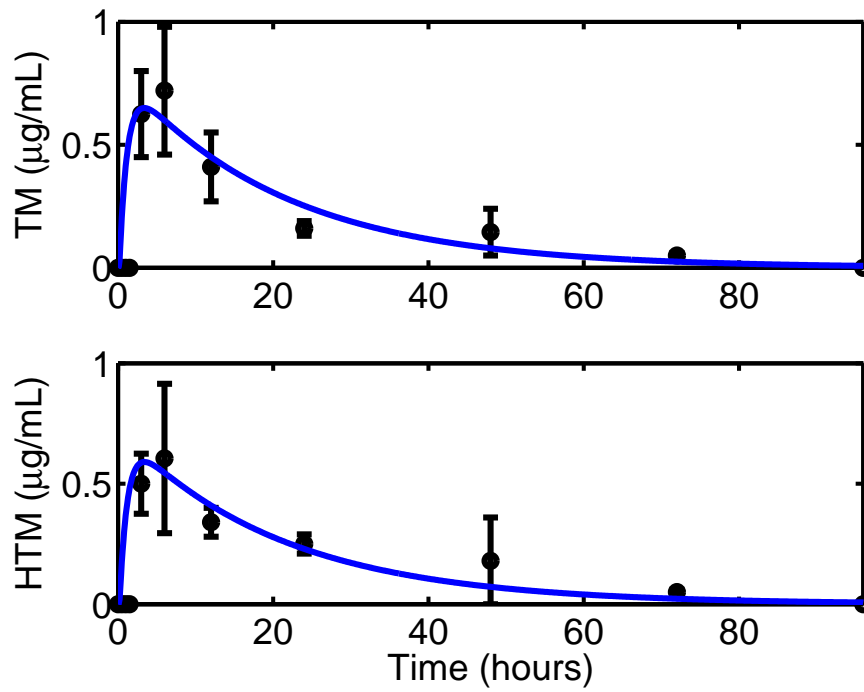


Figure 2.2: Actual (circles) vs. simulated (lines) PK for TM (top) and HTM (bottom) after a $200 \frac{\text{mg}}{\text{kg}}$ oral dose of TM. Each data point represents mean plasma concentrations from three mice; error bars are ± 1 standard deviation.

$$\frac{dX_G}{dt} = -k_{GS}X_G \ln\left(\frac{\theta}{N}\right) + 2k_{MG}X_M \ln\left(\frac{\theta}{N}\right) \quad (2.3)$$

$$\frac{dX_S}{dt} = -k_{SM}X_S + k_{GS}X_G \ln\left(\frac{\theta}{N}\right) \quad (2.4)$$

$$\frac{dX_M}{dt} = -k_{MG}X_M \ln\left(\frac{\theta}{N}\right) + k_{SM}X_S \quad (2.5)$$

$$N = X_G + X_S + X_M \quad (2.6)$$

Here X_i corresponds to the volume (mm^3) of cells in the G (growing), S (DNA synthesis), or M (mitosis) phases (assuming constant cell volume and 10^6 cells = 1 mm^3); k_{ij} 's denote transfer rates from cell phase i to phase j ($\frac{1}{\text{hr}}$); and θ is defined as above. The three states correspond to cells in G ($Q+G_1$), S , or M (G_2+M) phases of the cell-cycle which can be seen in Figure 2.4a. These groupings were based on flow cytometry analysis of DNA content using propidium iodine as a fluorescent marker [132]. Cell phases containing equivalent amounts of DNA have the same fluorescence and are indistinguishable from one another. Such is the case with Q and G_1 -phase, where one copy of DNA is present, and G_2 and M -phase, where there is twice the DNA content [133]. S -phase falls into the intermediate region between Q/G_1 - and G_2/M -phase groupings. A typical flow cytometry result with DNA staining is shown in Figure 2.4b. Figure 2.3 shows both the overall five-compartment cell-cycle model and the reduced three-compartment cell-cycle model.

The SCM predicts 90% of the cells in the tumor are within G -phase for tumor volumes exceeding 50 mm^3 [79]. This results in dynamic behavior analogous to a single-lumped ODE model, such as the GM, with all cells located within a single phase. As TM and its active metabolites (primarily HTM) affect G_1 -phase cells and not the quiescent Q -phase cells lumped within the state, the chemotherapeutic effect of tamoxifen is misrepresented in both the GM and SCM. These two models both incorporate non-susceptible cells (all phases except G_1 and Q -phase cells, respectively) within the effected cell population, possibly leading to an over prediction of the actual chemotherapeutic effect. One possible solution involves partitioning the G -phase cell equation into separate equations for Q and G_1 -phase cells, as follows:

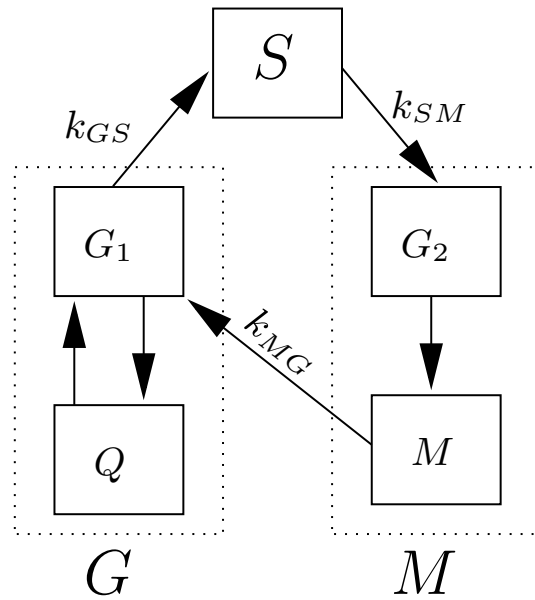


Figure 2.3: The five phases of the cell-cycle: Q (quiescent), G_1 (growth), S (DNA replication), G_2 (mitotic preparation), M (mitosis). Two cell-cycles models are developed: (i) a three-phase model considering G (lumped Q and G_1), S , and M (lumped G_2 and M) which is resolvable using DNA labeling and flow cytometry; or (ii) a four-phase structure with Q , G_1 , S , and M (lumped G_2 and M) which is resolvable using DNA and RNA labeling and subsequent flow cytometry.

$$\frac{dX_Q}{dt} = -k_{QG}X_Q + k_{GQ}X_{G_1} \quad (2.7)$$

$$\begin{aligned} \frac{dX_{G_1}}{dt} = & k_{QG}X_Q - k_{GQ}X_{G_1} - k_{GS}X_{G_1} \ln\left(\frac{\theta}{N}\right) \\ & + 2k_{MG}X_M \end{aligned} \quad (2.8)$$

$$\frac{dX_S}{dt} = -k_{SM}X_S + k_{GS}X_{G_1} \ln\left(\frac{\theta}{N}\right) \quad (2.9)$$

$$\frac{dX_M}{dt} = -k_{MG}X_M + k_{SM}X_S \quad (2.10)$$

$$N = X_Q + X_{G_1} + X_S + X_M \quad (2.11)$$

Here, X_S and X_M are defined as before, while X_Q and X_{G_1} represent the volume of tumor cells (mm^3) in the Q (quiescent) or G_1 (growth) phase, respectively. Additional rate constants, k_{ij} , have been introduced, and θ is still the plateau population which the tumor approaches asymptotically (mm^3). The saturating term from Equation (2.5) has been replaced with a linear exchange rate parameter in Equation (2.10) because a nonlinear term in M -phase was not required to reproduce saturating dynamics with the QCM. Furthermore, there is limited biological evidence to support a variable transition rate during M -phase. Exchange rates between the quiescent and growth phases were assumed to be linear with respect to population volume, and all cells resulting from mitosis were assumed to start in G_1 -phase rather than distributing between Q and G_1 -phase. This assumption eliminates the need for an additional distribution parameter which is poorly defined and for which little information is available in the literature.

Finally, it should be noted that cell-cycle information discriminating between Q and G_1 -phases can be obtained by labeling tumor cells for both DNA and RNA content. Labeling for DNA preserves the separation between Q/G_1 , S , and G_2/M -phase cells, while labeling the cells for RNA content using acridine orange distinguishes RNA-rich G_1 -phase cells from quiescent cells in Q -phase [4] (Figure 2.4c). Figure 2.4a shows the four-compartment cell-cycle model governed by Equations (2.7)-(2.10). The SCM results when Q and G_1 are grouped into one lumped phase, while the GM results from the combination of all five phases.

Table 2.2: Parameter values for the tumor growth models: QCM, SCM, and GM.

Parameter	Value		
	QCM	SCM	GM
$k_{QG} \left(\frac{1}{\text{hr}}\right)$	0.0066	—	—
$k_{GQ} \left(\frac{1}{\text{hr}}\right)$	0.0561	—	—
$k_{GS} \left(\frac{1}{\text{hr}}\right)$	0.0083	0.0013	—
$k_{SM} \left(\frac{1}{\text{hr}}\right)$	0.0790	0.0390	—
$k_{MG} \left(\frac{1}{\text{hr}}\right)$	0.0413	0.0169	—
$\frac{1}{\tau} \left(\frac{1}{\text{hr}}\right)$	—	—	0.0010
$\theta \text{ (mm}^3\text{)}$	10^4	10^4	10^4

Table 2.3: Calculated k_D 's from the four TM dose groups using tumor growth models; μ_{1-j} and σ_{1-j} represent the mean and standard deviation, respectively, of the lowest TM dose through the j th lowest TM dose.

TM Dose	$k_D \left(\frac{\text{mL}}{\mu\text{g hr}}\right)$		
	QCM	GM	SCM
$7.5 \frac{\text{mg}}{\text{kg}}$	0.0299	0.0049	0.0051
$15 \frac{\text{mg}}{\text{kg}}$	0.0398	0.0052	0.0061
$30 \frac{\text{mg}}{\text{kg}}$	0.0439	0.0043	0.0055
$60 \frac{\text{mg}}{\text{kg}}$	0.0340	0.0027	0.0035
$\mu_{1-3} \pm \sigma_{1-3}$	0.0379 ± 0.0072	0.0048 ± 0.0004	0.0056 ± 0.0004
$\mu_{1-4} \pm \sigma_{1-4}$	0.0369 ± 0.0062	0.0043 ± 0.0011	0.0051 ± 0.0010

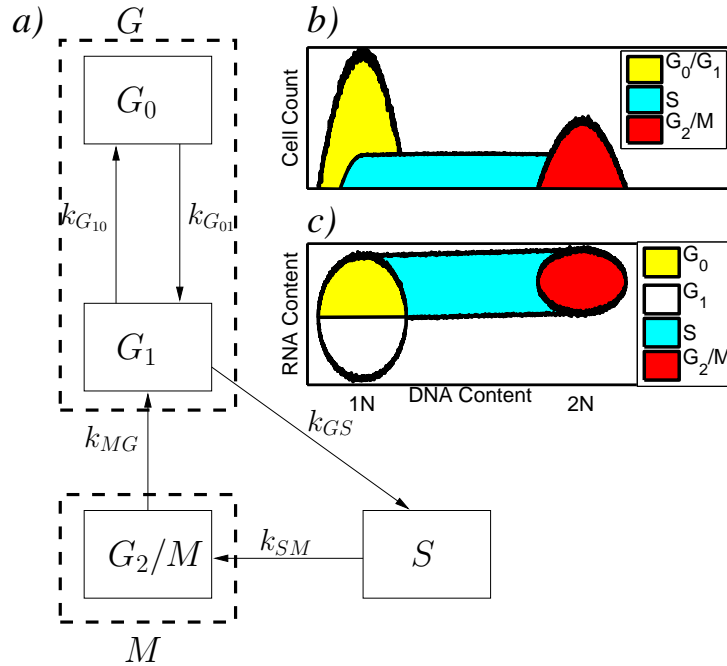


Figure 2.4: The cell-cycle (a) and typical flow cytometry results from DNA staining alone (b) or combination DNA and RNA staining (c). By staining for DNA it is possible to resolve three groupings of cells (G , S , and M) which can be modeled using three state equations (Equations (2.3)-(2.5)). Simultaneously staining for both DNA and RNA content allows for independent resolution of the G_0 - and G_1 -phases, and the overall population can be modeled using four state equations (Equations (2.7)-(2.10)). Figures adapted from Shapiro *et al.* [4]. Identifiable phases of the cell-cycle from combination staining for DNA and RNA content followed by flow cytometry (left) and typical flow cytometry result from DNA staining alone (upper right). The G_0/G_1 grouping could be further separated by staining for RNA content.

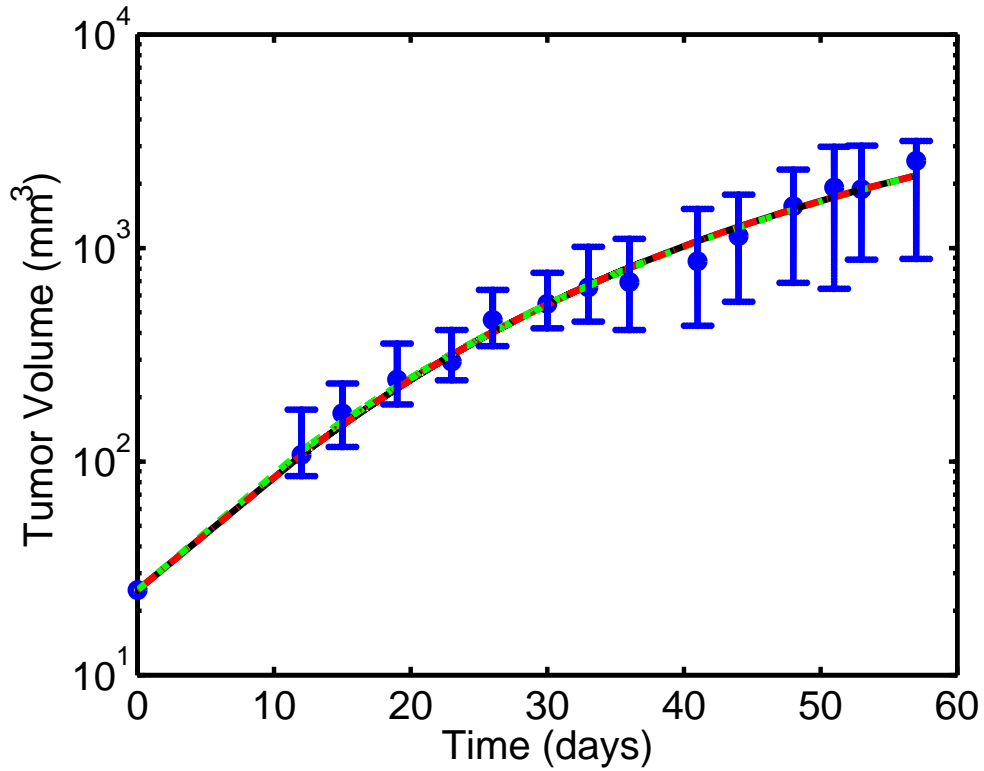


Figure 2.5: Measured tumor volumes (circles; mean from 20 untreated mice) for MCF-7 human ER+ breast cancer xenografts growing in athymic nude mice and simulated tumor size (lines) as a function of time for QCM (dash-dot), SCM (solid, overlay on dash-dot), and GM (dashed, overlay on dash-dot) models. Error bars represent a 95% confidence interval (CI) for measured tumor volumes.

Values for the parameters in the GM, SCM, and QCM were obtained by minimizing the squared difference between model predictions and animal data [130]. Parameter values are summarized in Table 2.2. All three models provide virtually identical predictions of the control tumor growth data (Figure 2.5) and the sum squared errors in fitting the data were similar (13.95 for the QCM and 13.98 for both the SCM and GM). The AIC, traditionally used to trade off model complexity versus improvements in model accuracy, is given by [134]:

$$\text{AIC} = n \ln \left(\frac{\text{SSE}}{n} \right) + 2 \cdot p \quad (2.12)$$

Here, SSE is the sum squared error between the data and the model prediction at the measurement points, n is the number of data points, and p is the number of parameters in the model; a lower AIC value indicates the model that better balances accuracy and complexity. Since the number of data points used ($n = 17$) and the SSE for all models were equivalent, the left-hand term in Equation (2.12) was equal for all three models. However, the QCM had five parameters, two more than the SCM and four more than the GM, so an AIC analysis clearly favored the GM, the least complex model structure. This result was expected since the GM accurately predicts bulk tumor growth dynamics, and additional parameters, which increase the AIC value, do not provide sufficient improvement in dynamic fit to offset the AIC increase. However, the improved biological correspondence should provide superior controller performance by more accurately accounting for the targeted effect of TM and HTM in the G_1 -phase of the cell-cycle [135].

A common method for incorporating drug effect in a tumor growth model involves introducing a bilinear kill term into the set of differential equations [63]. Conceptually, the bilinear structure implies that increases in either plasma drug concentration or in susceptible tumor populations will result in a greater treatment effect. For a cycle-specific chemotherapeutic, this bilinear kill term is introduced into the model equation that contains the cell-phase of drug action. As TM and HTM primarily affect cells within G_1 and not all of the model structures contain explicit G_1 -phase representation, the bilinear kill term was

included in the most applicable phase (Equations (2.8), (2.3), and (2.2), from the QCM, SCM, and GM, respectively). The new equations are given by:

$$\begin{aligned} \frac{dX_{G_1}}{dt} &= k_{QG}X_Q - k_{GQ}X_{G_1} - k_{GS}X_{G_1} \ln\left(\frac{\theta}{N}\right) \\ &\quad 2k_{MG}X_M - k_D X_{G_1} \left(\frac{[TM]}{V} + \frac{c[HTM]}{V}\right) \end{aligned} \quad (2.13)$$

$$\begin{aligned} \frac{dX_G}{dt} &= -k_G X_G \ln\left(\frac{\theta}{N}\right) + 2k_M X_M \ln\left(\frac{\theta}{N}\right) \\ &\quad - k_D X_G \left(\frac{[TM]}{V} + \frac{c[HTM]}{V}\right) \end{aligned} \quad (2.14)$$

$$\frac{dN}{dt} = \frac{1}{\tau} N \ln\left(\frac{\theta}{N}\right) - k_D N \left(\frac{[TM]}{V} + \frac{c[HTM]}{V}\right) \quad (2.15)$$

Here k_D is the drug-induced apoptotic rate ($\frac{\text{mL}}{\mu\text{g hr}}$), V is the distribution volume for the compounds (mL), $[TM]$ and $[HTM]$ correspond to the mass of TM and HTM in the plasma, respectively, and c represents the relative anti-tumor effectiveness of TM vs. HTM. Because treatment dependent tumor reduction depends on the binding of TM and HTM to an estrogen receptor, c can be approximated as the binding affinity ratio of HTM to TM. Previous experiments have determined HTM to possess a binding affinity 25-50 times that of TM [128] so the constant c was set to 25 for these studies, possibly underestimating HTM anti-tumor effect.

Using tumor growth parameters listed in Table 2.2 and previously identified pharmacokinetic parameters [79], k_D values for the QCM were determined individually for the four different TM treatment groups (7.5, 15, 30, and 60 $\frac{\text{mg}}{\text{kg}}$ TM per dose) by minimizing the squared difference between tumor data and model predictions. Individual k_D values at each TM dose for all three models are shown in Table 2.3. For both the SCM and GM, k_D estimates were consistent for the three lower TM dosing levels (7.5, 15, and 30 $\frac{\text{mg}}{\text{kg}}$ TM) while the estimated k_D corresponding to TM doses of 60 $\frac{\text{mg}}{\text{kg}}$ were significantly lower. Estimating an average k_D value from all four doses decreased the mean parameter value by 10% while doubling the associated standard deviation. It was postulated that at the highest doses of TM the receptor binding was saturated, resulting in no further increase in tumor death. Hence, subsequent controller studies were limited to a dosing range of $0 \leq u(t) \leq 30 \frac{\text{mg}}{\text{kg}}$ TM

per day to maintain k_D linearity, where $u(t)$ is the amount of TM delivered in a bolus dose per day.

In contrast, k_D predictions for the QCM agreed well across all four TM dose levels, and inclusion of the k_D estimated from the $60 \frac{\text{mg}}{\text{kg}}$ TM dose reduced parametric variability. Using this model, there is no evidence that k_D saturated since the estimated k_D for the lowest dose level ($7.5 \frac{\text{mg}}{\text{kg}}$ TM) was smaller than that of the $60 \frac{\text{mg}}{\text{kg}}$ TM dose level. Based on these results, the acceptable dosing range for TM was set at $0 \leq u(t) \leq 60 \frac{\text{mg}}{\text{kg}}$ per day for controller studies. Although the long term survival of mice on daily TM dosing beyond $40 \frac{\text{mg}}{\text{kg}}$ TM daily dosing has not been evaluated, the increased dosing range is deemed acceptable since closed-loop tumor treatment simulations rarely exceeded doses of $40 \frac{\text{mg}}{\text{kg}}$ TM and simulated treatment length was under 2 years [136]. Figure 2.6 shows the ability of the pharmacodynamic models to fit tumor growth data during treatment. Although Conley *et al.* [130] did not demonstrate long term survival of mice on daily TM dosing, other authors [136] have shown mouse longevity for up to 2 years at $40 \frac{\text{mg}}{\text{kg}}$ daily dosing, thereby validating the dosing range used here as within acceptable toxicity limits.

The model over-predicts drug effect for doses of 15 and $30 \frac{\text{mg}}{\text{kg}}$, however these over-predictions do not seriously impact overall tumor growth predictions over the 60 day period. A portion of this mismatch results from fixing the unperturbed tumor growth kinetics, which were different even among stratified groups. For example, at day twelve for $30 \frac{\text{mg}}{\text{kg}}$ dosing (Figure 2.6, bottom) the predicted tumor size is greater than the measured tumor size on day 12 before drug is administered. In addition, tumor growth kinetics after drug administration (after day 30) are noticeably less than predicted, possibly representative of a lingering drug effect. The model with fixed parameters cannot predict this variation and can only minimize total deviations over the remaining tumor data. Still, the model predicts the qualitative shape of drug-altered tumor growth and model predictions remain within the 95% confidence intervals. Furthermore, it should be noted that the error bars on tumor size measurements are significantly broader than the prediction errors.

While each model structure possesses similar bilinear drug effect terms, the dynamic structures have varying degrees of cell-phase complexity, and the affected cell population differs in each model. All three models predict treatment related changes within the

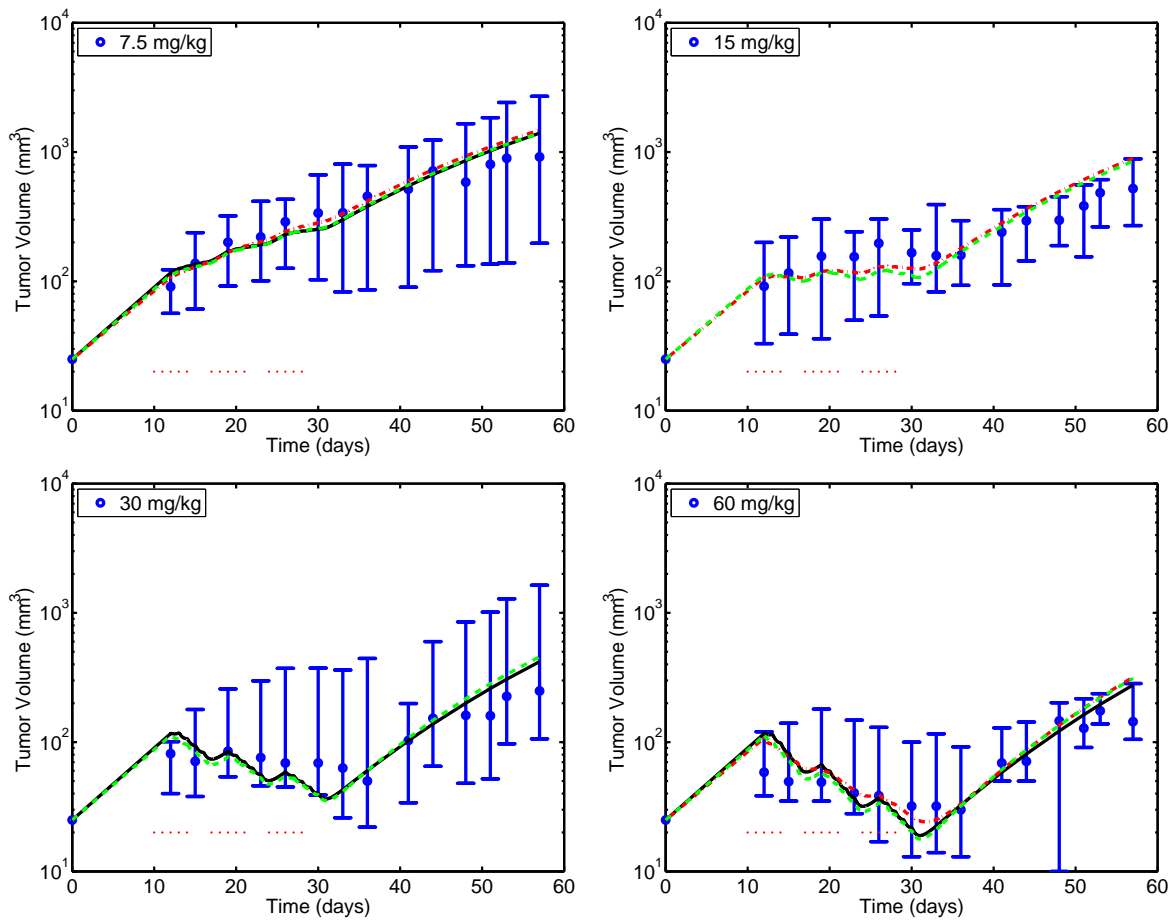


Figure 2.6: Measured MCF-7 tumor xenograft data from tumor-bearing athymic mice (circles with a 95% CI) vs. QCM (dash-dot), SCM (solid, overlay on dash-dot), and GM (dashed, overlay on dash-dot) model predictions. TM doses were administered starting on day 10 (dots, bottom) for five consecutive days, followed by two days off.

prediction errors of the experimental data and within close agreement of each another. This was expected because similar behavior was observed previously using the SCM [79]. When the drug effect was incorporated in a cell phase known to be incorrect (*i.e.* M - or S -phase), the model returned pharmacodynamic predictions of tumor growth equivalent to those obtained with drug effect incorporated in the biologically-correct phase [79]. Hence, some knowledge of cell-cycle phase-specific effects is required *a priori* because an accurate fit to experimental pharmacodynamic data does not guarantee a correct model structure for drug effect.

2.4 TAMOXIFEN CONTROLLER SYNTHESIS

NMPC has been employed in a number of industrial processes [137], however, it has not been applied to the cancer dosing problem despite its readily adaptable structure. The general form of the NMPC algorithm is shown below and contains three distinct parts: (i) an objective function; (ii) state equations; and (iii) input and state constraints.

$$\min_{\Delta u(k:k+m-1|k)} \quad \|\Gamma_y [R(k+1 : k+p|k) - Y(k+1 : k+p|k)]\|_2^2 + \|\Gamma_u \Delta u(k : k+m-1|k)\|_2^2 \quad (2.16)$$

$$\dot{x} = f(x, u) \quad (2.17)$$

$$u_{min} \leq u(t) \leq u_{max} \quad (2.18)$$

$$x_{min} \leq x(t) \leq x_{max} \quad (2.19)$$

The objective function (Equation (6.12)) serves as the metric for deciding the ideal doses to implement over a predicted horizon in time. For the above two-norm squared objective function [138], the controller minimizes the sum of two terms. The first is an error term calculating differences between predicted future tumor volume, $Y(k+1 : k+p|k)$ (model predicted future values of N as a function of future drug dosing predictions), and a desired tumor volume reference trajectory, $R(k+1 : k+p|k)$ where the index, k , denotes information at the present time. The second term is a noise-suppression term limiting magnitude changes

in the dosing level, $\Delta u(k : k + m - 1|k)$. A Δu formulation implies that the controller calculates alterations in dose level and not absolute dose magnitude. Furthermore, a Δu formulation of the NMPC algorithm allows for implicit integration ensuring the controller will converge to the desired reference trajectory without offset. The state equations, Equation (2.17) (*i.e.*, PK and PD equations) serve as the process model, allowing explicit prediction of future system behavior based on m controller-predicted dosing alterations over the prediction horizon, p , where $m \leq p$. The constraints, Equations (2.18) and (2.19), ensure that both the input (dosing level) and states (drug within tissues or plasma), respectively, do not exceed clinically-imposed bounds. A schematic representation of NMPC implementation is shown in Figure 2.7.

At each point in time, the controller predicts a series of m changes from the current dosing level based upon measurements currently available at time, k . For all future days beyond $m - 1$ until p , the algorithm makes no change in the administered dose. Based on the tumor volume predicted ($Y(k + 1 : k + p|k)$) over the following p days, the controller compares these values to a desired reference volume ($R(k + 1 : k + p|k)$) and calculates a weighted sum-squared error, with weighting matrix, Γ_y . Concurrently, the weighted sum of squared input manipulations, with weighting parameter, Γ_u , is calculated and added to the penalty for deviation from the reference trajectory. By evaluating changes to this objective function value based on m input alterations, inputs which minimize the objective function can be determined. It should be noted that changes in Δu affect the predicted Y through the PK and PD equations (Equation (2.17)). The first such calculated input is implemented, the resulting output is measured one step forward in time, and the entire procedure repeats.

Such a NMPC algorithm was constructed for the daily dosing of a “simulated mouse” having states based on PK equations described previously and pharmacodynamics governed by the QCM (Equations (2.7), (2.13), (2.9), and (2.10)). A daily dose of $13.4 \frac{\text{mg}}{\text{kg}}$ maintained a pseudo-steady state xenograft tumor size of 100 mm^3 . It should be noted that daily TM administration via oral gavage is the engineering equivalent of a bolus. While NMPC typically employs a continuous input profile with step changes at update intervals (dashed, bottom), many chemotherapeutics are administered orally and can be mathematically represented as a bolus (solid, vertical). Doses were scheduled as bolus inputs, but are

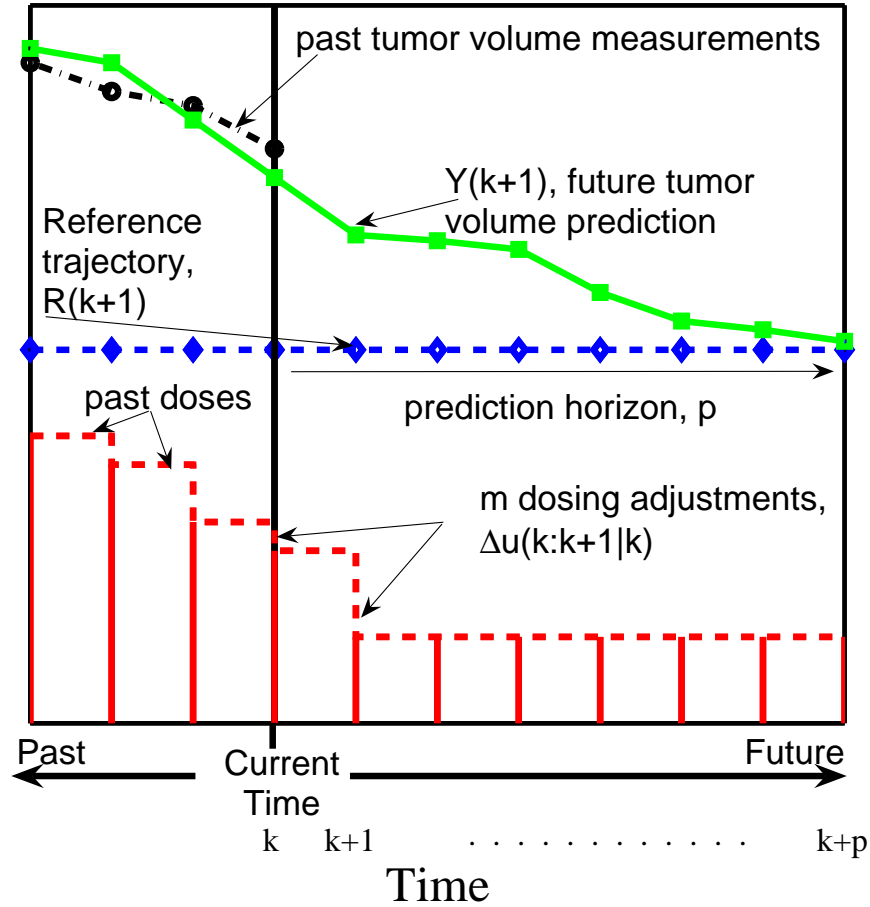


Figure 2.7: NMPC algorithm implementation schematic; as shown, $m = 2$, $p = 6$. Based on a current tumor volume measurement, the controller predicts m dosing alterations to minimize Equation 2.16 over p future days. While NMPC typically employs a continuous input profile with step changes at update intervals (dashed, bottom), many chemotherapeutics are administered as pills, mathematically represented as a bolus (solid, vertical). Doses were scheduled as bolus inputs, but are graphed as steps for easier viewing.

graphed as steps in Figure 2.8 for visual clarity. The weighting matrices Γ_y and Γ_u establish the relative importance of setpoint tracking error and manipulated variable movement, respectively. In the present work, these matrices were set to $\Gamma_y = 1$ and $\Gamma_u = 0$ for all simulations to emphasize reference tracking without regard to penalties for altering dosing level. Simulations were performed in MATLAB (©2005, The MathWorks, Natick, MA) and optimizations called the *fmincon* function.

Taking the “simulated mouse” as the QCM (plant), three NMPC controllers were designed from the QCM, SCM, and GM (models), respectively. The controller based on the QCM (QCMC) was the nominal case where the plant and model are identical while controllers for the SCM and GM represent structural plant-model mismatch. The controllers designed from the SCM (SCMC) and GM (GMC) were initialized at equivalent tumor volumes to the plant (100 mm³) resulting in steady-state inputs of 13.7 and 12.5 $\frac{\text{mg}}{\text{kg}}$, respectively. This initialization restricted the available dosing range ($0 \leq U(k|k) \leq 59.7 \frac{\text{mg}}{\text{kg}}$ for the SCMC and $0.9 \leq U(k|k) \leq 60 \frac{\text{mg}}{\text{kg}}$ for the GMC), but this truncation was acceptable because the doses in the eliminated range were not routinely used in closed-loop simulations.

Closed-loop simulations were compared for two test cases: (i) a three-step tumor reduction trajectory with 30% reduction in reference tumor volume every 28 days; and (ii) a large tumor reduction step with biweekly volume updates. In the three-step tracking case study (Figure 2.8), both the SCMC and the GMC had indistinguishable performance, but were sluggish compared to the nominal controller (QCMC). The mismatch controllers predicted lower initial drug delivery (though overall drug delivery differed by only 3%). Initial trajectory crossing (rise time) for each controller was equivalent following each step (44, 69, and 96 days, respectively), but the SCMC and GMC both displayed undershoot which persisted until the beginning of the next tumor volume reduction step.

The results from the biweekly tumor volume update case study are shown in Figure 2.9. The nominal controller settles to the reference trajectory after 28 days and delivers substantially less drug (total dose of 3067 $\frac{\text{mg}}{\text{kg}}$ TM vs. 4270 and 4240 $\frac{\text{mg}}{\text{kg}}$ TM for the SCMC and GMC, respectively). Comparing total drug delivery in this case is not particularly informative, as both mismatched controllers displayed “ringing” (alternating inputs between the maximum and minimal allowable dose) behavior around the desired reference trajectory.

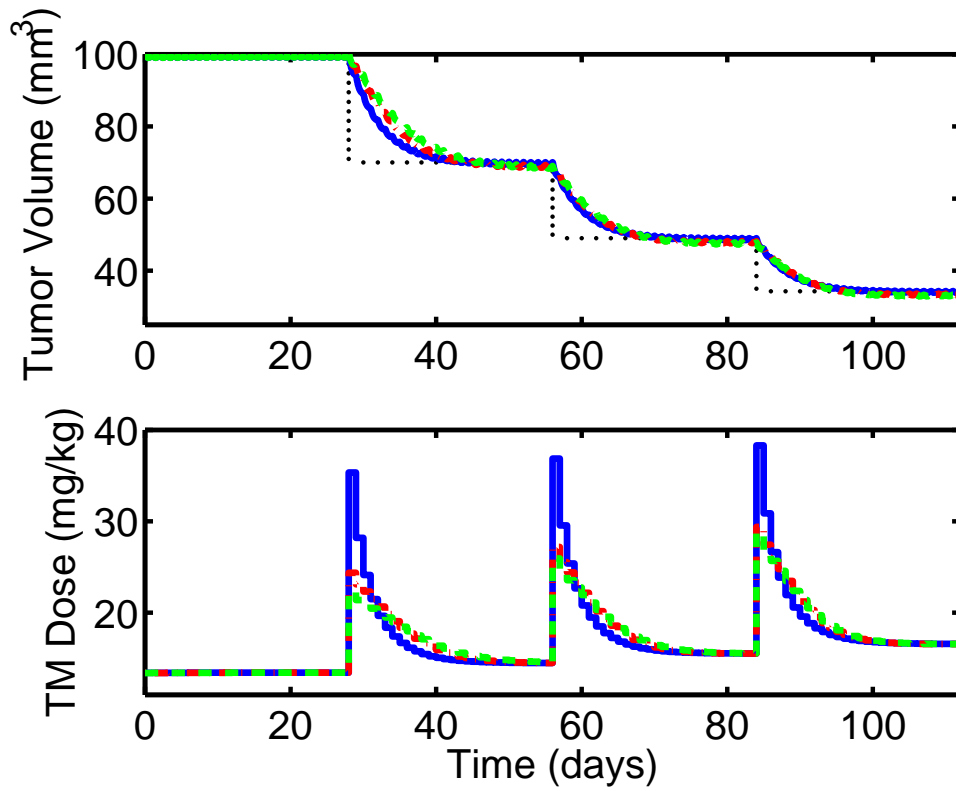


Figure 2.8: Tumor volume (top), reference volume (dotted, top) and TM dose representation (bottom) as a function of time. Tuning parameters for all three controllers (QCMC, solid; SCMC, dash-dot; GMC, dashed) were $m = 1$ and $p = 8$.

This may have resulted from the input/output relationship at low tumor volumes which required large alterations in dosing to obtain small changes in tumor volume. Both SCMC and GMC results demonstrate that failure to explicitly represent the susceptible G_1 -phase results in decreased controller performance and erroneous results.

2.5 CLINICAL APPLICABILITY

While these initial studies demonstrated that an NMPC algorithm could be used to track tumor response, this is not equivalent to improving treatment efficacy. First, reducing tumor volume along a prespecified trajectory may be viewed as unethical within the medical community, especially if it is possible to decrease tumor volume at a more rapid rate while satisfying toxicity constraints. Model results display tumor regression beneath the specified reference trajectory, followed by a reduction in dose, and subsequent regrowth of the tumor, to return to the specified reference trajectory. However, it has already been discussed that objective functions based solely on minimizing tumor volume at a final time point lead to clinically infeasible and unethical results as well. Inclusion of both measures in a properly weighted scheme or updating the reference trajectory are two alternatives, however, the more pressing issue is the implication of these results. In minimizing the final tumor volume with no cumulative toxicity constraint, the algorithm would predict maximum drug delivery at every dosing opportunity. Even for tamoxifen, which is given at the median dose for years, this is an unacceptable dosing prediction manifesting from an inaccuracy in the toxicity model.

Assuming this model could be scaled to humans, controller difficulties observed with sparse feedback information would be compounded even further. While tumor volume measurements can be obtained in the preclinical setting, where tumors are implanted subcutaneously on animal flanks, a majority of human tumors are located internally which requires expensive imaging that may not provide conclusive tumor size information. Also, clinical practice seeks to surgically remove accessible tumor masses whenever possible. Due to tumor volume being an unavailable feedback measure and unreliable therapy metric,

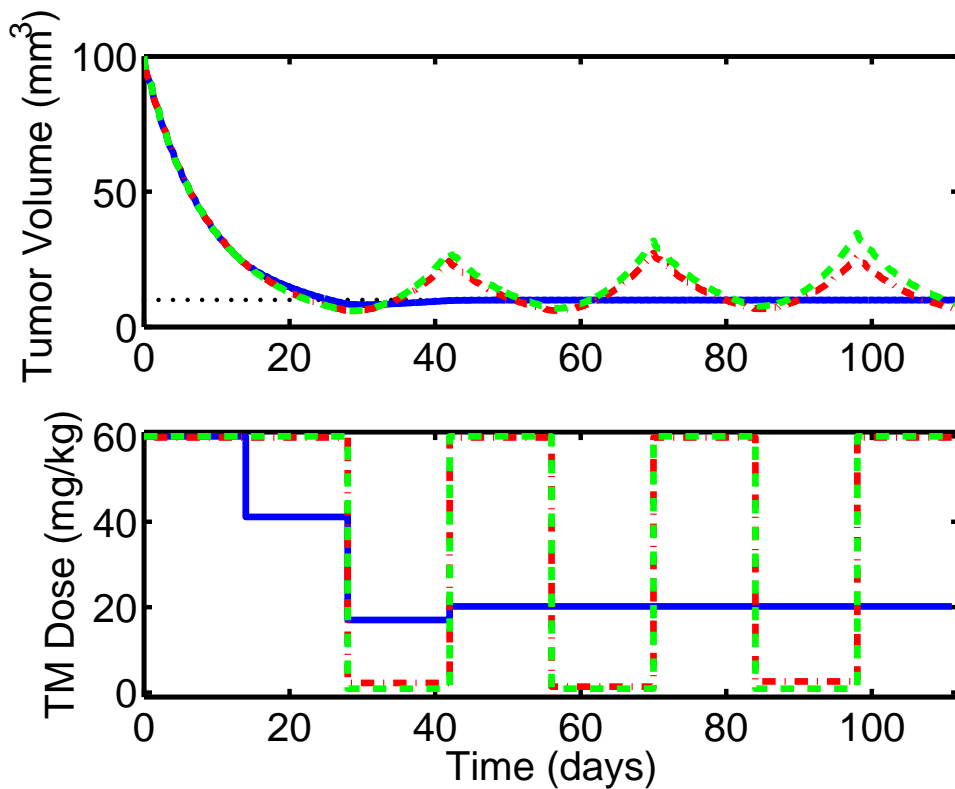


Figure 2.9: Tumor volume (top), reference volume (dotted, top, 10 mm^3), and TM dose representation (bottom) as a function of time. Tumor volumes are measured biweekly under NMPC and tuning parameters for all three controllers (QCMC, solid; SCMC, dash-dot; GMC, dashed) were $m = 1$ and $p = 21$.

alternative objective function metrics, such as targeted drug plasma concentrations [121], plasma drug concentration area under the curve, and white blood cell count may need to be substituted in place of reducing overall tumor volume. The appropriate metric, however, will likely be drug dependent and ideally correlate with the ultimate goal of cancer treatment, namely survival.

3.0 PBE TUMOR MODELS

Chemotherapeutics are often treated as having a lumped tumor effect, however, the growth state and exposure for individual cancer cells ultimately determines the response of the tumor to treatment. It was postulated that the TM treatment outcomes were a result of having lumped cell-cycle phase transition rates. Such lumped models treat all cells within a given cell phase as having equivalent drug exposure and phase transition rates. Apoptotic response is often modeled as a bilinear combination of drug concentration and susceptible population size, premultiplied by a rate constant corresponding to drug activity and tumor sensitivity. However, a tumor is a heterogeneous population of cells with drug exposures dependent on the surrounding vasculature for systemically delivered drugs [139]. Furthermore, drug-induced apoptosis may be a function of period of exposure or point of exposure within a cell phase. Even radiation therapy displays an apoptotic effect dually dependent on cell phase (increased susceptibility during G₂/M phase) and cellular oxygen concentration (increased probability of free radical formation) [140].

An alternative modeling structure that accounts for distributed properties in a cell population is the aptly named, cell population balance model. This mathematical formulation allows for distributed internal properties (*e.g.* mass, age, DNA, protein) among a population, including the partitioning of intracellular compounds following cell division. The general form for a population balance equation (PBE) is shown below:

$$\frac{\partial N(t, i, e)}{\partial t} + \nabla_i \cdot \dot{I}N + \nabla_e \cdot \dot{E}N = \kappa$$

Here, N represents the average number density of the cell population, i refers to internal cell properties (*e.g.*, mass, age, DNA), e refers to external cell properties (*e.g.*, spatial

coordinates), \dot{I} and \dot{E} refer to the rate of change of cell properties, and κ denotes intensity functions such as mitosis and phase transition.

While the original cell population description dates back to Fredrickson, Ramkrishna, and Tsuchiya [141], these models have recently seen increased use in bio-processes [142, 143, 144, 145, 146] and chemotherapeutic schedule development [80, 81, 82, 83, 84, 85, 86, 147]. Historically, the primary limitations on cell PBE implementation were the numerical complexity of the partial integro-differential equations resulting from model development and difficulty in determining partition and transition functions and single-cell growth rates. However, with the development of numerical algorithms capable of accurately approximating PBE solutions [144], along with experimental advances for evaluating cellular properties, PBEs represent a viable option for modeling intracellular states as distributed properties among a cell population.

3.1 PBE MODEL DEVELOPMENT

There are two common formulations for the cell population balance models which differ by the choice of internal coordinates. Models with intracellular properties that obey mass conservation are referred to as mass-structured, while age distribution models differentiate between cells of different ages within the system. Both model structures have been explored for chemotherapeutic schedule development [80, 81, 82, 83, 84, 85, 86, 147] and bioreactor applications, specifically the modeling of yeast cultures for single-phase, single-variable [142] and multi-phase, single variable [143, 144, 145, 146] cases with environmental coupling to the extracellular environment.

For implementation based on the three cell-cycle model in Figure 3.1, a mass structured model would require information on phase transition rates, a partitioning function for allocating cell properties following cell division, and single-cell growth rates for each phase. A model based solely on mass as the intrinsic variable would be unable to account for cell distributions within a quiescent phase (Q) where mass accumulation is theoretically zero [72]. Finally, a mass structured cell-cycle model does not allow for explicit period of drug exposure

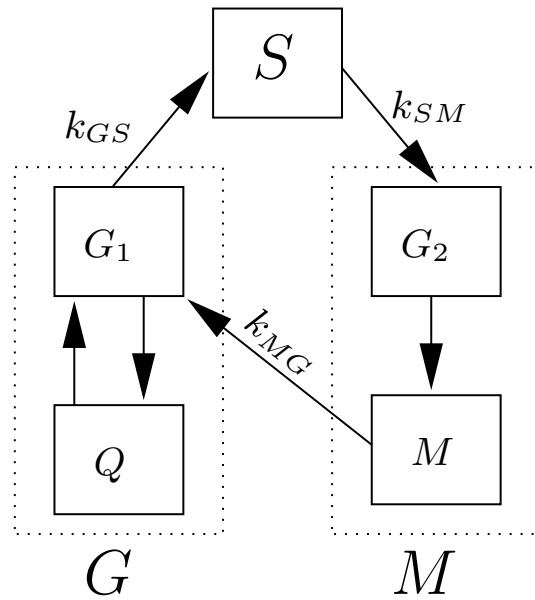


Figure 3.1: The five phases of the cell-cycle: Q (quiescent), G_1 (growth), S (DNA replication), G_2 (mitotic preparation), M (mitosis). Two cell-cycles models are developed: (i) a three-phase model considering G (lumped Q and G_1), S , and M (lumped G_2 and M) which is resolvable using DNA labeling and flow cytometry; or (ii) a four-phase structure with Q , G_1 , S , and M (lumped G_2 and M) which is resolvable using DNA and RNA labeling and subsequent flow cytometry.

calculation. Despite these limitations, a mass-structured model has proven advantageous for yeast bioreactors because the intrinsic variable, mass, is a measurable quantity and is passed from cell phase to cell phase.

Age-based models offer several advantages over mass structured cell population models even though age is not an available measure from a cell population. First, single cell rates of change for age correspond to unity, eliminating the need for experimentally determining three growth equations. Second, mass structured models formulate as partial integro-differential equations, a function of property partitioning following cell division, while age structured models result in simpler partial differential equations with an integral boundary condition. This integral boundary condition results from the accumulation of newborn cells, all of which possess an initial age of zero. Subsequently, calculation of a partition function is no longer required since age is not partitioned following cell division. Finally, tracking the internal property, age, allows for direct calculation of the period of drug exposure for any portion of the population. Drug-kill rates need not be constant throughout a cell phase, representative of complex interactions between a chemotherapeutic, intracellular targets, and the induction of apoptosis. For classes of problems where the dynamic effect of interest (tumor kill) is period or point of exposure dependent, an age structured model is both less complex and more relevant.

Both age- and mass-structured cell-cycle tumor growth PBEs were investigated. Additional model developments focused on extending both PBE model structures to account for saturating tumor growth dynamics.

3.2 MASS-STRUCTURED CELL CYCLE TUMOR GROWTH PBE

For the three cell phases, G , S , and M , the cell phase population density is given by N_G , N_S , and N_M , respectively. The complete PBE is given by Equations (3.1)-(3.3):

$$\begin{aligned} \frac{\partial N_G(m, t)}{\partial t} + \frac{\partial [N_G(m, t) \dot{R}(m)]}{\partial m} &= -\Gamma_G(m) N_G(m, t) \\ &\quad + 2 \int_m^{m_{max}} \Gamma_M(m') P(m, m') N_M(m') dm' \end{aligned} \quad (3.1)$$

$$\frac{\partial N_S(m, t)}{\partial t} + \frac{\partial [N_S(m, t) \dot{R}(m)]}{\partial m} = -\Gamma_S(m) N_S(m, t) + \Gamma_G(m) N_G(m, t) \quad (3.2)$$

$$\frac{\partial N_M(m, t)}{\partial t} + \frac{\partial [N_M(m, t) \dot{R}(m)]}{\partial m} = -\Gamma_M(m) N_M(m, t) + \Gamma_S(m) N_S(m, t) \quad (3.3)$$

$$\dot{R}(m_{min}) N_G(m_{min}, t) = \dot{R}(m_{max}) N_G(m_{max}, t) = 0 \quad (3.4)$$

$$\dot{R}(m_{min}) N_S(m_{min}, t) = \dot{R}(m_{max}) N_S(m_{max}, t) = 0 \quad (3.5)$$

$$\dot{R}(m_{min}) N_M(m_{min}, t) = \dot{R}(m_{max}) N_M(m_{max}, t) = 0 \quad (3.6)$$

Here m is the cell mass, m_{min} is the minimum cellular mass for the system, and m_{max} is the maximum cellular mass for the system. The growth rate, $\dot{R}(m)$, was set as a quadratic function of mass:

$$\dot{R}(m) = a_R(m_{max} - m)(m - m_{min}) \quad (3.7)$$

This satisfies the boundary condition on the upper and lower bounds of Equations (3.4)-(3.6). The same function for mass accumulation was utilized within all three cell phases. The transition functions out of cell phases G , S , and M are $\Gamma_G(m)$, $\Gamma_S(m)$, and $\Gamma_M(m)$, respectively. The transition functions were assumed to have the following forms, similar to those developed for yeast progression [146]:

$$\Gamma_i(m) = \begin{cases} 0 & m \leq m_{ci} \\ \beta_i(\exp^{\tau_i(m-m_{ci})} - 1) & m_{ci} \leq m \leq m_{ciup} \\ \beta_i(\exp^{\tau_i(m_{ciup}-m_{ci})} - 1) & m_{ciup} \leq m \end{cases}$$

Here, m_{ci} is the critical mass during phase i (where $i \in \{G, S, \text{ or } M\}$) representing the minimal mass necessary for phase transition, and β_i , τ_i , and m_{ciup} govern the ultimate

transition rate value through phase i , sharpness of the transition function relative to the current cell mass, and upper bound of cellular mass after which the phase transition rate was constant, respectively. Transition of cells from phase M to G follows cellular division resulting in two new cells and a division of the original mass defined by the following symmetric beta distribution:

$$P_M(m, m') = \begin{cases} 0 & m < m_{cM}, m' < m \\ \frac{1}{B(q,q)} \frac{1}{m} \left(\frac{m}{m'}\right)^{q-1} \left(1 - \frac{m}{m'}\right)^{q-1} & m_{cM} \leq m, m \leq m' \end{cases}$$

This function is similar to those used in describing yeast division [146]; however, a higher value of the constant, q , was selected to represent increased probability towards equal allocation of cellular mass following cell division for eukaryotic cells. Finally, the three $t = 0$ boundary conditions are given by:

$$N_G(m, 0) = N_{G0}(m)$$

$$N_S(m, 0) = N_{S0}(m)$$

$$N_M(m, 0) = N_{M0}(m)$$

A summary of the parameters used for simulations can be found in Table 3.1. The parameters in the present study were selected to characterize a tumor with an approximate doubling time of 9 days, representative of Ht29 human colon carcinoma xenograft tumor growth [148].

3.3 AGE-STRUCTURED CELL CYCLE TUMOR GROWTH PBE

This model was adapted from the age structured yeast model developed by Zamamiri *et al.* [146]. For the three cell phases, G , S , and M , the cell phase population density is given by N_G , N_S , and N_M , respectively. The complete PBE is as follows:

$$\frac{\partial N_G(a, t)}{\partial t} + \frac{\partial N_G(a, t)}{\partial a} = -\Gamma_G(a)N_G(a, t) \quad (3.8)$$

$$\frac{\partial N_S(a, t)}{\partial t} + \frac{\partial N_S(a, t)}{\partial a} = -\Gamma_S(a)N_S(a, t) \quad (3.9)$$

$$\frac{\partial N_M(a, t)}{\partial t} + \frac{\partial N_M(a, t)}{\partial a} = -\Gamma_M(a)N_M(a, t) \quad (3.10)$$

Here, a is the period of time a cell has resided within a given phase. The transition functions out of cell phase G , S , and M are $\Gamma_G(a)$, $\Gamma_S(a)$, and $\Gamma_M(a)$, respectively. The transition functions were assumed to have the following forms:

$$\Gamma_i(a) = \begin{cases} 0 & a \leq a_{c_i} \\ \beta_i \frac{a - a_{c_i}}{(m_i - 1)a_{c_i}} & a_{c_i} \leq a \leq m_i a_{c_i} \\ \beta_i & m_i a_{c_i} \leq a \end{cases} \quad (3.11)$$

Here, a_{c_i} is the critical age during cell phase i (where $i \in \{G, S, \text{ or } M\}$) representing the minimal age necessary for phase transition or cell division onset. β_i represents the maximum transition rate for the cell phase and m_i defines the sharpness of the transition function. The additional constraint, $m_i > 1$, ensures positive growth rates.

Finally, the three age-zero boundary conditions, which account for phase transition or division, are given by:

$$N_G(0, t) = \int_0^\infty 2\Gamma_M(a)N_M(a, t)da \quad (3.12)$$

$$N_S(0, t) = \int_0^\infty \Gamma_G(a)N_G(a, t)da \quad (3.13)$$

$$N_M(0, t) = \int_0^\infty \Gamma_S(a)N_S(a, t)da \quad (3.14)$$

A summary of the parameters used for simulations can be found in Table 3.2. These parameters were not estimated from data because there are multiple solutions for critical transition ages within the G -, S -, and M -phases that will provide a specified tumor doubling rate. Instead, the parameters were selected to characterize a tumor with an approximate doubling time of 9 days, representative of Ht29 human colon carcinoma xenograft tumor growth [148]. Furthermore, parameters were chosen to attain a phase fraction ratio ($G : S : M$) of 0.50 : 0.30 : 0.20, as observed from cell-cycle experiments [86]. In fact, the mean cell residence times in both the S - and M - phase are known to be inaccurate based upon cell cycling dynamics *in vitro* [86] and are a repercussion of attempting to describe solid tumor progression with phase fraction distributions observed from *in vitro* cells.

Table 3.1: Model, transition function, mass allocation, and division function parameters for the mass-structured cell-cycle PBE.

Parameter	Value	Parameter	Value
m_{cG}	$1.56 \cdot 10^{-9} \text{g}$	β_G	$0.05 \frac{1}{\text{day}}$
m_{cS}	$1.78 \cdot 10^{-9} \text{g}$	β_S	$0.5 \frac{1}{\text{day}}$
m_{cM}	$2.00 \cdot 10^{-9} \text{g}$	β_M	$0.5 \frac{1}{\text{day}}$
m_{min}	$0.44 \cdot 10^{-9} \text{g}$	τ_G	$1.0 \frac{1}{10^{-9} \text{g}}$
m_{max}	$2.67 \cdot 10^{-9} \text{g}$	τ_S	$1.0 \frac{1}{10^{-9} \text{g}}$
$m_{cG_{up}}$	$1.78 \cdot 10^{-9} \text{g}$	τ_M	$1.0 \frac{1}{10^{-9} \text{g}}$
$m_{cS_{up}}$	$2.00 \cdot 10^{-9} \text{g}$	a_R	$0.105 \cdot 10^{-9} \frac{\text{g}}{\text{day}}$
$m_{cM_{up}}$	$2.22 \cdot 10^{-9} \text{g}$	q	50

Table 3.2: Model, transition function, and division function parameters for the age-structured cell-cycle PBE.

Parameter	Value	Parameter	Value
a_{cG}	3.75 day	β_G	$4 \frac{1}{\text{day}}$
a_{cS}	2.4 day	β_S	$6 \frac{1}{\text{day}}$
a_{cM}	1.5 day	β_M	$6 \frac{1}{\text{day}}$
m_G	1.6	m_S	5
m_M	2.4		

3.4 NON-SATURATING PBE MODEL RESULTS AND DISCUSSION

Simulations for the unperturbed age and mass structured cell-cycle PBEs are shown below in Figures 3.2 and 3.3 for the age model and Figures 3.4 and 3.5 for the mass model. Both models were initialized with all cells distributed solely within G -phase to better illustrate growth phase transition and overall tumor growth progression. The age cell-cycle PBE was simulated with the following initial conditions:

$$N_G(a, 0) = 0.08e^{\frac{-(a-0.27)^2}{0.16}} \quad (3.15)$$

$$N_S(a, 0) = 0 \quad (3.16)$$

$$N_M(a, 0) = 0 \quad (3.17)$$

Population distributions for each phase (G , S , and M) can be found in Figure 3.3. Starting at time zero with all cells located within G -phase, the progression of the population can be observed through each of the cell phases.

Gradually, the distribution of cells spread out over all three phases, eliminating the semi-discrete increases in population seen every 9 days in Figure 3.2 (top). While the overall tumor growth rate becomes nearly exponential by day 35, damping oscillations continued to persist with respect to individual cell phase populations (Figure 3.2, bottom). The persistence of the oscillations was dependent on both the initial conditions of the system and the magnitude and structure of the phase transition kernels. Ultimately, an age-structured PBE with structure defined by Equations (3.8)-(3.10) would attain a steady state phase fraction distribution similar to that obtained during simulation of lumped cell-cycle models.

It is worth noting that the model parameters used for the age-structured PBE simulation were not evaluated against experimental data, nor were they constructed using information regarding cell cycling dynamics. Constructing a model based solely on bulk tumor doubling time results in a degenerate number of possible solutions where individual cell phases may compose an arbitrary percentage ($0 < f_i < 1$) of the overall tumor. Information from *in vitro* cell cycling studies can be used in place of the above phase transition parameters. However, observed *in vitro* cycling times are typically on the order of 1-2 days [9], significantly faster than the doubling times observed from studies involving solid tumors. Similarly, average G -

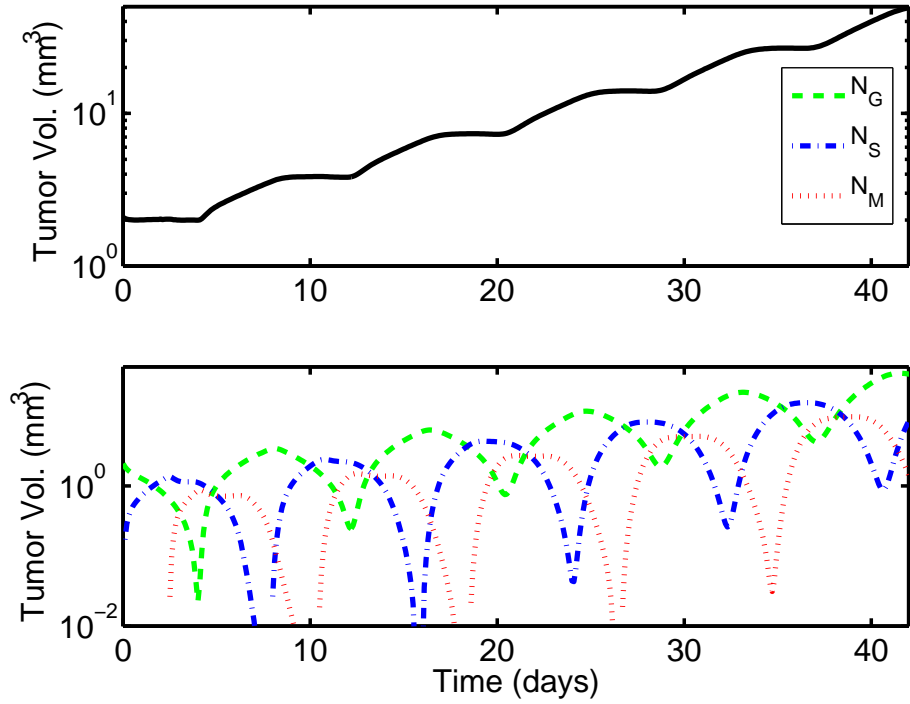


Figure 3.2: Tumor volume versus time. Top: Total volume starting from an initial cell distribution given by Equations (3.15)-(3.17). Bottom: Individual cell-cycle phase volumes for G -phase (N_G , dashed), S -phase (N_S , dash-dot), and M -phase (N_M , dotted) cells.

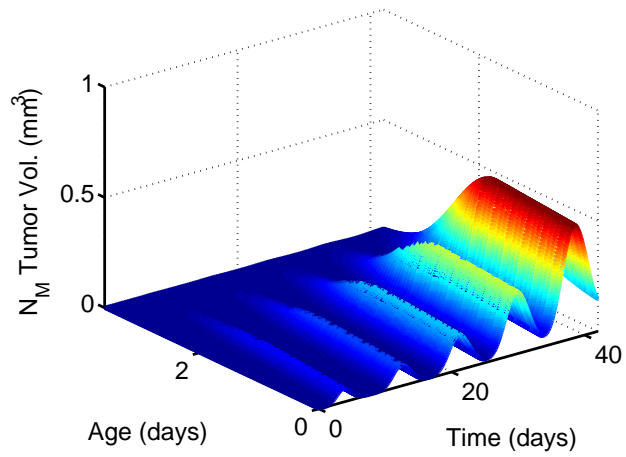
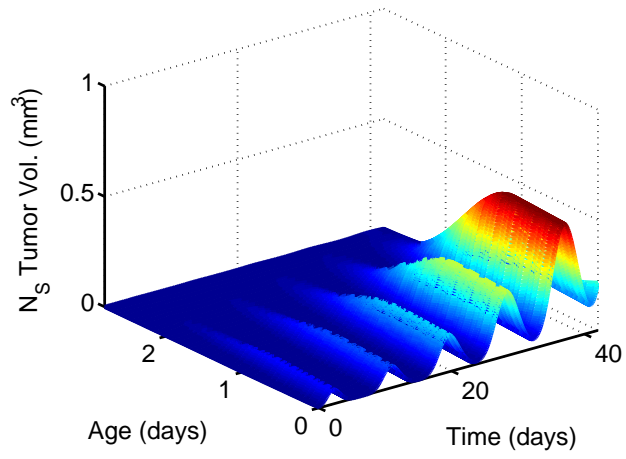
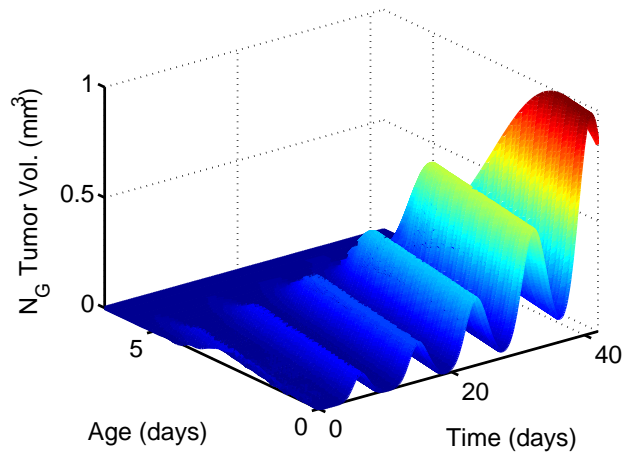


Figure 3.3: Cell distribution within G -phase (top), S -phase (middle), and M -phase (bottom) during unperturbed growth.

S -, and M -phase transition rates from *in vitro* studies are approximately 12-24, 4-8, and 4-6 hours, respectively, significantly shorter than the sum of critical ages incorporated within the age-structured PBE that serve as a lower bound on the doubling time of the modeled system (7.65 days).

The mass cell-cycle PBE was simulated with the following initial conditions:

$$N_G(m, 0) = 0.56e^{\frac{-(m-0.45)^2}{0.018}} \quad (3.18)$$

$$N_S(m, 0) = 0 \quad (3.19)$$

$$N_M(m, 0) = 0 \quad (3.20)$$

The overall tumor volume and individual phase progressions are shown in Figure 3.4, and the density progression over the initial seven days of the simulation are shown in Figure 3.5. Oscillations in the total tumor volume persisted for a longer period of time than in the age-structured PBE (out to 60 days, not shown), a result of the chosen model parameters.

Comparing both sets of model predictions, it is worth noting that incorporation of either mass or age of the cell population allowed for near identical results for overall tumor volume progression (Figures 3.2 and 3.4). However, both models also produced exponential tumor growth profiles, which is sufficient for describing blood-borne cancer progression but is inadequate for describing solid tumor growth. For solid tumors, both model structures need to be altered to display saturating growth kinetics as the overall population approaches a maximum value similar that observed from the lumped GM, SCM, and QCM model structures in Chapter 2.

3.5 MASS-STRUCTURED SATURATING CELL CYCLE PBE

For the saturating model, the ultimate goal was to have the G -phase fraction increase as the tumor size approaches a model-specific saturating value. This final allotment can be accomplished by having either the transition rate from G to S phase or the mass accumulation rate within Equation (3.1) saturate with increasing total tumor volume.

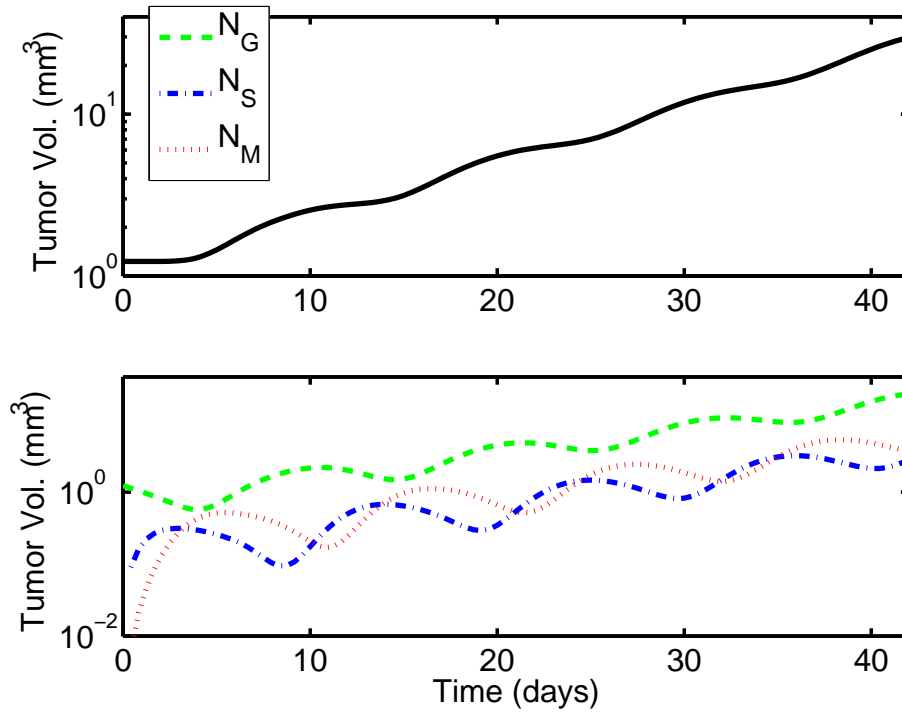


Figure 3.4: Tumor volume versus time. Top: Total volume starting from an initial cell distribution given in Equations (3.18)-(3.20) (m is normalized mass). Bottom: Individual cell-cycle phase volumes for G -phase (N_G , dashed), S -phase (N_S , dash-dot), and M -phase (N_M , dotted).

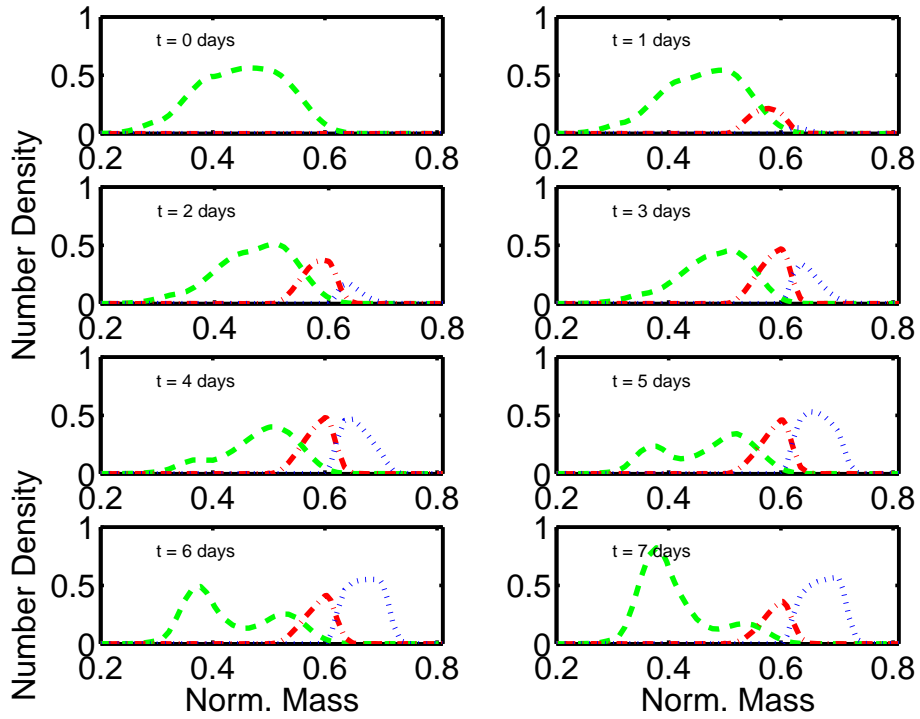


Figure 3.5: Total cell density distribution for G -phase (dashed), S -phase (dash-dot), and M -phase (dotted) during unperturbed growth. Density progression is shown starting from day 0 until day 7.

3.5.1 Saturating G -Phase Transition Rate

For the case of a saturating transition rate, $\Gamma_G(m, N_G(m, t), N_S(m, t), N_M(m, t))$, Equation (3.1) becomes:

$$\begin{aligned} \frac{\partial N_G(m, t)}{\partial t} + \frac{\partial [N_G(m, t)\dot{R}(m)]}{\partial m} &= -\Gamma_G(m, N_G(m, t), N_S(m, t), N_M(m, t))N_G(m, t) \\ &\quad + 2 \int_m^{m_{max}} \Gamma_M(m')P(m, m')N_M(m')dm' \end{aligned} \quad (3.21)$$

The transition function out of cell phase G , $\Gamma_G(m, N_G(m, t), N_S(m, t), N_M(m, t))$, was updated as follows:

$$\begin{aligned} \Gamma_G(m, N_t(t)) &= \begin{cases} 0 & m \leq m_{cG} \\ \beta_G(\exp^{\tau_G(m-m_{cG})} - 1) \ln\left(\frac{\theta}{N_t(t)}\right) & m_{cG} \leq m \leq m_{cG_{up}} \\ \beta_G(\exp^{\tau_{G_{up}}(m_{cG_{up}}-m_{cG})} - 1) \ln\left(\frac{\theta}{N_t(t)}\right) & m_{cG_{up}} \leq m \end{cases} \\ N_t(t) &= \int_{m_{min}}^{m_{max}} (N_G(m, t) + N_S(m, t) + N_M(m, t))dm \end{aligned}$$

Here, θ governs the saturation of tumor growth and places a pseudo-maximum on the total tumor volume for the system. A summary of the parameters used for simulations can be found in Table 3.3. Parameters were chosen to achieve an approximate tumor doubling time of 9 days, as before.

Results for the mass-structured PBE with saturating G -phase dynamics are shown in Figure 3.6 with cell density distributions over the course of the simulation shown in Figure 3.7. The model was initialized with the same initial conditions from Equations (3.18)-(3.20). While the model does display saturating growth kinetics, halting further tumor progression at approximately the θ value of the system ($t = 120$ days), the growth kinetics up until that point are approximately exponential, inconsistent with the dynamics observed from the GM, SCM, QCM, and in the literature [69]. This is confirmed in Figure 3.7, where it is shown that the individual phase distributions, while increasing in overall number, have the same distribution from day 50 until the overall tumor volume reaches θ . The only period where this does not hold is during the first 10 days (top four figures in Figure 3.7), where initial condition effects are still influencing phase density distributions, and after day 110 (bottom four figures in Figure 3.7), where the saturation in G -phase transition rate begins to

manifest. Despite using the same initial conditions from the non-saturating mass-structured PBE, this model displayed less extended phase oscillations, likely a result of introducing the saturating G -phase exit rate [84].

Some concerns regarding the model predictions included the abrupt alteration in growth dynamics predicted upon reaching the saturating tumor value and the behavior of the model upon reaching the plateau population (Figures 3.6 and 3.7). The overall tumor volume increased beyond the specified θ value as cells currently within S - and M -phase would still complete the cell-cycle despite cessation of G -phase transition. Furthermore, as no limit on mass accumulation was specified within the model, those cells which can no longer progress through G -phase continue to accumulate mass, progressing towards the specified maximum mass of the model. This introduces two problems: (i) model quality begins to degrade as the entire population converges to to the maximum mass of the system, all within a single phase; and (ii) if the population would decrease below θ , there would be instantaneous phase transition as the cell masses in G -phase already exceed the necessary value for progression through both S - and M -phase. Alternatively, it may be desirable to design the model structure to saturate mass accumulation rather than phase transition rate to avoid these problems.

3.5.2 Saturating G -Phase Mass Accumulation Rate

For the case of a saturating mass accumulation rate, Equations (3.2) and (3.3) and the associated mass accumulation rates remained unchanged. The mass accumulation rate for G -phase, $R_G(m, N_G, N_S, N_M)$, and Equation (3.1) were altered as follows:

$$\begin{aligned} \frac{\partial[N_G(m, t)\dot{R}_G(m, N_t(t))]}{\partial m} + \frac{\partial N_G(m, t)}{\partial t} &= -\Gamma_G(m)N_G(m, t) \\ &\quad + 2 \int_m^{m_{max}} \Gamma_M(m')P(m, m')N_M(m')dm' \end{aligned} \quad (3.22)$$

$$R_G(\dot{N}_t(t), m) = a_{mG}(m_{max} - m)(m - m_{min}) \ln \left(\frac{\theta}{N_t(t)} \right) \quad (3.23)$$

$$N_t(t) = \int_{m_{min}}^{m_{max}} (N_G(m, t) + N_S(m, t) + N_M(m, t))dm$$

Table 3.3: Model, transition function, mass allocation, and division function parameters for the mass-structured saturating cell-cycle PBE with saturating G -phase transition rate.

Parameter	Value	Parameter	Value	Parameter	Value
m_{cG}	$1.56 \cdot 10^{-9} \text{g}$	β_G	$0.70 \frac{1}{\text{day}}$	$m_{cG_{up}}$	$1.78 \cdot 10^{-9} \text{g}$
m_{cS}	$1.78 \cdot 10^{-9} \text{g}$	β_S	$1.0 \frac{1}{\text{day}}$	$m_{cS_{up}}$	$2.00 \cdot 10^{-9} \text{g}$
m_{cM}	$2.00 \cdot 10^{-9} \text{g}$	β_M	$1.0 \frac{1}{\text{day}}$	$m_{cM_{up}}$	$2.22 \cdot 10^{-9} \text{g}$
m_{min}	$0.44 \cdot 10^{-9} \text{g}$	τ_G	$1.0 \frac{1}{10^{-9} \text{g}}$	q	50
m_{max}	$3.33 \cdot 10^{-9} \text{g}$	τ_S	$1.0 \frac{1}{10^{-9} \text{g}}$	θ	10000 mm^3
a_R	$0.12 \cdot 10^{-9} \frac{\text{g}}{\text{day}}$	τ_M	$1.0 \frac{1}{10^{-9} \text{g}}$		

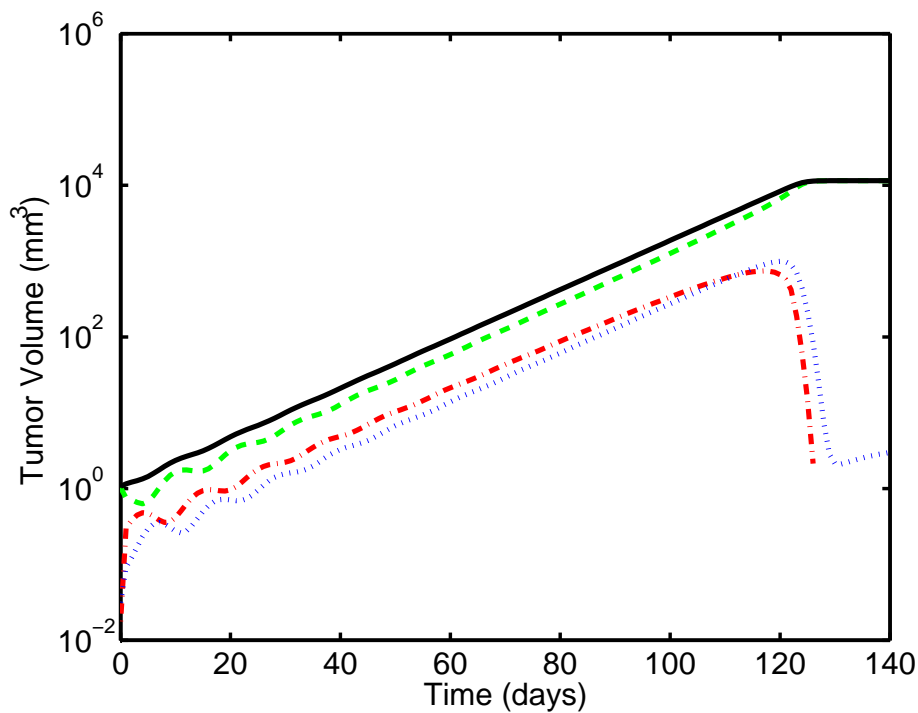


Figure 3.6: Tumor volume (solid) versus time starting from an initial cell distribution given in Equations (3.18)-(3.20) (m is normalized mass). Individual cell-cycle phase volumes are shown for G -phase (dashed), S -phase (dash-dot), and M -phase (dotted).

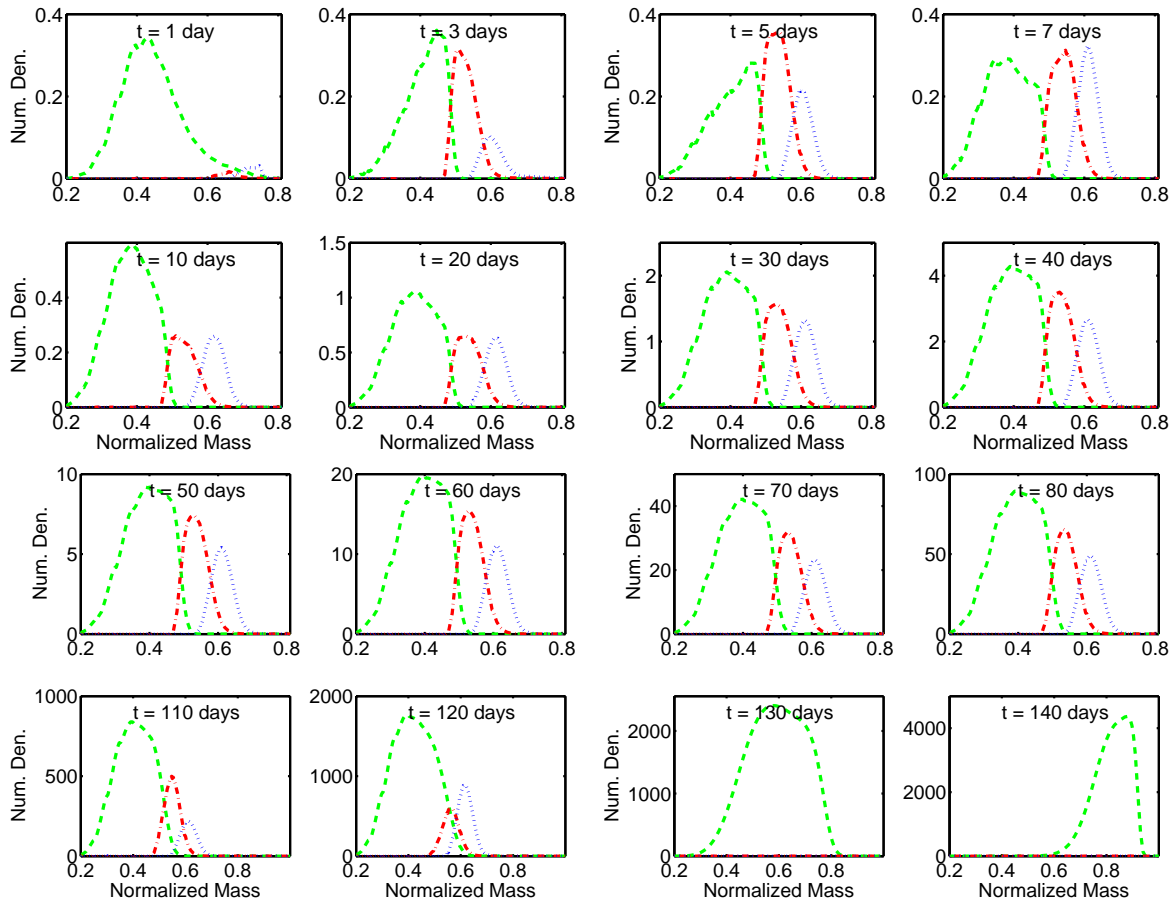


Figure 3.7: Total cell density distribution for G -phase (dashed), S -phase (dash-dot), and M -phase (dotted) during unperturbed growth. Cell cycle density plots are shown, starting from the upper left, for days 1, 3, 5, 7, 10, 20, 30, 40, 50, 60, 70, 80, 110, 120, 130, and 140.

A summary of the parameters used for simulations can be found in Table 3.4. Parameters were chosen to achieve an approximate tumor doubling time of 9 days.

Model predictions for the mass-structured cell-cycle PBE with saturating G -phase mass accumulation are shown in Figure 3.8 with cell-cycle density plots in Figure 3.9. Oscillations persisted for an extended period of time in this model; this is different from the previously observed response of the mass-structured model with saturating G -phase transition rate. These results implied that the saturating mass-accumulation rate model was capable of more accurately reproducing the exponential growth dynamics observed from the original mass-structured model. These oscillations persisted throughout the entire tumor progression, a result of model initial conditions, and it is unlikely that phase oscillations would still be observable in a solid tumor after such an extensive period of time (oscillations over weekly periods while a majority of bodily processes oscillate over a daily or more frequent schedule). The phase density plots (Figure 3.9) reveal that the model takes on the characteristics of exponential growth (Figure 3.9 days 1 to 90), then gradually accumulated a greater fraction of the tumor population within G -phase (Figure 3.9 days 90 to 190). Eventually, once the saturating tumor population is attained, mass accumulation completely halts within G -phase (Figure 3.9 days 190 to 240). While this model also attained a final tumor volume in excess of θ , the degree to which it exceeded θ was significantly less (0.001% vs. 15%) than the mass-structured PBE with phase transition saturation. This resulted from the different approaches to the plateau population predicted by both models.

While this mass-structured cell-cycle PBE with saturation in G -phase mass accumulation displayed the desired tumor growth dynamics without any mathematical degeneracy, there remain problems regarding appropriate parameters for such structures and the incorporation of treatment effect. Though the model contains the appropriate phases for cycle specific drug effects, there is no literature evidence relating cell mass and drug concentration to a PD effect. Furthermore, while there is greater uncertainty regarding average cell mass and cellular mass necessary for phase transition, the residence time of a cell within S - and M -phase is well characterized during unperturbed proliferation, likely a result of the mechanistic nature of DNA replication and cell division.

Table 3.4: Model, transition function, mass allocation, and division function parameters for the mass-structured cell-cycle PBE with saturating G -phase mass accumulation rate.

Parameter	Value	Parameter	Value	Parameter	Value
m_{cG}	$1.56 \cdot 10^{-9} \text{g}$	β_G	$0.70 \frac{1}{\text{day}}$	$m_{cG_{up}}$	$1.78 \cdot 10^{-9} \text{g}$
m_{cS}	$1.78 \cdot 10^{-9} \text{g}$	β_S	$1.0 \frac{1}{\text{day}}$	$m_{cS_{up}}$	$2.00 \cdot 10^{-9} \text{g}$
m_{cM}	$2.00 \cdot 10^{-9} \text{g}$	β_M	$1.0 \frac{1}{\text{day}}$	$m_{cM_{up}}$	$2.22 \cdot 10^{-9} \text{g}$
m_{min}	$0.44 \cdot 10^{-9} \text{g}$	τ_G	$1.0 \frac{1}{10^{-9} \text{g}}$	q	50
m_{max}	$3.33 \cdot 10^{-9} \text{g}$	τ_S	$1.0 \frac{1}{10^{-9} \text{g}}$	θ	10000 mm^3
a_R	$0.12 \cdot 10^{-9} \frac{\text{g}}{\text{day}}$	τ_M	$1.0 \frac{1}{10^{-9} \text{g}}$	a_{mG}	$0.10 \frac{\text{g}}{\text{day}}$

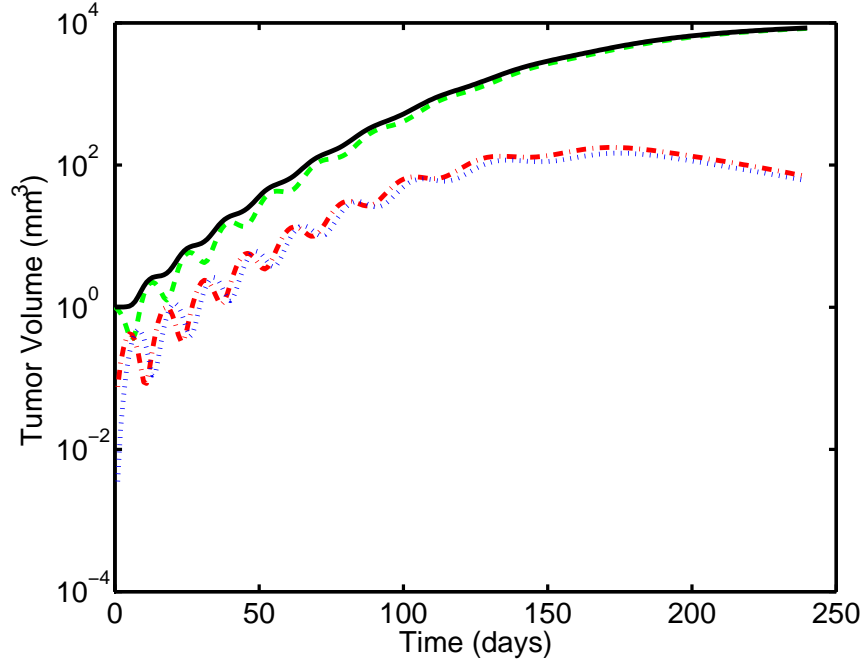


Figure 3.8: Total tumor volume (solid) versus time starting from an initial cell distribution of $N_G(m, 0) = 0.40e^{-\frac{(m-0.49)^2}{0.014}}$ with $N_S(m, 0) = N_M(m, 0) = 0$ (m is normalized mass). Individual cell-cycle phase volumes are shown for G -phase (dashed), S -phase (dash-dot), and M -phase (dotted).

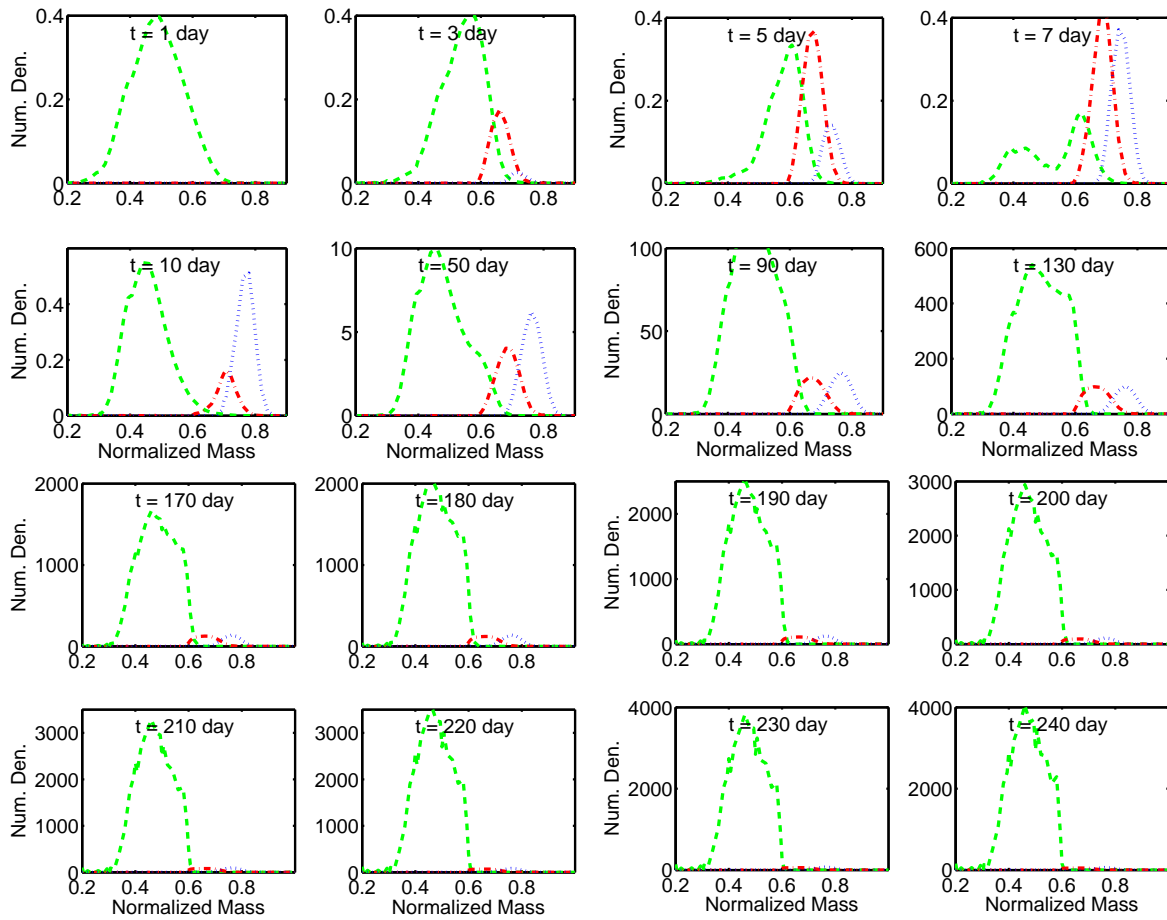


Figure 3.9: Total cell density distribution for G -phase (dashed), S -phase (dash-dot), and M -phase (dotted) during unperturbed growth. Cell cycle density plots are shown, starting from the upper left, for days 1, 3, 5, 7, 10, 50, 90, 130, 170, 180, 190, 200, 210, 220, 230, and 240.

3.6 AGE-STRUCTURED SATURATING CELL CYCLE PBE

Starting from the initial age-structured cell-cycle PBE Equations (3.8)-(3.10), two models were investigated: (i) a three phase cell-cycle PBE with a lumped G-phase population; and (ii) a four phase age structured cell-cycle PBE. These representations are analogous to the SCM and QCM developed previously in Chapter 2.

3.6.1 Three Phase Age-Structured Saturating Cell Cycle PBE

For case (i), Equations (3.8) and (3.13) are updated as Equations (3.24) and (3.25), respectively:

$$\frac{dN_G(t)}{dt} = -k_{GS} \ln\left(\frac{\theta}{N_t(t)}\right) + \int_0^\infty 2\Gamma_M(a)N_M(a, t)da \quad (3.24)$$

$$N_S(0, t) = k_{GS} \ln\left(\frac{\theta}{N_t(t)}\right) N_G(t) \quad (3.25)$$

$$N_t(t) = N_G(t) + \int_0^\infty (N_S(a, t) + N_M(a, t))da$$

Parameters for this model were taken from the literature, when possible, and are shown in Table 3.5. S - and M -phase transition times were set at 6-8 hours [9, 147] while the value of k_{GS} was selected to attain an approximate tumor doubling time of 9 days [147]. Overall tumor volume and individual phase progressions are shown in Figure 3.10 with initialization at $N_G(0) = 1 \text{ mm}^3$ and $N_S(a, 0) = N_M(a, 0) = 0$. Inclusion of a lumped representation for G -phase decreased the degree and magnitude of the phase progression oscillations during the simulation. While it was previously observed that inclusion of a lumped quiescent term in an age PBE decreases oscillations [84, 86], this model demonstrates that it may be a mathematical effect of including a lumped phase representation capable of constantly supplying cells to the next phase.

Table 3.5: Model, transition function, and division function parameters for the age-structured saturating cell-cycle PBE with three cell phases.

Parameter	Value	Parameter	Value
a_{c_S}	0.25 day	β_S	$25 \frac{1}{\text{day}}$
a_{c_M}	0.25 day	β_M	$25 \frac{1}{\text{day}}$
m_S	0.5 day	m_M	0.5 day
k_{GS}	$0.014 \frac{1}{\text{day}}$	θ	10000 mm^3

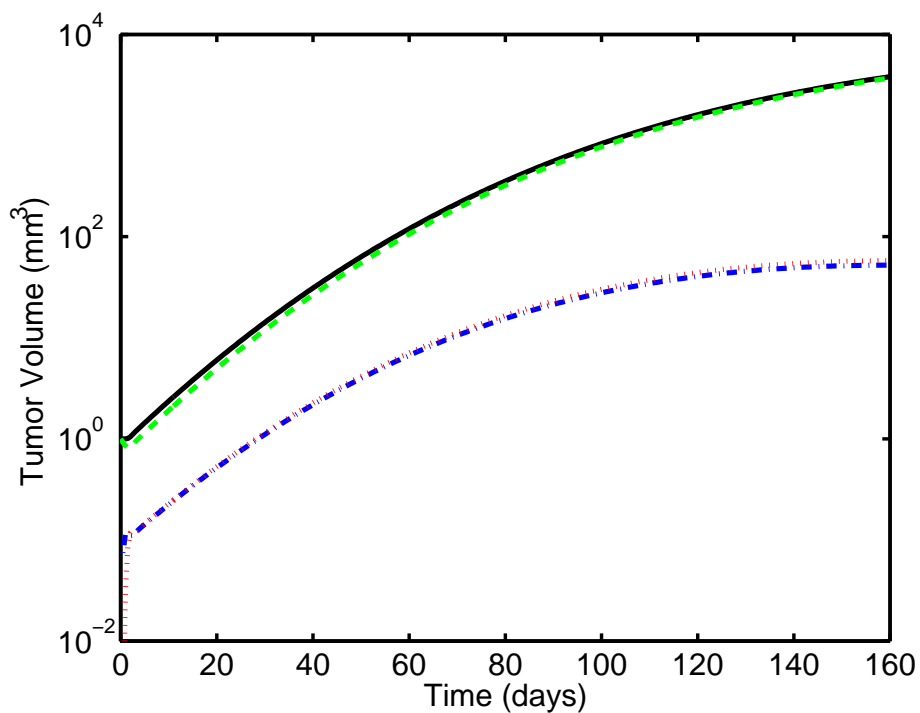


Figure 3.10: Total tumor volume progression (solid) starting from an initial cell distribution of $N_G(0) = 1.0$ with $N_S(a, 0) = N_M(a, 0) = 0$, and individual cell-cycle phase volumes for G -phase (dashed), S -phase (dash-dot), and M -phase (dotted).

3.6.2 Four Phase Age-Structured Saturating Cell Cycle PBE

For case (ii), Equations (3.9)-(3.10) remained unchanged while Equations (3.8) and (3.12) are updated as Equations (3.26) and (3.27):

$$\frac{\partial N_G(a, t)}{\partial t} + \frac{\partial N_G(a, t)}{\partial a} = -(1 + k_{GQ})\Gamma_G(a)N_G(a, t) \quad (3.26)$$

$$N_G(0, t) = k_{QG} \ln\left(\frac{\theta}{N_t(t)}\right) N_Q(t) + \int_0^\infty 2\Gamma_M(a)N_M(a, t)da \quad (3.27)$$

$$N_t(t) = N_Q(t) + \int_0^\infty (N_G(a, t) + N_S(a, t) + N_M(a, t))da$$

In addition, Equation (3.28) was appended to the model to represent the time varying volume of tumor in a quiescent state:

$$\frac{dN_Q(t)}{dt} = -k_{QG} \ln\left(\frac{\theta}{N_t(t)}\right) N_Q(t) + \int_0^\infty k_{GQ}\Gamma_G(a)N_G(a, t)da \quad (3.28)$$

Parameters for this model were also taken from the literature when possible and are shown in Table 3.6. S - and M -phase transition times were set at 6-8 hours while the value of k_{GQ} and k_{QG} were selected to attain an approximate tumor doubling time of 9 days. Figure 3.11 shows the total tumor and individual phase progression for the four phase age-structured saturating cell-cycle PBE using these parameters. As before, the inclusion of a lumped ODE within the model decreased both the degree and magnitude of the system oscillations. The tumor volume versus time profile was similar to that obtained from the three-phase age-structured saturating cell-cycle PBE, but, the two models displayed different dynamics in approaching the plateau volume.

3.6.3 Age-Structured Cell Cycle Model Comparison

As a final comparison, the original age-structured cell-cycle PBE (Equations (3.8)-(3.10)) was updated with the same transition, critical age, and maximum age parameters for S - and M -phase used in the previous two models. Overall tumor progression predictions for the three models are shown in Figure 3.12. Though exact overlap was not obtained between the three models, there is reasonable agreement over the region of exponential tumor volume progression. Deviation between the saturating and non-saturating models occurs for tumor

Table 3.6: Model, transition function, and division function parameters for the four phase age-structured saturating cell-cycle PBE.

Parameter	Value	Parameter	Value	Parameter	Value
a_{c_G}	0.5 day	β_G	$100 \frac{1}{\text{day}}$	k_{GQ}	$4.0 \frac{1}{\text{day}}$
a_{c_S}	0.25 day	β_S	$75 \frac{1}{\text{day}}$	k_{QG}	$0.030 \frac{1}{\text{day}}$
a_{c_M}	0.25 day	β_M	$75 \frac{1}{\text{day}}$	θ	10000 mm^3
m_G	1.0 day	m_S	0.5 day	m_M	0.5 day

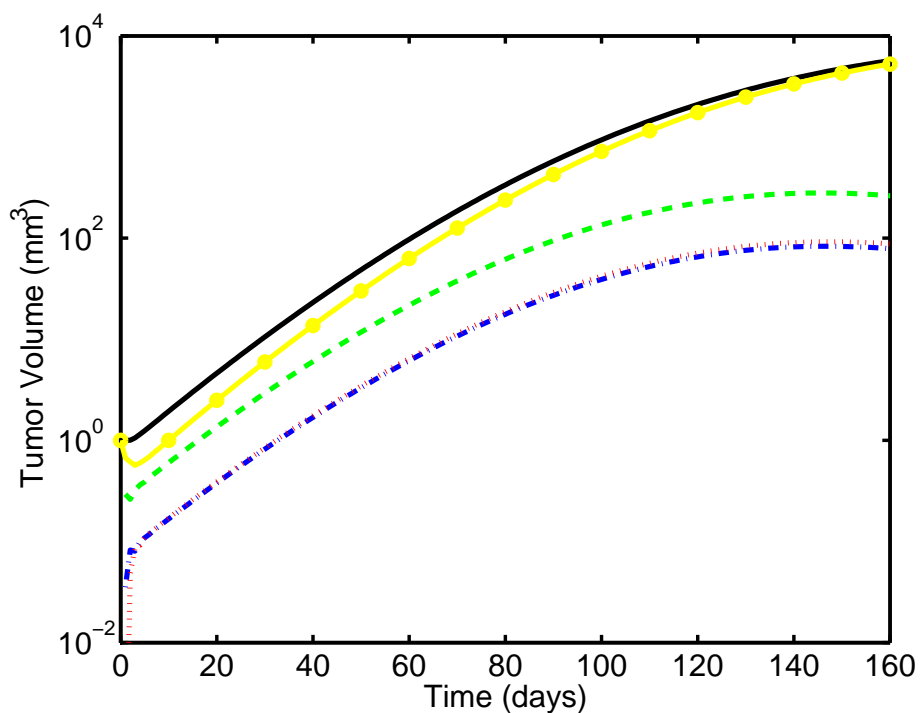


Figure 3.11: Total tumor volume progression (solid) starting from an initial cell distribution of $N_Q(0) = 1.0$ with $N_G(a, 0) = N_S(a, 0) = N_M(a, 0) = 0$, and individual cell-cycle phase volumes for the quiescent cells (Q , circles), G -phase (dashed), S -phase (dash-dot), and M -phase (dotted).

volumes beyond 100 mm^3 , with additional deviation present between the two saturating models as the plateau population was approached. This deviation resulted from the manner in which saturation was included within the model structure, necessitating a lower initial phase transition rate (k_{GS}) for the three-phase age-structured model in order to maintain an exponential tumor doubling time of approximately 9 days.

3.7 DOSE SCHEDULE EVALUATION AND DISCUSSION

Extensive evaluation of the linear age-structured cell-cycle PBE in the development of chemotherapeutic treatment schedules can be found in the literature [80, 81, 82, 83, 84, 85, 86, 147]. These studies evaluated the dynamics of tumor cells grown *in vitro*, developed models approximating this growth dynamic, and determined the necessary dosing interval for an administered therapeutic to attain a maximum effect by taking advantage of explicitly known cell-cycle dynamics. Within these models, oscillations are induced following treatment; this results in periods of time where the next dosing will be more or less effective, a phenomena referred to as resonance chemotherapy. PK drug profiles in such models are typically incorporated as either being “present” or “absent”, without evaluation of multiple dosing levels or accurate PK dynamics. Furthermore, drug effect was incorporated within these models as a bilinear kill term. Although this term is commonly used for approximating the overall effect between drug exposure and the susceptible population of cells, additional model information is not used in constructing the drug effect functionality (*e.g.*, cell susceptibility at certain periods during phase transition, increased likelihood of cell apoptosis based on period of exposure, etc.).

Studies by Sherer and coauthors have evaluated the extent of dosing necessary to “ensure” elimination of the tumor based on statistical measures, mainly focusing on the necessary duration of treatment [127] while studies by Gaffney have evaluated the probability of success of a treatment accounting for the evolution of drug resistance within the tumor [85]. Finally, age-structured cell cycle PBE models have also been used to construct models for the cycling of hematopoietic cells, utilizing a growth structure similar to tumor

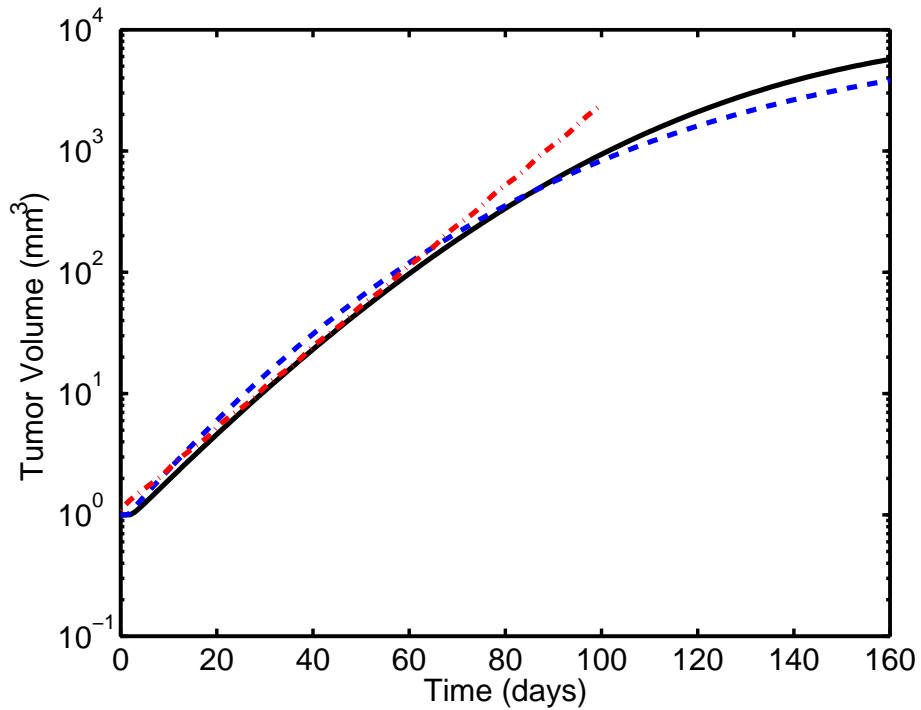


Figure 3.12: Total tumor volume progression for the original age-structured PBE (dash-dot), three-phase saturating age-structured PBE (dashed), and four-phase saturating age-structured PBE (solid).

progression but with the addition of a quiescent compartment. Together with developed tumor models, predictions from both the tumor and hematopoietic cell models were combined to evaluate therapeutic administration schedules for effectiveness against the tumor while sparing other normal functioning proliferating cells [84, 86]. The results of these experiments and simulation studies [84, 86] are conclusive that proper timing of doses to elucidate increased tumor kill is likely not achievable due to the similarities in growth dynamics observed between tumor and hematopoietic cells grown *in vitro*. However, these models neglect that the modeled tumor dynamics may not be representative of the *in vivo* setting. Indeed, experiments to validate even the proposed cycling of native hematopoietic cells have not been performed, though there is conclusive evidence for the cycling of the entire population following chemotherapeutic treatment (or disease). While it is likely that the susceptible cell population would be eliminated following treatment with a chemotherapeutic and oscillations can be induced in cultured cells, there is no experimental evidence for induced phase fraction oscillations *in vivo* in either solid tumors or native proliferating cell populations.

Researchers have investigated the effects of including quiescent cell populations as an additional lumped ODE [84, 86], however evaluation of age-structured PBEs with saturating growth dynamics have not been evaluated within the literature. Furthermore, the incorporation of accurate PK dynamics and multiple chemotherapeutics targeting different phases of the cell cycle have not been investigated. This latter area requires investigation as a possible dynamic explanation, at least in part, of the macroscopic observations of synergism and antagonism observed during combination chemotherapy delivered over different treatment schedules.

Three case studies were proposed for evaluating treatment outcomes, as measured by tumor volume. In these cases, the tumor was: (i) the non-saturating age-structured PBE (Equations (3.8)-(3.10)); (ii) the three-phase saturating age-structured PBE (Equations (3.9), (3.10), and (3.24)); or (ii) the four-phase saturating age-structured PBE (Equations (3.9), (3.10), (3.24), and (3.28)). Treatment occurred with two drugs, where were *S*-phase and *M*-phase specific, respectively. The dosing schedules employed for the three case studies are summarized as follows: Schedule 1 evaluated two drugs having the

same PK and PD dynamics and parameter values. Dosing of the *S*-phase drug began on day 42 and was repeated every 7 days through day 70. Dosing of the *M*-phase therapeutic also occurred at 7 day intervals beginning between 6 days prior (day 36) and 6 days after (day 48) the initiation of treatment with the *S*-phase therapeutic. Schedule 2 evaluated a *M*-phase therapeutic having PK dynamics that persist for an entire week (*e.g.*, Doc), while the *S*-phase therapeutic PK lasted for one day. Dosing of the compounds occurred as described for Schedule 1. Schedule 3 used the same PK as Schedule 2, however, dosing of the *S*-phase drug began on day 42, was repeated daily for 4 more days, and this five day on two day off schedule was repeated through day 70. Dosing of the *M*-phase therapeutic was the same as the previous two schedules.

The schedules were motivated by the following rationale. Schedule 1 results would reveal if the developed models were more susceptible to treatment during specific phases. Schedule 2 investigates more clinically-relevant PK dynamics for the two drugs, using PK profiles similar to that observed from common *S*-phase active camptothecins (plasma half-lives on the order 2-4 hours) and *M*-phase active taxanes (plasma half-lives of 12-24 hours); The PK profiles and dosing schedules for Schedule 3 are similar to preclinical regimens evaluated for the treatment of SCID mice implanted with Ht29 human tumor xenografts and treated with 9-nitrocamptothecin (9NC) and docetaxel. Results from this 9NC/Doc animal study revealed a possible synergistic interaction between 9NC and docetaxel treatment that was schedule dependent (*i.e.*, statistically-significant improvement in final tumor volume was achieved if docetaxel was delivered on the fifth day of 9NC treatment versus the first day).

Each of the drugs (D_1 and D_2) in this simulation study were modeled using two compartments in series with first order transfer and elimination rates to more accurately represent PK dynamics observed in implanted xenografts following drug administration.

The equations for the drugs and phase-specific kill effects are as follows:

$$\frac{dE_1(t)}{dt} = -\tau_{11}E_1(t) + u_1(t) \quad (3.29)$$

$$\frac{dD_1(t)}{dt} = -\tau_{21}D_1(t) + \tau_{11}E_1(t) \quad (3.30)$$

$$\frac{dE_2(t)}{dt} = -\tau_{12}E_2(t) + u_2(t) \quad (3.31)$$

$$\frac{dD_2(t)}{dt} = -\tau_{22}D_2(t) + \tau_{12}E_2(t) \quad (3.32)$$

$$\frac{\partial N_S(a, t)}{\partial t} + \frac{\partial N_S(a, t)}{\partial a} = -\Gamma_S(a)N_S(a, t) - k_S N_S(a, t)D_1(t) \quad (3.33)$$

$$\frac{\partial N_M(a, t)}{\partial t} + \frac{\partial N_M(a, t)}{\partial a} = -\Gamma_M(a)N_M(a, t) - k_M N_M(a, t)D_2(t) \quad (3.34)$$

Here, $u_1(t)$ and $u_2(t)$ are the amounts of the S - and M -phase drug administered, τ_{ij} is the transfer rate ($\frac{1}{\text{day}}$) of input j through state i , and k_S and k_M are the tumor kill rates ($\frac{\mu M}{\text{day}}$ for S - and M -phase cells, respectively). Values for τ_{ij} and kill rates for the three schedules can be found in Table 3.7. Representative plots of the drug PK can be found in Figure 3.13. For each respective dose, $10\mu M$ of the drug was delivered as a bolus at the specified time.

While the PK models presented above were only representative approximations of actual drug PK, and the tumor growth dynamics were not modeled based upon the untreated control tumor growth dynamics, the focus of these studies was to determine if significant improvements in final tumor volume were achievable when multiple drugs and realistic PK profiles were incorporated into nonlinear age-structured PBEs.

The final tumor volumes after 100 days for each of the three models are shown in Tables 3.8-3.10. The notation in column 1 refers to which day delivery of the M -phase therapeutic was initiated relative to delivery of the S -phase therapeutic, which was always initiated on day 42. The organization structure is chosen for comparing treatment outcomes for individual schedules studies and should not serve as a comparison between individual model results.

As seen in Table 3.8, equivalent final tumor volumes were predicted at the end of the simulation for two therapeutics with activity during different cell-cycle phases when the phase transition rates were equivalent. These results were expected, and they served as a validation of the model simulations. The general trend of final tumor volumes obtained,

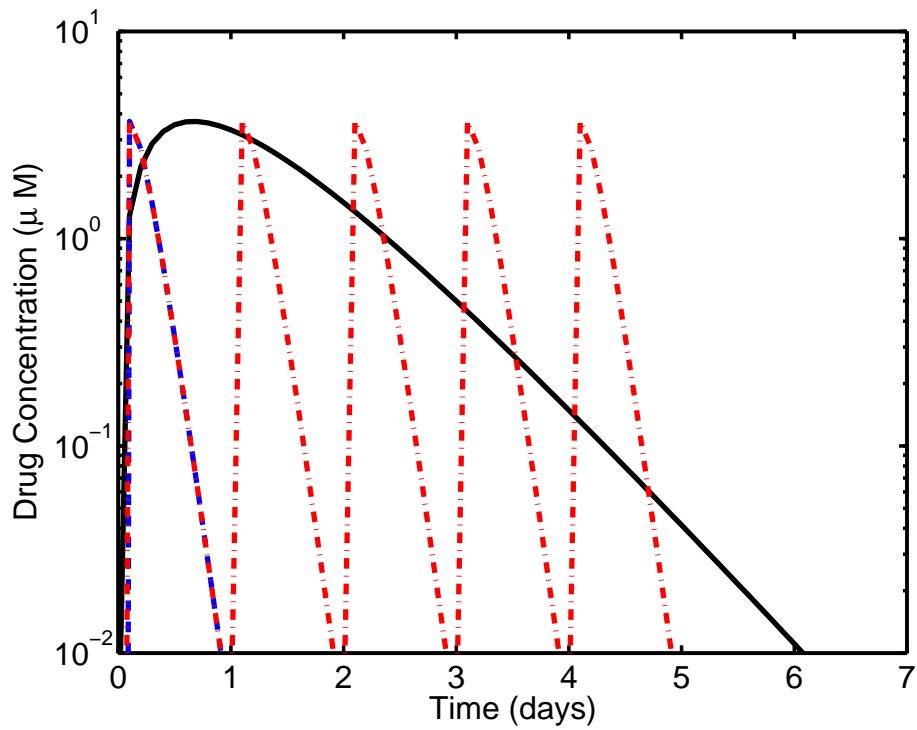


Figure 3.13: PK profiles for the *S*-phase chemotherapeutic for Schedule 1 (solid), Schedule 2 (dashed, overlay on first “hump” of Schedule 3), and Schedule 3 (dash-dot). The *M*-phase PK profile for all three schedules is the same as the *S*-phase profile for Schedule 1.

Table 3.7: PK and PD parameters used for evaluating the treatment of three age-structured PBEs with S - and M -phase therapeutics.

	Model 1		Model 2		Model 3	
Schedule 1	τ_{11}	$1.5 \frac{1}{\text{day}}$	τ_{11}	$1.5 \frac{1}{\text{day}}$	τ_{11}	$1.5 \frac{1}{\text{day}}$
	τ_{21}	$1.5 \frac{1}{\text{day}}$	τ_{21}	$1.5 \frac{1}{\text{day}}$	τ_{21}	$1.5 \frac{1}{\text{day}}$
	τ_{12}	$1.5 \frac{1}{\text{day}}$	τ_{12}	$1.5 \frac{1}{\text{day}}$	τ_{12}	$1.5 \frac{1}{\text{day}}$
	τ_{22}	$1.5 \frac{1}{\text{day}}$	τ_{22}	$1.5 \frac{1}{\text{day}}$	τ_{22}	$1.5 \frac{1}{\text{day}}$
	k_S	$1.2 \frac{\mu M}{\text{day}}$	k_S	$1.6 \frac{\mu M}{\text{day}}$	k_S	$2.4 \frac{\mu M}{\text{day}}$
	k_M	$1.2 \frac{\mu M}{\text{day}}$	k_M	$1.6 \frac{\mu M}{\text{day}}$	k_M	$2.4 \frac{\mu M}{\text{day}}$
Schedule 2	τ_{11}	$1.5 \frac{1}{\text{day}}$	τ_{11}	$1.5 \frac{1}{\text{day}}$	τ_{11}	$1.5 \frac{1}{\text{day}}$
	τ_{21}	$10.0 \frac{1}{\text{day}}$	τ_{21}	$10.0 \frac{1}{\text{day}}$	τ_{21}	$10.0 \frac{1}{\text{day}}$
	τ_{12}	$10.0 \frac{1}{\text{day}}$	τ_{12}	$10.0 \frac{1}{\text{day}}$	τ_{12}	$10.0 \frac{1}{\text{day}}$
	τ_{22}	$1.5 \frac{1}{\text{day}}$	τ_{22}	$1.5 \frac{1}{\text{day}}$	τ_{22}	$1.5 \frac{1}{\text{day}}$
	k_S	$200.0 \frac{\mu M}{\text{day}}$	k_S	$250.0 \frac{\mu M}{\text{day}}$	k_S	$60.0 \frac{\mu M}{\text{day}}$
	k_M	$1.2 \frac{\mu M}{\text{day}}$	k_M	$1.6 \frac{\mu M}{\text{day}}$	k_M	$2.4 \frac{\mu M}{\text{day}}$
Schedule 3	τ_{11}	$1.5 \frac{1}{\text{day}}$	τ_{11}	$1.5 \frac{1}{\text{day}}$	τ_{11}	$1.5 \frac{1}{\text{day}}$
	τ_{21}	$10.0 \frac{1}{\text{day}}$	τ_{21}	$10.0 \frac{1}{\text{day}}$	τ_{21}	$10.0 \frac{1}{\text{day}}$
	τ_{12}	$10.0 \frac{1}{\text{day}}$	τ_{12}	$10.0 \frac{1}{\text{day}}$	τ_{12}	$10.0 \frac{1}{\text{day}}$
	τ_{22}	$1.5 \frac{1}{\text{day}}$	τ_{22}	$1.5 \frac{1}{\text{day}}$	τ_{22}	$1.5 \frac{1}{\text{day}}$
	k_S	$40.0 \frac{\mu M}{\text{day}}$	k_S	$50.0 \frac{\mu M}{\text{day}}$	k_S	$300.0 \frac{\mu M}{\text{day}}$
	k_M	$1.2 \frac{\mu M}{\text{day}}$	k_M	$1.6 \frac{\mu M}{\text{day}}$	k_M	$2.4 \frac{\mu M}{\text{day}}$

Table 3.8: Day 100 tumor volume predicted for the three models treated with Schedule 1. The first two entries are the final tumor volumes obtained from dosing with only the *S*-phase or *M*-phase therapeutic, respectively. The remainder are combination dose schedule regimens with the *S*-phase treatment started on day 42, and the *M*-phase treatment initiated the listed number of days prior (-) or after (+).

Schedule 1	Model 1	Model 2	Model 3
Only <i>S</i> -phase	2168.4 mm ³	488.6 mm ³	524.9 mm ³
Only <i>M</i> -phase	2222.1 mm ³	488.6 mm ³	524.9 mm ³
-6 days	629.7 mm ³	251.5 mm ³	341.4 mm ³
-5 days	199.0 mm ³	185.4 mm ³	289.9 mm ³
-4 days	85.5 mm ³	144.2 mm ³	254.1 mm ³
-3 days	92.0 mm ³	139.4 mm ³	252.5 mm ³
-2 days	344.0 mm ³	174.2 mm ³	290.8 mm ³
-1 days	944.5 mm ³	254.0 mm ³	360.4 mm ³
0 days	1416.7 mm ³	349.8 mm ³	433.2 mm ³
+1 days	1013.2 mm ³	302.3 mm ³	397.8 mm ³
+2 days	428.7 mm ³	208.8 mm ³	322.7 mm ³
+3 days	115.5 mm ³	151.3 mm ³	266.6 mm ³
+4 days	115.5 mm ³	137.8 mm ³	248.7 mm ³
+5 days	140.4 mm ³	161.3 mm ³	269.0 mm ³
+6 days	545.0 mm ³	218.6 mm ³	315.5 mm ³

however, was not expected, with the smallest tumors resulting when the *M*-phase therapeutic was administered three or four days prior to administration of the *S*-phase agent for all three models. An oscillatory trend in final tumor volume was apparent for the dose schedules evaluated, with a period of approximately seven days and slight variation depending on whether the *S*- or *M*-phase agent was administered first (*e.g.*, compare final tumor volumes from -3 days vs. +4 days schedules, -2 days vs. +5 days schedules, etc.). Perhaps most surprising were the results indicating the highest tumor volumes when both drugs were administered on the same day. These results were counter to the traditionally accepted methodology for administering multiple chemotherapeutic agents that advocates the co-delivery of agents to increase both the overall amount of “cellular stress” and the likelihood of apoptosis.

A possible explanation for these dosing results was the manner in which the PD effect was incorporated within the age-structured PBE models. Both of the therapeutics only affected cells in a specific cell-cycle phase, did not affect any phase transition rates, and were not designed to display either increased or decreased effect based on the presence on an additional therapeutic. While there were minimum age requirements before phase transitions could occur, cells would continue to progress through the cell-cycle even in the presence of a phase-specific chemotherapeutic, analogous to the results observed during TM dosing [80]. For the two cell-cycle specific chemotherapeutic problem investigated here, the therapeutic effect of the *M*-phase agent was reduced following co-administration of the *S*-phase agent as cells would undergo apoptosis in *S*-phase, never reaching *M*-phase (Figures 3.14-3.16). With identical PK, the combined PD effects from both agents would be reduced when delivered on the same day when compared to delivery of the drugs three to four days apart. Furthermore, the PD structure ignored the possibility of heterogeneous drug susceptibility within the tumor population, which is a prime clinical motivator for the co-delivery of chemotherapeutics. It remains to be evaluated whether offsetting delivery of a secondary or tertiary therapeutic to increase tumor regression would prove advantageous for situations involving resistant cell populations or is feasible from a monetary perspective.

For Schedule 2, the smallest final tumor volumes were attained when the *M*-phase therapeutic was administered either four to five days prior or two to three days after the

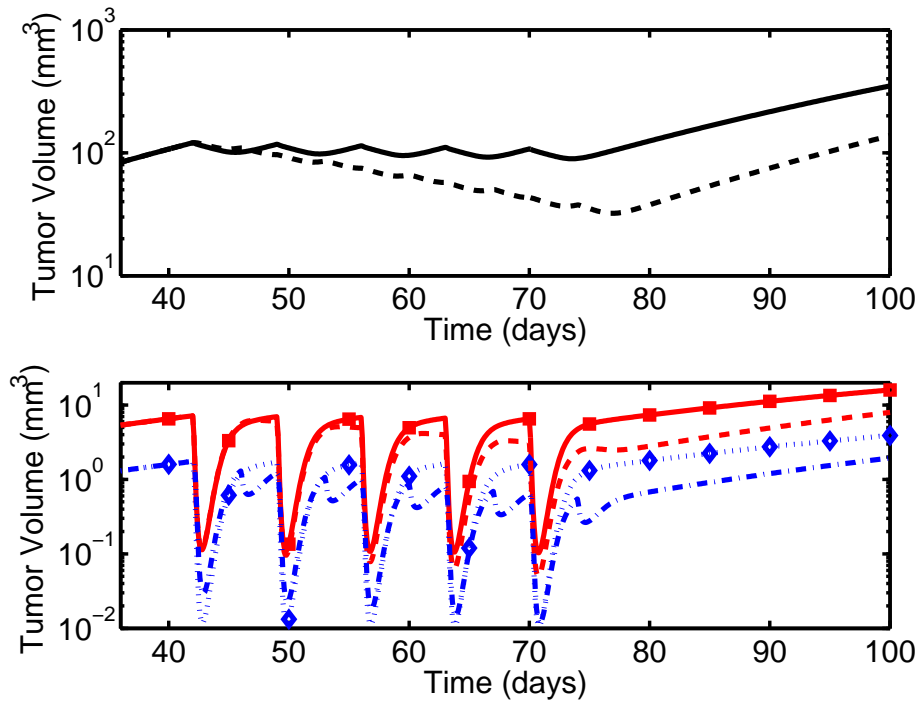


Figure 3.14: Top: Tumor growth profiles predicted for the three-phase saturating age-structured PBE using the regimen from Schedule 1 with a separation of 0 days (solid) and +4 days (dashed) between D_1 and D_2 therapeutic administration. Bottom: S - (0 days, squares; +4 days, dashed) and M -phase (0 days, diamonds; +4 days, dash-dot) cell cycle progression.

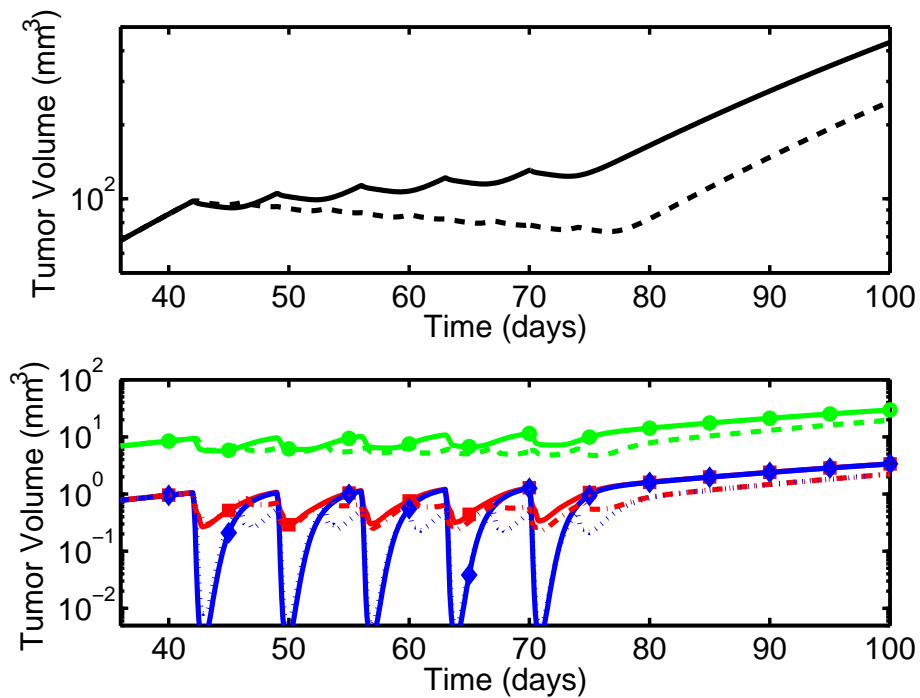


Figure 3.15: Top: Tumor growth profiles predicted for the four-phase saturating age-structured PBE using the regimen from Schedule 1 with a separation of 0 days (solid) and 4 days (dashed) between D_1 and D_2 therapeutic administration. Bottom: G - (0 days, circles; +4 days, dashed), S - (0 days, squares; +4 days, dash-dot), and M -phase (0 days, diamonds; +4 days, dotted) cell cycle progression.

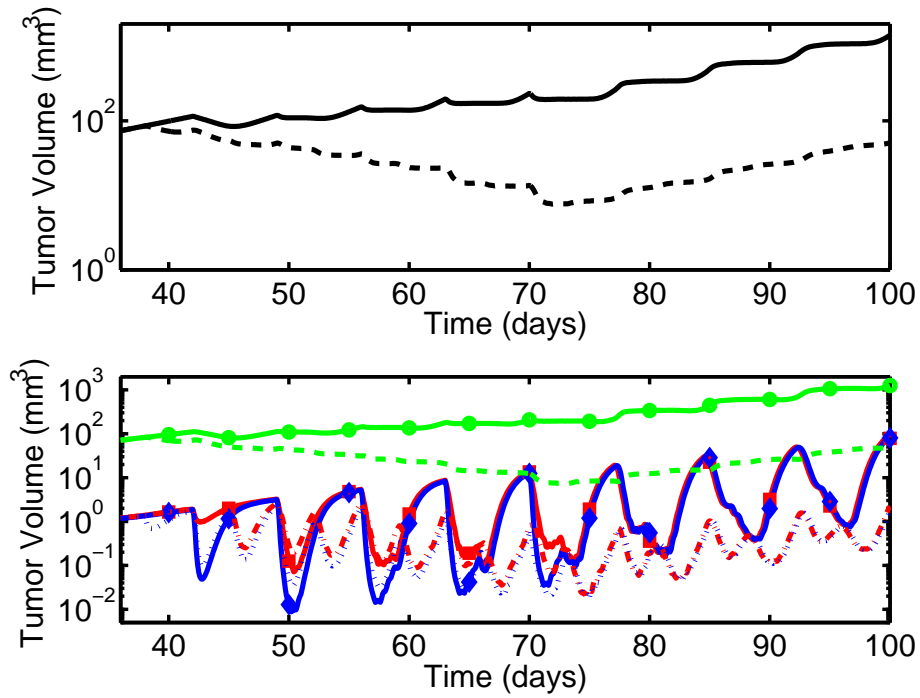


Figure 3.16: Top: Tumor growth profiles predicted for the three-phase non-saturating age-structured PBE using the regimen from Schedule 1 with a separation of 0 days (solid) and 4 days (dashed) between D_1 and D_2 therapeutic administration. Bottom: G - (0 days, circles; +4 days, dashed), S - (0 days, squares; +4 days, dash-dot), and M -phase (0 days, diamonds; +4 days, dotted) cell cycle progression.

Table 3.9: Day 100 tumor volume predicted for the three models treated with Schedule 2. The first two entries are the final tumor volumes obtained from dosing with only the *S*-phase or *M*-phase therapeutic, respectively. The remainder are combination dose schedule regimens with the *S*-phase treatment started on day 42, and the *M*-phase treatment initiated the listed number of days prior (-) or after (+).

Schedule 2	Model 1		Model 2		Model 3	
Only <i>S</i> -phase	5255.8	mm ³	1006.2	mm ³	909.1	mm ³
Only <i>M</i> -phase	2222.1	mm ³	488.6	mm ³	524.9	mm ³
-6 days	717.3	mm ³	332.9	mm ³	408.7	mm ³
-5 days	320.0	mm ³	323.5	mm ³	383.4	mm ³
-4 days	508.1	mm ³	331.5	mm ³	393.9	mm ³
-3 days	1317.7	mm ³	356.0	mm ³	431.1	mm ³
-2 days	2045.9	mm ³	410.9	mm ³	483.9	mm ³
-1 days	2375.8	mm ³	467.8	mm ³	517.9.0	mm ³
0 days	2168.1	mm ³	482.7	mm ³	523.0	mm ³
+1 days	1169.6	mm ³	336.5	mm ³	421.0	mm ³
+2 days	508.6	mm ³	323.6	mm ³	384.1	mm ³
+3 days	311.8	mm ³	330.0	mm ³	387.1	mm ³
+4 days	783.9	mm ³	349.5	mm ³	414.4	mm ³
+5 days	1600.7	mm ³	392.3	mm ³	454.4	mm ³
+6 days	2212.9	mm ³	436.0	mm ³	480.1	mm ³

S-phase therapeutic. While different than the results obtained from Schedule 1, these are conceptually similar, spacing the delivery of the two therapeutics to minimize the duration of overlapping effect. Simulated results displayed oscillations that repeated every 7 days and were not dependent on which agent was delivered initially. Also, the results do not indicate that simply administering the chemotherapeutics at the latest available time would result in the smallest final tumor volume, a result counter to the optimal control solutions obtained from single-agent, lumped, tumor progression models [65, 149].

Recovery of the *S*-phase cells following *S*-phase active agent took one to two days for this schedule, as shown in Figure 3.17. For the three-phase saturating model, the simulation converged to the nominal cell-cycle fraction by 1.5 days following the start of treatment. In contrast, the four-phase saturating model was slower to damp, taking 3 days to return to the pseudo-steady state cell-cycle fraction distribution, and it displayed at least one plateau in the fractional progression (Figure 3.18). For both saturating PBE models, all observed oscillations in cell-cycle fraction were a direct PD effect, calling into question the ability of either model to generate the cell-cycle oscillations ideal for resonance chemotherapy. Only dosing with the three-phase non-saturating age-structured PBE predicted extended cell-cycle fraction oscillations (Figure 3.19) which persisted for the duration of the study due to the phase transition parameters selected for the model.

Finally, the results for Schedule 3 indicated that the smallest final tumor volume was obtained if the *M*-phase agent was delivered either one to two days prior or five to six days after initial administration of the *S*-phase agent (Table 3.10). This corresponds to administering the *M*-phase therapeutic on one of the two days during the week where the *S*-phase therapeutic was not administered. Again, the projected final tumor volumes oscillated over a seven day cycle and did not display consistently lower final tumor volumes for treatments initialized at earlier time points.

Figures 3.20 and 3.21 show the simulation results for the three-phase and four-phase saturating age-structured PBEs, respectively, with the *M*-phase therapeutic dosed on either the initial day the *S*-phase therapeutic was administered (day 0) or on the fifth day the *S*-phase therapeutic was administered (day +4). For the three-phase model there was near total recovery of the *S*-phase population between daily therapeutic administrations with

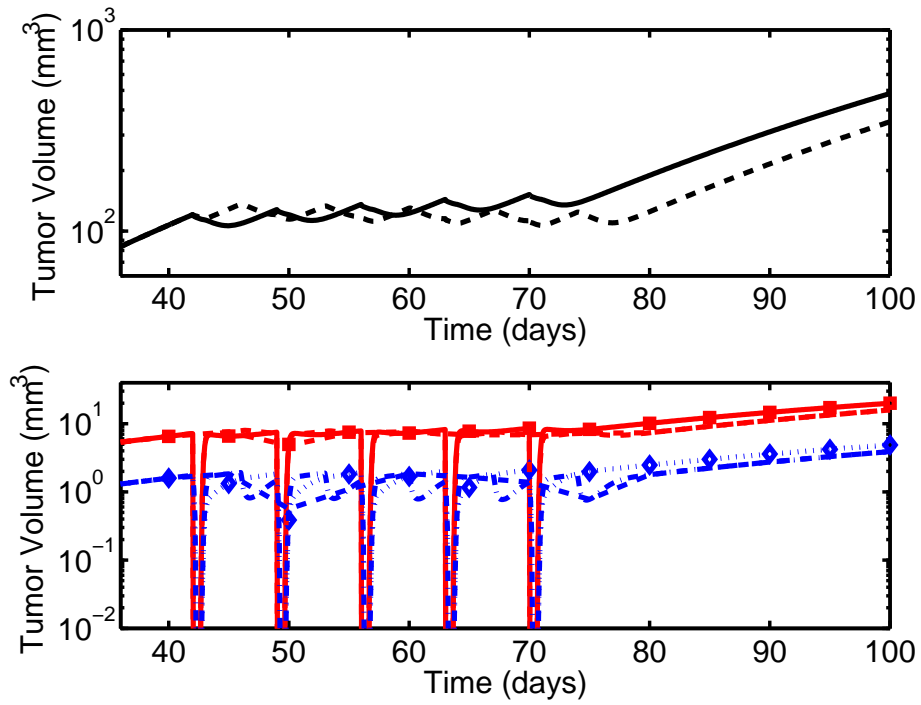


Figure 3.17: Top: Tumor growth profiles predicted for the three-phase saturating age-structured PBE using the regimen from Schedule 2 with a separation of 0 days (solid) and +4 days (dashed) between D_1 and D_2 therapeutic administration. Bottom: S - (0 days, squares; +4 days, dashed) and M -phase (0 days, diamonds; +4 days, dash-dot) cell cycle progression.

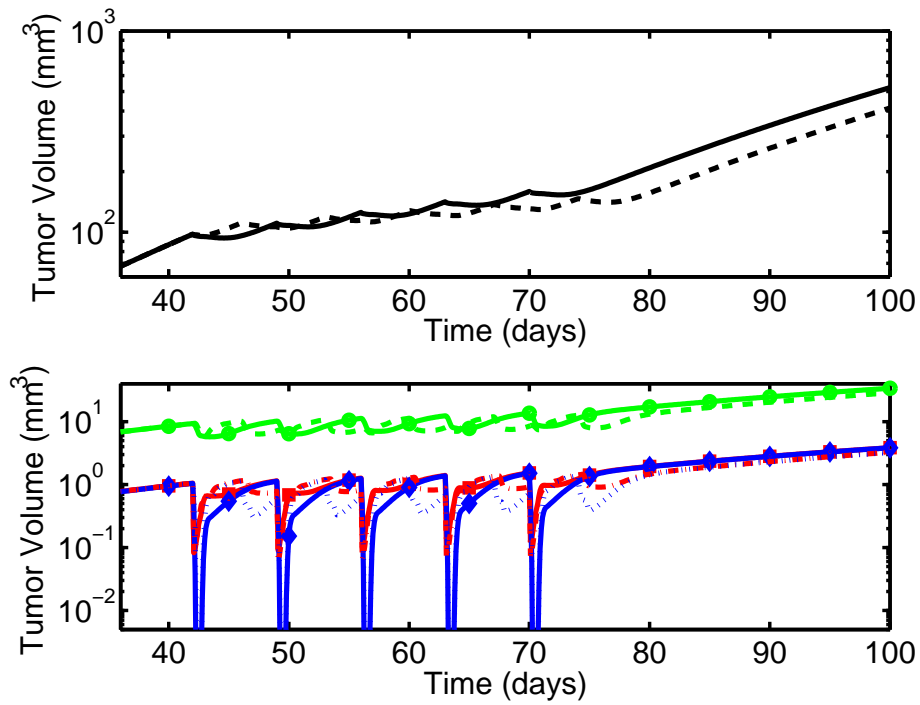


Figure 3.18: Top: Tumor growth profiles predicted for the four-phase saturating age-structured PBE using the regimen from Schedule 2 with a separation of 0 days (solid) and +4 days (dashed) between D_1 and D_2 therapeutic administration. Bottom: G^- (0 days, circles; +4 days, dashed), S^- (0 days, squares; +4 days, dash-dot), and M^- phase (0 days, diamonds; +4 days, dotted) cell cycle progression.

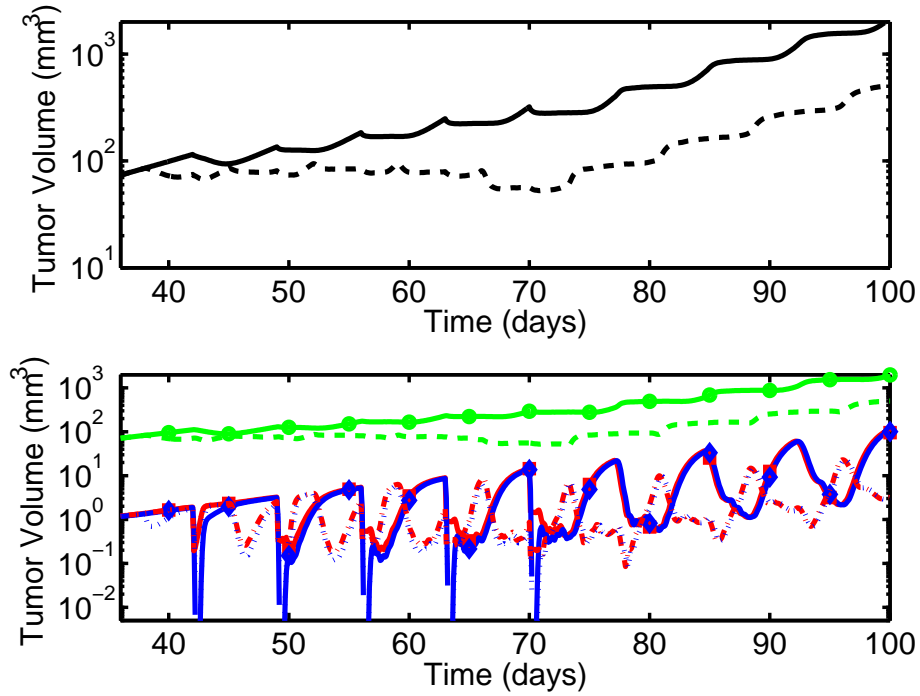


Figure 3.19: Top: Tumor growth profiles predicted for the three-phase non-saturating age-structured PBE using the regimen from Schedule 2 with a separation of 0 days (solid) and +4 days (dashed) between D_1 and D_2 therapeutic administration. Bottom: G_2 - (0 days, circles; +4 days, dashed), S - (0 days, squares; +4 days, dash-dot), and M -phase (0 days, diamonds; +4 days, dotted) cell cycle progression.

Table 3.10: Day 100 tumor volume predicted for the three models treated with Schedule 3. The first two entries are the final tumor volumes obtained from dosing with only the *S*-phase or *M*-phase therapeutic, respectively. The remainder are combination dose schedule regimens with the *S*-phase treatment started on day 42, and the *M*-phase treatment initiated the listed number of days prior (-) or after (+).

Schedule 3	Model 1		Model 2		Model 3	
Only <i>S</i> -phase	1109.4	mm ³	670.0	mm ³	548.4	mm ³
Only <i>M</i> -phase	2222.1	mm ³	488.6	mm ³	524.9	mm ³
-6 days	522.2	mm ³	289.2	mm ³	334.1	mm ³
-5 days	267.3	mm ³	277.8	mm ³	322.0	mm ³
-4 days	101.1	mm ³	254.2	mm ³	300.6	mm ³
-3 days	115.2	mm ³	229.9	mm ³	285.3	mm ³
-2 days	99.2	mm ³	223.1	mm ³	286.3	mm ³
-1 days	201.7	mm ³	271.9	mm ³	327.5	mm ³
0 days	624.6	mm ³	327.1	mm ³	385.2	mm ³
+1 days	646.8	mm ³	324.7	mm ³	383.3	mm ³
+2 days	431.5	mm ³	308.4	mm ³	363.2	mm ³
+3 days	183.2	mm ³	274.4	mm ³	326.4	mm ³
+4 days	115.2	mm ³	236.4	mm ³	292.1	mm ³
+5 days	110.0	mm ³	213.5	mm ³	272.4	mm ³
+6 days	118.4	mm ³	250.1	mm ³	295.7	mm ³

the trough of the M -phase population increasing as the week continues. In contrast, when the dosing was separated by four days, the M -phase population was lowest on the day of drug delivery and does not return to a sufficient volume by the time the S -phase schedule begins again, limiting the PD effect. Similar results were obtained for the four-phase model, though neither the population in S - or M -phase completely recovered week-to-week when the treatments were separated by four days, possibly due to the exchange of cells between the G -phase and Q -phase populations. For the three-phase non-saturating model, the week-to-week trough behavior changed as the cycle repeated, initially displaying its lowest point during days 1-3 of treatment with the S -phase therapeutic, then displaying a downward trough trend during later weeks. As a whole, the non-saturating model also predicted greater disparity between treatment regimens which cannot be described solely by the exponential growth dynamics of the system following treatment. Rather, the rate constants selected (long G -phase residence time) for this simulation ensured a constant, rapid transition of cells from G -phase to the other phases, increasing the total number of cells exposed to the therapeutic.

Schedule 3 was demonstrated that delivery of an S -phase therapeutic (9NC) and an M -phase therapeutic (Doc) yielded final tumor volumes dependent on the delivery schedule of the two therapeutics [150]. The mouse study demonstrated that for mice dosed daily for five days with 9NC followed by two days off, with the schedule repeated for an additional week, tumor volumes at the end of treatment were significantly smaller if Doc was administered on the fifth day of 9NC treatment ($103.7 \pm 73.9 \text{ mm}^3$) versus the initial day ($229.4 \pm 160.9 \text{ mm}^3$). While the ratio of final tumor volumes achieved during the simulation study was not as large as that obtained from the PK/PD study (1.4:1 for the three-phase saturating model and 1.3:1 for the four-phase saturating model versus 2.2:1 experimentally), the results did demonstrate schedule dependent final tumor volumes. From here, the parameters for untreated and treated tumor progression could be evaluated for the specific PBE models, and the actual tumor drug PK could be included for predicting PD effect. Furthermore, by shortening the window of effect for the M -phase therapeutic (*e.g.*, defining the M -phase PD parameter as zero if the age within M -phase was less than 5.5 hours), consistent with the 30-60 minutes duration of cell mitosis, final tumor volume ratios of 1.8:1 and 1.7:1 were obtained with the three-phase and four-phase saturating age-structured PBEs, respectively.

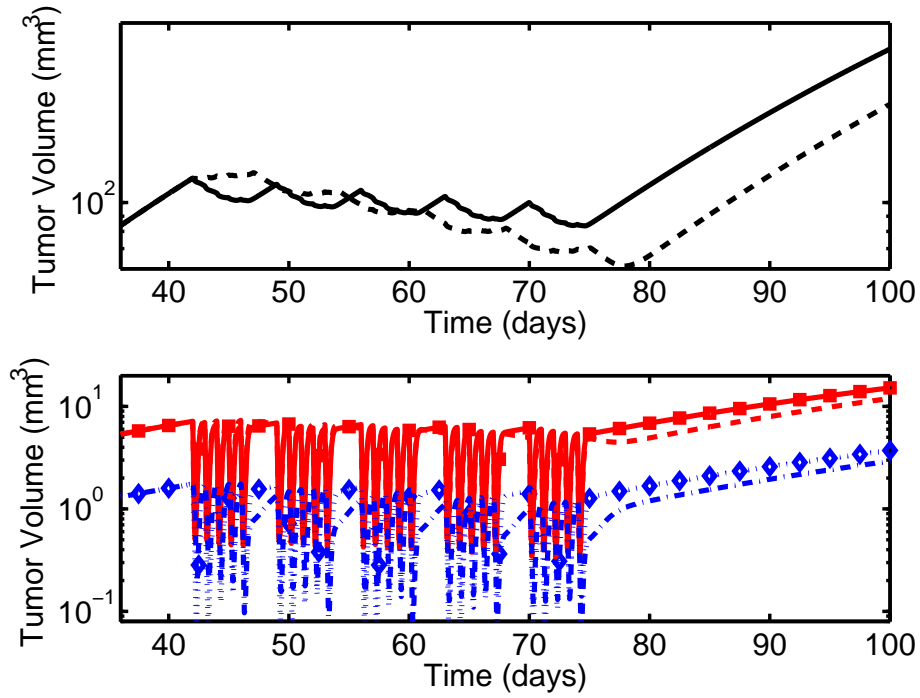


Figure 3.20: Top: Tumor growth profiles predicted for the three-phase saturating age-structured PBE using the regimen from Schedule 3 with a separation of 0 days (solid) and +4 days (dashed) between D_1 and D_2 therapeutic administration. Bottom: S - (0 days, squares; +4 days, dashed) and M -phase (0 days, diamonds; +4 days, dash-dot) cell cycle progression.

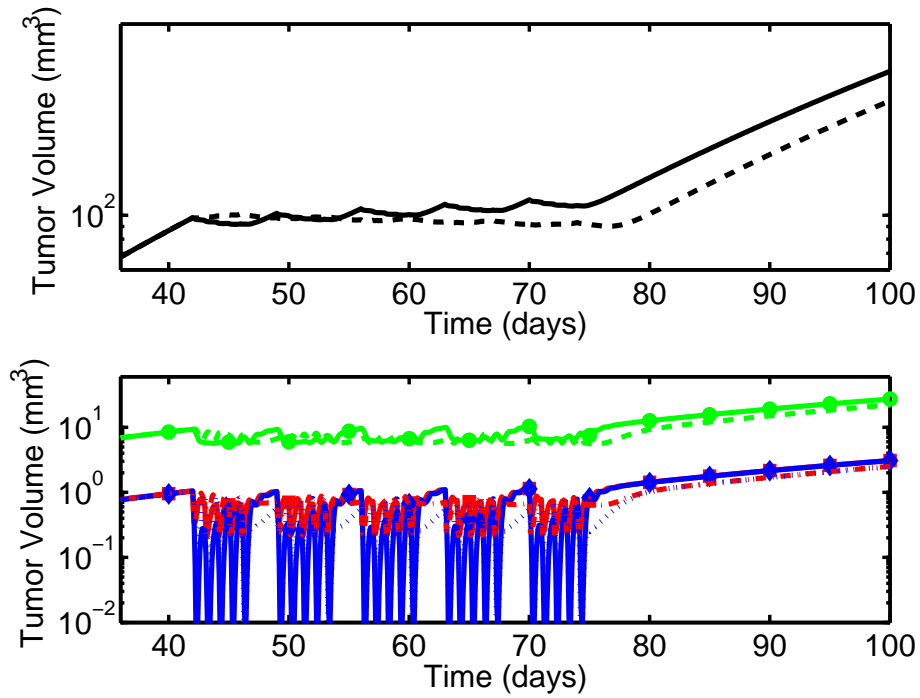


Figure 3.21: Top: Tumor growth profiles predicted for the four-phase saturating age-structured PBE using the regimen from Schedule 3 with a separation of 0 days (solid) and +4 days (dashed) between D_1 and D_2 therapeutic administration. Bottom: G^- (0 days, circles; +4 days, dashed), S^- (0 days, squares; +4 days, dash-dot), and M^- phase (0 days, diamonds; +4 days, dotted) cell cycle progression.

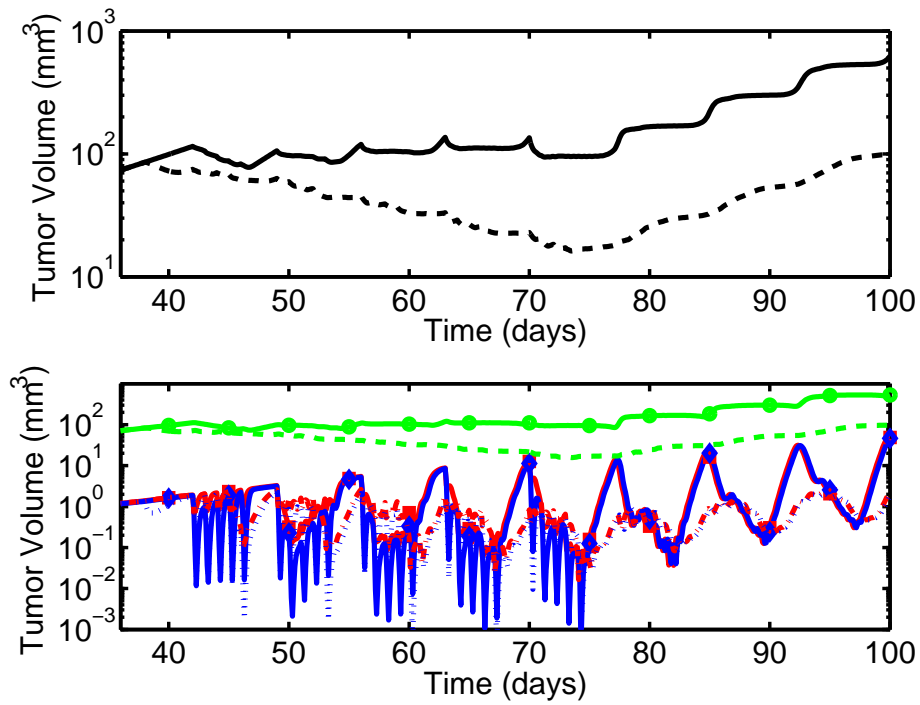


Figure 3.22: Top: Tumor growth profiles predicted for the three-phase non-saturating age-structured PBE using the regimen from Schedule 3 with a separation of 0 days (solid) and +4 days (dashed) between D_1 and D_2 therapeutic administration. Bottom: G - (0 days, circles; +4 days, dashed), S - (0 days, squares; +4 days, dash-dot), and M -phase (0 days, diamonds; +4 days, dotted) cell cycle progression.

3.8 DISCUSSION AND SUMMARY

This chapter investigated the model development of both non-saturating and saturating PBE cell-cycle tumor growth models, incorporating either the cell mass or age as intrinsic system variables. Non-saturating models based on both age and mass were constructed and displayed exponential bulk tumor progression, which is descriptive of hematological cancers and solid tumor growth over short periods of time, but is insufficient for describing solid tumor growth over an extended period of time. To address this shortcoming, two mass-structured PBEs with either saturating G -phase transition rate or G -phase mass accumulation rate were investigated. The former model displayed undesirable growth properties, namely exponential growth up to the saturating population followed by a rapid plateauing effect and subsequent numeric instability as the number density mass for G -phase cells converged to the upper bound on the system mass. The latter model, while displaying the desired saturating tumor growth characteristics, was ultimately set aside due to an inability to relate downstream PD effects to cell mass. Two saturating age-structured PBEs were then investigated, one containing a lumped G -phase and age-distributed S - and M -phases for a total of three phases; the other included a lumped Q -phase and age-distributed G -, S - and M -phases for a total of four phases. Both models accurately described bulk tumor progression, and could be updated with parameters for individual tumor lines.

To evaluate whether the increased complexity of these models was capable of describing multiple chemotherapeutic schedule dependent outcomes, a series of dosing schedules were simulated. Three dosing schedules involving two cycle-specific therapeutic drugs, PK dynamics, and PD effects were evaluated against the three age-structured PBE models developed within this chapter. While the S -phase treatment always started on day 42 of the simulation, treatment with the M -phase agent began up to 6 days prior or after the S -phase treatment. Results indicated that age-structured PBEs are capable of generating schedule dependent differences in final tumor volumes that are not achievable using traditional lumped models. Furthermore, the simulations indicated that for multi-agent chemotherapies, greater final tumor volumes resulted when the drugs were administered concurrently and that separating drug delivery to reduce the extent of PK overlap resulted in the the smallest final

tumor volumes. These results run counter with how typical chemotherapeutics are currently delivered in clinical practice and may have resulted from the PD relationship incorporated for these simulations and failure to include distributed drug sensitivities amongst the tumor population. The employed model structure was also not capable of achieving the degree of oscillations necessary for resonance chemotherapy treatment, only manifesting cell-cycle phase alterations immediately following drug delivery. The four-phase saturating age-structured model displayed perturbations to the cell-cycle distribution following treatment, though these perturbations did not result in oscillations of the cell-cycle fractions. These results were expected as previous papers exploring resonance therapy demonstrated that the inclusion of a quiescent cell population, gradually declining PD effects, PK transport dynamics, or any comparable filtering dynamic damped the discrete transitions necessary for manifesting the cell-cycle fraction oscillations seen during resonance chemotherapy simulations.

Increased tumor regression over the results obtained during this simulation study could likely be attained by altering the frequency of drug administration (*i.e.*, resonance therapy) and the dosing level. However, not only would these schedules with more frequent administration have results mediated by the quiescent cell population, but uncertainty and variability regarding phase transition rates could lead to over an prediction of tumor effect. For dose schedules specifically timed according to the overall cell-cycle transition rate, slight parameter errors may even result in worse treatments. Further, due to the duration and gradual elimination of drug effect (as opposed to a sharp transition of drug removal) compared to the phase transition times incorporated within the models, there were not sufficient phase oscillations for supporting resonance therapy.

Final tumor volumes obtained following treatment were also independent of when the schedule was initialized, though, final volume was schedule dependent; similar results are obtained using lumped models for tumor progression. These results support the administration of chemotherapeutic on an established schedule regardless of the size of the tumor when treatment is initiated, a practice that is currently used clinically. However, this result disagrees with preclinical observations where smaller tumors exhibit larger regression and likelihood of total elimination. Further, clinical success is correlated with the initial size

of the tumor, though these clinical results may not coincide with greater tumor regression. It is clinically recognized that blood flow rate, and hence, drug deposition, is non-uniform in solid tumors, increasing in heterogeneity as the volume of the tumor increases. To address this, it is necessary to establish a relationship between plasma PK and the observed tumor volume for predicting how local drug exposure may change during treatment.

Of concern are the diminished returns in developing more involved tumor models when the PD effect does not incorporate the additional cell state variables introduced into the model for describing cell cycle dynamics. Unperturbed bulk tumor progression is already readily described using any number of deterministic or stochastic tumor growth models found in the literature [68, 69, 74, 75, 76, 77]. The ability to describe tumor regression following treatment, however, especially with multiple agents over a set administration schedule, often leads to inaccurate PD model predictions. The likely cause of these inaccuracies is the PD effect structure, not only for multi-agent therapies, but also for single agent treatments. Common practice in tumor modeling, even employed within this dissertation, is the inclusion of PD effect as a bilinear term, the product of the susceptible population and drug concentration premultiplied by a constant. This formulation of a kill term, while applicable to steady state drug exposure experiments conducted *in vitro*, may introduce error when extrapolated to an *in vivo* setting where drug concentrations may vary over orders of magnitude due to administration methods (*i.e.*, bolus injection versus infusion).

Furthermore, the PD models only assumed elimination of cells based on the susceptible population and plasma PK, neglecting growth inhibition due to the chemotherapeutic. Drug effect is a combination of both growth hindrance and apoptosis; however, the exact contribution of each is neither thoroughly investigated, nor can it be estimated through macroscopic measures obtained from preclinical (or clinical) trials. The necessary information could be obtained through *in vitro* cell cycle transition and tumor cell progression studies under control and treated conditions obtained at multiple time points. Titrated conditions mimicking an *in vivo* PK profile can also be evaluated to assess cell-cycle progression under concentration conditions similar to those encountered following *in vivo* dosing.

Overall both saturating and non-saturating PBEs offer a unique structure for the evaluation of single- or multiple-agent chemotherapies. These models, however, are not suitable for closed-loop controller evaluation of cancer treatment at present due to: (i) continued reliance on a feedback tumor volume metric; and (ii) the computation time of the model. In contrast, open-loop schedule evaluation is an ideal application of these models, allowing for the off-line simulation and evaluation of multiple drug combinations, dosing schedules, and dosing levels, areas that cannot be explored clinically or even preclinically due to constraints on financial costs, ethics, and time. The tumor growth progression portion of these models would need to be updated for individual tumor lines; however, the variability that exists in bulk tumor growth dynamics can be obtained from concurrent control experiments, leaving *S*- and *M*-phase progression rates largely unaltered while updating dynamics involving *G*-phase transitions. Likewise, while individual PK profiles are drug dependent, this information is typically obtained throughout the course of preclinical investigations. Finally, the tumor progression model could be appended with a reliable toxicity assessment model to simultaneously evaluate whether the evaluated dose schedule has increased or decreased toxicity relative to other schedules and/or changes in predicted tumor efficacy.

4.0 MOUSE PBPK MODEL FOR DOC

Docetaxel (Doc) is a semi-synthetic taxane that displays activity against a wide range of solid tumors and is approved for use in treating metastatic breast, non-small cell lung, and androgen-independent prostate cancers [151]. It is a cell-cycle-specific chemotherapeutic agent that promotes tubulin assembly and inhibits depolymerization of assembled tubulin, which results in blockage of cell-cycle progression during *M*-phase and leads to apoptosis [151]. The primary Doc elimination route (>80%) involves metabolism in the liver by the CYP3A enzyme family, yielding inactive metabolites [152]. The remainder of the parent compound is eliminated either through fecal (<10%) or renal (<10%) excretion [153, 154].

Typically, Doc is administered as a 1-hour IV infusion every three weeks (q3w regimen) at 60-100 $\frac{\text{mg}}{\text{m}^2}$ with neutropenia as the primary dose-limiting toxicity [155, 156, 157]. Alternative schedules, such as administration of Doc once a week for three weeks followed by a week off (35-40 $\frac{\text{mg}}{\text{m}^2}$ “weekly” schedule) or every other week are also actively being used or investigated [7, 8, 157, 158]. These alternative schedules display equivalent efficacy to the q3w schedules and produce significantly less neutropenia than the q3w schedule. However, these alternative schedules display cumulative increases in other toxicities such as fatigue, hyperlacrimation, and nail-toxicity [159]. At present, there is no clear consensus on which schedule is ideal for treatment; however, the clinical acceptability of weekly schedules offers the possibility of individualized treatment for those patients who might experience adverse hematological effects during typical Doc treatment regimens that use the q3w dosing schedule. Further complicating Doc treatment is the highly variable inter-patient pharmacokinetics (PK) observed, which are due to a number of patient-specific factors including plasma α_1 -acid glycoprotein (AAG) concentrations, serum albumin concentrations, hepatic function, and body surface area [2, 97].

The plasma PK of Doc, which have been studied previously in a number of animal species and humans, display tri-phasic elimination from the plasma following i.v. administration, appreciable tissue uptake from the plasma, and linear kinetics over various infusion durations and dosing levels [5, 150, 160, 161, 162]. Distribution studies of radiolabeled Doc in mice have shown rapid tissue uptake, primarily in the liver, intestine, spleen, and bone marrow, though radioactivity was detectable in virtually all evaluated tissues [160]. Doc PK in tissues displayed biphasic elimination with a terminal half-life of 2-4.5 hours compared to a terminal half-life of 1.2 hours in plasma. Even slower elimination was observed in mice implanted with adenocarcinoma xenografts, where tumor tissue displayed selective Doc drug retention relative to normal tissue and a terminal half-life of approximately 22 hours [160]. Other mouse studies have obtained terminal plasma and tissue half-lives significantly longer than those reported in previous studies, with plasma half-lives ranging from 4.5-8.6 hours over a Doc dosing range of 5-20 $\frac{\text{mg}}{\text{m}^2}$ [5, 150]. Tissue half-lives also increased, ranging from 3.2-6.1 hours [5]. This latter study also noted an increase in both plasma and tissue half-lives with increasing Doc dosing level [5].

More complex models, such as physiologically-based pharmacokinetic (PBPK) models, utilize knowledge of the anatomy and physiology of the studied species to develop a PK model that accurately describes plasma, tissue, and, in some cases, tumor concentrations following drug delivery. A representative illustration of this model structure is shown in Figure 4.1. These models have found extensive use in toxicity studies [34, 35], anesthetic therapy [37], treating diabetes [39, 163], and describing chemotherapeutic distribution to sites of action and regions of susceptible toxicity [5, 41, 42]. Individual tissue compartments are represented by ordinary differential equations; tissues are included based on PK interest and available data, while the remaining tissues are combined together into “rapidly” and “slowly” perfused tissue compartments or as a composite “peripheral” compartment. These types of models can be applied to drugs that are administered via i.v. injection (into the venous compartment), orally (into the gastrointestinal tract), via inhalation (necessitating a pulmonary compartment in addition to the lungs), or via subcutaneous injection (under the skin).

System-wide distribution of Doc and construction of an accompanying mouse PBPK model was previously investigated at dosing levels of 5 and 20 $\frac{\text{mg}}{\text{kg}}$ in a study by Bradshaw-Pierce *et al.* [5]. Tissue samples for both studies were obtained over 24 hrs, and model compartments included plasma, liver, kidney, intestine, and total fecal elimination over the course of the study. The model included nonlinear relationships for the metabolism of parent compound in the liver, elimination by fecal or urinary excretion, and extended tissue retention based on tissue specific tubulin content and binding affinity. The goal of the present study was to use data from Doc distribution following i.v. administration to severe combined immunodeficient (SCID) mice bearing human SKOV-3 ovarian cancer xenografts to develop a more extensive mouse PBPK model that included additional normal tissue and tumor compartments. Furthermore, the model was structured utilizing solely linear dynamics, as Doc plasma PK in mice has been observed to be linear at the investigated dosing levels.

4.1 MATERIALS AND METHODS

4.1.1 Mouse Doc PK Study

Data for PBPK modeling was obtained from a PK study performed on female C.B.-17 SCID mice bearing SKOV-3 human ovarian cancer xenografts [150, 164]. At 21 days after xenograft implantation, tumor-bearing mice were stratified into three groups such that group body weights and tumor volumes were not statistically different. Doc was administered intravenously to mice at 10 $\frac{\text{mg}}{\text{kg}}$ over the course of 10-15 seconds. Mice ($n = 3$ per time point) were euthanized by CO₂ asphyxiation at 0.083, 0.25, 0.5, 1, 2, 4, 6, 7, 18, and 24 hours after Doc administration. Venous blood was collected from the right ventricle via cardiac puncture into heparinized syringes and placed on ice until centrifuged at $12,000 \times g$ for 4 min. After centrifugation, plasma was collected, snap frozen in liquid N₂, and stored at -80 °C until analysis by LC-MS [165]. Similarly, collected tissues (lung, liver, brain, tumor, spleen, heart, kidney, muscle, and fat) and tumor were removed, weighed, frozen in liquid nitrogen, and stored at -80 °C until analysis by LC-MS [165].

4.1.2 Sample Processing and LC-MS Analysis

Plasma samples (100 μL) were mixed with 400 μL of control plasma and 10 μL of 1 μM paclitaxel internal standard (I.S.). Samples were vortexed and then centrifuged at $21,000 \times g$ for 6 min at 4 $^{\circ}\text{C}$ followed by solid phase extraction (SPE) as described previously [165]. Ten μL of the sample were then injected into the LC-MS [165].

Tumor and normal tissue samples were homogenized in phosphate-buffered saline at pH 7.4 (1:3, w/v) and subjected to acetonitrile protein precipitation using a 200 μL tissue homogenate aliquot, 10 μL I.S., and 1 mL acetonitrile. Samples were vortexed and then centrifuged at $21,000 \times g$ for 6 min @ 4 $^{\circ}\text{C}$. The supernatant was decanted and evaporated to dryness under nitrogen at 37 $^{\circ}\text{C}$. The dried residues were re-suspended in 1 mL of 0.01 M ammonium acetate buffer, each at pH 5.0:methanol, (80:20, v/v), which was then processed by SPE as described previously [165]. Ten μL of the processed tissue sample were then injected into the LC-MS [165].

4.1.3 Mouse PBPK Model Formulation

The system-wide distribution of Doc was described using a PBPK model, as shown in Figure 4.1. IV administration is included in the model as an infusion into the venous compartment, which subsequently distributes throughout the rest of the body. In PBPK models, tissue compartments are typically treated as either perfusion-limited (one compartment), as in Equation (4.1),

$$\frac{dC_i}{dt} = \frac{F_i}{V_i} \left(C_{in} - \frac{C_i}{P_i} \right) \quad (4.1)$$

or diffusion-limited (two compartments), as in Equations (4.2)-(4.3):

$$\frac{dC_{i_v}}{dt} = \frac{F_i}{V_{i_v}} (C_{in} - C_{i_v}) - k_{i_{ve}} f_{unb} C_{i_v} + \frac{V_{i_e}}{V_{i_v}} k_{i_{ev}} C_{i_e} \quad (4.2)$$

$$\frac{dC_{i_e}}{dt} = \frac{V_{i_v}}{V_{i_e}} k_{i_{ve}} f_{unb} C_{i_v} - k_{i_{ev}} C_{i_e} \quad (4.3)$$

For the perfusion-limited system (Equation (4.1)), C_i is the drug concentration in tissue i , F_i is the blood flow rate into tissue i , V_i is the volume of tissue i , and C_{in} is the inlet drug

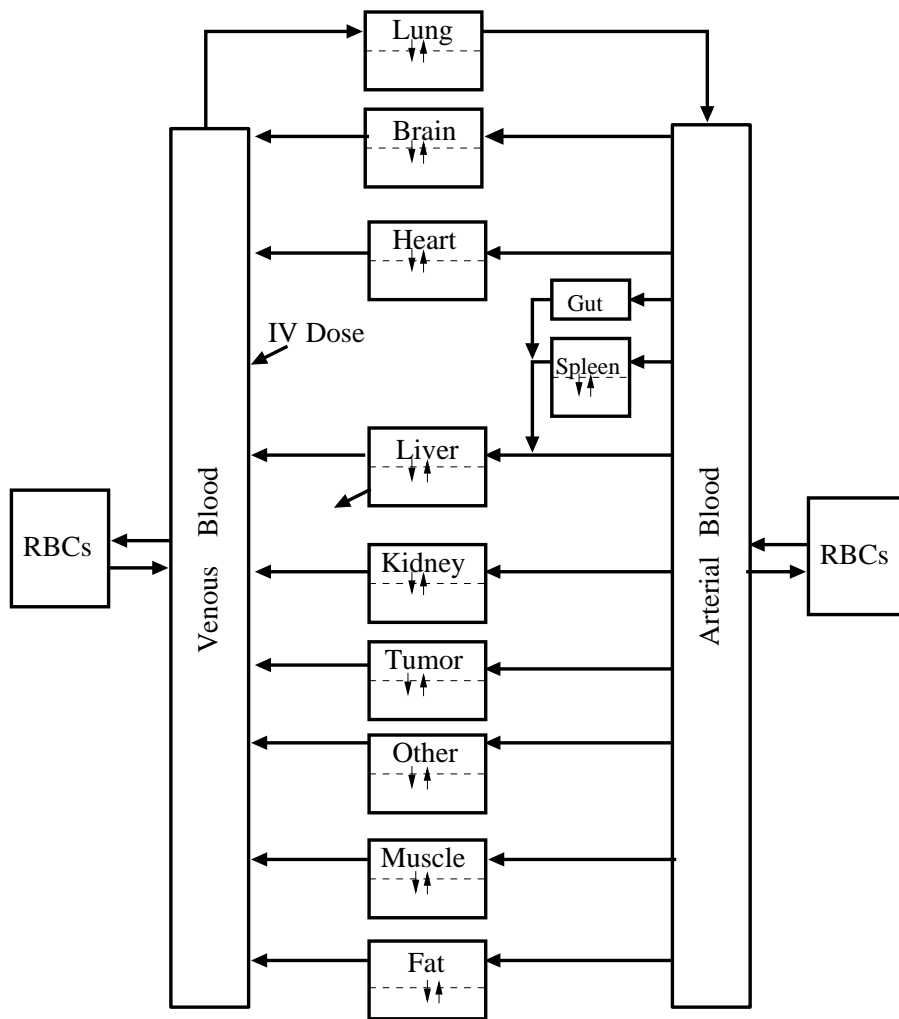


Figure 4.1: PBPK model for the distribution of Doc in plasma, various mouse tissues, and subcutaneously implanted tumor xenografts.

concentration for tissue i , which comes from: (i) the venous blood supply in the case of the lungs; (ii) from the spleen, gut, and arterial compartment for the liver; or (iii) from the arterial compartment for all other body tissues. Diffusion-limited tissues (Equations (4.2)-(4.3)) have both a vascular (v) and extra-vascular tissue (e) space (volumes V_{iv} , and V_{ie} , respectively), with separate concentrations, C_{iv} and C_{ie} , intratissue transfer rates, k_{ive} and k_{iev} , and an unbound drug fraction (f_{unb}) approximated as 15% for mice. Due to the long Doc retention times observed in tissues, an effect of intracellular Doc binding and transport, all modeled tissues had improved fits using diffusion-limited compartments. However, a number of these tissue models were still incapable of simultaneously fitting rapid post-dose dynamics and Doc retention. To improve model fits, an additional subcompartment was added to each tissue. The resulting model for tissues that do not eliminate drug is as follows:

$$\frac{dC_{iv}}{dt} = \frac{F_i}{V_{iv}} (C_{in} - C_{iv}) - k_{ive} f_{unb} C_{iv} + \frac{V_{ie}}{V_{iv}} k_{iev} C_{ie} \quad (4.4)$$

$$\frac{dC_{ie}}{dt} = \frac{V_{iv}}{V_{ie}} k_{ive} f_{unb} C_{iv} - k_{iev} C_{ie} + k_{bindout} C_{ib} - k_{bindin} C_{ie} \quad (4.5)$$

$$\frac{dC_{ib}}{dt} = -k_{bindout} C_{ib} + k_{bindin} C_{ie} \quad (4.6)$$

Here, C_{ib} is the drug concentration in the additional “bound” subcompartment, and $k_{bindout}$ and k_{bindin} are retention rates within the tissue. The binding rate parameters were kept the same for all investigated tissues to limit the overall number of model parameters. For drug eliminating tissues, primarily the liver in the case of Doc, Equations (4.5)-(4.6) add a clearance term, as follows:

$$\frac{dC_{ie}}{dt} = \frac{V_{iv}}{V_{ie}} k_{ive} f_{unb} C_{iv} - k_{iev} C_{ie} + k_{bindout} C_{ib} - k_{bindin} C_{ie} - k_{cli} C_{ie} \quad (4.7)$$

$$\frac{dC_{ib}}{dt} = -k_{bindout} C_{ib} + k_{bindin} C_{ie} - k_{cli} C_{ib} \quad (4.8)$$

Here, k_{cli} is the rate of drug clearance from the liver. Note, that clearance was allowed to occur in both the extravascular space in addition to the bound subcompartment, and the same parameter was utilized in both tissue spaces due to data limitations regarding

liver metabolism. Finally, venous plasma and red blood cell (RBC) concentrations were represented by the following equations:

$$\frac{dC_{ven}}{dt} = \frac{\sum_j F_j C_{j_e} - F_{tot} C_{ven}}{V_{ven}(1 - f_{hem})} + \frac{u}{V_{ven}(1 - f_{hem})} + \frac{f_{hem}}{(1 - f_{hem})} k_{rbcplasma} C_{rbcv} - k_{plasma} f_{unb} C_{ven} \quad (4.9)$$

$$\frac{dC_{rbc}}{dt} = -k_{rbcplasma} C_{rbc} + \frac{(1 - f_{hem})}{f_{hem}} k_{plasma} f_{unb} C_{ven} \quad (4.10)$$

Here, C_{ven} and C_{rbc} are the concentrations in venous plasma and circulating red blood cells, respectively, f_{hem} is the hematocrit fraction in mice ($f_{hem} = 0.45$, [1]), F_j and C_j are the flow rates and extravascular concentrations, respectively, from tissue j , and u represents IV administration of Doc. Transition rates between plasma and RBCs are given by k_{plasma} and $k_{rbcplasma}$, respectively. RBCs were represented as a side compartment to the venous plasma concentration as shown in Figure 4.1. For the arterial concentration, Equations (4.9)-(4.10) are left unchanged except for the removal of the drug input term, u , and the use of “art” in place of “ven”. The overall set of ordinary differential equations governing the PBPK model can be found in Appendix B.

To reduce the number of parameters requiring estimation, tissue and tumor masses from the mouse PK study were adjusted based on tissue densities obtained from the literature [1] and incorporated as the appropriate tissue volumes. Blood flow rates, vascular tissue fractions f_i , and masses for tissues not entirely extracted (fat and muscle) were also obtained from the literature [1]. These parameters are summarized in Table 4.1. Tumor blood flow rate was calculated based on the following equation for ovarian xenografts taken from the literature [166]:

$$\log(\text{tumor blood flow}) = -0.808 \log(\text{tumor wet weight}) - 0.436 \quad (4.11)$$

Here, the tumor wet weight and tumor blood flow are in units of g and $\frac{\text{mL}}{\text{g min}}$, respectively. Vascular and extra-vascular tissue volumes were calculated as $V_{iv} = V_i f_i$ and $V_{ie} = V_i - V_{iv}$. Similarly, the tissue volume and blood flow rate for the other compartment was calculated as $V_o = V_{tot} - \sum_{i \neq o} V_i$ and $F_o = F_{tot} - \sum_{i \neq o, l} F_i$. The remaining parameters (tissue-specific exchange rates, plasma-RBC exchange rates, tissue binding rates, and liver clearance rate)

were estimated by minimizing the weighted sum squared error between model predictions and mouse PK data, as follows:

$$\min_{\rho} (Y_{act} - Y_{pred}(\rho))^T W_1^T W_1 (Y_{act} - Y_{pred}(\rho)) \quad (4.12)$$

Here, Y_{act} and Y_{pred} are vectors of the actual PK study data and model predictions, respectively, W_1 is a diagonal matrix of the inverse standard deviations from the PK study, and ρ are the system parameters. The estimated parameters are summarized in Table 4.1.

Parameter estimation and structure selection was accomplished by sequentially adding tissues while minimizing the weighted sum of squares between the model predictions and collected experimental data. The inverse square of the variance at individual points was used as the weights ($W_1^T W_1$), and simulations were performed in MATLAB (©2007, The MathWorks, Natick, MA) using the *fmincon* function. The steps are summarized below:

1. A compartmental model was fit to the Doc plasma data.
2. Parameters for the lung compartment, assuming a perfusion-limited structure, were estimated, and then the structure was reevaluated as diffusion-limited and as diffusion-limited with internal binding to assess which structure provided the most accurate representation of lung Doc PK.
3. RBC binding rates were estimated using the estimated plasma Doc profile as the input.
4. A PBPK model with those compartments deemed essential (RBC, lung, liver, gut, spleen, tumor, and “other”) was constructed, with each tissue evaluated first as perfusion-limited. Tissues were then evaluated individually as diffusion-limited then diffusion-limited with internal binding.
5. Additional tissues were added and evaluated sequentially, in the following order: brain, kidney, heart, muscle, and fat.

4.1.4 Model Quality Assessment

The quality of the model was determined by calculating the performance error (PE) at individual data points, the mean performance error (MPE), the mean absolute performance

Table 4.1: Parameter values for the mouse PBPK model. Tissue values in bold depict the mean ($\pm\sigma$) tissue volumes from the entire set of mice in the PK study. Total blood flow rate, individual tissue blood flow rates, and vascular fraction were fixed based on literature values [1] while blood volume and tissue volumes for the gut, muscle, and adipose tissue were calculated based on percent of body weight values found in the literature [1]. Finally, the volume of the “other” compartment was calculated using the average weight of mice in the study (22.89 grams) minus the sum of all other tissues.

Units	Fixed Parameters			Estimated Parameters		
	$\frac{\text{mL}}{\text{min}}$	mL	—	$\frac{1}{\text{min}}$	—	$\frac{1}{\text{min}}$
Liver	F_{li} 0.23	V_{li} 1.08±0.14	f_{li} 0.31	$k_{li_{ve}}$ 10.253±0.271	$k_{li_{ev}}$ 0.0965±0.0050	
Liver	—	—	—	k_{cli} 0.1023±0.0002	—	—
Lung	F_l 9.20	V_l 0.17±0.02	f_l 0.50	$k_{l_{ve}}$ 0.2662±0.0107	$k_{l_{ev}}$ 0.0365±0.0013	
Tumor	F_t 0.50	V_t 1.22±0.65	f_t 0.10	$k_{t_{ve}}$ 0.110 ± 0.001	$k_{t_{ev}}$ 0.0006±0.0005	
Gut	F_g 1.72	V_g 1.21	f_g —	—	—	—
Muscle	F_m 1.05	V_m 11.3	f_m 0.04	$k_{m_{ve}}$ 0.5952±0.0089	$k_{m_{ev}}$ 0.0158±0.0020	
Spleen	F_s 0.10	V_s 0.08±0.03	f_s 0.17	$k_{s_{ve}}$ 1.8667±0.1054	$k_{s_{ev}}$ 0.0445±0.0023	
Heart	F_h 0.32	V_h 0.11±0.01	f_h 0.04	$k_{h_{ve}}$ 2.246±0.0289	$k_{h_{ev}}$ 0.0495±0.0008	
Fat	F_f 0.27	V_f 1.52	f_f 0.02	$k_{f_{ve}}$ 0.2161±0.0026	$k_{f_{ev}}$ 0.0079±0.0002	
Kidney	F_k 1.50	V_k 0.29±0.03	f_k 0.24	$k_{k_{ve}}$ 2.924±0.124	$k_{k_{ev}}$ 0.1859±0.0072	
Brain	F_b 0.46	V_b 0.40±0.02	f_b 0.03	$k_{b_{ve}}$ 0.0547±0.0140	$k_{b_{ev}}$ 0.0573±0.0134	
Other	F_o 3.05	V_o 4.39	f_o 0.04	$k_{o_{ve}}$ 0.7451±0.0141	$k_{o_{ev}}$ 0.0099±0.0002	
Blood	F_{tot} 9.20	$V_{ven} + V_{art}$ 1.12	—	$k_{rbcplac}$ 0.05107±0.0023	$k_{placrbc}$ 0.0139±0.0018	
Bind	—	—	—	$k_{bind-in}$ 0.00203±0.00020	$k_{bind-out}$ 0.00179±0.00008	

error (MAPE), the weighted sum squared error (WSSE), and root mean squared performance error (RMSPE) for each tissue. The performance error was defined as:

$$PE = \frac{Y_{act} - Y_{pred}(\rho)}{Y_{act}} \times 100\% \quad (4.13)$$

Similarly, MPE and MAPE, which represent the bias and accuracy of the predictions, respectively, are defined as the mean and absolute mean of PE values for a given tissue. The weighted sum squared error, a measure of the accuracy of tissue predictions with respect to measurement error is given by Equation (4.12). Finally, RMSPE is defined as,

$$RMSPE = \frac{1}{n} \sqrt{\sum_{i=1}^n PE_i^2} \quad (4.14)$$

where n is the number of data points per tissue.

4.1.5 Parameter Sensitivity Analysis

Sensitivity analysis was performed to identify which of the estimated model parameters and literature values had the most influence on tissue, plasma, and tumor Doc concentration estimate on predictions. Each estimated or literature parameter was increased by 0.1% and the normalized sensitivity (NS) for that parameter with respect to the resulting model output at each time point was calculated as follows:

$$NS_{i,j,k} = \frac{\partial y_i(t_j)}{\partial \rho_k} \frac{\rho_k}{y_i(t_j)} \quad (4.15)$$

Here, $y_i(t_j)$ is the value of the i th model output (concentration) at time t_j , and ρ_k is the k th model parameter. To calculate the relative sensitivity of the model outputs to changes in the model parameters over all sampled times, the relative sensitivity (RS) was calculated as follows:

$$RS_{i,k} = \frac{1}{J} \sqrt{\sum_{j=1}^J (NS_{i,j,k})^2} \quad (4.16)$$

Here J is the total number of samples obtained for the tumor, plasma, and each tissue.

4.2 RESULTS

The final model fit to SCID mouse plasma, tissue, and tumor data following intravenous administration of $10 \frac{\text{mg}}{\text{kg}}$ of Doc is shown in Figures 4.2-4.4. The constructed model is able to describe both the rapid drug absorption after bolus administration and late time drug retention observed in all tissues. Of particular note is the Doc concentration profile obtained for the tumor, which displays long-term retention of Doc beyond the 24-hour sample. This leads to uncertainty in estimating the tumor extravascular to vascular transport rate (k_{tev}) as minimal dynamic information on drug elimination from the tumor is available from the data. Also, many of the tissues typically classified as perfusion-limited (*i.e.*, kidney, spleen, and lung) could not be accurately described using Equation (4.1). One reason that perfusion-limited tissue approaches were unable to capture the mouse Doc data was the different dynamic profile obtained for Doc plasma concentrations compared to any of the other sampled tissues (*i.e.*, plasma concentration falls four orders of magnitude while most tissues fall three orders of magnitude or less). In addition, improved fits were obtained with the incorporation of an additional retention subcompartment within each tissue (Equation (4.6)). As Doc is both lipophilic and binds intracellularly to tubulin, it was not unexpected to observe long-term Doc retention in a majority of the sampled tissues [151, 167]. However, given the dynamic profile of plasma Doc concentration (rapid decrease over the first 16 hours) compared to tissue dynamics (rapid initial reduction in concentration over 1 hour followed by a more gradual decrease over time), the model structure would not be capable of representing such dynamic behavior without the inclusion of either a nonlinear transport rate or the addition of another tissue subcompartment with linear transition rates.

Individual compartment accuracy was assessed by evaluating the MAPE, MPE, and terminal half-lives of individual tissues. Predictions for the heart, spleen, and kidney were the least accurate fits with MAPE values of 27.9%, 32.9%, and 34.7% and MPE values of 12.4%, 19.1%, and 23.9% respectively. These inaccuracies were a direct result of using a single set of values for all tissue binding kinetics and could be improved by introducing separate binding kinetic rates for the muscle and other compartments that displayed long terminal half-lives. Plasma had the fourth largest MAPE value, which resulted from the 16 and 24

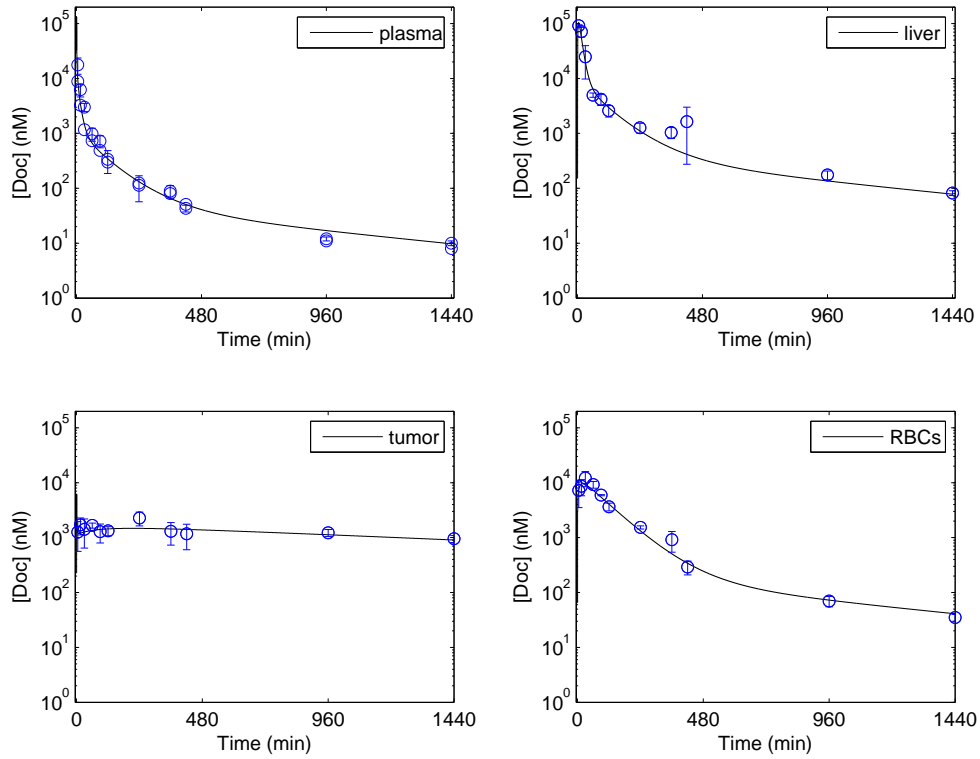


Figure 4.2: Measured Doc concentration versus time data from tumor-bearing SCID mice (circles, μ , with $\pm\sigma$ error bars, $n = 3$ mice per point) compared with mouse PBPK model predictions (lines) for plasma, liver, tumor, and red blood cells.

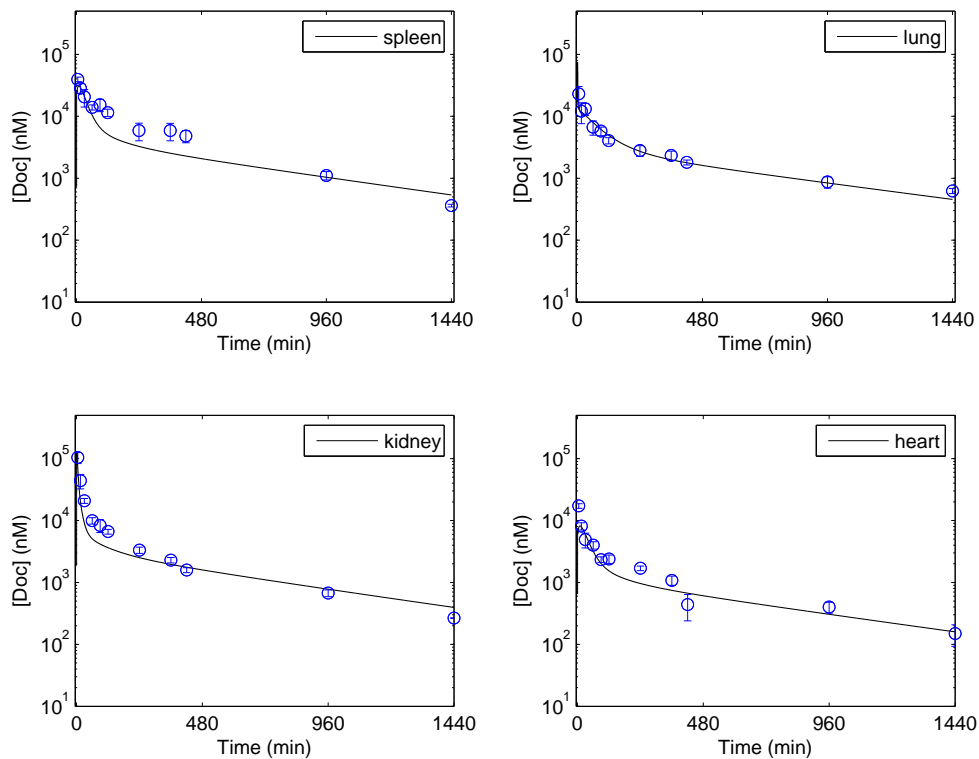


Figure 4.3: Measured Doc concentration versus time data from tumor-bearing SCID mice (circles, μ , with $\pm\sigma$ error bars, $n = 3$ mice per point) compared with mouse PBPK model predictions (lines) for spleen, lung, kidney, and heart.

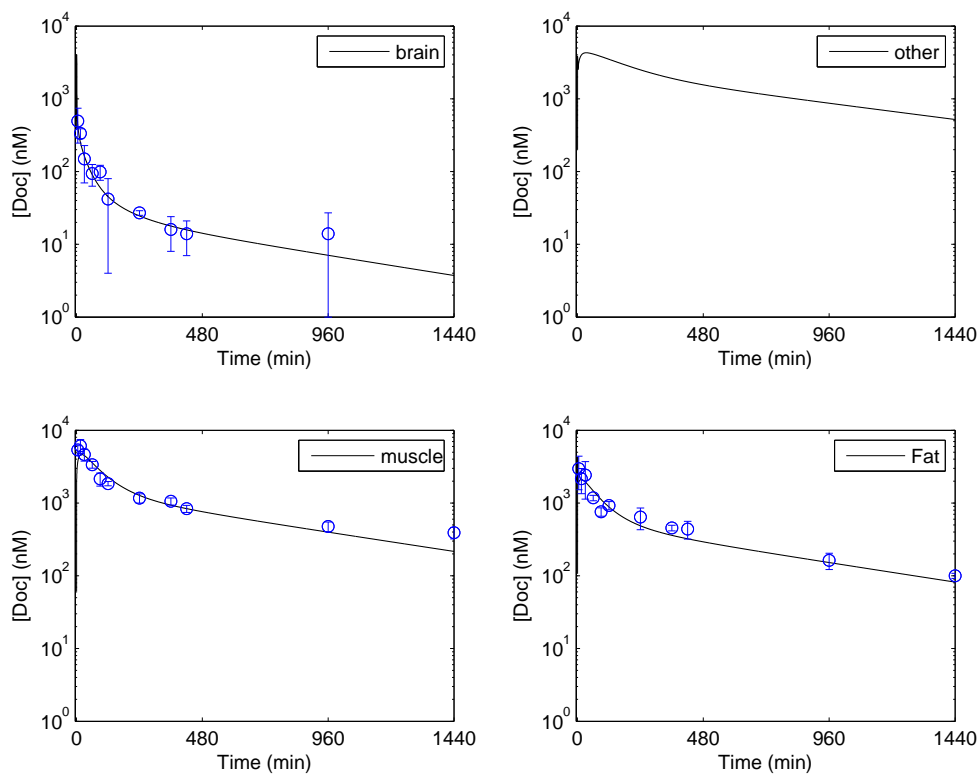


Figure 4.4: Measured Doc concentration versus time data from tumor-bearing SCID mice (circles, μ , with $\pm\sigma$ error bars, $n = 3$ mice per point) compared with mouse PBPK model predictions (lines) for brain, “other”, muscle, and fat compartment.

hour Doc plasma concentration data points having equal values (*i.e.* the data predicts no change in Doc plasma concentration over the final 8 hours of sampling). Model predictions split the difference between these two points resulting in a 5.4% increase in MAPE versus the same calculation without the two final time points. The remaining tissues have MAPE values that are within the mean standard error of individual data points and represent a combination of assay error and individual mouse variability. While the MPEs for plasma, tumor, and tissues were near zero (range

$$4.4\% - 23.9\%$$

), the model displayed a bias towards overpredicting tissue concentrations. This bias could similarly be addressed by introducing individual tissue binding rates, or by assigning two separate sets of tissue binding rates (*i.e.* specific sets for slowly and rapidly perfused tissues). Estimated half-lives from the data were 4.7 hours for plasma, 31.2 hours for tumor, and ranged from 3.4-10.6 hours for the tissues. Similarly, model predicted half-lives were 7.9 hours for plasma, 29.1 hours for tumor, and ranged from 6.1-10.4 hours for the remaining tissues. The higher tissue half-lives were again a result of using a single set of binding rates for all tissues, and estimation would be improved by using at least two separate sets of parameters. The large discrepancy between actual and predicted tumor half-life resulted from tumor Doc concentration data that was relatively constant over the entire PK study; half-life estimates could be improved by including tumor concentrations sampled at later time points (beyond 24 hours) when identifying model parameters.

Parameter sensitivity results for the literature and estimated parameters for all 12 model outputs are shown in Figure 4.5. The ordering of the parameters are the flow rates (parameters 1-8), tissue volumes (9-21), vascular fractions (22-31), and finally transition rates entering and exiting each tissue (32-56). Sensitivity analysis revealed that the most sensitive parameters for each tissue were: the vascular fraction for that tissue, the interstitial-to-vascular transition rate, and the vascular-to-interstitial transition rate. These results were not unexpected, as the vascular fraction for a tissue and interstitial-to-vascular transition rate are not independent system parameters. Furthermore, small alterations to the vascular fraction can result in large alterations to predicted tissue concentration, especially for

Table 4.2: PBPK model predicted performance for the incorporated tissues. Half-lives ($t_{\frac{1}{2}}$) were calculated using the last four data time points (360, 420, 960, and 1440 minutes).

Tissue	MAPE	MPE	WSSE	RMSPE	$t_{\frac{1}{2}}$ data (hours)	$t_{\frac{1}{2}}$ model (hours)
Plasma	26.4	-0.2	186.6	8.1	4.7	7.0
Tumor	10.6	2.3	16.9	6.7	31.2	29.4
Liver	12.3	5.7	159.7	9.7	4.4	6.9
RBCs	12.6	5.5	68.6	5.4	3.4	5.5
Heart	30.0	9.7	83.2	9.6	6.1	6.4
Kidney	32.3	20.0	48.3	10.5	5.2	6.3
Spleen	43.1	40.7	55.9	12.1	4.5	6.5
Lung	10.3	0.7	109.2	4.6	8.4	7.4
Brain	16.4	-4.1	6.0	10.2	6.8	7.2
Muscle	24.1	1.5	110.1	8.6	10.6	11.2
Fat	19.6	14.3	40.0	7.9	7.0	7.1

tissues where the vascular fraction is especially small (*i.e.*, muscle and fat) or when there is concentration-dependent metabolism occurring within a tissue (*i.e.*, liver). Doc plasma concentration was most dependent on the liver parameters, both estimated and from the literature, though the hepatic arterial blood flow rate was less important than the venous flow from the intestine and gut. Of secondary importance to the plasma concentration were the transition rates and vascular fractions for the muscle and “other” compartment and the tissue Doc binding parameters.

Figure 4.6 depicts Doc deposition in various tissues as a percentage of the originally administered dose. Drug was administered to the venous compartment over a 1-min infusion and rapidly distributed into surrounding body tissues. The liver, in particular, was predicted to contain 44% of the dose within the first 5 minutes following dosing (not including the rapid, initial elimination that occurred within the liver). Concurrently, there was rapid redistribution of Doc from the plasma to red blood cells during early time points; however, the rate of redistribution decreases rapidly as drug within the plasma is absorbed by systemic tissues (an effect of maintaining the plasma and red blood cell compartments in equilibrium). Of the remaining tissues, the only two accounting for substantial (>10%) portions of the total administered dose were the muscle and “other” compartments, which had peak percentages of the dose at 20 and 34 minutes, respectively. By the end of 24 hours, the model predicts that only 2.6% of the original dose remains in the system, predominantly in the muscle (0.8%) and “other” (1.0%) compartments, with approximately 0.4% in the remaining normal tissues. Accumulation within the tumor was predicted as 0.6% of the total administered dose, which remains essentially constant for the entire 24 hour sampling period, falling off to 0.4% at 24 hours.

Finally, comparisons between the Doc PBPK model developed above and a nonlinear PBPK model for Doc with fewer compartments [5] were evaluated at two separate Doc dosing levels: $10 \frac{\text{mg}}{\text{kg}}$ and $20 \frac{\text{mg}}{\text{kg}}$. Tissue concentrations were digitally acquired from Bradshaw-Pierce *et al.* at 800% magnification [5]. The PK data from the $5 \frac{\text{mg}}{\text{kg}}$ Doc dose in [5] was not used in comparisons as the data predictions were in excess of those obtained at equivalent time points from mice dosed at $10 \frac{\text{mg}}{\text{kg}}$ Doc in this mouse study, possibly a result of the different mouse species evaluated by the two studies. Furthermore, the human dose

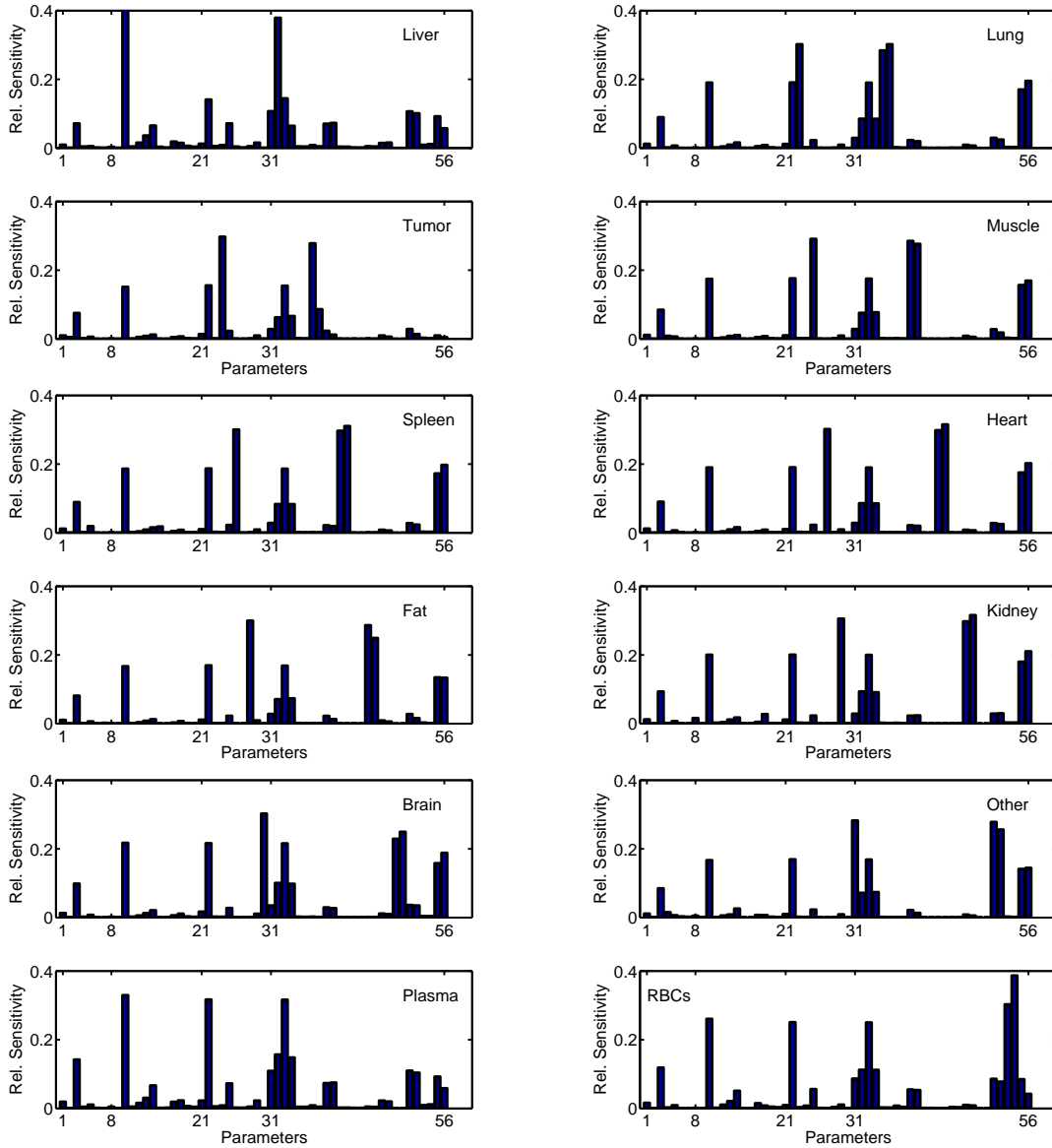


Figure 4.5: Relative sensitivity plots for liver, lung, tumor, muscle, spleen, heart, fat, kidney, brain, “other”, plasma, and RBCs. Parameters are arranged in groups: flow rates (1-8); tissue volumes (9-21); vascular fractions (22-31); and tissue transition rates (32-56). Parameter ordering within those subgroups follow the ordering from Table 4.1: liver, lung, tumor, gut, muscle, spleen, heart, fat, kidney, brain, “other”, plasma, RBC binding, and tissue binding.

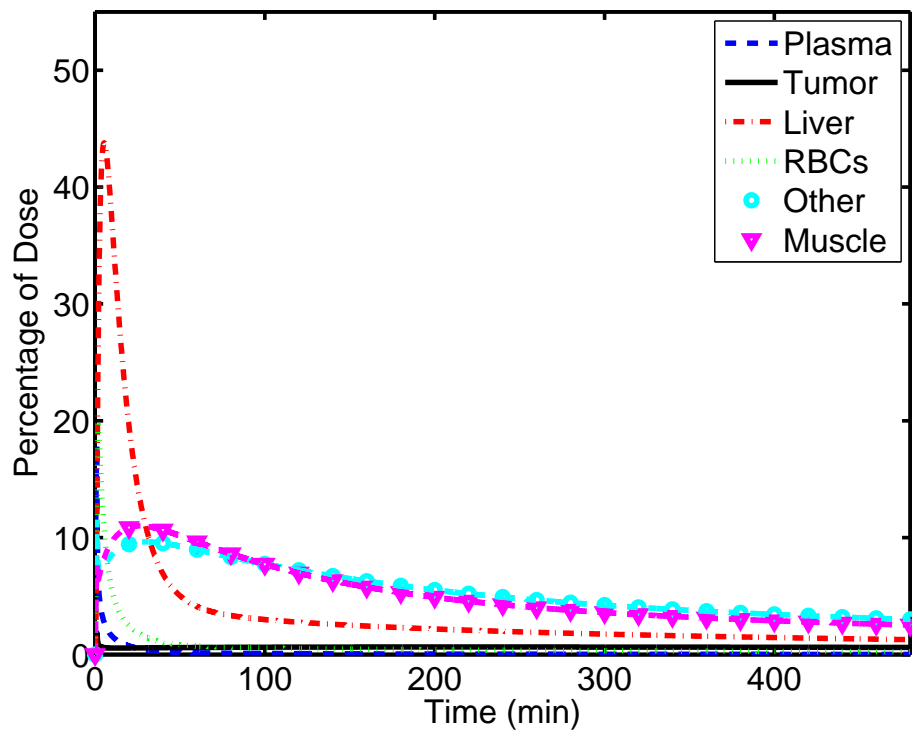


Figure 4.6: Predicted percentage of administered dose in plasma, liver, tumor, muscle, red blood cells, or the other compartment as a function of time.

equivalent of $5 \frac{\text{mg}}{\text{kg}}$ Doc in mice is beneath typically administered dosing levels, corresponding to 17-20 $\frac{\text{mg}}{\text{m}^2}$. Tissues investigated by both studies included plasma, kidney, and liver. Comparisons of the model predictions for the 10 and 20 $\frac{\text{mg}}{\text{kg}}$ doses are shown in Figures 4.7 and 4.8 and Table 4.3.

Both models accurately described the data set they were developed to fit. For the 10 $\frac{\text{mg}}{\text{kg}}$ data set, the PBPK model developed by Bradshaw-Pierce *et al.* over predicted the data slightly at early times and significantly at later times (see MPE and MAPE in Table 4.3). The PBPK model from this paper, likewise, under predicted data for mice dosed at 20 $\frac{\text{mg}}{\text{kg}}$, but was capable of describing the kidney data just as well as the Bradshaw-Pierce PBPK model. The PBPK model developed here was slightly worse at describing the plasma (MAPE of 39.0 versus 38.4) and liver (MAPE of 64.2 versus 59.1) data for the mice dosed at 20 $\frac{\text{mg}}{\text{kg}}$. However, the liver PK profile predicted by the Bradshaw-Pierce model, while more accurate based on these model quality assessment metrics, displayed dynamic behavior between 2-6 hours that was inconsistent with the observed data, a repercussion of including nonlinear elimination and transport rates within their PBPK model. Still, both models predicted accurate Doc tissue and plasma PK when extrapolated to dose levels not included during original model design development.

4.3 DISCUSSION

PBPK models provide a convenient structure for depicting systemic distribution of chemotherapeutics following administration, provided that sufficient data are available to support the more involved model structure. Using plasma, tumor, and tissue Doc concentration versus time data obtained from SKOV-3 bearing SCID mice dosed i.v. at 10 $\frac{\text{mg}}{\text{kg}}$, a mouse PBPK model was constructed with separate compartments for plasma, tumor, liver, kidney, lung, heart, spleen, brain, muscle, fat, and red blood cells. Due to the presence of tissue concentration PK with significantly different concentration versus time profiles from plasma (tissues had bi-phasic elimination while plasma was tri-phasic), it was necessary to include two tissue subcompartments, corresponding to tissue transport

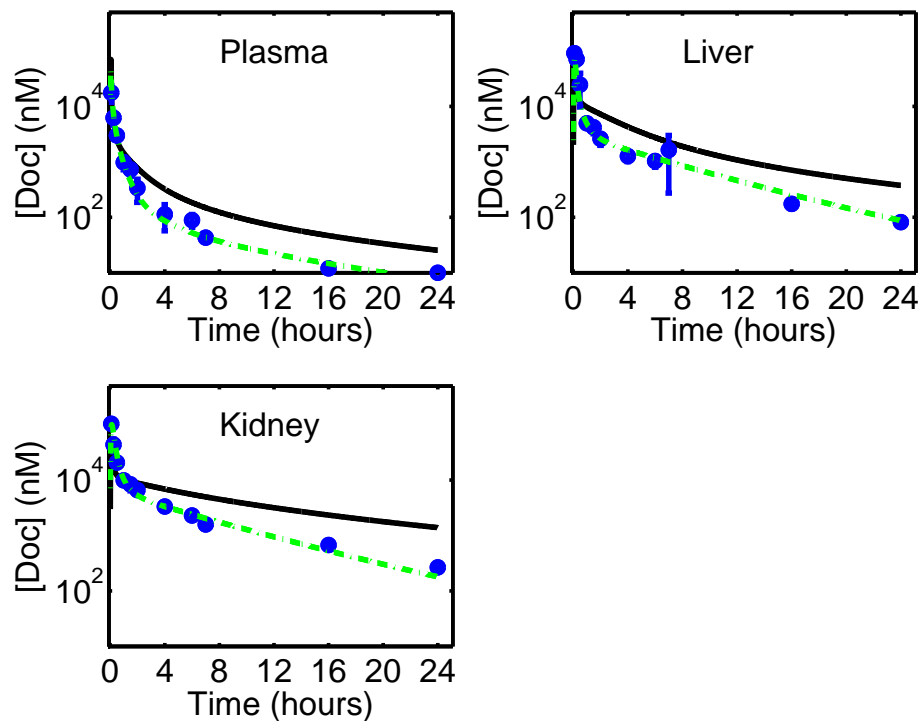


Figure 4.7: Plasma (top left), liver (top right), and kidney (bottom left) Doc predictions from the model developed in Figure 4.1 (dash-dot) and those predicted by a PBPK model from the literature [5] (solid) compared with actual plasma Doc concentration versus time data from tumor-bearing SCID mice (circles, μ , with $\pm\sigma$ error bars, $n = 3$ mice per point) dosed at $10 \frac{\text{mg}}{\text{kg}}$.

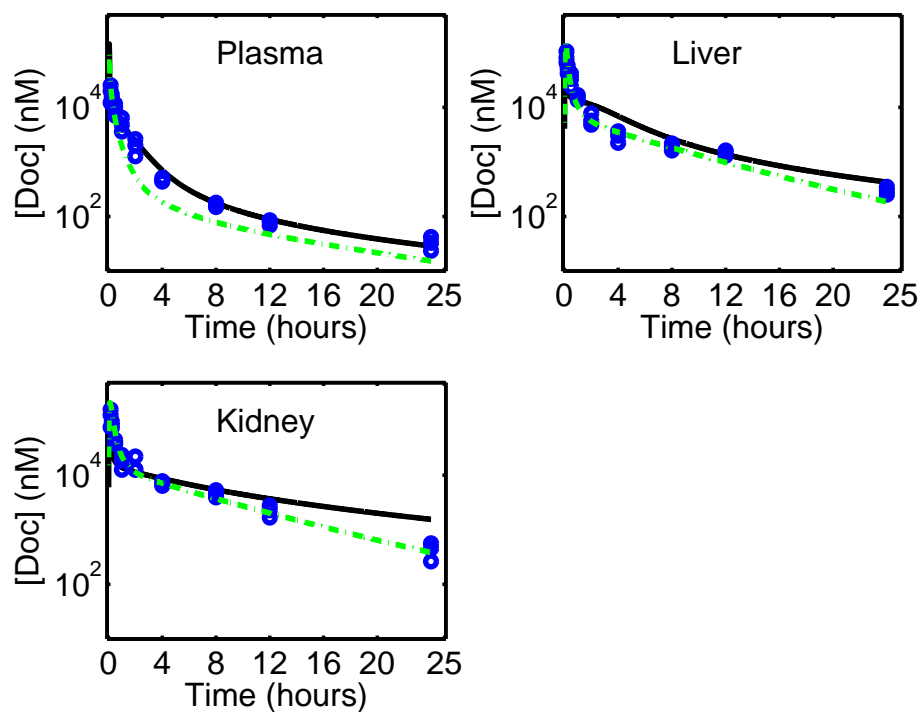


Figure 4.8: Plasma (top left), liver (top right), and kidney (bottom left) Doc predictions from the model developed in Figure 4.1 (dash-dot) and those predicted by a PBPK model from the literature [5] (solid) compared with actual plasma Doc concentration versus time data from BALB/c mice (circles) dosed at $20 \frac{\text{mg}}{\text{kg}}$.

and tissue retention of Doc, respectively. To minimize the number of parameters requiring estimation, the same parameter values for Doc retention were used for all tissues. While this provides a reasonable approximation, two separate sets of parameter values are likely necessary based upon inspection of tissue half-lives in Table 4.2.

Tissue half-lives reveal that the longest drug retention is predicted within the tumor, which agrees with previous Doc tumor studies, though the half-life seen from the current study was significantly longer than that described in others [160]. This increased retention may be tumor-type specific, however, samples at later time points are required to characterize the Doc elimination from the tumor appropriately. While the half-lives of Doc in plasma, tumor, and normal tissues were longer in the current study than those previously reported in the literature [160], the values agreed with half-lives reported from Bradshaw-Pierce *et al.* [5]. This latter study, which was performed more recently and without radiolabeled Doc, may more accurately represent actual Doc tissue concentrations versus time. Muscle had the second longest Doc half-life at 10.6 hours. While the Doc C_{max} of muscle was 2-15 fold lower than Doc C_{max} in other tissues, the Doc concentration at 24 hours in muscle was similar to that in the majority of other tissues with the exception of tumor. Given the overall percentage of body weight represented by muscle as compared to other tissues, muscle may be the primary contributor to terminal Doc retention following dosing.

Comparisons between the mouse PBPK model developed in this chapter and a previous one [5] agreed well for mouse Doc dosing levels of 10 and 20 $\frac{\text{mg}}{\text{kg}}$, despite using different model structures. More compartments were included within the PBPK model developed within this chapter, while the previous PBPK model included intestinal compartment concentrations and additional routes of elimination, including urinary and fecal excretion, that account for approximately 10% of drug removal. Furthermore, the previous model [5] has nonlinear elimination rates and binding relationships within tissues, while the model developed in this chapter has only linear components. However, our PBPK model also utilized a structure seen as less desirable in the literature due to the large number of model parameters and uncertainty associated with the vascular fraction term within the model. Therefore, the ideal model may depend on the needs of the user, whether a lower-order system with nonlinearities, or a higher-order linear system is preferred. It is likely, though, that a linear model is sufficient

for describing Doc PK dynamics in humans, as no nonlinearities over a range of dosing levels have been observed [161] and the human scale-up model of the previously published PBPK model did not exhibit any nonlinear behavior regarding patient Doc plasma concentration predictions. Also, even for patients with altered CYP3A enzyme levels, these alterations would affect the enzymatic rate of elimination, and not the saturation. Therefore, a linear elimination rate should be sufficient for describing Doc elimination. Furthermore, for Doc administration of 5, 10, and 20 $\frac{\text{mg}}{\text{kg}}$, all common tissues (kidney and liver) had similar half-life values, though plasma half-life was 2-fold greater for the 20 $\frac{\text{mg}}{\text{kg}}$ dosing level. Combined with the extensive preclinical and clinical work performed using Doc, these results suggest that a linear model may be sufficient for describing systemic Doc distribution.

The incorporation of a tumor compartment within the current Doc PBPK model structure also represents an extension of the earlier mouse PBPK model [5] and may aid human scale-up predictions of total tumor Doc exposure. Furthermore, the 3-fold greater tumor half-life compared to the next longest tissue may explain why similar efficacy is attainable on weekly versus q3w Doc schedules. Model simulations have demonstrated that week-to-week tumor accumulation of Doc is predicted to occur (results not shown), and these findings will be further explored in Chapter 5.

Additional Doc distribution studies from our group have revealed that extended Doc tumor retention also applies to Pc-3 human tumor xenografts [150]. Measured tumor tissue Doc concentrations from these xenografts were lower than those obtained from SKOV-3 human tumor xenografts, necessitating a reevaluation of the model parameters for tumor distribution. Either a reduction in the tumor vascular fraction (f_t) from 10% (for SKOV-3) to 3.1%, or a one-third reduction in the $k_{t_{ve}}$ parameter, were necessary to describe the measured Pc-3 tumor Doc concentrations (Figure 4.9). Finding two parameter alterations capable of describing the new data was not unexpected based upon the parameter sensitivity and coupling previously discussed in this Chapter. However, given that Pc-3 xenografts are typically less vascularized than SKOV-3 xenografts [150], alterations to f_t may be suitable for predicting tumor concentration variation between different tumor lines. Also, Doc samples in Pc-3 tumor xenografts were obtained out to 72 hours, as opposed to the 24-hour sampling utilized in the modeling study. While the estimated interstitial-to-vascular transition rate

for tumor could not be properly estimated due to limited dynamic information in docetaxel tumor concentration over the 24-hour sampling window, this additional data demonstrates that the elimination rate predicted by the model may indeed be accurate.

Table 4.3: PBPK model predictive performance comparison at dosing levels of $10 \frac{\text{mg}}{\text{kg}}$ and $20 \frac{\text{mg}}{\text{kg}}$.

Model	Tissue	$10 \frac{\text{mg}}{\text{kg}}$			$20 \frac{\text{mg}}{\text{kg}}$		
		MAPE	MPE	RMSPE	MAPE	MPE	RMSPE
Florian <i>et al.</i>	Plasma	26.4	-0.2	8.1	39.0	39.0	15.4
	Liver	12.3	5.7	12.5	64.2	7.5	32.9
	Kidney	32.3	20.0	13.6	29.7	27.4	14.5
Bradshaw-Pierce <i>et al.</i> [5]	Plasma	61.3	-37.4	48.7	38.4	38.4	14.1
	Liver	82.4	-82.4	189.5	59.1	-59.1	69.0
	Kidney	62.7	8.9	45.2	46.5	36.3	34.6

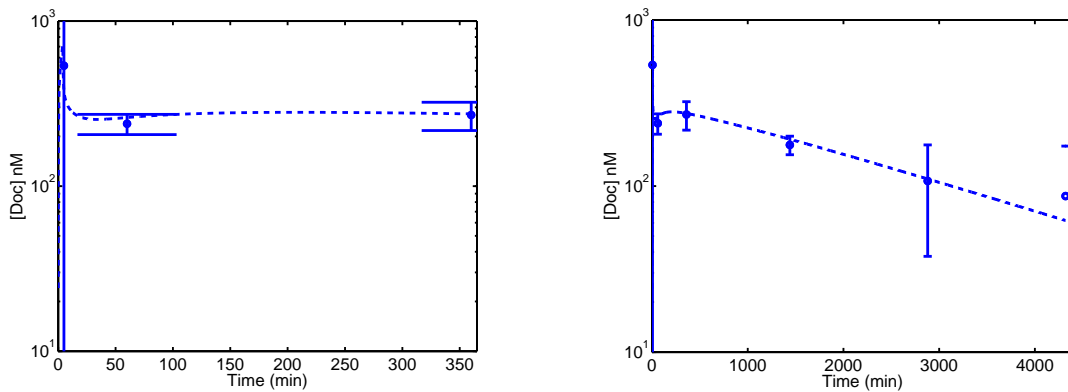


Figure 4.9: Measured Doc concentration versus time data from Pc-3 tumor-bearing SCID mice (circles, μ , with $\pm\sigma$ error bars, $n = 3$ mice per point) compared with mouse PBPK model predictions (lines) for the tumor compartment.

5.0 SCALE-UP OF THE MOUSE DOC PBPK TO HUMANS

Doc, a semi-synthetic taxane, promotes the polymerization of microtubules and induces cell apoptosis during cell division [151]. It is a potent chemotherapeutic, displaying efficacy across a wide range of solid tumors, and it is currently approved as treatment against metastatic breast, non-small cell lung, and androgen-independent prostate cancers [151]. Typical Doc doses range from 60-100 $\frac{\text{mg}}{\text{m}^2}$ delivered over 1-hour every three weeks (q3w schedule) or 30-45 $\frac{\text{mg}}{\text{m}^2}$ delivered over 30-minutes every week for three weeks, followed by a week of no treatment (“weekly”). These two regimens have drastically different toxicity profiles despite displaying similar efficacy results [155, 168, 169, 170]. Grade 3 or 4 neutropenia occurs in upwards of 90% of patients treated q3w with 100 $\frac{\text{mg}}{\text{m}^2}$ Doc [151]. In contrast, the incidence of grade 3/4 neutropenia in patients receiving “weekly” 35-40 $\frac{\text{mg}}{\text{m}^2}$ doses of Doc was significantly less (2.5-16%) [155, 159, 171]. However, “weekly” Doc is associated with other serious treatment side-effects including fatigue, hyperlacrimation, and nail toxicity [172]. Myelosuppression associated with q3w Doc has been correlated with Doc clearance, however the fact that similar AUCs are delivered in q3w and “weekly” Doc regimens implies that Doc exposure-toxicity relationships may not be similar across different dosing schedules.

Docetaxel PK displays high intra-patient variability, predominantly influenced by patient body weight (partially accounted for using body surface area (BSA) scaled dosing), extensive protein binding, and metabolic enzyme activity. Elimination routes for Doc are predominantly metabolic, are mediated by isoforms CYP3A4 and CYP3A5 [173], and account for >80% of total Doc elimination. Inter-individual variations in expression of CYP3A isoforms, can substantially influence Doc clearance [174, 175]. Urinary and fecal elimination comprise the remainder of Doc clearance, with each contributing <10% [153, 154]. An addition factor in Doc elimination is the high plasma protein binding of Doc, which

may exceed 92% (91%-98%) [8, 176]. This binding percentage is highly dependent on plasma concentrations of albumin, and to a greater extent, α_1 -acid glycoprotein (AAG) serum concentrations. Increased concentrations of serum AAG result in a decreased free fraction of circulating Doc and, as a result, decreased Doc clearance, according to a linear relationship developed by Baker *et al* [8]. Other studies by Baker *et al.* have demonstrated an influence of the formulation vehicle, polysorbate 80, on the plasma binding of Doc, resulting in an increased Doc free fraction at the end of a Doc infusion [177]. As both efficacy and toxicity are correlated with Doc clearance, the ability to predict individual patient Doc PK, including clearance, may allow for improvements in treatment efficacy and reduced toxicity. Furthermore, as Doc exposure (*i.e.*, AUC) does not correlate with toxicity across q3w and weekly Doc regimens, an understanding of system-wide Doc deposition may provide insight into how the two regimens can be associated with similar efficacy but differing toxicity.

One PK model for predicting patient Doc plasma concentrations in the absence of samples is the population PK model developed by Bruno *et al.* [2, 178]. This three-compartment structure uses set population values for the volume and intra-compartment transition rates. However, clearance from the plasma compartment is calculated based upon a series of patient covariates including BSA, albumin, age, hepatic function, and AAG. The primary advantages of this model are its ability to describe individual PK without the need for sample processing and its ability to identify those patients whose clearance may significantly deviate from the population median. Further studies with this model revealed clearance-dependent correlations with both toxicity and efficacy [2]. Also, investigations into optimal sampling strategies revealed that as few as two plasma samples, corresponding to the end of infusion and six hours following the start of infusion, would allow for improved estimates of individual patient clearance [2].

An alternative model in the literature is the Doc PBPK mouse model developed by Bradshaw-Pierce *et al.*, and subsequently scaled to humans [5]. This model uses six coupled nonlinear ODEs to describe Doc deposition within liver, kidney, gut, plasma, rapidly perfused tissue, and slowly perfused tissue. In addition, elimination pathways for Doc via metabolism, urinary excretion, and fecal excretion are also included within the model, consistent with typical elimination percentages observed in patients. This model, developed

in mice was scaled to humans by adjusting blood flow rates, tissue volumes, and metabolic parameters, while leaving partition coefficients, tubulin binding affinity, and tissue-specific tubulin binding capacity unchanged. When model results were compared against actual patient Doc plasma data for doses of 30, 36, and 100 $\frac{\text{mg}}{\text{m}^2}$, the model was capable of describing Doc plasma PK, but it had a tendency to under-predict Doc concentrations at the end of the infusion as well as patient data associated with the 30 and 36 $\frac{\text{mg}}{\text{m}^2}$ Doc doses. Also, while it is understood that a PBPK model may offer more insight regarding drug deposition than traditional compartmental PK models, no comparison was made between the PBPK model predictions and those produced by existing Doc population PK models in the literature.

The goal of the current study was to evaluate how well the tissue-intensive mouse PBPK model from Chapter 4 could predict human Doc plasma PK after scale-up. The validation of the scale-up was performed on human Doc plasma data collected from three separate Phase 1 clinical trials [6, 7, 179] with patients dosed over a range of 35-75 $\frac{\text{mg}}{\text{m}^2}$. Furthermore, human plasma Doc predictions from the scaled tissue-intensive PBPK model were compared against those predicted by models developed by Bruno *et al.* and Bradshaw-Pierce *et al.* [2, 5]. Estimates of plasma Doc free fraction were made from patient data to assess the potential improvement resulting from including patient-specific information. Also, the scaled tissue-intensive PBPK model was updated with model parameters to better describe cardiac output and tissue distributions observed in elderly patients. Finally, alterations in simulated tumor Doc concentrations based on changes in dosing level, patient body weight, tumor volume, (which determines tumor blood flow rate based on Equations (4.11)), and dosing schedule were investigated using the tissue-intensive PBPK model.

5.1 MATERIALS AND METHODS

5.1.1 Human Doc Clinical Data

Human plasma Doc data were obtained from Phase 1 studies performed at the University of Pittsburgh Cancer Institute (UPCI) [179] and Memorial Sloan-Kettering Cancer Center

(MSKCC) [6, 7]. The UPCI study involved 25 patients dosed q3w with 50 (n=7), 60 (n=13), or $75 \frac{\text{mg}}{\text{m}^2}$ (n=5). Drug was administered via IV infusion over 1-hour, and plasma samples were collected before dosing and at 0.5, 0.92, 1.25, 1.5, 2, 3, 4, 5, 7, 9, 11, 13, 14, 17, and 25 hours following the start of Doc administration. The MSKCC Phase I study samples [6] were collected at various times (6-9 per patient) out to 50.5 hours from 50 patients dosed either “weekly” 35 (n = 8) or q3w with 55 (n = 3), 70 (n = 27), or $75 \frac{\text{mg}}{\text{m}^2}$ (n = 12). The MSKCC study in elderly patients [7] involved 20 patients dosed at $35 \frac{\text{mg}}{\text{m}^2}$ (n=20) “weekly”. Infusion duration was 30 minutes with samples (10-11) collected at pretreatment, 0.25 (mid infusion), 0.48, 0.67, 1, 1.5, 3.5, 8, 24.5, 48.5, and 168.5 hours (approximately one week with the sample collected prior the following dose). A summary of the patient groups from all three clinical trials is shown in Table 5.1.

Plasma concentrations of Doc from the two Phase I clinical trials were determined using a LC-MS assay that was developed by Parise *et al.* [165]. Plasma samples from the MSKCC elderly patient study were evaluated using a validated method based on high-performance LC-MS as described previously [155]. Plasma AAG concentrations values were measured using an immunoturbidometric method using the Roche AAG Diagnostic Kit on a Cobas Integra 800 System (Roche Diagnostics, Alameda, CA) as previously described [180].

5.1.2 Human PBPK Model Scale-Up

A structurally equivalent PBPK Doc distribution model was constructed for humans based upon the mouse PBPK model previously developed in Chapter 4. Blood flow rates and tissue volumes were based on literature values for humans and subsequently scaled for individual patient weights [1]. Representative parameters for a 70 kg male are shown in Table 5.2. Tissues volumes and blood flow rates were adjusted linearly based on actual patient weight. Tissue vascular fractions were updated, when applicable, to typical values observed in humans, while liver metabolic rate was left unchanged. The internal transport rate for Doc in all tissues was uniformly decreased by a factor of 2. This change was implemented as the unbound fraction of Doc in humans is approximately 5%, which is half the unbound fraction in mice [8]. Also, the RBC exchange rate was decreased by a factor

Table 5.1: Patient characteristics from the Phase 1 Doc studies performed at UPCI and MSKCC. Values are reported as the study median and range.

	UPCI [179]	MSKCC[6]	MSKCC Elderly [7]
Number of Patients	25	50	20
Males/Females	21/4	42/7	8/12
Age (years)	63 (43-78)	60.3 (32-78)	75 (66-84)
Doc Dose ($\frac{\text{mg}}{\text{m}^2}$)			
35	—	8	20
50	7	—	—
55	—	3	—
60	13	—	—
70	—	27	—
75	5	12	—
BSA (m^2)	1.72 (1.30-1.93)	1.90 (1.38-2.64)	1.85 (1.49-2.25)
Weight (kg)	88 (52-109)	83 (48-145)	—
AAG ($\frac{\text{g}}{\text{L}}$)	1.24 (0.28-2.47)	1.37 (0.60-2.55)	—
Albumin ($\frac{\text{g}}{\text{L}}$)	3.7 (2.8-4.5)	4.4 (3.5-5.0)	—

of 40 as the RBC-to-plasma ratio in humans has been determined to be 1:10, versus the 2:1 ratio observed in SCID mice [150, 181]. Model quality was assessed using the methods in section 4.1.4.

5.1.3 Model Validation

Model comparisons of this tissue-intensive human PBPK model were performed against two existing Doc models from the literature: (i) a three-compartment population PK developed by Bruno *et al.*; and (ii) a five-tissue, PBPK model developed by Bradshaw-Pierce *et al.*

For the Bruno PK model, the transition rates between compartments were equivalent for all patients and are summarized in Table 5.3. Clearance (CL , $\frac{L}{hr}$) was calculated per patient using the following equation:

$$CL = BSA(22.1 - 3.55AAG - 0.095AGE + 0.2245ALB)(1 - 0.334HEP12) \quad (5.1)$$

Here BSA is the body surface area of the patient (m^2), AGE is the age of the patient in years, and AAG and ALB represent α_1 -acid glycoprotein and albumin concentrations ($\frac{g}{L}$) in plasma, respectively. HEP12 is a measure of the hepatic function of the patient given a default value of 0. For patients with alanine aminotransferase (ALT) or aspartate aminotransferase (AST) > 60 IU and alkaline phosphatase > 300 IU, HEP12 was assigned a value of 1. Of the patients enrolled in both Phase 1 clinical studies whose data was used in scale-up, all had HEP12 values of 0 based on their individual ALT, AST, and alkaline phosphatase values. Albumin values for 8 of the UPCI patients were not available. In their place, mean population values from the UPCI patient group were used. AAG values for 18 of the patients from the MSKCC patient group were also not available and were assumed equivalent to the MSKCC patient group mean for simulation within the Doc population PK model of Bruno. BSA for 11 of the patients from the elderly MSKCC dataset was unavailable. Simulations on these patients used a population average BSA of $1.75 m^2$, however, these patients were not included when analyzing model performance metrics.

The Bradshaw-Pierce model used the same approach as our model, adjusting tissue volume and blood flow rates based on the actual weight of the patient. Partition coefficients,

Table 5.2: Parameter values from the literature for the human PBPK model (70 kg) [1]. F , V , and f denote tissue blood flow rates, tissue volumes, and tissue vascular fractions, respectively.

Units	$\frac{\text{L}}{\text{min}}$		L		—	
Liver	F_{li}	0.45	V_{li}	1.80	f_{li}	0.16
Lung	F_l	5.60	V_l	0.53	f_l	0.30
Tumor	F_t	0.03	V_t	0.2	f_t	0.05
Gut	F_g	1.13	V_g	1.19	f_g	—
Muscle	F_m	0.59	V_m	28.0	f_m	0.03
Spleen	F_s	0.02	V_s	0.18	f_s	0.20
Heart	F_h	0.26	V_h	0.33	f_h	0.02
Fat	F_f	0.74	V_f	15.0	f_f	0.03
Kidney	F_k	1.24	V_k	0.31	f_k	0.24
Brain	F_b	0.78	V_b	1.40	f_b	0.04
Other	F_o	0.36	V_o	15.8	f_o	0.05
Blood	F_{tot}	5.60	V_{blood}	5.53		

Table 5.3: Parameter values for the Bruno *et al.* Doc population PK model [2]. k_{ij} are transition rates from compartment i to compartment j , and V_i is the volume of model compartment i .

Parameter	Value	Parameter	Value
k_{12} ($\frac{1}{\text{hr}}$)	1.06	k_{21} ($\frac{1}{\text{hr}}$)	1.74
k_{13} ($\frac{1}{\text{hr}}$)	1.28	k_{31} ($\frac{1}{\text{hr}}$)	0.08
V_1 (L)	10		

tubulin retention, and binding affinity parameters were left unaltered from their mouse PBPK model. Parameters pertaining to metabolism and excretion (urinary and fecal) were altered based on literature values [5].

5.2 RESULTS

5.2.1 Doc Plasma Model Predictions

Doc plasma concentration predictions from the tissue-intensive PBPK were compared to actual patient Doc concentrations obtained in the three clinical trials. Actual versus predicted patient Doc plasma concentrations for all three models (Bruno population PK model [2], Bradshaw-Pierce PBPK model [5], and the tissue-intensive PBPK model) are shown in Figure 5.2, and a summary of individual model performance based on dosage and study is shown in Tables 5.4-5.5. Representative patient plots over the evaluated Doc dosing range are shown in Figure 5.1, and a comprehensive set of individual patient plots can be found in Appendix C, Figures C1-C11.

Both the PBPK model developed within this dissertation and the original population model of Bruno were capable of describing Doc plasma AUC and clearance across the range of investigated doses. However, the Bradshaw-Pierce *et al.* PBPK model tended to under-predict the AUC observed for each dosing group. This under-prediction occurred despite the Bradshaw-Pierce *et al.* PBPK model having accurate overall performance metrics for both the UPCI and MSKCC study patients. It should be noted that the fits from both PBPK models were achieved based solely on the Doc dose, BSA, and body weight, and may be improved through the inclusion of additional patient-specific metrics.

For all three studies, all three models had difficulty predicting Doc concentrations during the infusion (highest concentrations), as shown in Figure 5.2. Both the tissue-intensive PBPK and population PK models were centered around the unity line, however, neither model predicted the variation in peak Doc plasma concentrations observed within the population dataset. For the UPCI study, both PBPK models over-predicted the 50 $\frac{\text{mg}}{\text{m}^2}$ and under

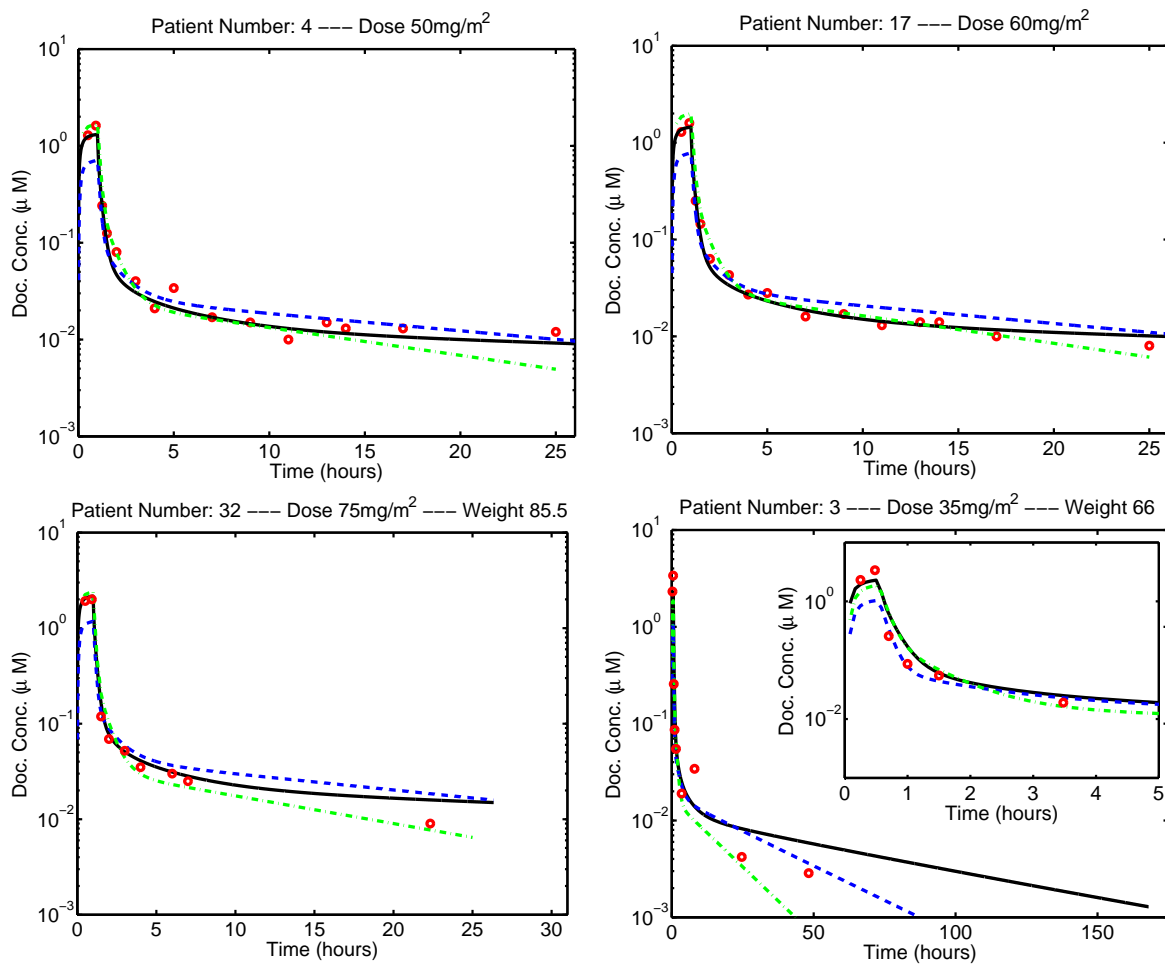


Figure 5.1: Measured Doc plasma concentration data in humans dosed at 50 (top left), 60 (top right), 75 (bottom left) and 35 (bottom right) $\frac{\text{mg}}{\text{m}^2}$ vs. time. Human PBPK model predictions are from the tissue-intensive PBPK (solid), the Bradshaw-Pierce PBPK (dashed), and the Bruno population PK (dash-dot) models.

Table 5.4: Doc plasma AUC and clearance mean (standard deviation) values from study data and model predictions.

Clinical Trial	Doc Dose	Actual			Florian <i>et al.</i>		
		AUC ₀₋₂₄ ($\mu\text{M hr}$)	Clearance ($\frac{\text{L}}{\text{hr}}$)	AUC ₀₋₂₄ ($\mu\text{M hr}$)	Clearance ($\frac{\text{L}}{\text{hr}}$)	AUC ₀₋₂₄ ($\mu\text{M hr}$)	Clearance ($\frac{\text{L}}{\text{hr}}$)
MSKCC Elderly [7] (n=9)	35 $\frac{\text{mg}}{\text{m}^2}$	4.14 (1.13)	18.3 (7.9)	2.28 (0.18)		35.2 (0.3)	
MSKCC [6] (n=8)	35 $\frac{\text{mg}}{\text{m}^2}$	2.11 (1.20)	35.1 (11.3)	1.61 (0.69)		43.4 (14.1)	
UPCI [179] (n=7)	50 $\frac{\text{mg}}{\text{m}^2}$	1.62 (0.24)	71.9 (11.6)	2.09 (0.19)		55.8 (10.3)	
MSKCC [6] (n=3)	55 $\frac{\text{mg}}{\text{m}^2}$	1.95 (0.68)	64.3 (24.8)	2.38 (0.31)		46.5 (11.5)	
UPCI [179] (n=13)	60 $\frac{\text{mg}}{\text{m}^2}$	2.37 (0.60)	64.9 (18.6)	2.43 (0.23)		59.8 (8.2)	
MSKCC [6] (n=27)	70 $\frac{\text{mg}}{\text{m}^2}$	3.62 (2.19)	54.3 (17.4)	3.51 (0.28)		48.4 (9.1)	
UPCI [179] (n=5)	75 $\frac{\text{mg}}{\text{m}^2}$	3.18 (0.98)	56.9 (21.3)	3.19 (0.25)		52.7 (9.0)	
MSKCC [6] (n=12)	75 $\frac{\text{mg}}{\text{m}^2}$	3.57 (1.22)	59.7 (21.7)	3.65 (0.30)		53.0 (11.2)	

Clinical Trial	Doc Dose	Bradshaw <i>et al.</i> [5]			Bruno <i>et al.</i> [2]		
		AUC ₀₋₂₄ ($\mu\text{M hr}$)	Clearance ($\frac{\text{L}}{\text{hr}}$)	AUC ₀₋₂₄ ($\mu\text{M hr}$)	Clearance ($\frac{\text{L}}{\text{hr}}$)	AUC ₀₋₂₄ ($\mu\text{M hr}$)	Clearance ($\frac{\text{L}}{\text{hr}}$)
MSKCC Elderly [7] (n=9)	35 $\frac{\text{mg}}{\text{m}^2}$	0.96 (0.08)	84.1 (0.9)	1.46 (0.12)		54.9 (0.5)	
MSKCC [6] (n=8)	35 $\frac{\text{mg}}{\text{m}^2}$	0.71 (0.31)	98.9 (33.6)	1.03 (0.47)		66.0 (8.9)	
UPCI [179] (n=7)	50 $\frac{\text{mg}}{\text{m}^2}$	0.84 (0.09)	137.8 (26.6)	1.86 (0.09)		61.8 (6.9)	
MSKCC [6] (n=3)	55 $\frac{\text{mg}}{\text{m}^2}$	1.26 (0.15)	94.6 (26.5)	2.26 (0.21)		51.3 (6.3)	
UPCI [179] (n=13)	60 $\frac{\text{mg}}{\text{m}^2}$	1.00 (0.11)	144.9 (21.7)	2.24 (0.09)		64.4 (5.6)	
MSKCC [6] (n=27)	70 $\frac{\text{mg}}{\text{m}^2}$	1.63 (0.15)	104.5 (20.8)	2.64 (0.53)		65.1 (9.3)	
UPCI [179] (n=5)	75 $\frac{\text{mg}}{\text{m}^2}$	1.38 (0.13)	122.1 (22.6)	2.94 (0.35)		57.6 (11.9)	
MSKCC [6] (n=12)	75 $\frac{\text{mg}}{\text{m}^2}$	1.71 (0.16)	113.8 (26.1)	3.00 (0.68)		65.9 (13.2)	

Table 5.5: Model performance mean (standard deviation) values for three Doc studies across multiple Doc dosing levels.

Clinical Trial	Doc Dose	Florian <i>et al.</i>		Bradshaw <i>et al.</i> [5]		Bruno <i>et al.</i> [2]	
		MPE	RMSPE	MPE	RMSPE	MPE	RMSPE
All	35-75 $\frac{\text{mg}}{\text{m}^2}$ (n=84)	-3.0 (42.2)	16.3 (9.5)	8.1 (44.5)	17.6 (7.2)	16.9 (35.8)	16.5 (8.4)
	50-70 $\frac{\text{mg}}{\text{m}^2}$ (n=25)	-2.5 (30.1)	11.4 (5.9)	0.6 (31.7)	13.7 (3.9)	14.6 (23.9)	12.4 (5.7)
	50 $\frac{\text{mg}}{\text{m}^2}$ (n=7)	-22.9 (24.9)	11.5 (5.0)	-18.7 (25.4)	13.9 (3.9)	0.2 (20.7)	12.5 (4.6)
	60 $\frac{\text{mg}}{\text{m}^2}$ (n=13)	2.2 (32.4)	11.1 (4.6)	4.1 (36.3)	13.9 (4.2)	19.1 (26.1)	12.5 (4.6)
	75 $\frac{\text{mg}}{\text{m}^2}$ (n=5)	13.8 (15.2)	12.0 (10.3)	18.6 (5.8)	13.1 (4.0)	22.9 (14.9)	12.2 (10.4)
MSKCC[6]	55-75 $\frac{\text{mg}}{\text{m}^2}$ (n=50)	-9.0 (46.7)	18.6 (10.5)	3.4 (48.2)	19.2 (9.8)	11.8 (40.0)	17.7 (9.1)
	55 $\frac{\text{mg}}{\text{m}^2}$ (n=3)	-47.6 (28.4)	22.4 (3.4)	41.6 (31.8)	23.2 (6.9)	-35.6 (34.8)	20.2 (8.9)
	70 $\frac{\text{mg}}{\text{m}^2}$ (n=27)	-28.5 (44.9)	20.7 (13.1)	-15.5 (47.7)	22.6 (11.6)	-1.4 (35.3)	18.4 (10.8)
	75 $\frac{\text{mg}}{\text{m}^2}$ (n=12)	21.4 (31.8)	13.9 (5.8)	36.2 (30.8)	14.0 (4.0)	31.3 (35.7)	15.9 (8.1)
	35 $\frac{\text{mg}}{\text{m}^2}$ (n=8)	26.0 (29.5)	16.9 (3.1)	34.7 (28.7)	14.1 (4.0)	45.0 (25.7)	16.9 (3.4)
MSKCC Elderly [7]	35 $\frac{\text{mg}}{\text{m}^2}$ (n=9)	27.9 (34.3)	17.7 (7.2)	54.7 (22.3)	19.5 (2.0)	51.9 (16.0)	21.3 (6.6)

predicted the 60 and 75 $\frac{\text{mg}}{\text{m}^2}$ data; based on RMSPE and MPE metrics, model inaccuracies across all three dosing ranges were consistent. Model predictions for the MSKCC data set were worse for all three models compared to predictions from the UPCI study, even compared against results from similar dosing levels (75 $\frac{\text{mg}}{\text{m}^2}$), which was likely a function of fewer total samples and more sporadic plasma sampling.

For the MSKCC elderly patient data set, neither weights nor gender were available, so model performance was evaluated for both a 66 kg (woman) and 79 kg (man) person, and the better performing model was selected as the representation of the patient. The elderly patient study was better described by the tissue-intensive PBPK model (RMSPE and MPE of 17.7 ± 7.2 and 27.9 ± 34.3 , respectively) compared to predictions from the Bradshaw-Pierce PBPK (RMSPE and MPE of 19.5 ± 2.0 and 54.7 ± 22.3 , respectively) and Bruno population PK (RMSPE and MPE of 21.3 ± 6.6 and 51.9 ± 16.0 , respectively) models. Observed C_{max} concentrations from this data set were 1-3 fold higher than those obtained from the other studies, and hence, C_{max} was under predicted by both PBPK models. Overall, this data set was the worst characterized of the three, both by performance metrics and qualitative fits. Part of this performance loss was due to the lack of actual patient body weights, but with all elderly patients, age-related alterations to clearance, cardiac output, and tissue contributions may also be involved.

Performance error versus sampled time point (Figure 5.3) was also investigated for the UPCI patients to determine if model predictions were biased towards individual portions of the sampling schedule. Similar analysis was not performed on the MSKCC data sets as the number of samples per patient and the time of samples were not equivalent for individual patients. The tissue-intensive model predicted mean errors per point which over-predicted the observed concentrations following the end of the infusion, but otherwise demonstrated unbiased error across the sample set. As mentioned previously, the Bradshaw-Pierce model under-predicted concentrations during the infusion with a trend towards over-predicting concentrations as $t \rightarrow 24$. Finally, the Bruno model displayed accurate predictions at time points during and immediately preceding the end of the infusion with predictive accuracy decreasing at later time points. In addition, the percent error was seen to increase at the later time points, reaching 30 and 44% at 16 and 24 hours, respectively. This poor performance

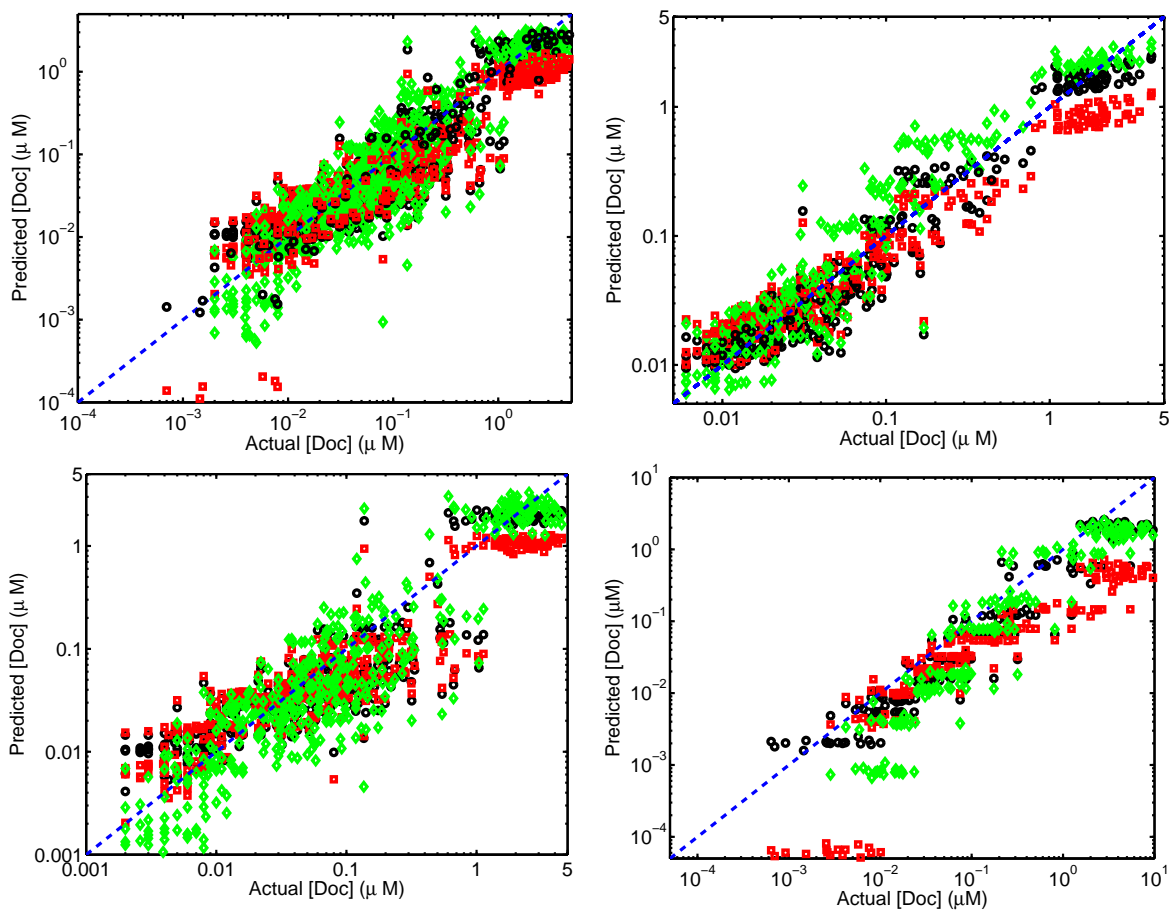


Figure 5.2: Actual versus model predicted human plasma Doc concentrations (tissue-intensive PBPK model - circles; Bradshaw-Pierce PBPK model - squares; Bruno population PK model - diamonds) for all patients (top left), UPCI protocol 01-150 (top right), MSKCC study (bottom left), and the MSKCC study comprised only of elderly patients (bottom right).

was not unexpected as the Bruno model also displayed the worst overall predictions of the UPCI patient group.

5.2.2 Unbound Doc

As mentioned previously, both evaluated PBPK models did not incorporate any patient specific metrics for predicting Doc plasma concentrations. Inaccuracies in the above model predictions were partly due to measurement and processing noise, but the majority of variations between patients can only be captured by introducing additional parameters consistent with inter-individual variability (*i.e.*, BSA and body weight are significant but only describe a portion of the overall variability). An important metric in predicting the efficacy and toxicity of Doc is the unbound fraction present in plasma, which has been demonstrated to be correlated with patient AAG levels [155]. Both PBPK models specified a uniform unbound fraction value, however, estimating individual patient free fractions would improve individual patient predictions.

Unbound fraction of Doc was estimated for each patient with respect to both PBPK models by minimizing the sum squared error between observed and model predicted Doc plasma concentrations. For the Bradshaw-Pierce model, lower weights were used for the concentration time points obtained during the infusion as the model under predicted those values and uniform weighting for all time points resulted in non-physiological unbound fraction predictions during the optimization. Estimating free fraction reduced the overall error predicted by both PBPK models, with updated model performance shown in Tables 5.6-5.7. Model performance metrics for individual patients from all three studies are shown in Figures 5.4-5.7. These figures illustrate that there was general improvement in the model performance metrics when unbound Doc was included as an estimated parameter for the tissue-intensive PBPK model. The same did not hold true for the Bradshaw-Pierce PBPK model, however, as the model already displayed a tendency to under predict peak Doc plasma concentrations, including additional degrees of freedom within this model was not expected to improve its performance. These figures also reveal that there were some patients that were not fit well by any of the three Doc PK models discussed in the previous section, nor

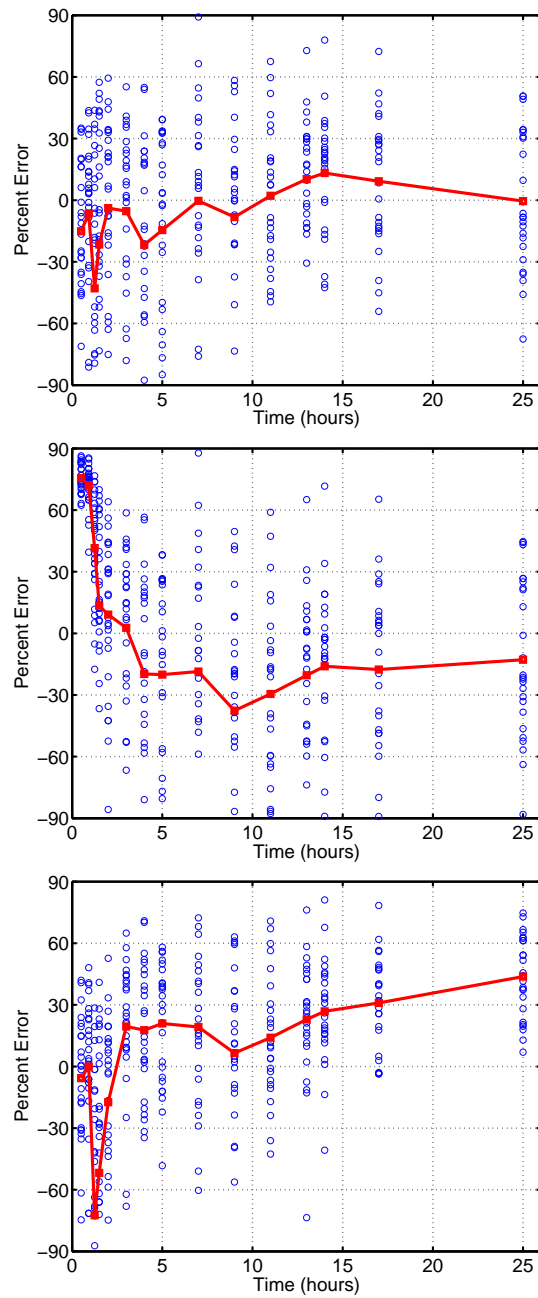


Figure 5.3: Individual patient performance error at sampled time points (circles) and median performance error for a sampled time point (squares) versus time for the three investigated models (tissue-intensive PBPK model, left; Bradshaw-Pierce PBPK model, middle; Bruno population PK model, right) for all 25 patients from UPCI protocol 01-150.

were they fit by either of the PBPK models when unbound Doc fraction was included as an additional parameter (*i.e.*, Patient 20 from the UPCI study, Patients 4 and 47 from the MSKCC study).

The median predicted unbound Doc percentages were 3.7% (0.5-8.9%) and 1.8% (0.5-4.3%) for the tissue-intensive PBPK and Bradshaw-Pierce PBPK models, respectively. However, estimating free fraction based on plasma data is not ideal as it would require substantial sampling and sample processing. Furthermore, the predictions from these estimates may not be valid. Estimated unbound fractions were compared against those obtained by two other groups from the literature [8, 109]. The values estimated for the PBPK models are plotted in Figure 5.8 against individual patient AAG levels, along with the linear correlation estimated by Baker *et al.* relating unbound percentage of Doc to AAG concentrations. Histograms reflecting the unbound fraction distributions are shown in Figure 5.9. Fits for both PBPK models, while displaying the same trend determined by Baker *et al.* (*i.e.*, increasing unbound fraction with decreasing AAG) displayed a lower slope. Accuracy of the linear fit was also worse, and the estimated unbound fractions versus AAG may be better represented using an inverse relationship (*e.g.*, unbound Doc = $\frac{p}{\text{AAG}}$). Also, for patients with $\text{AAG} > 1.5 \frac{\text{g}}{\text{L}}$, unbound percentage was lower for both PBPK models (tissue-intensive and [5]), with median values of 2.9% (1.4-5.3%) and 1.6% (0.7-2.5%) versus 3.9% (0.5-8.9%) and 1.9% (0.5-4.3%) for patients with $\text{AAG} < 1.5 \frac{\text{g}}{\text{L}}$.

5.2.3 Simulated Doc Concentration Profiles in Tumors

The inclusion of a tumor compartment in this tissue-intensive PBPK model may have clinical applicability in predicting Doc concentrations in tumor tissues. As no data were available regarding Doc concentration in human tumors, simulations were performed to determine expected tumor Doc concentration versus time profiles under a variety of conditions, including different dosing levels, different starting tumor volumes, different dosing schedules, and variations in patient body weight. Initial simulations focused on the case study of a 100-g tumor subjected to a 1-hour infusion of Doc at 30-90 $\frac{\text{mg}}{\text{m}^2}$. All patient BSA were assumed to be 1.75 m^2 . The resulting profiles are shown in Figure 5.10 (left), with calculated C_{max} and

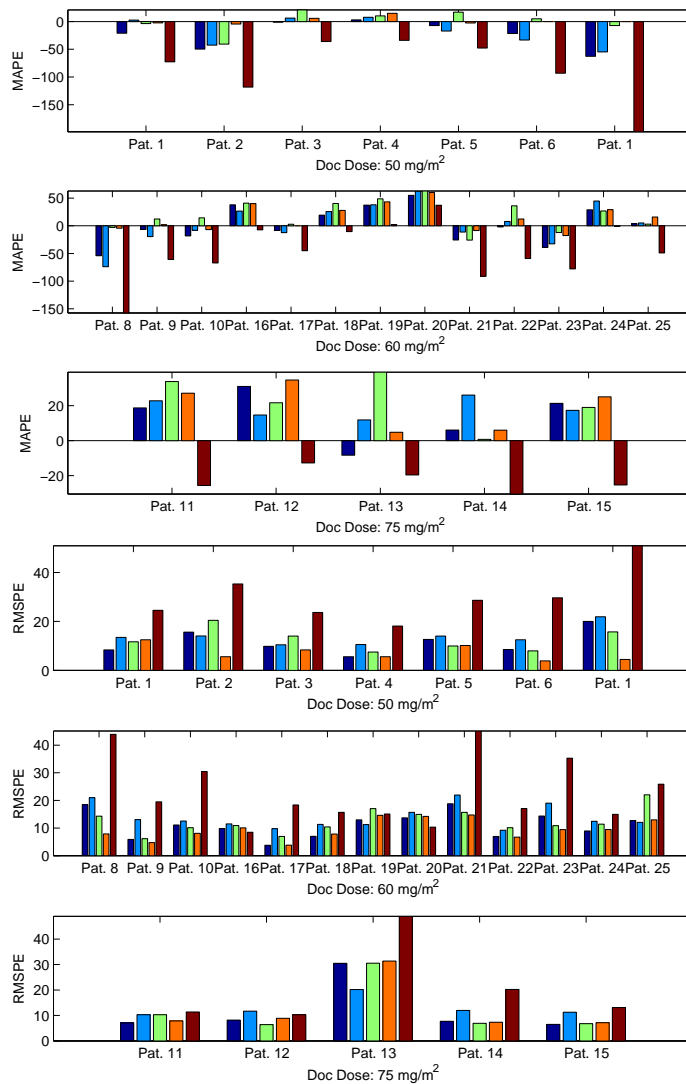


Figure 5.4: Model predicted performance metrics (MAPE and RMSPE) for all 25 patients from UPCI protocol 01-150. Each patient has 5 associated bars: (1) tissue-intensive PBPK model; (2) Bradshaw-Pierce PBPK model [5]; (3) Bruno population PK model [2]; (4) tissue-intensive PBPK model estimating unbound Doc fraction; and (5) Bradshaw-Pierce PBPK model estimating unbound Doc fraction.

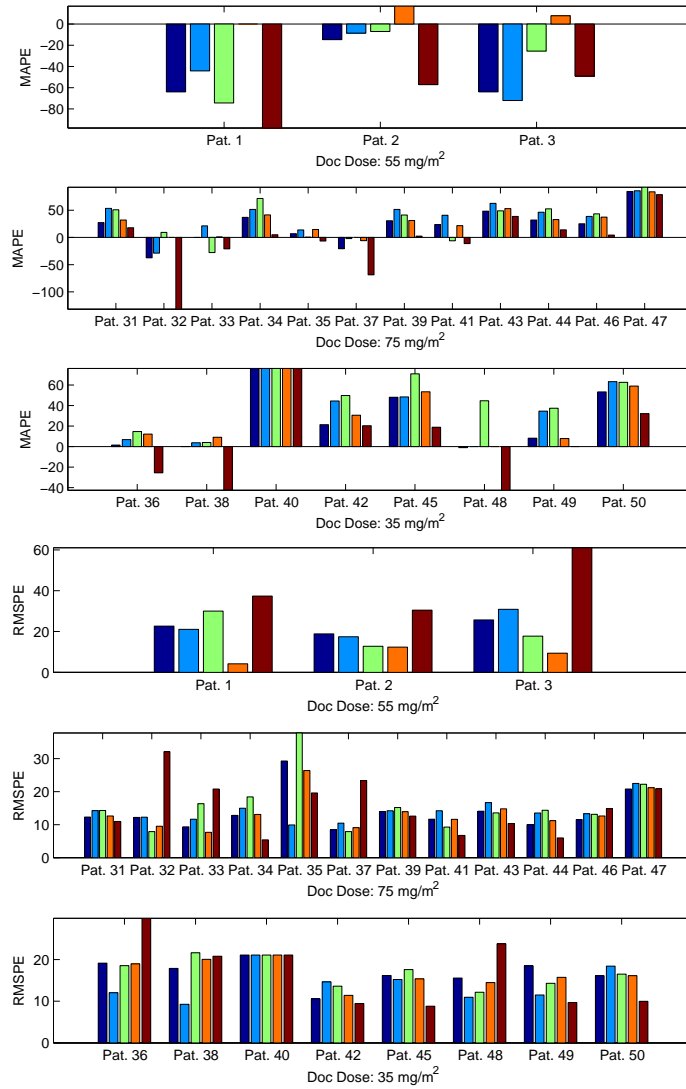


Figure 5.5: Model predicted performance metrics (MAPE and RMSPE) for patients from the MSKCC clinical trial [6] dosed at either 55, 75, or 35 $\frac{\text{mg}}{\text{m}^2}$. Each patient has 5 associated bars: (1) tissue-intensive PBPK model; (2) Bradshaw-Pierce PBPK model [5]; (3) Bruno population PK model [2]; (4) tissue-intensive PBPK model estimating unbound Doc fraction; and (5) Bradshaw-Pierce PBPK model estimating unbound Doc fraction.

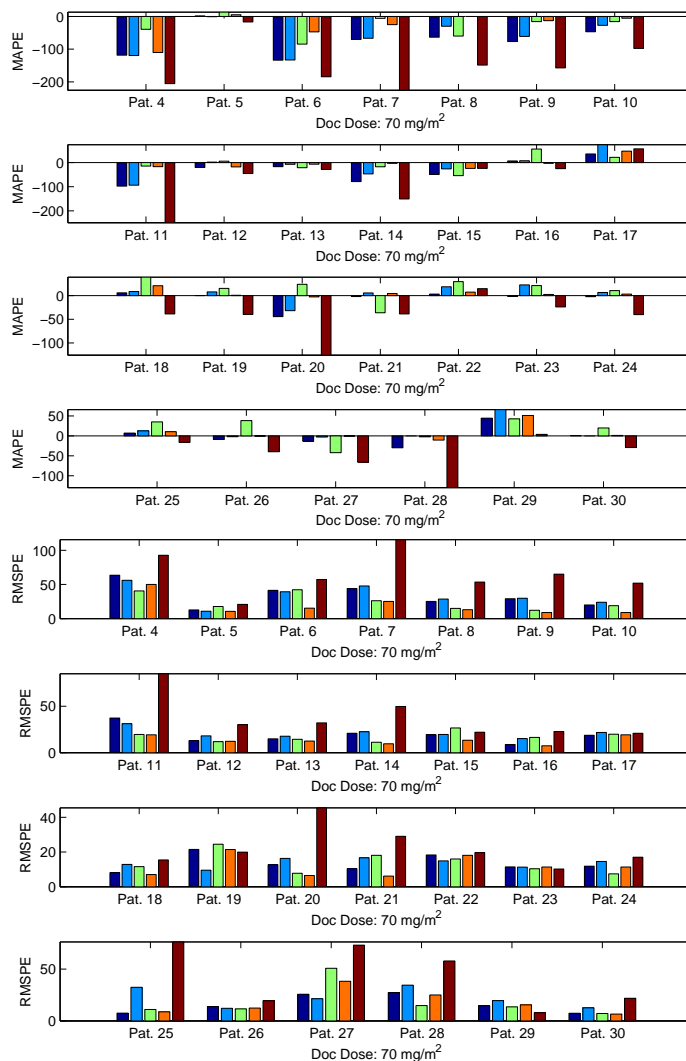


Figure 5.6: Model predicted performance metrics (MAPE and RMSPE) for patients from the MSKCC clinical trial [6] dosed at $70 \frac{\text{mg}}{\text{m}^2}$. Each patient has 5 associated bars: (1) tissue-intensive PBPK model; (2) Bradshaw-Pierce PBPK model [5]; (3) Bruno population PK model [2]; (4) tissue-intensive PBPK model estimating unbound Doc fraction; and (5) Bradshaw-Pierce PBPK model estimating unbound Doc fraction.

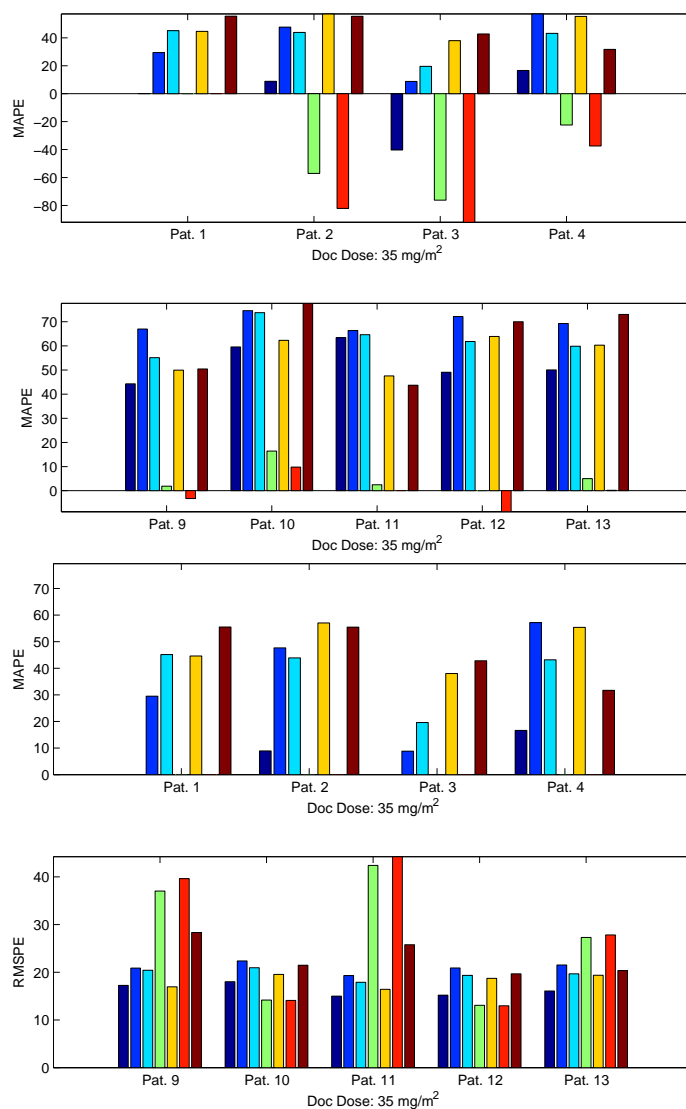


Figure 5.7: Model predicted performance metrics (MAPE and RMSPE) for patients from the elderly MSKCC clinical trial [7] dosed at $35 \frac{\text{mg}}{\text{m}^2}$. Each patient has 7 associated bars: (1) tissue-intensive PBPK model; (2) Bradshaw-Pierce PBPK model [5]; (3) Bruno population PK model [2]; (4) tissue-intensive PBPK model estimating unbound Doc fraction; (5) Bradshaw-Pierce PBPK model estimating unbound Doc fraction; (6) tissue-intensive PBPK model estimating unbound Doc fraction and liver metabolism; and (7) Bradshaw-Pierce PBPK model estimating unbound Doc fraction and liver metabolism.

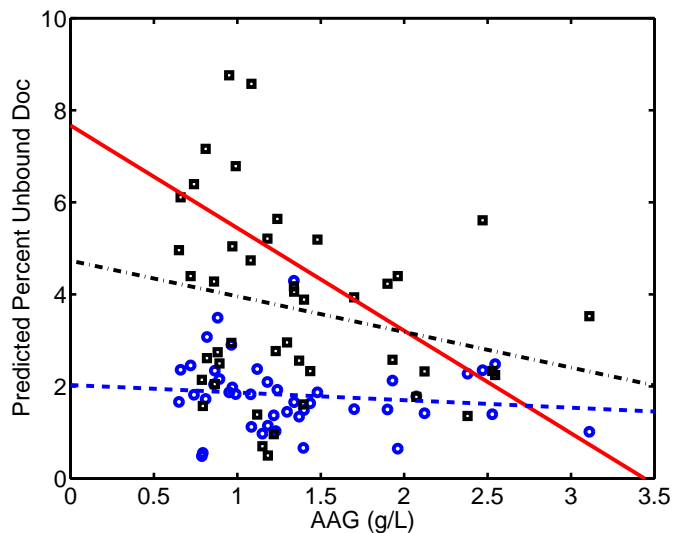


Figure 5.8: Tissue-intensive (square) and Bradshaw-Pierce (circles) PBPK model estimates for unbound fraction versus actual patient AAG concentrations. Linear regressions for the tissue-intensive (dash-dot) and Bradshaw-Pierce (dashed) PBPK models are shown plotted against the linear correlation identified by Baker *et al.* (solid) [8].

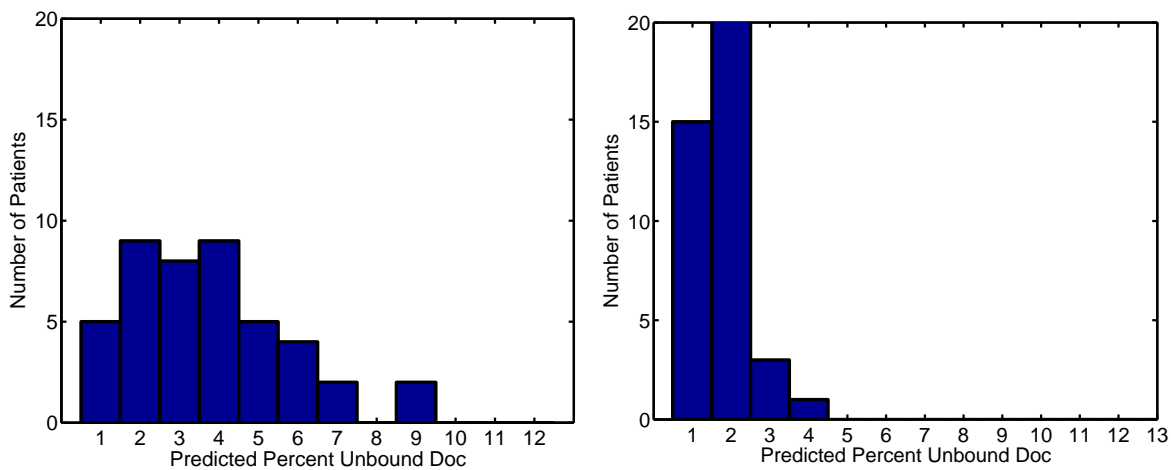


Figure 5.9: Estimated unbound fraction histograms ($n = 48$) for the tissue-intensive PBPK (left) and Bradshaw-Pierce PBPK (right) models.

Table 5.6: Doc plasma AUC and clearance mean (standard deviation) values from study data and model predictions obtained from estimating the unbound Doc fraction on a per patient basis. ^a were results obtained by including both unbound Doc fraction and liver metabolism as model parameters.

Clinical Trial	Doc Dose	Actual			Florian <i>et al.</i>			Bradshaw <i>et al.</i> [5]		
		AUC ₀₋₂₄ ($\mu\text{M hr}$)	CL ($\frac{\text{L}}{\text{hr}}$)	AUC ₀₋₂₄ ($\mu\text{M hr}$)	CL ($\frac{\text{L}}{\text{hr}}$)	AUC ₀₋₂₄ ($\mu\text{M hr}$)	CL ($\frac{\text{L}}{\text{hr}}$)	AUC ₀₋₂₄ ($\mu\text{M hr}$)	CL ($\frac{\text{L}}{\text{hr}}$)	
MSKCC Elderly [7] (n=9)	35 $\frac{\text{mg}}{\text{m}^2}$	4.14 (1.13)	18.3 (7.9)	3.38 (0.39)	23.9 (2.1)	1.29 (0.24)	64.2 (11.0)			
MSKCC Elderly ^a [7] (n=20)	35 $\frac{\text{mg}}{\text{m}^2}$	4.14 (1.13)	18.3 (7.9)	3.85 (0.51)	20.4 (2.5)	1.64 (0.37)	51.1 (11.4)			
MSKCC [6] (n=8)	35 $\frac{\text{mg}}{\text{m}^2}$	2.11 (1.20)	35.1 (11.3)	1.51 (0.63)	45.6 (12.4)	1.43 (0.62)	49.2 (16.0)			
UPCI [179] (n=7)	50 $\frac{\text{mg}}{\text{m}^2}$	1.62 (0.24)	71.9 (11.6)	1.63 (0.21)	70.9 (8.9)	1.26 (0.14)	92.6 (18.0)			
MSKCC [6] (n=3)	55 $\frac{\text{mg}}{\text{m}^2}$	1.95 (0.68)	64.3 (24.8)	2.43 (0.89)	56.2 (34.8)	2.40 (0.89)	57.6 (29.5)			
UPCI [179] (n=13)	60 $\frac{\text{mg}}{\text{m}^2}$	2.37 (0.60)	64.9 (18.6)	2.27 (0.29)	69.8 (12.9)	1.50 (0.16)	97.2 (14.7)			
MSKCC [6] (n=27)	70 $\frac{\text{mg}}{\text{m}^2}$	3.62 (2.19)	54.3 (17.4)	2.89 (0.56)	60.6 (14.7)	3.44 (1.05)	55.1 (24.8)			
UPCI [179] (n=5)	75 $\frac{\text{mg}}{\text{m}^2}$	3.18 (0.98)	56.9 (21.3)	2.90 (0.29)	58.2 (11.3)	2.08 (0.19)	81.5 (15.2)			
MSKCC [6] (n=12)	75 $\frac{\text{mg}}{\text{m}^2}$	3.57 (1.22)	59.7 (21.7)	3.36 (0.37)	58.0 (12.7)	3.56 (0.74)	56.7 (18.4)			

Table 5.7: Model performance mean (standard deviation) values for three Doc studies across multiple Doc dosing levels. ^a were results obtained by including both unbound Doc fraction and liver metabolism as model parameters.

Clinical Trial	Doc Dose	Florian <i>et al.</i>		Bradshaw <i>et al.</i> [5]	
		MPE	RMSPE	MPE	RMSPE
All	35-75 $\frac{\text{mg}}{\text{m}^2}$ (n=84)	7.8 (29.0)	15.1 (11.6)	-37.4 (71.2)	28.0 (20.9)
UPCI [179]	50-70 $\frac{\text{mg}}{\text{m}^2}$ (n=25)	12.1 (19.2)	9.5 (5.6)	-52.1 (51.7)	24.6 (12.6)
	50 $\frac{\text{mg}}{\text{m}^2}$ (n=7)	1.6 (6.7)	7.2 (3.2)	-85.8 (58.6)	30.1 (10.6)
	60 $\frac{\text{mg}}{\text{m}^2}$ (n=13)	14.9 (23.6)	9.5 (3.6)	-45.1 (50.3)	23.1 (12.1)
	75 $\frac{\text{mg}}{\text{m}^2}$ (n=5)	19.5 (13.4)	12.4 (10.6)	-22.8 (6.8)	20.8 (16.2)
MSKCC[6]	55-75 $\frac{\text{mg}}{\text{m}^2}$ (n=50)	9.6 (31.2)	14.7 (8.0)	-46.3 (74.7)	31.6 (25.0)
	55 $\frac{\text{mg}}{\text{m}^2}$ (n=3)	8.2 (8.4)	8.6 (4.1)	-68.0 (26.2)	43.0 (16.0)
	70 $\frac{\text{mg}}{\text{m}^2}$ (n=27)	-4.9 (28.7)	15.3 (10.0)	-76.7 (79.3)	42.0 (28.3)
	75 $\frac{\text{mg}}{\text{m}^2}$ (n=12)	28.5 (25.1)	13.6 (5.2)	-6.6 (52.7)	15.3 (8.2)
	35 $\frac{\text{mg}}{\text{m}^2}$ (n=8)	31.0 (28.4)	16.6 (3.1)	4.6 (40.9)	16.7 (8.2)
MSKCC Elderly [7]	35 $\frac{\text{mg}}{\text{m}^2}$ (n=9)	-14.4 (31.6)	33.0 (21.1)	53.2 (8.8)	18.0 (1.2)
All ^a	35-75 $\frac{\text{mg}}{\text{m}^2}$ (n=84)	6.8 (30.6)	15.0 (11.1)	50.1 (22.9)	16.3 (4.3)
MSKCC Elderly ^a [7]	35 $\frac{\text{mg}}{\text{m}^2}$ (n=9)	27.9 (34.3)	17.7 (7.2)	54.7 (22.3)	19.5 (2.0)

AUC_{0-21} (within this section the subscript with AUC refers to days and not the traditional units of hours) from the simulations shown in Table 5.8. Both C_{max} and AUC_{0-21} increased linearly with increasing dose level. This result was expected as the underlying PBPK model is linear, so that alterations to the dosing level for a specified tumor volume and body weight should be additive.

The next simulation (Figure 5.10, right) evaluated the effects of body weight on Doc tumor exposure. C_{max} and AUC_{0-21} increased nonlinearly with increasing body weight. It should be cautioned that these results may not actually reflect realized increases in tumor deposition as BSA was kept constant. Furthermore, it should be noted that BSA was only included within the model for adjusting the total administered dose, and the linearity of varying dose level has already been validated with the first set of tumor simulations (Figure 5.10, left). Hence, it is possible to predict C_{max} and AUC_{0-21} for each of the simulated body weights at any desired BSA (*i.e.*, for a BSA of 2.00 m² and 90 kg body weight, $C_{max} = (\frac{2.00}{1.75}) 0.452 = 0.516$).

Changes in tumor concentration as a function of tumor volume (with corresponding alterations to the tumor blood flow rate) are shown in Figure 5.11 (left). There was a tumor-size dependent increase in C_{max} , with the smallest simulated tumor having the highest C_{max} value. Despite this, the predicted AUC_{0-21} was relatively constant across all four tumor volumes and is indeed equivalent when comparing $AUC_{0-\infty}$. Finally, tumor concentration predictions over 21 days with administration of Doc either every three weeks or every week are shown in Figure 5.11 (right). There was dose-to-dose accumulation of Doc within the tumor with “weekly” administered Doc, resulting in a C_{max} for the 30 $\frac{mg}{m^2}$ “weekly” Doc simulation that was greater than one-third of the C_{max} from 90 $\frac{mg}{m^2}$ Doc q3w. While dose-to-dose accumulation of Doc in human plasma has not been observed during “weekly” Doc treatments (which is consistent with our model simulations), this model predicts that dose-to-dose accumulation may occur within the tumor.

Table 5.8: Calculated C_{max} and AUC for simulated tumors. AUC for all tumor profiles was calculated over a period of 21 days due to the extended retention times exhibited by the tumor tissue.

	Doc Dose ($\frac{\text{mg}}{\text{m}^2}$)	30	54	72	90
70 kg body weight, 100 g tumor	C_{max} (μM)	0.233	0.419	0.559	0.700
	AUC ₀₋₂₁ (μM day)	0.678	1.220	1.627	2.034
	body weight (kg)	50	70	90	110
72 $\frac{\text{mg}}{\text{m}^2}$, 100 g tumor	C_{max} (μM)	0.743	0.559	0.452	0.382
	AUC ₀₋₂₁ (μM day)	2.143	1.627	1.325	1.124
	Tumor weight (g)	5	20	100	500
72 $\frac{\text{mg}}{\text{m}^2}$, 70 kg body weight	C_{max} (μM)	0.880	0.788	0.559	0.274
	AUC ₀₋₂₁ (μM day)	1.628	1.628	1.627	1.601
	Doc Dose ($\frac{\text{mg}}{\text{m}^2}$)	90 q3w	72 q3w	30 “weekly”	42 “weekly”
70 kg body weight, 100 g tumor	C_{max} (μM)	0.700	0.559	0.252	0.352
	AUC ₀₋₂₁ (μM day)	2.034	1.220	1.977	2.767

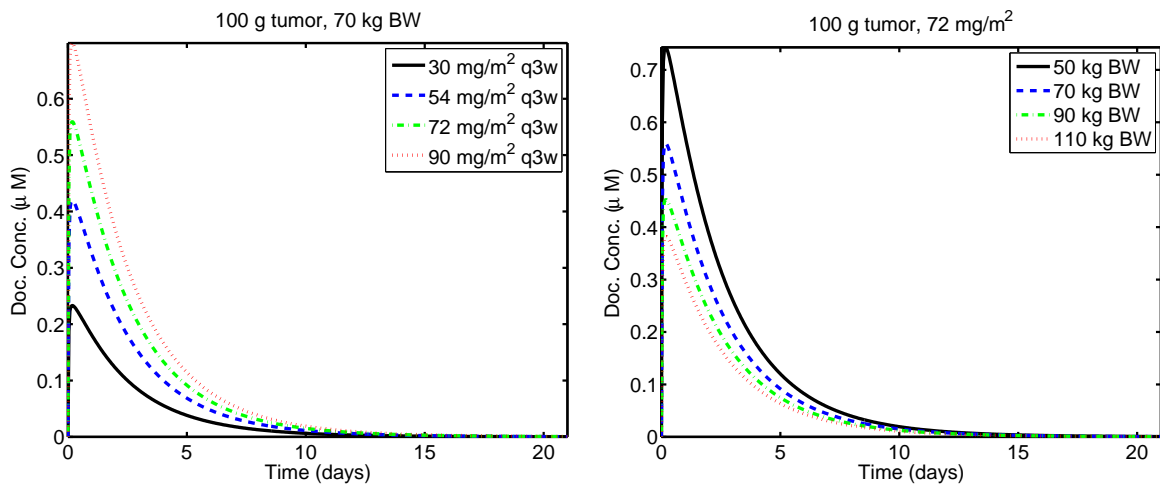


Figure 5.10: Simulated Doc tumor concentration versus time plots using the tissue intensive Doc PBPK model for varying dose levels (left) and body weight (right). Left: Simulated tumor concentrations assuming a 100 g tumor in 70 kg human treated with 30 (solid), 54 (dashed), 72 (dash-dot), or 90 (dotted) $\frac{\text{mg}}{\text{m}^2}$ Doc as a 1-hour infusion. Right: Simulated Doc tumor concentrations assuming a 100 g tumor in 50 (solid), 70 (dashed), 90 (dash-dot), or 110 (dotted) kg human treated with 72 $\frac{\text{mg}}{\text{m}^2}$ Doc as a 1-hour infusion.

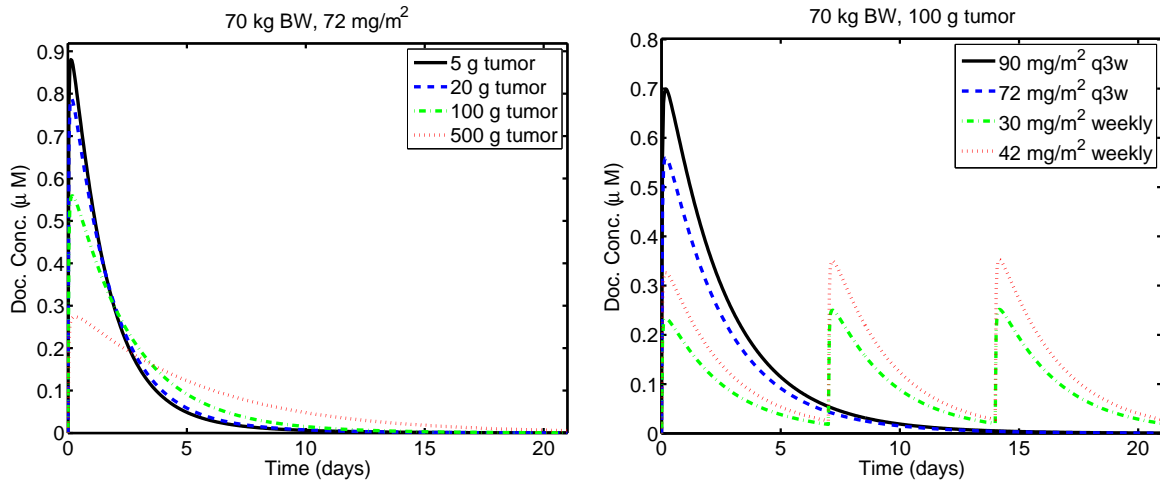


Figure 5.11: Simulated Doc tumor concentration versus time plots using the tissue intensive Doc PBPK model for varying tumor volume (left) and dosing schedules (right). Left: Simulated tumor concentrations assuming a 5 (solid), 20 (dashed), 100 (dash-dot), or 500 (dotted) g tumor in 70 kg human treated with $72 \frac{\text{mg}}{\text{m}^2}$ Doc as a 1-hour infusion. Right: Simulated tumor concentrations assuming a 100 g tumor in a 70 kg human treated with either 72 (solid) or 90 (dashed) $\frac{\text{mg}}{\text{m}^2}$ Doc as a 1-hour infusion every three weeks or weekly administration of 30 (dash-dot) or 42 (dotted) $\frac{\text{mg}}{\text{m}^2}$ Doc as a 1-hour infusion.

5.3 DISCUSSION AND SUMMARY

Overall, the tissue-intensive PBPK model was capable of describing Doc plasma distributions observed following IV infusions of 35, 50, 55, 60, 70, and 75 $\frac{\text{mg}}{\text{m}^2}$ Doc. Performance of this tissue-intensive PBPK model was similar to that observed from the population model of Bruno despite lacking patient-specific measures within the model structure. Furthermore, both the tissue-intensive PBPK and population PK models were more accurate in predicting observed AUC across a range of Doc doses compared to a previously developed PBPK model for Doc. During-infusion Doc concentrations were poorly predicted by all three PK models, though the predictions for the tissue-intensive PBPK and population PK model were distributed along the line of unity. A portion of this error likely resulted from the tissue-intensive PBPK model being developed from data generated with a different administration schedule (bolus versus infusion), such that no information about infusion dynamics was included within the mouse model. Polysorbate 80 may also influence Doc plasma concentration, and hence, distribution dynamics, during the infusion by altering the unbound fraction of Doc.

Prediction results for the tissue-intensive PBPK model were when the unbound fraction of Doc was estimated on an individual patient basis. While this is not practical in a clinical setting, it did establish a theoretical population distribution of Doc unbound fractions. This distribution qualitatively agrees with the results from Minami *et al.* [109] and Baker *et al.* [8], who reported median (range) unbound fractions of Doc of 4.0 (1.2-22.6) and 4.6 (1.2-8.6), respectively. Individual patient AAG values were plotted against estimated unbound fractions as previous studies have demonstrated a correlation between the two measures. However, while Baker *et al.* observed a linear relationship between unbound fraction and AAG, estimates of unbound fraction for the tissue-intensive PBPK model were more representative of a non-linear relationship with $\text{AAG} < 1.5 \frac{\text{g}}{\text{L}}$ predicting patient Doc unbound fractions of 3.9% (0.5-8.9%) and $\text{AAG} > 1.5 \frac{\text{g}}{\text{L}}$ predicting patient Doc unbound fractions of 2.9% (1.4-5.3%). Actual Doc unbound fraction data from the modeled patients are now being pursued in order to validate predicted unbound Doc fractions. Alternatively, additional patients with both Doc plasma concentration and unbound fraction data can

be used for evaluating whether unbound fraction is indeed a measure that improves the predictive performance of both PBPK models.

Attempts to fit the MSKCC elderly patient data set with the existing PBPK models were largely unsuccessful, with all three models under-predicting observed Doc concentrations along the entire sampled time course. By altering the tissue-intensive PBPK model to be more representative of an elderly population (*e.g.*, decreased cardiac output, increased percent body fat) improvements in the model performance were obtained. Estimates for patient unbound fraction and body weights were consistent with unbound fraction distributions from previous studies and a predominantly elderly female data set. Metabolic rates for this data set were also predicted to decrease, and should be explored further as an additional patient-specific metric, similar to hepatic function, that can be used for predicting Doc plasma PK in individual patients.

Using the tissue-intensive PBPK model, tumor Doc concentrations were also simulated for conditions of changing dosing level, body weight, tumor mass, and dosing schedule. The model predicts a linear relationship between C_{max} and AUC for different dose levels delivered over the same schedule. Patient body weight reduced the observed tumor concentration C_{max} , though this was likely a result of using a constant BSA regardless of patient body weight. Tumor-size-dependent C_{max} was predicted, though differences in AUC were insignificant at 21 days. This size-dependent effect on C_{max} resulted from the tumor volume-blood flow rate relationship used within the model, where the tumor volume increased disproportionately with tumor blood flow. The fact that the AUC was relatively constant reflects the fact that the amount of drug delivered to the tumor remained the same, but due to the increased tumor volume, a lower whole tumor concentration was observed. Furthermore, as blood flow and distribution within tumors is heterogeneous, this prediction is representative of delivering the same amount of drug in localized regions of the tumor. Macroscopically, this would result in a lower overall observed tumor concentration. Finally, a dose-to-dose accumulation of Doc was also observed for “weekly” administration versus delivery on a q3w regimen. However, whether tumor Doc AUC is a valid correlate of treatment efficacy remains to be validated.

While there is no guarantee that model predictions of tissues are accurate, additional studies are being pursued to validate the model-predicted Doc tumor concentrations using

a combination of radio-labeled Doc and positron emission topography (PET) in head and neck cancer patients. At least two time points are necessary, ideally occurring an hour after infusion (corresponding to radio-labeled Doc) and four or more hours following the initial sample (necessitating a biopsy). Given the predicted long retention of Doc within a tumor, these two points should be sufficient for updating the model to describe human tumor Doc concentrations more accurately if, indeed, discrepancies exist between the model predictions and sampled data. Alternatively, single biopsy samples from multiple head and neck patients may be sufficient for updating intra-tumor transition rates given the extended retention time of Doc observed from implanted human xenografts.

6.0 DOC NEUTROPHIL TOXICITY MODEL

The degree of inter-patient PD variability observed during chemotherapeutic treatment is extensive, ranging from tumor regression and elimination to the lack of any treatment response and/or life-threatening toxicity. The lack of a treatment response has been shown to correlate primarily with the PK of a patient (*i.e.*, high clearance values as indicative of lower response rates) and tumor characteristics (*i.e.*, resistance to the therapeutic, lower exposure due to decreased transport, etc.). On the opposite end of the spectrum is patient toxicity, primarily manifesting as neutropenia during q3w treatment with Doc. As treatment related toxicity requires more immediate attention, relationships capable of predicting patient toxicity prior to the initialization of treatment are highly desirable for both limiting danger to the patient and ensuring that stoppage of the treatment schedule can be avoided.

The extent of neutropenia observed during q3w Doc treatment primarily correlates with decreased drug clearance and the plasma AUC of unbound Doc. Alterations to clearance, in turn, may result from changes in patient AAG levels and the liver function of the patient. Completing the circle, and as alluded to within Chapter 5, Baker *et al.* have demonstrated that serum AAG and the unbound fraction of Doc are correlated, with increasing unbound fractions manifesting as serum AAG decreases [8]. Heuristic relationships between the likelihood of grade 3/4 neutropenia and AAG levels, C_{max} of unbound Doc, and hepatic function have been developed and serve as metrics for predicting probable patient toxicity following treatment [109]. However, such models are schedule dependent, may even be dosing level dependent, and provide only an “end point” representation of toxicity rather than its progression. Furthermore, the AUC measure, while scaling with dose level on a given schedule, is grossly inaccurate for different administration schedules. Schedules involving

the “weekly” administration of Doc ($35\text{-}40 \frac{\text{mg}}{\text{m}^2}$) have demonstrated a decreased incidence of neutropenia (2.5-23% versus upwards of 90% in q3w regimens) while overall patient efficacy has remained equivalent to q3w regimens [151, 155, 159, 171]. As the PK of Doc is linear, the 3-week inclusive AUC from this treatment is in the range of Doc treatments involving $100 \frac{\text{mg}}{\text{m}^2}$ q3w, invalidating the use of exposure-based relationships between the two delivery schedules [151]. Decreased clearance is still a predictive factor of hematological toxicity, as is an increase in AUC compared amongst patients treated on the same schedule, however there is no unifying explanation of patient toxicity across both Doc dosing schedules. Ideally, the development of a representative PD model for neutrophil progression may address each of these concerns.

A few PK/PD models have been developed in the literature for predicting the time course of neutropenia following treatment, with varying levels of complexity ranging from indirect response models [114, 115] to higher-order models representing the maturation of hematopoietic stem cells in addition to regulatory cytokines [66]. A recent semi-mechanistic model developed by Friberg *et al.* accounts for both the maturation time and overshoot above baseline neutrophil count observed following treatment [3]. Furthermore, this low-order (five equation) model has proven effective at describing the time course of neutrophils and leukocytes following administration of a number of therapeutics (paclitaxel, etoposide, irinotecan, epirubicin, 2'-deoxy-2'-methylidenecytidine, and perimetrexed) including Doc [3, 111, 112]. The study by Friberg *et al.* [3] investigated neutrophil progression in 601 patients administered either 75 or $100 \frac{\text{mg}}{\text{m}^2}$ Doc over a 1-hour infusion, with Doc plasma concentration versus time profiles generated using patient-specific metrics and the Bruno population PK model for Doc [2]. Both a linear and E_{max} drug effect formulation were evaluated, though no increase in predictive accuracy was observed from using the E_{max} model. The results from this study were later extrapolated to the co-administration of Doc and epirubicin at 75 and $70 \frac{\text{mg}}{\text{m}^2}$, respectively, however no validation of the model at lower dosing levels nor alternative Doc dosing schedules has been performed in the literature.

The model structure was extended to include various patient-specific covariates, revealing a strong correlation between AAG and the “slope” value in the drug effect relation (in addition to estimating a new parameter value 2-fold greater than their previous paper) with

sex, previous therapy, restricted performance status, and AAG levels having a minor effect on baseline neutrophil count [106]. This drug effect observation follows from experimental evidence where Doc clearance may decrease with increasing AAG, but this is accompanied by a concurrent decrease in the unbound fraction of Doc which induces the PD effect (*i.e.*, tumor response, or in this case, the elimination of progenitor cells in the bone marrow). These studies all focused on q3w Doc, but alternative schedules, such as “weekly” Doc are gaining interest due to the lower incidence of neutropenia with equivalent efficacy observed during treatment [151, 155, 159, 171, 172]. The extension of the Friberg *et al.* model to “weekly” Doc has not been performed, however.

This chapter takes the model developed by Friberg *et al.* and evaluates alternative PD effect terms (log-linear and Hill-relationship) and model structures for the prediction of neutrophil progression across multiple Doc dosing schedules. Additionally, the two drug effect relationships originally investigated by Friberg *et al.* were reevaluated to determine if they were applicable across multiple Doc dosing regimens and to determine if plasma Doc PK predictions from the human scaled tissue-intensive PBPK model returned similar parameter estimates to those obtained using the Bruno population PK model. Using both the original and updated neutrophil models, simulations for all patients were performed using multiple dosing levels ($28-100 \frac{\text{mg}}{\text{m}^2}$) and multiple Doc dosing schedules (q3w, “weekly”, every other week) commonly employed clinically to assess if the appropriate incidences of toxicity were represented. Patient parameterizations representative of average, high risk, and low risk were identified from the results, and these patients served as the basis for downstream Doc dose schedule development. Using a NMPC structure, an objective function was proposed for maximizing the total amount of drug delivered over a 12 week period, subject to objective function penalties due to neutropenia. Finally, the estimated Doc schedules were evaluated against those currently implemented clinically for toxicity and predicted accumulation of Doc within a tumor compartment.

6.1 MATERIALS AND METHODS

6.1.1 Patient Data

Neutrophil and leukocyte counts were obtained during the first treatment cycle of two Phase 1 studies performed at UPCI and MSKCC [6, 179] to monitor patient toxicity. While both Phase 1 studies involved the co-administration of therapeutics (Doc and imatinib for the UPCI study and Doc and 17-allylamino-17-demethoxygeldanamycin for the MSKCC study), the additional chemotherapeutic neither altered the observed Doc PK nor had overlapping toxicity with Doc during the treatment. As such, the PK data and collected neutrophil data were treated as resulting solely from treatment with Doc. Samples in the UPCI study were obtained on days 1, 8, 15, and 22. Of the 25 patients enrolled in the study, 21 patients had all four neutrophil counts recorded, corresponding to Doc doses of 50 ($n = 5$), 60 ($n = 11$), and 75 ($n = 3$) $\frac{\text{mg}}{\text{m}^2}$. For the MSKCC study, samples were obtained on days 1, 3, 8, 15, and 22. Of the 50 patients enrolled, 42 patients had 4 or more neutrophil counts recorded, corresponding to doses of 35 ($n = 5$, “weekly”), 55 ($n = 3$, q3w), 70 ($n = 17$, q3w) and 75 ($n = 10$, q3w) $\frac{\text{mg}}{\text{m}^2}$. In both studies, patients who displayed any type of Grade 4 or multiple incidents of Grade 3 toxicity had their Doc dose reduced for future treatments. None of the patients from these data sets had hematological evaluation after the first four weeks of treatment.

6.1.2 Model Development

As the primary toxicity associated with Doc is neutropenia, a low-order model of neutrophil response following administration of Doc was taken from the literature [3]; this model is shown schematically in Figure 6.1. This model has been validated previously for a number of chemotherapeutics [3, 111, 112, 182, 183], including Doc [3]; however, the Doc evaluation was primarily from patients dosed at 100 $\frac{\text{mg}}{\text{m}^2}$ q3w. The model consists of five differential

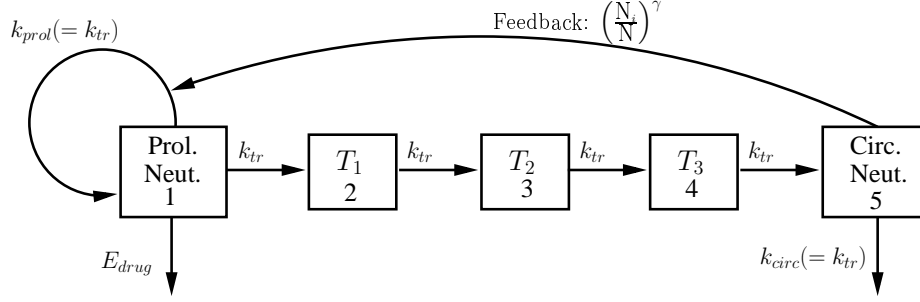


Figure 6.1: Neutrophil model structure for coupling human Doc plasma concentration to PD effect [3].

equations, as follows:

$$\frac{dP}{dt} = k_{tr}P(1 - E_{drug}) \left(\frac{N_i}{N}\right)^{\gamma_1} - k_{tr}P \quad (6.1)$$

$$\frac{dT_1}{dt} = k_{tr}P - k_{tr}T_1 \quad (6.2)$$

$$\frac{dT_2}{dt} = k_{tr}T_1 - k_{tr}T_2 \quad (6.3)$$

$$\frac{dT_3}{dt} = k_{tr}T_2 - k_{tr}T_3 \quad (6.4)$$

$$\frac{dN}{dt} = k_{tr}T_3 - k_{tr}N \quad (6.5)$$

Here, as seen in Figure 6.1, cell proliferation occurs in compartment 1 (counting from left to right), maturation occurs in the transit compartments (2-4), and circulating neutrophil count is represented by compartment 5. Feedback between circulating neutrophil count and the normal baseline neutrophil value ($N_i, \frac{10^9 \text{ cells}}{\text{L}}$), raised to the power, γ_1 , was included to permit an absolute neutrophil count (ANC) count following treatment to exceed the baseline neutrophil count. The parameter γ_1 governs the aggressiveness of the rebound observed following treatment, with larger values leading to both faster recovery and a greater overshoot over the baseline neutrophil value. Transfer rates between compartments, elimination from the circulating neutrophil compartment, and proliferation rate were all modeled using the same parameter, k_{tr} ($\frac{1}{\text{day}}$), to reduce the overall number of model parameters. This simplification was necessary due to the limited sampling frequency and total number of

collected data points (4 samples) from individual patients. Rates for some parameters, such as circulating neutrophil elimination rate, can be found in the literature, but previous results from Friberg *et al.* showed that inclusion of such literature parameters did not significantly increase the accuracy of the model [3]. Based on the model structure and transition rate parameter, an alternative parameter was defined, as follows:

$$\text{MTT} = \frac{n + 1}{k_{tr}} \quad (6.6)$$

Here, MTT is the mean transit time for a cell to reach the circulating neutrophil compartment after leaving the proliferating neutrophil compartment, and n is the number of transit compartments in the model.

The drug effect (E_{drug}) was limited to compartment 1; four different functions were investigated as possible PD terms: (i) linear; (ii) log-linear; (iii) Michaelis-Menten; and (iv) Hill-relationship:

$$E_{drug} = m[\text{Doc}] \quad (6.7)$$

$$E_{drug} = \alpha[\text{Doc}]^\beta \quad (6.8)$$

$$E_{drug} = \frac{E_{max}[\text{Doc}]}{EC_{50} + [\text{Doc}]} \quad (6.9)$$

$$E_{drug} = \frac{E_{max}[\text{Doc}]^{\gamma_2}}{EC_{50}^{\gamma_2} + [\text{Doc}]^{\gamma_2}} \quad (6.10)$$

Here, m , α , and E_{max} are estimated model parameters which scale PK concentration with units of $\frac{1}{\mu M}$, $\frac{1}{\mu M^\beta}$, and (dimensionless), respectively. β is the slope of the log-linear function, EC_{50} (μM) is the concentration at which half the drug effect is obtained, γ_2 , with value >1 describes the steepness of transition to E_{max} within the Hill relationship, and $[\text{Doc}]$ is the patient plasma concentration of Doc (μM). Michaelis-Menten and linear functions have previously been investigated by Friberg *et al.* for describing neutrophil progression following Doc administration. They concluded that the increase in model complexity resulting from the Michaelis-Menten kinetics was not justified by the small increase in accuracy. However, these modeling studies were performed on patients administered Doc on a q3w schedule, and alternative PD relationships may be necessary for describing Doc administration on alternative schedules.

Finally, other authors have demonstrated that inclusion of an effect site was necessary for predicting schedule dependent neutrophil profiles resulting from treatment [183]. Inclusion of such a compartment within the PD model given by Equations (6.1)-(6.5) is accomplished by appending the following additional equation:

$$\frac{dF_1}{dt} = -k_f F_1 + k_f [Doc] \quad (6.11)$$

and replacing all occurrences of $[Doc]$ within E_{drug} with F_1 . The parameter, k_f sets the speed of the response of the filtered plasma concentration of Doc ($\frac{1}{\text{day}}$). Inclusion of an effect-compartment formulation within the model dampens infusion duration-dependent effects in the model output. The filtered formulation may also be more indicative of drug concentration profiles observed within tissues where the drug effect is taking place.

6.1.3 PK/PD Drug Schedule Simulations

The clinically approved Doc regimen calls for drug administration via a 1-hour IV infusion every three weeks (q3w regimen), however, a repercussion of this regimen is the high incidence of Grade 3 and 4 neutropenia in treated patients [159]. In an effort to reduce this toxicity, other Doc dosing regimens have been investigated, most notably once a week for three weeks followed by a week off (“weekly” regimen), for six weeks with two weeks off, or every other week. Initial trial results have demonstrated equivalent efficacy between the q3w and “weekly” dosing regimens, with a significant reduction in Grade 3 or higher neutropenia in patients treated on the “weekly” Doc regimen [184]. Treatment on every other week Doc regimens, though limited, has also displayed a reduction in the primary toxicity compared to the q3w regimen. Efficacy from the every other week regimen, while similar to the q3w regimen, has not been validated as equivalent because the trail was under powered [158].

Neutrophil progression profile were simulated based on these literature results, the tissue-intensive human PBPK model developed in the previous section, and the PD model developed above. Individual patient PK profiles were used for providing the Doc plasma concentrations, while both patient-specific and population neutrophil parameters were evaluated. Three different dosing schedules (q3w, “weekly”, and every other week) were

simulated for each of the patients at dosing levels ranging from 70-100 $\frac{\text{mg}}{\text{m}^2}$, 28-40 $\frac{\text{mg}}{\text{m}^2}$, and 40-60 $\frac{\text{mg}}{\text{m}^2}$, for the three dosing studies, respectively.

6.1.4 PK/PD Drug Schedule Control Algorithm

Nonlinear model predictive control (NMPC) has been employed in a number of industrial processes [137] and drug dosing applications [58, 79, 185, 186, 187, 188, 189] due to its readily adaptable structure, which requires a process model, output measurements, and manipulations at regular intervals. The general form of the NMPC algorithm has three distinct parts: (i) an objective function; (ii) dynamic model equations; and (iii) constraints. A typical NMPC formulation would be as follows:

$$\min_{\Delta u(k:k+m-1|k)} \quad \|\Gamma_y [R(k+1 : k+p|k) - Y(k+1 : k+p|k)]\|_2^2 \\ + \|\Gamma_{\Delta u} \Delta u(k : k+m-1|k)\|_2^2 + \|\Gamma_u u(k+1 : k+p|k)\|_2^2 \quad (6.12)$$

$$\dot{x}_{PK} = f(x_{PK}, u) \quad (6.13)$$

$$\dot{x}_{PD} = f(x_{PK}, x_{PD}, u) \quad (6.14)$$

$$\dot{x}_{CN} = f(x_{CN}, x_{PK}, x_{PD}, u) \quad (6.15)$$

$$u_{min} \leq u(t) \leq u_{max} \quad (6.16)$$

$$x_{min} \leq x(t) \leq x_{max} \quad (6.17)$$

The objective function (Equation (6.12)) serves as the metric for deciding the ideal doses to implement over a predicted horizon in time. For the above two-norm squared objective function [138], the controller minimizes the sum of three terms. The first is an error term that calculates differences between predicted future output, $Y(k+1 : k+p|k)$, and a desired reference trajectory, $R(k+1 : k+p|k)$, over a horizon of length p . The index, k , denotes the present time. The second term is a noise-suppression term that penalizes magnitude changes in the input level, $\Delta u(k : k+m-1|k)$ on the move horizon, m ($m \leq p$). Besides reducing actuator wear, a Δu formulation of the NMPC algorithm allows for implicit integral action which ensures the controller will converge to the desired reference trajectory without offset. The third term penalizes for total manipulated variable use, $u(k+1 : k+p|k)$. This term is often omitted in traditional MPC formulations. However, it is a necessary inclusion if the

input functions solely in disturbance rejection or the total input administered is of concern (*i.e.*, monetary costs, toxicity).

The state equations, (6.13)-(6.15), corresponding to the PK model, PD model, and circulating neutrophil state, serve as the dynamic process model that explicitly predicts future system behavior based on m controller-calculated dosing alterations over the prediction horizon, p , where $m \leq p$. The constraints, (6.16) and (6.17), ensure that both the input (dosing level) and states (drug within tissues or plasma), respectively, do not exceed clinically-imposed bounds. In the case of the coupled neutrophil (PD) and Doc plasma (PK) models, input constraints were set at $0 \frac{\text{mg}}{\text{m}^2} \leq u(k+1 : k+p|k) \leq 100 \frac{\text{mg}}{\text{m}^2}$. These represent no delivery of the Doc for a given week and the highest single Doc dose administered clinically (via the q3w regimen) [151]. Patient toxicity is one of the main causes for treatment failure, necessitating dose reduction or treatment cessation, thereby motivating the inclusion of state constraints on patient circulating neutrophil count. While dose alteration criteria vary depending on the tumor type being treated and the clinician involved, common metrics for dose reduction include any occurrence of Grade 4 toxicity or week-to-week persistence of life-threatening Grade 3 toxicities. These can mathematically be posed as constraints as follows:

$$B_1 \leq x_{CN}(k+1 : k+p|k) \quad (6.18)$$

$$-M_2\phi_i + B_2 \leq x_{CN}(k+i|k) \quad (6.19)$$

$$x_{CN}(k+i|k) \leq M_2(1 - \phi_i) + B_2 \quad (6.20)$$

$$\phi_i + \phi_{i+1} \leq 1 \quad (6.21)$$

where ϕ is an integer-valued binary vectors ($\{\phi_i\} \in \{0, 1\}$, $\{i \in \mathcal{I} | 1 \leq i \leq p\}$) of length p , M_2 is a large number termed a big-M constraint, and B_1 and B_2 are state bounds. For the conditions described above, these would have values of $B_1 = 0.5 \times 10^9 \frac{\text{cells}}{\text{L}}$ (Grade 4) and $B_2 = 1.0 \times 10^9 \frac{\text{cells}}{\text{L}}$ (Grade 3), respectively. Constraining neutrophil counts at the maximum acceptable limit of neutropenia may be ill-advised, and a less aggressive set of constraints, maintaining the patient above Grade 3 toxicity and avoiding week-to-week persistence midway between Grade 2 and 3 toxicities, may be employed ($B_1 = 1.0 \times 10^9 \frac{\text{cells}}{\text{L}}$; $B_2 = 1.5 \times 10^9 \frac{\text{cells}}{\text{L}}$).

Incorporating state constraints may lead to infeasible solutions in an NMPC formulation, especially if the initial input effect on the system is rapid compared to the subsequent recovery. Instead, state constraints are placed within the objective function (*i.e.*, relaxed or softened) to facilitate solutions and appended with a suitably large weighting penalty [40, 135]. These penalties are typically at least 10^3 more than the contribution from the sum of the other objective function terms to ensure that constraints on the circulating neutrophil count are enforced. The relaxed state constraints were posed as follows:

$$-M_1\kappa + B_1 \leq x_{CN}(k+1 : k+p|k) \quad (6.22)$$

$$x_{CN}(k+1 : k+p|k) \leq M_1(1 - \kappa) + B_1 \quad (6.23)$$

$$-M_2\phi_i + B_2 \leq x_{CN}(k+i|k) \quad (6.24)$$

$$x_{CN}(k+i|k) \leq M_2(1 - \phi_i) + B_2 \quad (6.25)$$

$$-M_3(1 - \eta_i) + 2 \leq \phi_i + \phi_{i+1} \quad (6.26)$$

$$\phi_i + \phi_{i+1} \leq M_3\eta_i + 1 \quad (6.27)$$

where κ and ϕ are integer-valued binary vectors ($\{\kappa_i, \phi_i\} \in \{0, 1\}$, $\{i \in \mathcal{I} | 1 \leq i \leq p\}$) of length p , η is a binary vector ($\{\eta_j\} \in \{0, 1\}$, $\{j \in \mathcal{I} | 1 \leq j \leq p-1\}$) of length $p-1$, and M_1 , M_2 and M_3 are large numbers termed big-M constraints. A reference trajectory formulation, like that in Chapter 2, may not be appropriate as a specific neutrophil trajectory does not ensure increased Doc delivery and “driving” the neutrophil count of a patient to a specified value is not a clinically relevant objective. Also, explicit incorporation of the two-norm of the administered dose was included within the objective function (with a negative weighting term) to ensure maximum delivery of Doc during the simulation and to preferentially favor single, large dose administration over multiple small doses. This is consistent with the viewpoint of the clinician regarding Doc treatment, which is to administer as much drug to the patient as often as possible subject to patient toxicity [190, 191]. Likewise, the magnitude change in dosing level is less of a concern to clinicians than is the absolute amount of drug delivered (dose schedule predictions requiring separate doses at each week, however, are undesirable due to schedule complexity). The modified form of Equation (6.12),

the objective function employed in the rest of the chapter, is represented as follows:

$$\min_{\Delta u(k:k+m-1|k)} -\|\Gamma_u u(k+1:k+p|k)\|_2^2 + \Gamma_\eta \eta + \Gamma_\kappa \kappa \quad (6.28)$$

Here, $\Gamma_y = 0$, $\Gamma_{\Delta u} = 0$, and $\Gamma_u = 0.1$. A two-norm formulation for total administered drug is ideal as it preferentially favors large single doses rather than low doses spread over the entire treatment regimen. Γ_η and Γ_σ are chosen sufficiently large (*i.e.*, $> 10^6$ and $> 10^7$, respectively), to ensure that the individual contribution from these terms is significantly greater than the maximum contribution from the drug administration term. Algorithm predictions were limited to a 12-week treatment horizon with Doc administration possible once a week at the beginning of each week. Simulations were performed in MATLAB (©2007, The MathWorks, Natick, MA) and optimizations called the *fmincon* function.

6.2 RESULTS

6.2.1 Neutrophil Model Evaluation

Initially, the model structure from Friberg *et al.* was left unchanged. Using the original parameters, neutrophil profiles for the average UPCI patient were simulated and compared against the actual counts obtained during cycle 1 of treatment (Figure 6.2, dashed). Initial predictions did not agree well with the patient data, displaying significant overshoot of the observed neutrophil count at the end of cycle 1 and necessitating a reevaluation of the model parameters. Because only four points per patient were available, it was assumed that the collected neutrophil counts would repeat over the following treatment cycles; this assumption underpredicts the cycle-to-cycle effects of Doc administration. Model parameters were estimated for each patient by minimizing the weighted sum squared error using the *fmincon* function in MATLAB (©2007, The MathWorks, Natick, MA). The resulting parameters were averaged to obtain a parameter set for the entire population, and these are summarized in Table 6.1 along with the original parameters from the study by Friberg *et al.*. Neutrophil profiles using the updated parameter set for the average UPCI patient at each dosing level are shown in Figure 6.2 (solid).

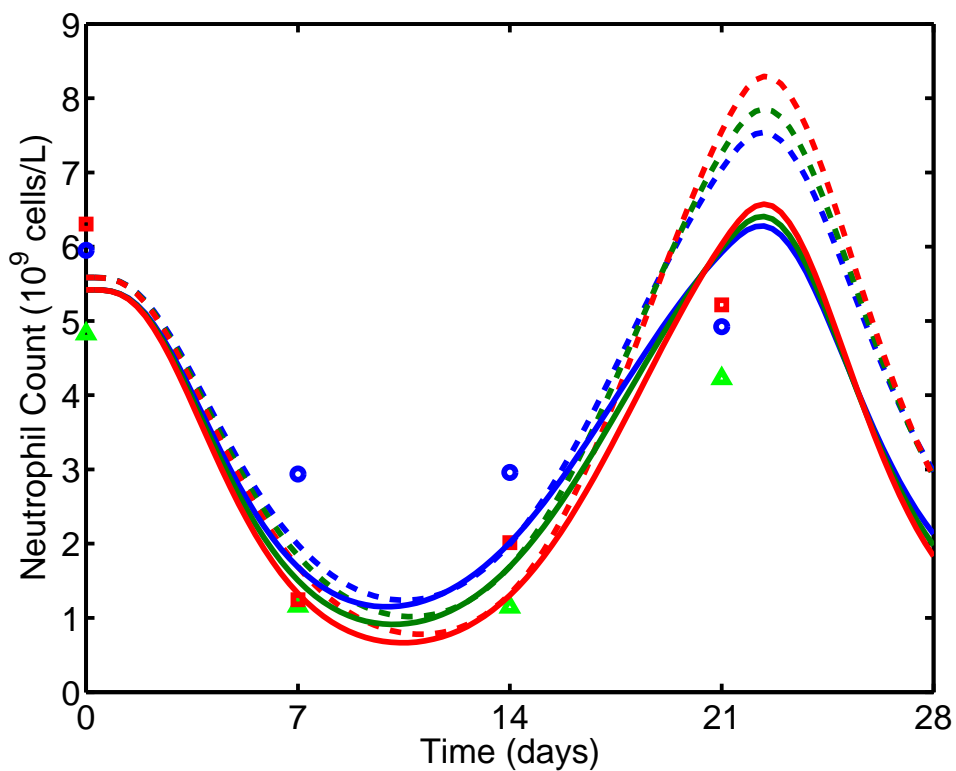


Figure 6.2: Patient neutrophil counts obtained during the first cycle of q3w Doc treatment at 50 (circle), 60 (triangle), and 75 (square) $\frac{\text{mg}}{\text{m}^2}$. Neutrophil profile predictions are based on the original (dashed) and updated (solid) parameter sets.

Finally, observed versus predicted individual and population neutrophil predictions are shown in Figure 6.3. Due to the limited data available for each patient, the model structure was over parameterized for even this four parameter system, as evidenced by individual neutrophil predictions lying almost uniformly on the line of unity. The over-fitting of individual data propagates to increased uncertainty in the population neutrophil model parameters and less accurate population neutrophil predictions. Estimating parameters for the entire population simultaneously would likely improve these model predictions, as would the inclusion of an intra-patient variability model for individual parameters [3].

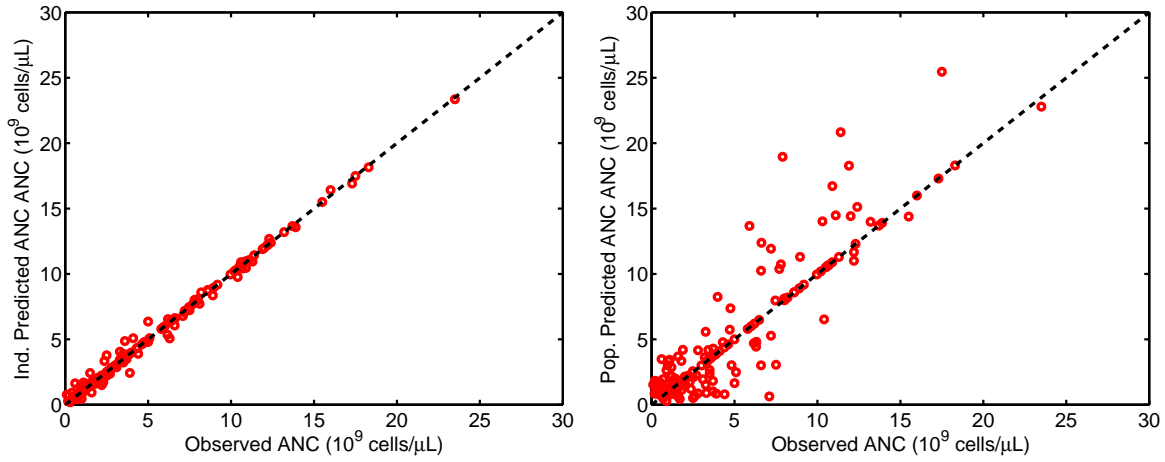


Figure 6.3: Individual (left) and population (right) predicted patient neutrophil counts versus actual patient neutrophil count measurements.

Table 6.1: Parameter values compared for the neutrophil model from the literature [3] and those estimated using the linear PD effect in Equation (6.7) and patient neutrophil counts from two Phase I clinical trials.

	Friberg <i>et al.</i> Linear PD effect	Florian <i>et al.</i> Linear PD effect
k_{tr} day ⁻¹	1.08	0.84
m $\frac{1}{\mu\text{M}}$	8.58	33.3
γ_1	0.161	0.187
$N_0 \times 10^9$ cells	5.05	5.09

6.2.2 Coupled PK and PD Predictions

Typical dosing ranges for the three schedules (q3w, weekly, and biweekly) are 70-100 $\frac{\text{mg}}{\text{m}^2}$, 28-40 $\frac{\text{mg}}{\text{m}^2}$, and 40-60 $\frac{\text{mg}}{\text{m}^2}$, respectively, and simulated absolute neutrophil count (ANC) profiles in response to treatment are shown in Figures 6.4a, b, and c, respectively. Grade 2, 3, and 4 neutropenia are represented as horizontal lines in the figure, with toxicity grades corresponding to $2.0 \times 10^9 \frac{\text{cells}}{\text{L}}$, $1.0 \times 10^9 \frac{\text{cells}}{\text{L}}$, and $0.5 \times 10^9 \frac{\text{cells}}{\text{L}}$, respectively. At the lowest q3w dose (70 $\frac{\text{mg}}{\text{m}^2}$), toxicity is predicted to approach Grade 3 neutropenia (nadir at $1.0 \times 10^9 \frac{\text{cells}}{\text{L}}$) following the first Doc dose and $1.3 \times 10^9 \frac{\text{cells}}{\text{L}}$ (between Grade 2 and 3 neutropenia) on proceeding doses. Likewise, the extent of toxicity at the highest q3w dose approaches Grade 4 neutropenia ($0.5 \times 10^9 \frac{\text{cells}}{\text{L}}$) following the first dose and $0.8 \times 10^9 \frac{\text{cells}}{\text{L}}$ (between Grade 3 and 4 neutropenia) on proceeding doses. While there is no observable increase in patient neutropenia from dose to dose, clinical results do not demonstrate nadir values of increasing magnitude following the first cycle (no clear pattern is observed). Rather, this behavior is a consequence of perturbing the neutrophil model from its initial conditions and may not reflect quantitative biological values.

Simulated neutrophil profiles for “weekly” Doc administration display a rapid fall following the first week of treatment, followed by a less gradual reduction in neutrophil count after the second dose, then a small rebound and subsequent drop-off in neutrophil count following the third dose, and finally, neutrophil recovery during the week without dosing (week four). The nadir for the 28 $\frac{\text{mg}}{\text{m}^2}$ regimen occurred at $1.5 \times 10^9 \frac{\text{cells}}{\text{L}}$ while the nadir for the 40 $\frac{\text{mg}}{\text{m}^2}$ regimen was $0.8 \times 10^9 \frac{\text{cells}}{\text{L}}$, though this dose is employed in “weekly” dosing less frequently than 35 $\frac{\text{mg}}{\text{m}^2}$ (Grade 3 neutropenia, $1.0 \times 10^9 \frac{\text{cells}}{\text{L}}$).

Likewise, the profiles for every other week 60 $\frac{\text{mg}}{\text{m}^2}$ Doc administration display a nadir following the week of drug delivery (Grade 2 neutropenia, $1.3 \times 10^9 \frac{\text{cells}}{\text{L}}$), recovery during the week without Doc dosing (though the recovery does not reach the baseline neutrophil count), and subsequent repetition of the pattern as dosing continues. The median every other week regimen, 50 $\frac{\text{mg}}{\text{m}^2}$, reaches nadir at $1.7 \times 10^9 \frac{\text{cells}}{\text{L}}$, and the lowest every other week regimen dose, 40 $\frac{\text{mg}}{\text{m}^2}$, predicts a nadir of $2.0 \times 10^9 \frac{\text{cells}}{\text{L}}$ (barely classifying as Grade 2

neutropenia), despite delivering approximately the same Doc over a twelve week period as the $70 \frac{\text{mg}}{\text{m}^2}$ q3w and $28 \frac{\text{mg}}{\text{m}^2}$ “weekly” schedules (Grade 3 and 2 neutropenia, respectively).

The median dose level from each regimen is shown in Figure 6.4d for comparison. Qualitatively, these behaviors are accurate as the weekly and biweekly dosing have higher nadir values than the q3w regimen. However, the model is not quantitatively predictive for neutrophil progression in patients dosed “weekly” with Doc with results from the literature indicating an 2.5-23% incidence of grade 3 and 4 neutropenia during “weekly” Doc treatment [151, 155, 159, 171, 172, 192]. Furthermore, the decreased toxicity predicted by the “weekly”, Doc regimen in Figure 6.4d was found to be infusion duration dependent. It should be noted that while typical “weekly” treatments have an infusion duration of 30-minutes, the above simulations utilized a 60-minute infusion duration. If the infusion duration was altered to be representative of clinical practice, model predictions of decreased toxicity under “weekly” treatment were no longer realized. This indicates a flaw in the underlying PD model structure.

As an additional comparison, data from the MSKCC study with a patient dosed “weekly” and the accompanying neutrophil progression prediction is shown in Figure 6.5. While the model predicts a nadir value of neutrophils that persists for the three weeks of dosing, the patient data depicts more rapid recovery of neutrophils between treatments and a gradual decline in the number of circulating neutrophils over the three dosing weeks. In order to describe weekly dosing quantitatively, the PD model structure must be altered, either at the feedback or drug effect term, so as to simultaneously describe both the q3w and weekly dosing schedule. This is needed if model predictions are to be used in subsequent dose schedule development.

6.2.3 Updated Neutrophil Model

Initial model alterations focused on evaluating alternative PD effect structures within the neutrophil model as described in Equations (6.7)-(6.10). Parameters were estimated for the 51 patients available, and the model predicted incidence of grade 3/4 neutropenia was calculated for the entire population. Neither a Michaelis-Menten nor a sigmoidal formulation

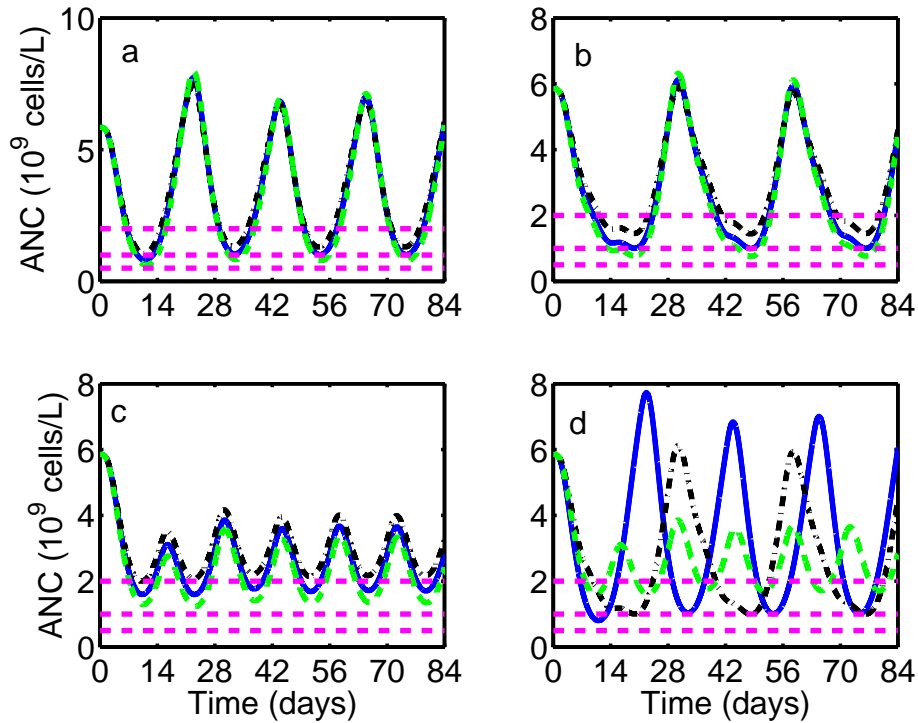


Figure 6.4: Predicted ANC resulting from administration of Doc at various dose level and schedule combinations (a) q3w at 70, 85, and 100 $\frac{\text{mg}}{\text{m}^2}$ (represented by dash-dot, solid, and dashed lines), (b) “weekly” at 28, 35, and 40 $\frac{\text{mg}}{\text{m}^2}$ (represented by dash-dot, solid, and dashed lines), or (c) every other week at 40, 50, and 60 $\frac{\text{mg}}{\text{m}^2}$ (represented by dash-dot, solid, and dashed lines). Subfigure (d) compares the median delivered dose for each of the three regimens, corresponding to q3w 85 $\frac{\text{mg}}{\text{m}^2}$ (solid), biweekly 50 $\frac{\text{mg}}{\text{m}^2}$ (dashed), and “weekly” 35 $\frac{\text{mg}}{\text{m}^2}$ (dash-dot).

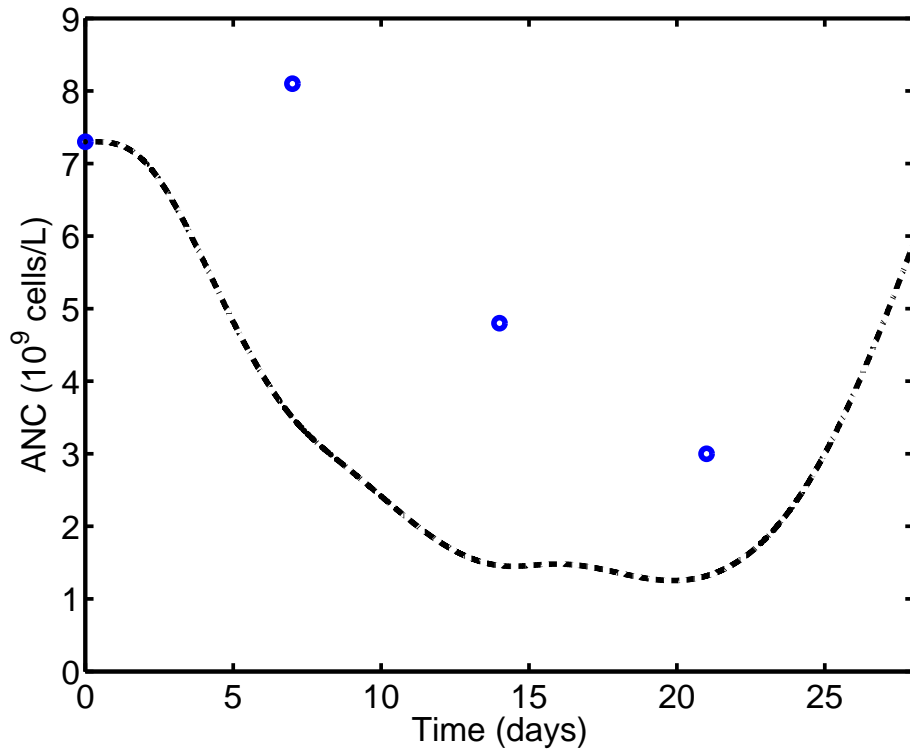


Figure 6.5: Predicted ANC (solid) and representative patient ANC data (circles) versus time. Doc dose was $35 \frac{\text{mg}}{\text{m}^2}$ “weekly”.

for E_{drug} allowed for any differences between the predicted incidence of neutropenia on the two treatment schedules. Separation was achieved using a log-linear PD effect term, but this only reduced the grade 4 neutropenia ($\approx 10\%$ of the population) while the incidence of grade 3 neutropenia ($\approx 40\%$ of the population) remained outside the range observed in the literature. Upon closer inspection, it was observed that this separation was only attained for values of $\beta > 3.0$. In essence, selection of such a large parameter value allowed for exploitation of the small concentration differences observed during the course of the infusion between the q3w and “weekly” treatment schedules. This concept is further illustrated in Figure 6.6. For a linear effect structure following treatment with $70 \frac{\text{mg}}{\text{m}^2}$ Doc over a 1-hour infusion, the time course of drug effect was limited to two hours following the start of treatment (infusion duration and an additional hour). This result was expected as infusion duration dependency of the model structure had already been established during initial model evaluations using multiple treatment regimens (Figure 6.4).

As noted in the previous section, the current PD structure is over parameterized, and attempting to estimate individual patient neutrophil model parameters with more complex drug effect terms only increased the over parameterization. While the above results did not predict the desired separation between treatment schedules, this may have resulted from identifying model parameters on an individual patient basis (*i.e.*, multiple parameter sets for describing the dataset may exist). To address this question, parameters were evaluated by randomly pairing two patients from the population, one selected from the group dosed Doc q3w, the other selected from patients administered Doc “weekly”. Results from this analysis demonstrated that a subset of patients dosed Doc q3w could be identified concurrently with patients treated “weekly”. However, closer inspection revealed that only q3w patients whose baseline was at or below the population average returned model parameters capable of simultaneously fitting neutrophil profiles from both administration schedules. While this would seem to be ideal (*i.e.*, the model is predictive at the average population neutrophil baseline), it should be noted that the limited population data for patients administered Doc “weekly” ($n = 5$) possessed an average baseline neutrophil count of $9.5 \times 10^9 \frac{\text{cells}}{\mu\text{L}}$, nearly two-fold the value of the actual population baseline count. As such, the model was exploiting this difference in initial neutrophil count when predicting patient neutrophil progression and

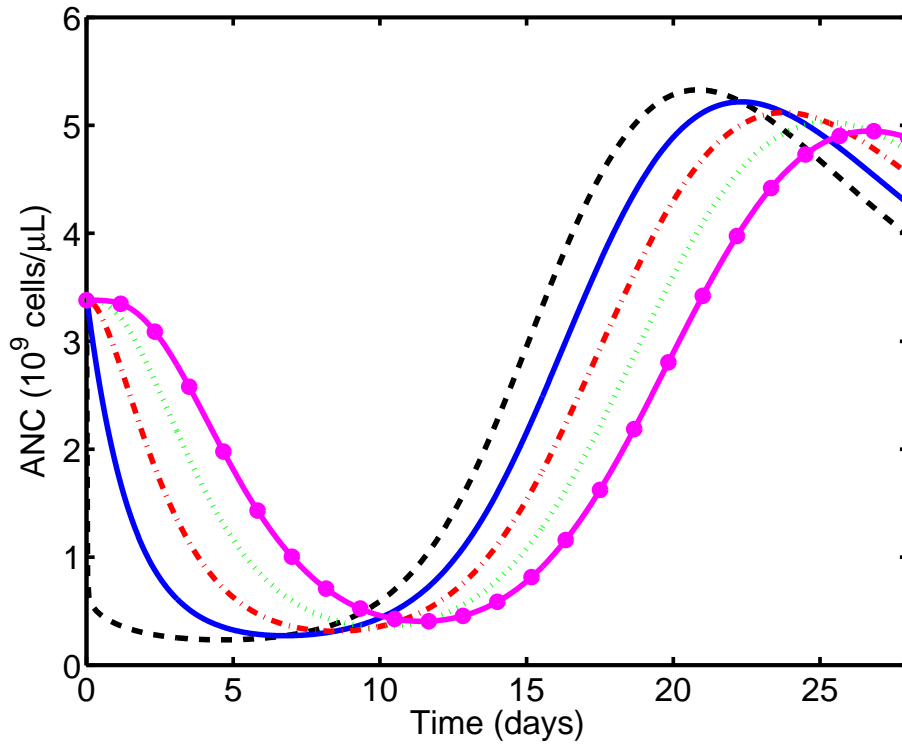


Figure 6.6: Model predicted progression of each state (P -dashed, T_1 -solid, T_2 -dash-dot; T_3 -dotted; N -circles) from the Friberg *et al.* neutrophil model following administration of $70 \frac{\text{mg}}{\text{m}^2}$ Doc over a 1-hour infusion on day 0.

did not actually predict a reduced incidence of neutropenia for patients administered Doc “weekly”.

The next neutrophil modeling approach utilized for describing neutrophil progression on different treatment regimens explored the inclusion of an effect-site compartment in the model structure (Equation (6.11)) with all four PD effect structures. Due to model over parameterization, and as the purpose of this compartment was to eliminate the infusion duration effect on neutrophil count, k_f was bounded as $1 \frac{1}{\text{day}} < k_f < 20 \frac{1}{\text{day}}$ ($k_f = 40 \frac{1}{\text{day}}$ results in an effect compartment profile that was nearly identical to plasma). Such a parameter restriction was necessary as arbitrarily large values of k_f would behave as if no filter was incorporated (*i.e.*, effect-compartment Doc concentrations would be equivalent to plasma Doc concentrations), which is already known to describe q3w but not “weekly” data. Furthermore, k_f values of less than $1 \frac{1}{\text{day}}$ altered the predicted effect-compartment concentrations so as to no longer mimic tissue Doc concentrations predicted by the tissue-intensive PBPK model. A representative plot of these predicted effect-compartment Doc concentrations for k_f values of 1, 5, and $20 \frac{1}{\text{day}}$, compared to the original plasma profile and tissue predictions are shown in Figure 6.7. While these k_f values alter the effect profile and do not match dynamics observed from highly perfused tissues, the dynamics were representative of tissue dynamics observed from slowly perfused tissues (fat, muscle, and “other”). As the primary goal of including the effect-compartment was to eliminate the effect of infusion duration on the predicted neutrophil effect, the k_f range above was deemed acceptable.

However, any parameter value within this range would result in model parameters capable of describing the observed patient neutrophil counts. Furthermore, simultaneous evaluation of q3w and “weekly” patients would result in the same problem encountered previously. Hence, three separate values for k_f were selected (1, 5, and $20 \frac{1}{\text{day}}$), with estimated population model parameters and predicted population occurrences of Grades 2, 3, and 4 neutropenia summarized in Table 6.2. Of the three evaluated filter parameterizations, only values of $k_f = 5 \frac{1}{\text{day}}$ returned population predicted incidences of grade 3/4 neutropenia for q3w and “weekly” treatment schedules of Doc consistent with the literature (2.5-23% versus upwards of 90% in q3w regimens) [151, 155, 159, 171, 172, 192].

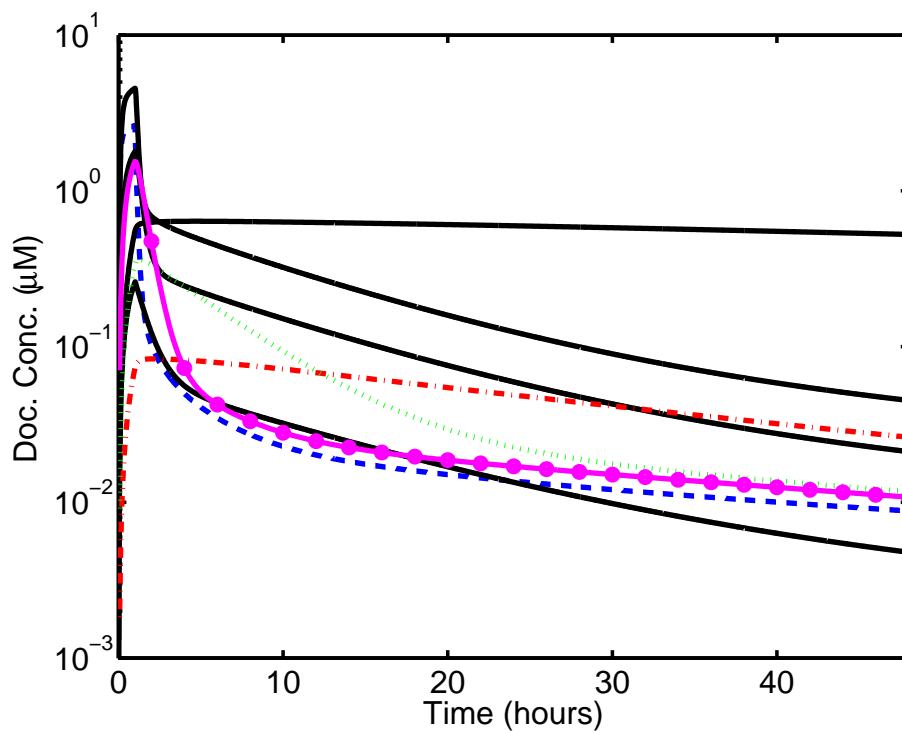


Figure 6.7: Model predicted effect-site concentration as a function of k_f value versus time for a Doc dose of $70 \frac{\text{mg}}{\text{m}^2}$ over a 1-hour infusion to a typical patient (k_f values of 1, 5, and 20 given by circles, dotted, and dash-dot, respectively). Also shown are the original Doc plasma concentration (dashed) and selected tissue Doc concentrations (solid) predicted by the tissue-intensive PBPK model.

Table 6.2: Parameter values for the neutrophil model of Friberg *et al.* [3] and estimated PD model parameters using altered PD effect terms and/or model structures. Neutropenia grade predictions were made using neutrophil model parameters identified for individual patients.

	Friberg Linear	Linear			Linear with filter			Log-linear with filter			Sigmoidal with filter			
		—	1	5	20	1	5	20	1	5	20	1	5	20
$k_f \text{ day}^{-1}$	—	—	0.87	0.82	0.82	0.84	0.79	0.77	0.83	0.78	0.77	0.83	0.78	0.77
$k_{tr} \text{ day}^{-1}$	1.08	0.84	0.87	0.82	0.82	0.84	0.79	0.77	0.83	0.78	0.77	0.83	0.78	0.77
γ_1	0.161	0.187	0.172	0.178	0.179	0.173	0.176	0.174	0.171	0.176	0.174	0.171	0.176	0.171
$N_0 \times 10^9 \text{ cells}$	5.05	5.09	5.16	5.16	5.16	5.09	5.10	5.10	4.99	5.13	5.10	4.99	5.13	5.13
$m \frac{1}{\mu\text{M}}$	8.58	33.3	25.0	25.9	28.1	—	—	—	—	—	—	—	—	—
β	—	—	—	—	—	1.2	1.4	2.0	—	—	—	—	—	—
$\alpha \frac{1}{\mu\text{M}^\beta}$	—	—	—	—	—	52.1	66.8	60.0	—	—	—	—	—	—
E_{max}	—	—	—	—	—	—	—	—	60.0	76.1	—	60.0	76.1	79.5
$EC_{50} (\mu\text{M})$	—	—	—	—	—	—	—	—	0.27	0.52	—	0.27	0.52	0.78
γ_2	—	—	—	—	—	—	—	—	2.35	2.37	—	2.35	2.37	2.83
Grade 2 neutropenia q3w	—	7/51	10/51	6/51	8/51	10/51	10/51	9/51	9/51	16/51	9/51	9/51	16/51	10/51
Grade 3 neutropenia q3w	—	12/51	12/51	12/51	8/51	10/51	5/51	16/51	6/51	5/51	16/51	6/51	5/51	12/51
Grade 4 neutropenia q3w	—	24/51	28/51	26/51	28/51	30/51	29/51	19/51	34/51	23/51	19/51	34/51	23/51	22/51
Grade 2 neutropenia “weekly”	—	10/51	14/51	8/51	10/51	11/51	11/51	11/51	20/51	15/51	11/51	20/51	15/51	9/51
Grade 3 neutropenia “weekly”	—	9/51	11/51	10/51	12/51	14/51	7/51	14/51	3/51	4/51	14/51	3/51	4/51	18/51
Grade 4 neutropenia “weekly”	—	24/51	25/51	22/51	22/51	16/51	8/51	12/51	5/51	6/51	12/51	5/51	6/51	10/51

Finally, population predicted neutrophil progression for the original Friberg neutrophil model (with updated parameters), along with the progressions predicted by the Friberg model appended with an effect-compartment and PD effects from Equations (6.7), (6.8), and (6.10) are shown in Figures 6.8 and 6.9. As before, grade 2, 3, and 4 neutropenia, are represented as horizontal lines in the figure, with toxicity grades corresponding to $2.0 \times 10^9 \frac{\text{cells}}{\text{L}}$, $1.0 \times 10^9 \frac{\text{cells}}{\text{L}}$, and $0.5 \times 10^9 \frac{\text{cells}}{\text{L}}$, respectively.

For the updated Friberg model (Figure 6.8, top), median nadir values for the population were predicted at 0.5 for treatment on both the q3w and “weekly” Doc schedules. Even the maximum predicted neutrophil counts from the population predicted a nadir of $1.1 \times 10^9 \frac{\text{cells}}{\text{L}}$, signifying that the neutrophil model predicts grade 3 neutropenia in almost the entire population. The inclusion of an effect-compartment within the Friberg model (Figure 6.8, bottom) allowed for an increase in separation between the two treatment schedules with median nadir values for both q3w and “weekly” schedules at 0.5 and $0.7 \times 10^9 \frac{\text{cells}}{\text{L}}$, respectively. However, the predicted incidence of grade 3/4 neutropenia within the population differed by only 12%. The incidence of grade 3/4 neutropenia (38/51) is approximately that observed for q3w treatments in the literature, but the population predicted occurrence (32/51) exceeds the value from patients dosed “weekly”.

If the PD effect was then altered to either a log-linear or sigmoidal formulation (Figure 6.9, top and bottom, respectively) further separation between q3w and “weekly” treatment schedules was achieved. Predicted median nadir values for the log-linear formulation were $0.5 \times 10^9 \frac{\text{cells}}{\text{L}}$ for the q3w schedule and $1.1 \times 10^9 \frac{\text{cells}}{\text{L}}$ for the “weekly” schedule. Similarly, the predicted incidence of grade 3/4 neutropenia was 34/51 and 15/51 for q3w and “weekly” treatment schedules, respectively, approximately equivalent to the values observed in the literature. Even further separation between the two treatment schedules was obtained using the sigmoidal PD effect structure, though the model predicted occurrences of grade 3/4 neutropenia for “weekly” Doc treatment were beginning to under-predict observed literature values. In the absence of data for further validating the log-linear and sigmoidal models with an effect-compartment, both models were deemed reasonable descriptions of neutrophil progression for treating patients on either q3w or “weekly” Doc schedules, and dose schedule development was pursued using both model structures.

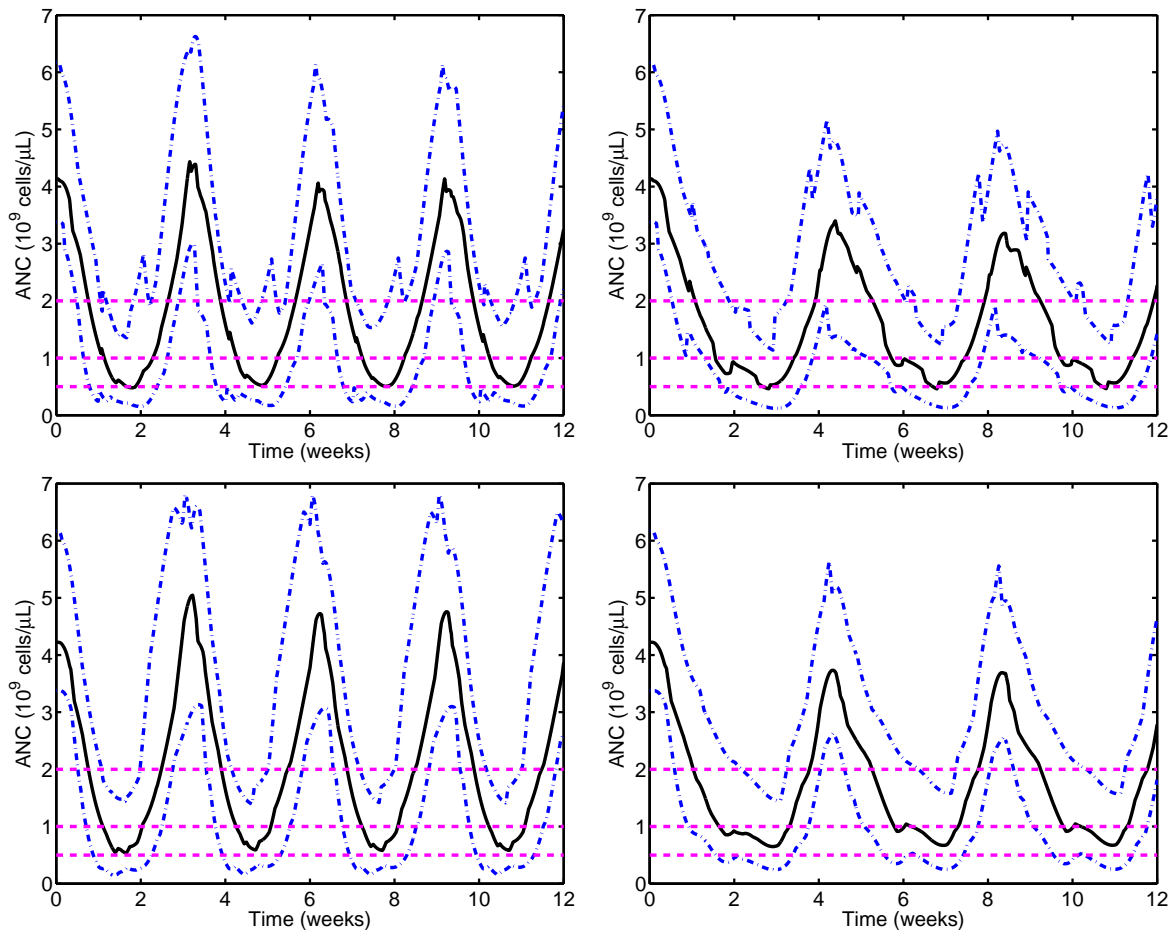


Figure 6.8: Median (solid), min (dash-dot), and max (dash-dot) model predicted neutrophil count progressions for the population using either the updated Friberg neutrophil model (top) or the Friberg model appended with an effect-compartment having a linear PD effect, and $k_f = 5 \text{ day}^{-1}$ (bottom). Treatment results over a 12 week cycle are shown with Doc administered q3w at $70 \frac{\text{mg}}{\text{m}^2}$ (left) and “weekly” at $30 \frac{\text{mg}}{\text{m}^2}$ (right).

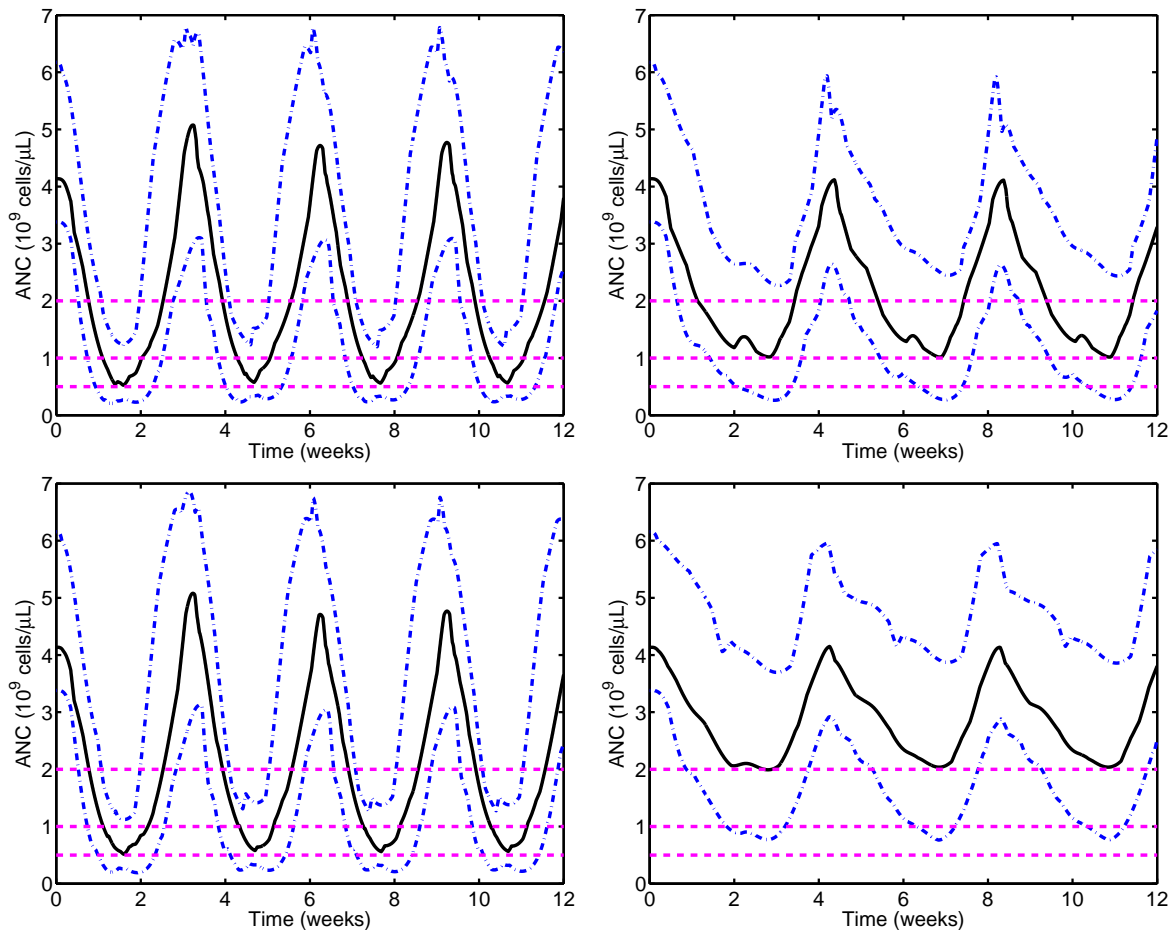


Figure 6.9: Median (solid), min (dash-dot), and max (dash-dot) model predicted neutrophil count progressions for the population using the Friberg model appended with an effect-compartment, $k_f = 5 \text{ day}^{-1}$, and either a log-linear (top) or sigmoidal (bottom) PD effect term. Treatment results over a 12 week cycle are shown with Doc administered q3w at $70 \frac{\text{mg}}{\text{m}^2}$ (left) and “weekly” at $30 \frac{\text{mg}}{\text{m}^2}$ (right).

6.2.4 Human PBPK Model Reduction

Model reduction tools were applied to the human PBPK model in order to aid subsequent controller synthesis. As the primary toxicity associated with Doc treatment is neutropenia, which is commonly represented as a function of plasma drug concentration, and tumor regression depends on tumor drug exposure, it was necessary to maintain accurate predictions for both plasma and tumor drug concentrations. All other tissue predictions, while potentially relevant for other toxicity metrics, are not concentrations that are commonly obtained in humans; explicit representation of these tissues were removed to reduce model order. The full model can be employed in subsequent analysis if the predicted concentrations in other tissues prove informative for treatment or toxicity evaluation.

Using the *balmr* function from MATLAB (©2007, The MathWorks, Natick, MA), Hankel singular values (HSVs) were calculated for the original 36 ODE PBPK model; these are shown in Figure 6.10. The upper bound on error introduced by truncating the original n -state linear model, $G(jw)$, to a k -state representation, $G_r(jw)$, is given by [135]:

$$\|G(jw) - G_r(jw)\|_\infty = 2 \sum_{i=k+1}^n \sigma_i^H \quad (6.29)$$

Here σ_i^H is the i^{th} HSV of the full order model. In a balanced realization, the magnitude of the HSV serves as a measure of the contribution of an individual state to the overall process behavior. Convention holds that the total of the sum in Equation (6.29) should not exceed 0.05-0.10 to ensure the accuracy of the reduced model. Furthermore, the truncation point is typically selected at a “knee” in the HSV curve. A closer inspection of Figure 6.10 (inset) reveals such a behavior between the 6th and 7th HSVs, and the upper bound on the truncated error using $k = 6$ was calculated at 0.020, within acceptable error bounds. As such, the model was reduced to 6 ODEs, and the resulting structure was used to provide plasma and tumor Doc concentration predictions when coupled with the PD model developed above.

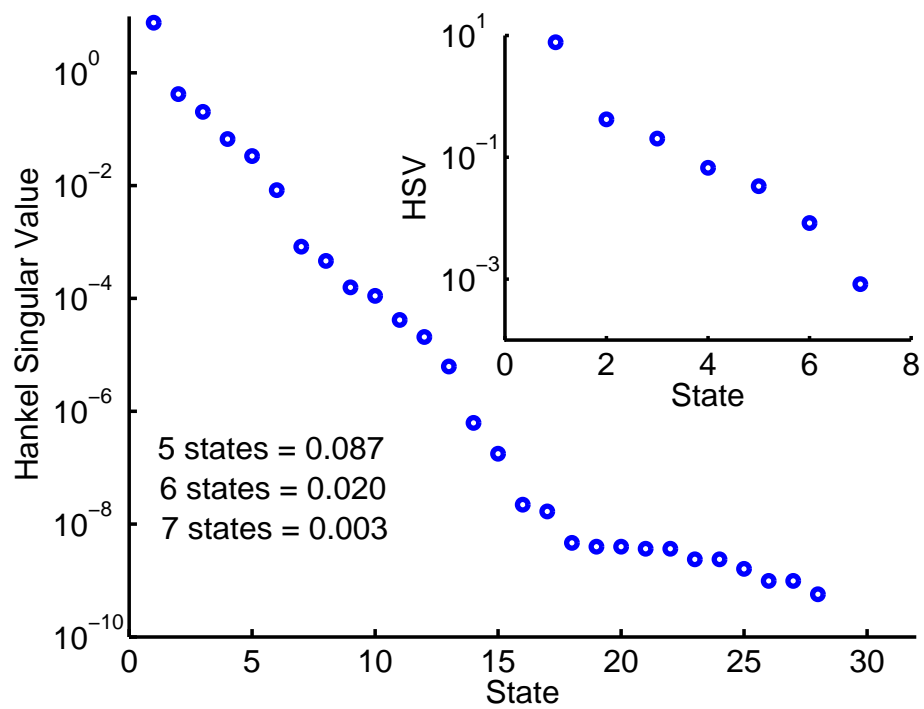


Figure 6.10: HSVs for the full 36 ODE human PBPK model. Inset: HSVs for the first 7 states.

6.2.5 Dose Schedule Development

Doc dose schedule design simulations were performed using model parameters representative of a median, a high risk of neutropenia, and a low risk of neutropenia patient. Three different model structures were evaluated for dose schedule development: (i) Friberg model with updated parameters; (ii) effect-compartment with log-linear drug effect; and (iii) effect-compartment with sigmoidal drug effect. Previous investigations involving Grade 3 and 4 neutropenia constraints resulted in a Doc treatment schedule which predicted ANCs within 1% of the lower specified toxicity constraint on an every other week basis. When this regimen was simulated for the entire population, excessive toxicity was predicted and as such the use of these constraints in algorithm development was rejected. Constraining neutrophil counts at the minimum acceptable limit of neutropenia was deemed ill-advised, and a less aggressive set of constraints maintaining the patient above Grade 3 toxicity or week-to-week persistence midway between Grade 2 and 3 toxicities were employed ($B_1 = 1.0 \times 10^9 \frac{\text{cells}}{\text{L}}$; $B_2 = 1.5 \times 10^9 \frac{\text{cells}}{\text{L}}$).

NMPC algorithm results ($m = 1$, and $p = 2$) for the above constraints using the updated Friberg model and a low risk patient are shown in Figure 6.11. It should be noted that Doc doses in this figure and the remaining figures in this chapter are plotted in the traditional MPC convention (*i.e.*, step profile) while actual Doc administration was limited to a 1-hour infusion at the start of each treatment week. For the evaluated patient, a nadir value of $1.0 \times 10^9 \frac{\text{cells}}{\text{L}}$ was attained on week two of treatment. Thereafter, the predicted ANC never fell below $1.2 \times 10^9 \frac{\text{cells}}{\text{L}}$, despite model predicted Doc administration never going below $36 \frac{\text{mg}}{\text{m}^2}$. For this patient, total administered Doc over a 12 week period was predicted to be $556 \frac{\text{mg}}{\text{m}^2}$, far exceeding administered Doc during any clinically practiced treatment regimen. However, such dosing is not recommended, not even for patients exhibiting limited neutrophil response (as in the case of this patient) during the first course of treatment. This Doc treatment result is an artifact of limited neutrophil progression sampling for this low risk patient, further supported by the total administered Doc calculated for low risk patients for case (ii) and (iii) (817 and $703 \frac{\text{mg}}{\text{m}^2}$, respectively).

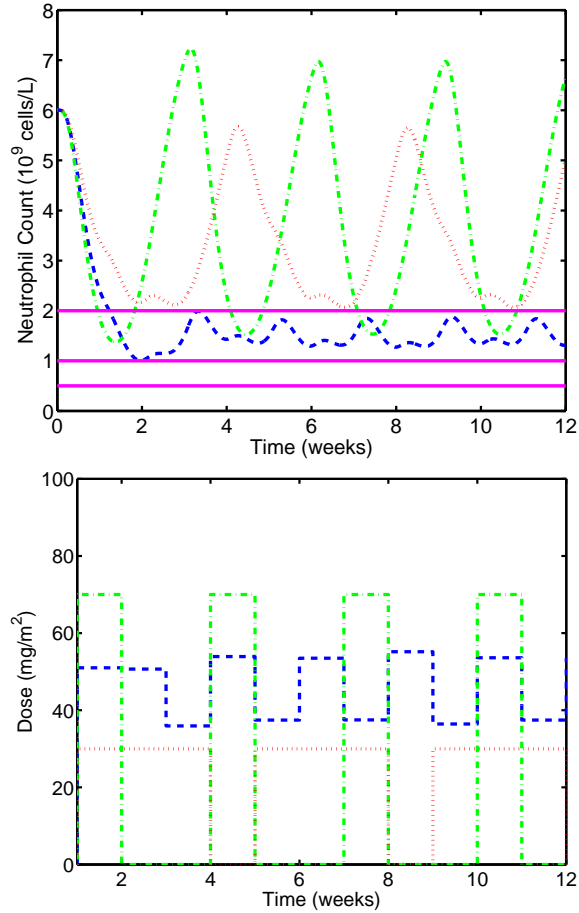


Figure 6.11: ANC predictions (top) and input profiles (bottom) for three separate Doc dosing regimens: $70 \frac{\text{mg}}{\text{m}^2}$ q3w (dash-dot); $30 \frac{\text{mg}}{\text{m}^2}$ “weekly” (dotted); and dosing constrained to maximize delivered drug subject to Grade 2 and 3 neutropenia constraints (dashed), for a low risk patient modeled using the updated Friberg neutrophil model. Neutropenia toxicity Grade 2, 3, and 4 are represented as horizontal lines (dashed) in the top figure, with toxicity grades corresponding to $2.0 \times 10^9 \frac{\text{cells}}{\text{L}}$, $1.0 \times 10^9 \frac{\text{cells}}{\text{L}}$, and $0.5 \times 10^9 \frac{\text{cells}}{\text{L}}$, respectively.

More clinically relevant schedules evaluated for a median and a high risk patient for case (i) are shown in Figure 6.12. For this case study, total Doc of 307 and $120 \frac{\text{mg}}{\text{m}^2}$ were predicted for the median and high risk patient, respectively, over the treatment cycle. This corresponds to a 10% increase and a 57% decrease from Doc administered q3w at $70 \frac{\text{mg}}{\text{m}^2}$. The administration schedule for the median patient displayed a three-level profile, though it also resembles high dosing for two weeks followed by a week of low dosing similar to regimens currently being investigated clinically. A similar result was obtained for the high risk patient; the schedule approaches a two-level formulation as the treatment cycle progresses (starting on week 6). However, it has already been shown that the neutrophil model used in these Doc schedule evaluations is not capable of accurately predicting neutrophil progression for both q3w and “weekly” treatment regimens so Doc schedule calculation and inferences drawn from this set should be approached with caution.

Case (ii) simulations (Figure 6.13) for the median patient predicted a trough ANC value of $1.0 \times 10^9 \frac{\text{cells}}{\text{L}}$ that repeated every 6 weeks for the controller-calculated treatment schedule. The treatment schedule for the case (ii) median patient was unique in that four weeks of high dosing were followed by a two week cessation of treatment. Still, the developed schedule predicted a total of $340 \frac{\text{mg}}{\text{m}^2}$ Doc administered over the treatment cycle, exceeding that administered during q3w Doc at $70 \frac{\text{mg}}{\text{m}^2}$ by 21% while maintaining grade 3 toxicity constraints. As before, the total amount of Doc delivered to the high risk patient was substantially less (50%) than that administered over a standard q3w $70 \frac{\text{mg}}{\text{m}^2}$ regimen. Furthermore, the administration schedule predicted for the case (ii) high risk patient displayed no perceivable pattern beyond daily low-dose administration similar to that used during metronomic Doc treatments.

Case (iii) simulations (Figure 6.14) for the median patient predicted a trough ANC value of $1.0 \times 10^9 \frac{\text{cells}}{\text{L}}$ that repeated every 3 weeks during the course of treatment. The administration schedule for the case (iii) median patient was similar to that obtained for the case (i) median patient (two-level sequence), with the exception that no drug was administered every third week. Total Doc administered over this cycle was $367 \frac{\text{mg}}{\text{m}^2}$ (31% increase versus $70 \frac{\text{mg}}{\text{m}^2}$ q3w), which was the largest predicted for a median patient of all three case studies. Likewise, the predicted Doc for a high risk patient was $229 \frac{\text{mg}}{\text{m}^2}$, only 18% less

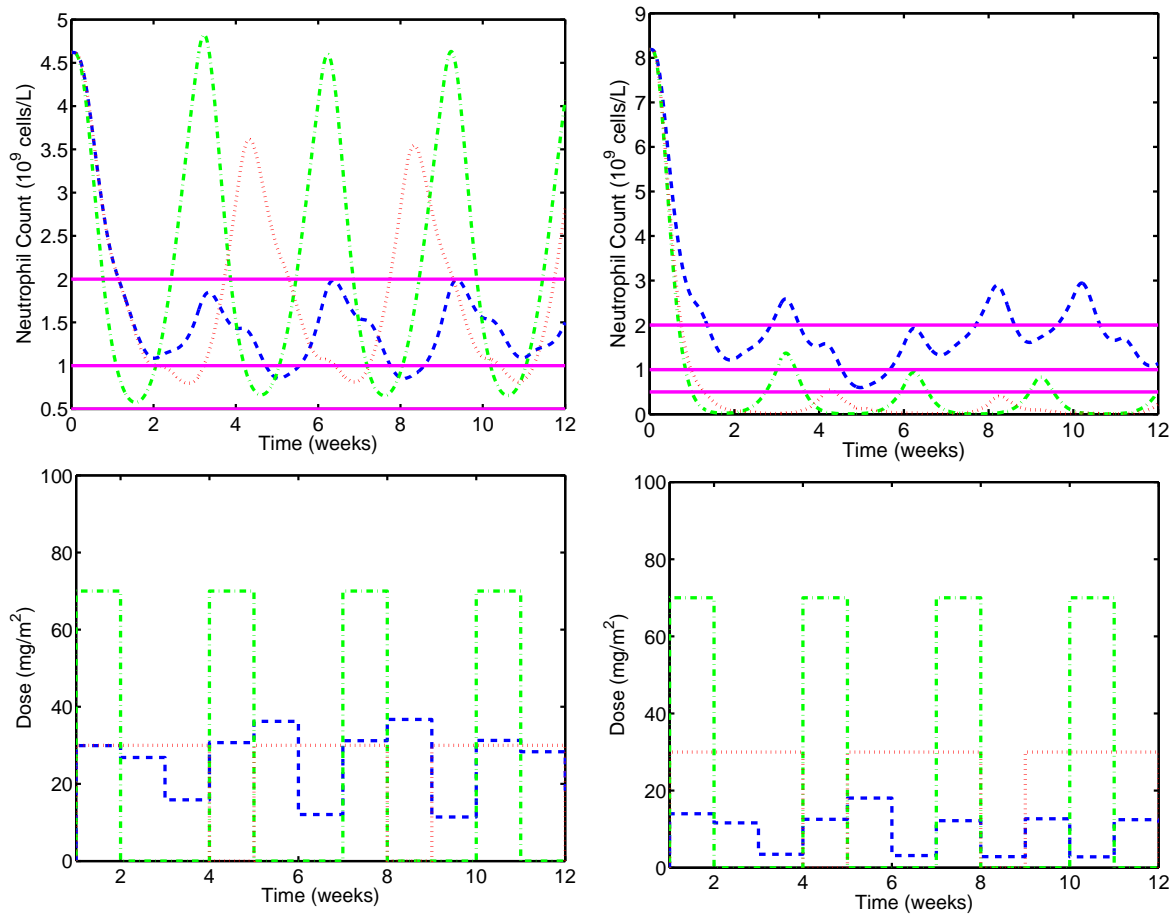


Figure 6.12: ANC predictions (top) and input profiles (bottom) for Doc regimen predictions constrained to maximize delivered drug subject to Grade 2 and 3 neutropenia constraints (dashed) for a median (left) and high risk (right) patient with the updated Friberg neutrophil model. Also shown are two standard Doc regimens: $70 \frac{\text{mg}}{\text{m}^2}$ q3w (dash-dot) and $30 \frac{\text{mg}}{\text{m}^2}$ “weekly” (dotted). Neutropenia toxicity Grade 2, 3, and 4 are represented as horizontal lines (dashed) in the top figure, with toxicity grades corresponding to $2.0 \times 10^9 \frac{\text{cells}}{\text{L}}$, $1.0 \times 10^9 \frac{\text{cells}}{\text{L}}$, and $0.5 \times 10^9 \frac{\text{cells}}{\text{L}}$, respectively.

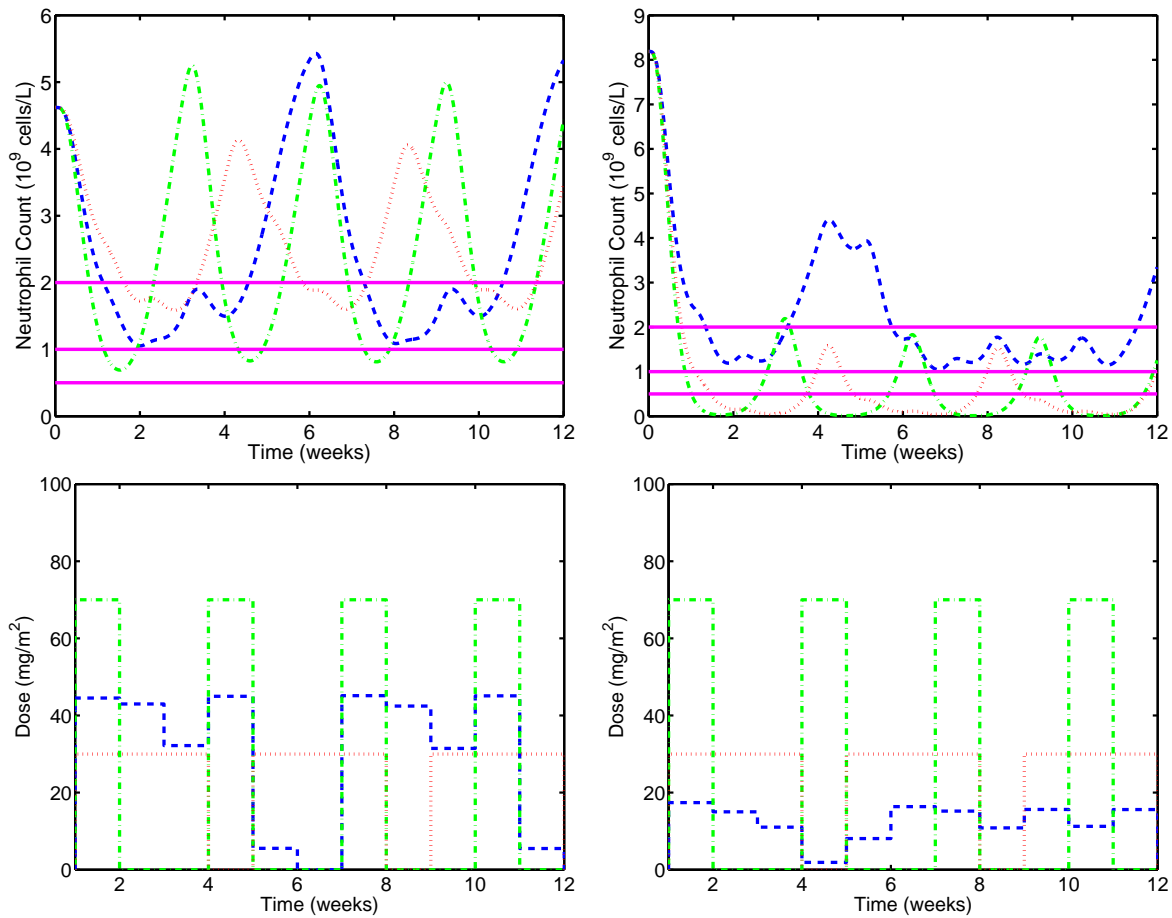


Figure 6.13: ANC predictions (top) and input profiles (bottom) for Doc regimen predictions constrained to maximize delivered drug subject to Grade 2 and 3 neutropenia constraints (dashed) for a median (left) and high risk (right) patient with a log-linear PD effect and effect-compartment ($k_f = 5 \frac{1}{\text{day}}$). Also shown are two standard Doc regimens: $70 \frac{\text{mg}}{\text{m}^2}$ q3w (dash-dot) and $30 \frac{\text{mg}}{\text{m}^2}$ “weekly” (dotted). Neutropenia toxicity Grade 2, 3, and 4 are represented as horizontal lines (dashed) in the top figure, with toxicity grades corresponding to $2.0 \times 10^9 \frac{\text{cells}}{\text{L}}$, $1.0 \times 10^9 \frac{\text{cells}}{\text{L}}$, and $0.5 \times 10^9 \frac{\text{cells}}{\text{L}}$, respectively.

than that administered during q3w at $70 \frac{\text{mg}}{\text{m}^2}$. However, as mentioned in the previous section, the neutrophil model used for case (iii) slightly under-predicts the incidence of grade 3/4 neutropenia in the population. In those simulations involving a standard “weekly” treatment schedule, the minimum ANC at $30 \frac{\text{mg}}{\text{m}^2}$ (total of $270 \frac{\text{mg}}{\text{m}^2}$ Doc) was predicted to be grade 2 neutropenia (Figure 6.9, lower right). The remaining ANCs from other models predicted grade 3 neutropenia or worse (Figure 6.9, upper right). As such, it was not unexpected that the case (iii) high risk patient predicted the highest administered Doc total of all the high risk patient cases, nor that it almost predicted equivalent dosing to that used during standard treatment regimens.

A final evaluation took the predicted treatment schedules for case (ii) and (iii) from the median and high risk patients and simulated those schedules for the entire population. Population predicted median, min, and max ANC are shown in Figure 6.15. The median ANC for case (ii) now predicted nadir values of approximately $0.5 \times 10^9 \frac{\text{cells}}{\text{L}}$ (grade 4 neutropenia), however, this was not unexpected as the simulated schedule delivered 21% more Doc than the standard q3w schedule (with a similar toxicity profile). Given the likelihood of grade 4 neutropenia from this treatment schedule, however, it is recommended that an alternative median patient be used for developing a Doc treatment regimen. For case (iii) the median patient was now predicted to have a nadir ANC of $0.7 \times 10^9 \frac{\text{cells}}{\text{L}}$ with 31% more Doc delivered than the standard q3w regimen. Finally, both high risk regimens returned population ANC where the minimum never resulted in grade 3 neutropenia. Again, this was not unexpected as a representative patient from the high risk group was used for schedule development and the imposed model constraints highly penalized the occurrence of grade 3 neutropenia.

6.3 DISCUSSION

The semi-mechanistic neutrophil model developed by Friberg *et al.* [3] was used to describe patient neutrophil progression following treatment with 50-75 $\frac{\text{mg}}{\text{m}^2}$ Doc. While parameters for this model had been evaluated previously, updated model parameters were necessary to

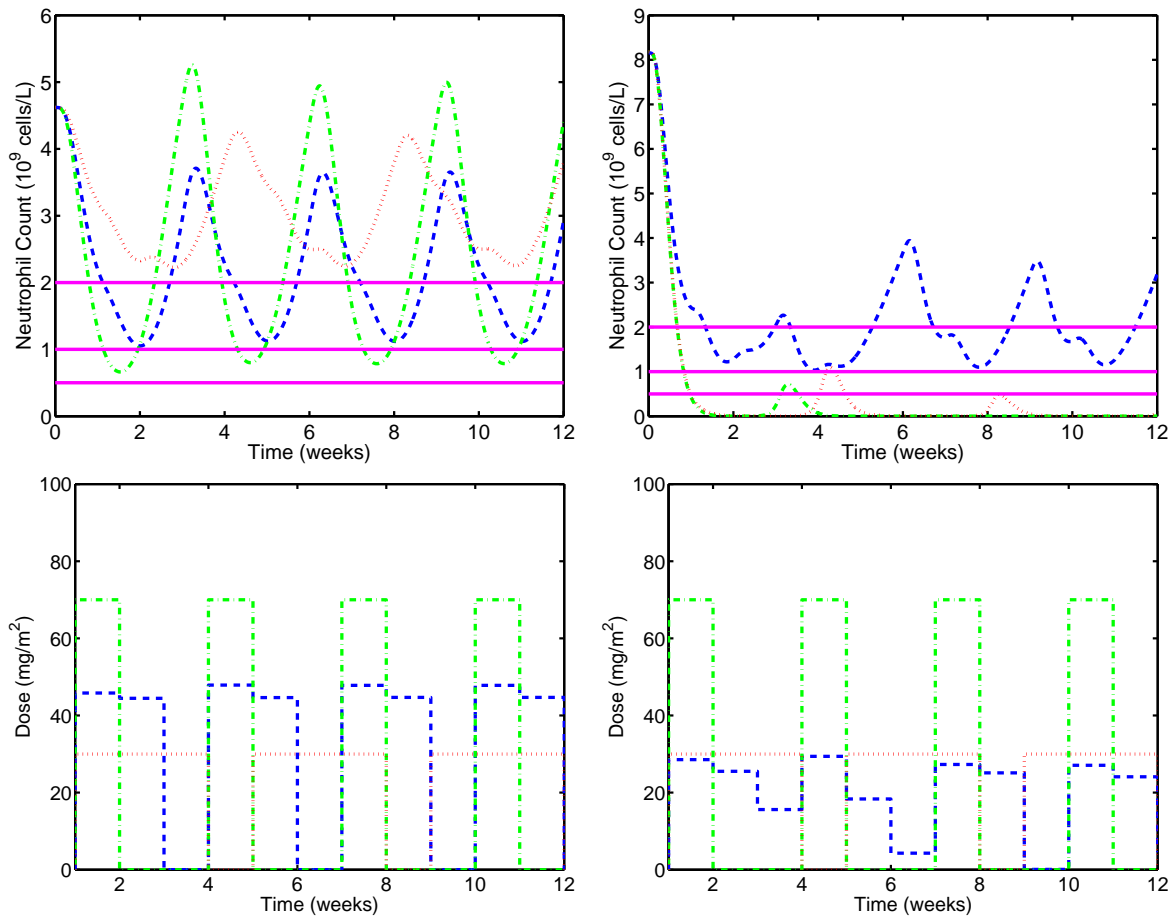


Figure 6.14: ANC predictions (top) and input profiles (bottom) for Doc regimen predictions constrained to maximize delivered drug subject to Grade 2 and 3 neutropenia constraints (dashed) for a median (left) and high risk (right) patient with a sigmoidal PD effect and effect-compartment ($k_f = 5 \frac{1}{\text{day}}$). Also shown are two standard Doc regimens: $70 \frac{\text{mg}}{\text{m}^2}$ q3w (dash-dot) and $30 \frac{\text{mg}}{\text{m}^2}$ “weekly” (dotted). Neutropenia toxicity Grade 2, 3, and 4 are represented as horizontal lines (dashed) in the top figure, with toxicity grades corresponding to $2.0 \times 10^9 \frac{\text{cells}}{\text{L}}$, $1.0 \times 10^9 \frac{\text{cells}}{\text{L}}$, and $0.5 \times 10^9 \frac{\text{cells}}{\text{L}}$, respectively.

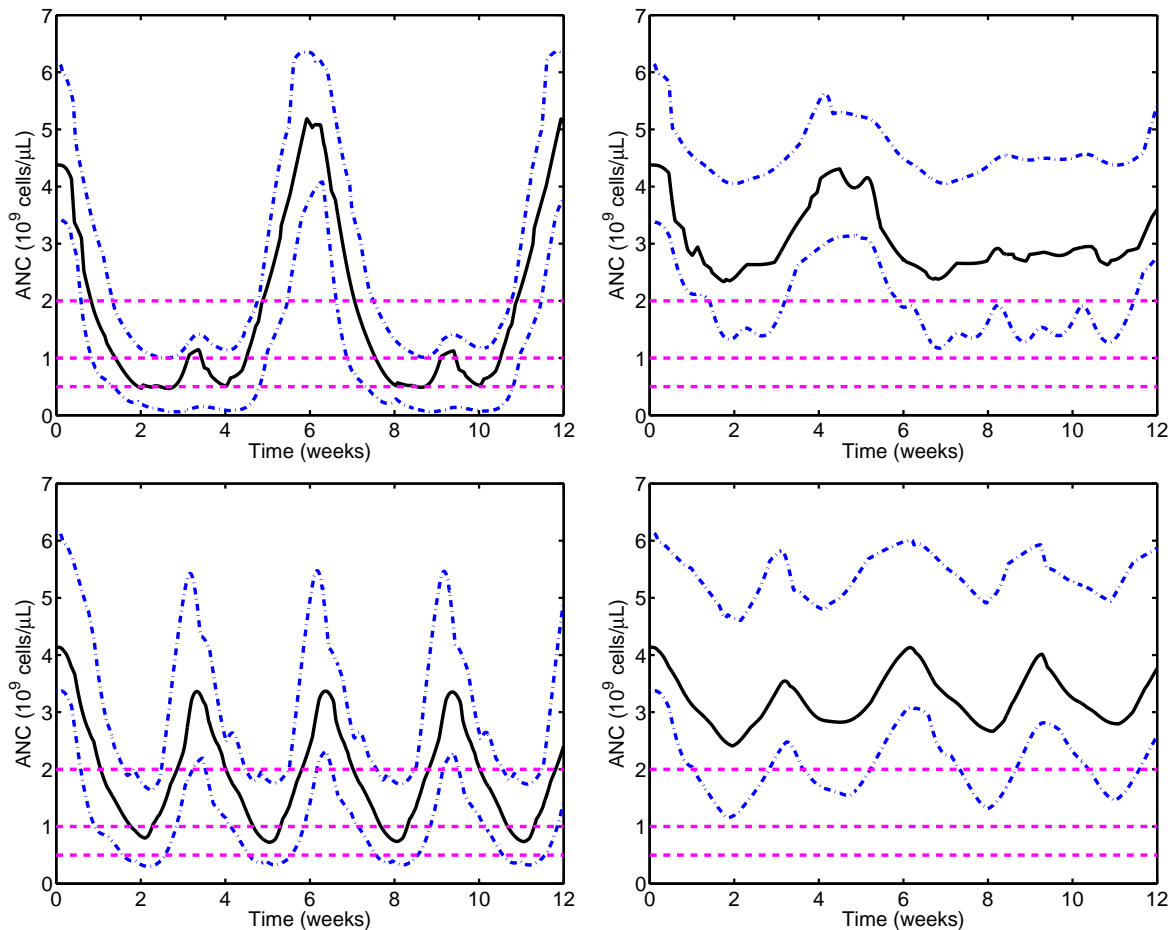


Figure 6.15: Median (solid), min (dash-dot), and max (dash-dot) model predicted neutrophil count progressions for the population using the Friberg model appended with an effect-compartment, $k_f = 5 \text{ day}^{-1}$, and either a log-linear (top) or sigmoidal (bottom) PD effect term. Treatment results over a 12 week cycle are shown with Doc administered according to the Doc schedule developed for a median (left) and high risk (right) patient.

properly describe the observed neutrophil progression for patients from the two investigated clinical studies [6, 179]. Various factors may have contributed to this including different Doc dosing levels used for model development (previous parameters were developed from patients dosed either 75 or 100 $\frac{\text{mg}}{\text{m}^2}$ with a majority of the patients receiving higher doses), using patient-specific Doc plasma concentrations predicted by the tissue-intensive PBPK model (previous parameters used the Bruno population PK model for Doc plasma predictions [2]), and the smaller dataset investigated (58 patients versus 601 from the previous study). The developed neutrophil model was capable of describing observed neutrophil progression following Doc treatment on a q3w schedule and initial results indicated that alternate PD effect terms would allow for prediction of additional Doc treatment schedules. However, it was discovered that these model results were dependent upon the Doc infusion duration and if the “weekly” treatment was simulated using a 30-minute infusion, as is practiced clinically, then the results no longer predicted decreased toxicity for “weekly” Doc treatments.

Initial attempts to adapt the neutrophil model for “weekly” Doc treatment schedules investigated altering the PD effect term to either a log-linear, Michaelis-Menten, or sigmoidal formulation. However, none of these PD effect structures were capable of achieving significantly different population predictions of grade 3/4 neutropenia for different administration schedules as observed in the literature. An attempt was made to simultaneously identify parameters for patients administered Doc q3w and “weekly”. However, due to limited data on “weekly” patients, in addition to the data for those patients displaying a baseline circulating neutrophil count bias (nearly two-fold that of the typical population), these simulations were not able to properly identify patient parameters. Note that additional “weekly” patient data may allow this, and it will be a topic of future study as data is available.

Investigating the time evolving states of the neutrophil model, particularly compartment P where the drug effect was incorporated, it was revealed that nearly the entire Doc drug effect on proliferating neutrophils was limited to the first two hours of treatment for the q3w regimen (infusion duration plus one additional hour). This is a failing of the semi-mechanistic model, as on-board Doc is likely having an effect extending for multiple days. However, due to the inclusion of multiple filter compartments (three transition states), infrequent neutrophil

sampling rates, and a slowly progressing patient neutrophil profile, the semi-mechanistic model was able to predict neutrophil progression results following q3w treatment with Doc that agreed well with data collected from the literature.

A final evaluation focused on the inclusion of an effect compartment to filter Doc plasma concentration similar to that used by Hing *et al.* [183] for describing the effect of trabectedin on circulating neutrophil count across multiple dose schedules. As the neutrophil model was already over parameterized prior to the addition of the filter compartment, acceptable values for the filter constant, k_f , were bounded by comparing effect compartment concentration predictions to those predicted in tissues by the tissue-intensive PBPK model. Values beneath $1 \frac{1}{\text{day}}$, while completely removing the infusion duration effect from the PD model, returned compartment concentrations with Doc retention dynamics that exceeded those predicted for tissues. Similarly, values above $40 \frac{1}{\text{day}}$ returned effect compartment profiles that were not substantially different from the original plasma profile. As such, this term was bounded between 1 and $40 \frac{1}{\text{day}}$. Using three separate k_f parameterizations (1, 5, and $20 \frac{1}{\text{day}}$), neutrophil model parameters for the population were identified. Of the various PD effects investigated, only the log-linear and sigmoidal PD effects were capable of predicting the observed separation in incidence of grade 3/4 neutropenia between the q3w and “weekly” Doc treatment. While a number of assumptions were made in constructing this updated neutrophil model, these alterations were rooted in systems biology. Techniques were employed that were successful for other authors in describing multiple treatment schedules [183] and ensuring that the profile predicted within the effect compartment was similar to predicted Doc tissue profiles. As such, additional data on Doc bone marrow concentrations (ideally from mouse, which could be scaled to humans) would allow for validation of these effect compartment predictions. Alternatively, more frequent measurements of neutrophil count, and additional data from patients dosed “weekly”, may allow for a population analysis of the model parameters.

Finally, Doc dose schedule control simulations were performed using median, high risk of neutropenia, and low risk of neutropenia patients. Three different model structures were evaluated for dose schedule development: (i) Friberg model with updated parameters; (ii) effect-compartment with log-linear drug effect; and (iii) effect-compartment with sigmoidal

drug effect. For the objective function, reference trajectory tracking of neutrophil count was deemed irrelevant as attaining a set neutrophil count is not a clinical goal during treatment. Rather, initial goals of treatment are to avoid primary toxicities, in this case neutropenia, while still delivering sufficient drug to attain an efficacious tumor response. Given the discrete nature of neutropenia toxicity grades and to ensure feasible solutions during controller simulation, state constraints pertaining to incidence or week-to-week occurrences of neutropenia grades were “relaxed” and included in the objective function, premultiplied by a suitably large penalty weight. In addition, objective function weights (negative) were placed on the two-norm of administered drug to allow for maximization of total drug delivered over the simulation, subject to toxicity constraints, and to ensure that dosing predictions favored large dose administrations. This is consistent with the viewpoint of the clinician regarding treatment, which is to administer as much drug to the patient as often as possible subject to patient toxicity [190, 191]. Granted, such statements represent an absolute viewpoint and are easily refuted with results from the literature pertaining to saturating effects [193, 194]. However, clinical results with Doc indicate that patients who complete the most weeks of treatment without requiring treatment adjustments are probabilistically more likely to have longer survival times and a longer duration before tumor recurrence [190, 191].

Controller simulations were performed in an NMPC formulation with $m = 1$ and $p = 2$. Alternative NMPC parameter selection is also feasible, however, as are controller simulations over the entire treatment cycle (*e.g.*, $m = 12$, $p = 14$ to ensure that large dosing to the patient would not be predicted by the algorithm on the final day of treatment [63, 64]). Predictions for low risk patients for all three evaluated models, while allowing for increased Doc delivery ($556\text{-}817 \frac{\text{mg}}{\text{m}^2}$ over a 12 week period) are likely artifacts from limited patient neutrophil count samples and should not imply that such an amount of Doc could be delivered to any patient over a 12 week interval. Dose schedule predictions for the median patient using each of the three models allowed for increased administration of Doc over a 12 week period, compared to a q3w $70 \frac{\text{mg}}{\text{m}^2}$ regimen, and these may allow for improved treatment efficacy without an increase in accompanying toxicity. Doc delivery schedules for high risk patients allowed that

patient group to avoid grade 3 occurrences of neutropenia while delivering 38-62% less total Doc than the schedule for the median patient and 18-52% less total Doc than q3w 70 $\frac{\text{mg}}{\text{m}^2}$.

Overall, the NMPC control algorithm using the tissue-intensive PBPK model for PK predictions and the altered Friberg neutrophil model was capable of returning Doc dosing schedules that were qualitatively similar with on-going clinical research. Additional “weekly” patient data is necessary for validating the underlying model, however, the coupled models are now capable of quantitatively predicting the incidence of grade 3 and 4 neutropenia for two different Doc treatment regimens. This lends credence to the Doc treatment schedule predicted by the algorithm. Future algorithm development will focus on the effects of NMPC parameters m and p on Doc schedule predictions. Also, as the tissue-intensive PBPK model incorporates a tumor compartment within the model structure, all of the above simulations also possess model predicted Doc tumor concentration for each of the above schedules. This would allow for future inclusion of a projected tumor response in addition to a toxicity measure as presented within this chapter. Furthermore, alterations to the objective function to include both patient toxicity and a measure of efficacy are being pursued as a topic of future work.

7.0 CONTRIBUTIONS

7.1 CONCLUSIONS

The work within this dissertation has presented dose schedule development for chemotherapeutics, beginning with the classical focus of tumor regression and concluding with monitoring toxicity effects manifesting during treatment. Each problem possessed similar components, focusing first on the development of accurate PK models following drug administration. PK model predictions were used as the driving-force for downstream PD effect models for both tumor regression and toxicity. Finally, based upon a user supplied objective function, alterations to established dosing regimens were evaluated, obtaining solutions which were mathematical solutions to the specified problem, but not always clinically applicable.

7.1.1 Tamoxifen

NMPC algorithm was developed to dose the chemotherapeutic agent tamoxifen based on a novel saturating-rate, cell-cycle model (SCM). Using daily tumor measurements, the algorithm decreased tumor volume along a specified reference trajectory in simulated animals over 4 months. In mismatch case studies, controllers based on the Gompertz model (GM) yielded equivalent total drug delivered and elapsed time to $t_{99\%}$ reference step convergence to those obtained using the SCM, though this performance was dependent on the cell-cycle phase of drug effect. Overall, the NMPC algorithm is suitable for dosing chemotherapeutics with regular administration schedules and may be adapted for regularly administered

chemotherapeutics other than tamoxifen. Alterations to the objective function, however, may be necessary to increase the clinical applicability of predictions from the algorithm.

7.1.2 PBE Models

Both non-saturating and saturating PBE cell-cycle tumor growth models were investigated incorporating either mass or age as intrinsic system variables. Non-saturating models displayed exponential bulk tumor progression, which is descriptive of hematological cancers and solid tumor growth over short periods of time, but is insufficient for describing solid tumor growth over an extended time period. Saturating mass-structured PBEs, with either saturating G -phase transition rate or G -phase mass accumulation rates, displayed saturating growth characteristics, but this may hinder incorporation of a PD effect (*i.e.*, correlations between cell mass and PD effect are typically not investigated). Two saturating age-structured PBEs were investigated, one containing a lumped G -phase and age distributed S - and M -phases for a total of three phases; the other included a lumped Q -phase and age distributed G -, S - and M -phases for a total of four phases. Both models accurately described bulk tumor progression, and could be updated with parameters for individual tumor lines.

Three dosing case studies involving two cycle-specific therapeutic drugs with separate administration schedules, PK dynamics, and PD effects were evaluated against the three age-structured PBE models developed. While the S -phase treatment always started on day 42 of the simulation, treatment with the M -phase agent began up to 6 days prior or after the S -phase treatment. Results indicated that age-structured PBEs are capable of generating schedule dependent differences in final tumor volumes that are not achievable using traditional lumped models. Furthermore, the simulations indicated that for multi-agent chemotherapies, greater final tumor volumes resulted when the drugs were administered concurrently and that separating drug delivery to reduce the extent of PK overlap resulted in the the smallest final tumor volumes.

The employed model structure was not capable of achieving the degree of oscillations necessary for resonance chemotherapy treatment, only manifesting cell-cycle phase alterations immediately following drug delivery. These results were expected as previous papers

exploring resonance therapy demonstrated that the inclusion of a quiescent cell population, gradually declining PD effects, PK transport dynamics, or any comparable filtering dynamic were non-ideal for creating the discrete transitions necessary for manifesting the cell-cycle fraction oscillations seen during resonance chemotherapy simulations.

Overall both saturating and non-saturating PBEs offer a unique structure for the evaluation of single or multiple agent chemotherapies. These models, however, are not suitable for closed-loop controller evaluation of cancer treatment at present due to: (i) continued reliance on a feedback tumor volume metric; and (ii) the computation time of the model. In contrast, open-loop schedule evaluation is an ideal application of these models, allowing for the off-line simulation and evaluation of multiple drug combinations, dosing schedules, and dosing levels, areas that cannot be explored clinically or even preclinically (some may even argue in culture) due to constraints on financial costs, ethics, and time.

7.1.3 Docetaxel

Using data obtained from a pharmacokinetic study in mice ($n = 30$) dosed intravenously at $10 \frac{\text{mg}}{\text{kg}}$, a linear PBPK model was developed for Doc. Model compartments included plasma, tumor, liver, lung, kidney, heart, spleen, muscle, and fat. Tissues were initially assumed to be perfusion-limited, and then extended to diffusion-limited if the additional model complexity was justified by a corresponding increase in model quality. Due to a combination of rapid tissue absorption after the dose and prolonged retention of Doc in tissues, a third subcompartment was necessary in each tissue to describe the observed data. Rates into this compartment were kept equivalent for each tissue to limit the overall number of model parameters. Nonlinear transfer rates into extravascular tissue space could likewise describe the observed Doc data; however, the focus was on maintaining a linear model structure because the literature describes Doc plasma kinetics as linear.

The scale up this tissue intensive, linear mouse PBPK model to humans was then investigated. Model Doc plasma predictions were compared against data from three separate Phase 1 clinical trials (Doc doses ranging from $35\text{-}75 \frac{\text{mg}}{\text{m}^2}$) and two Doc models available in the literature: (i) the five-tissue PBPK model of Bradshaw-Pierce *et al.*; and (ii) the three

compartment population PK model developed by Bruno *et al.* Predictive accuracy of the tissue-intensive PBPK model and population PK model were of the same order despite not incorporating patient-specific correlates beyond body weight and body surface area within the PBPK model. Estimating unbound Doc percentage in individual patients improved the tissue-intensive PBPK model predictions with a mean predicted unbound Doc fraction of 3.7% (0.5-8.9%). While these means and ranges are in agreement with previous studies, additional validation is required to determine if the predicted unbound fractions correspond to individual patient values. The elderly patient data was poorly described. By altering cardiac output and tissue volume percentages for muscle and fat, the tissue-intensive model fit the data. Finally, simulated tumor concentration profiles revealed that Doc may accumulate with weekly administration.

The developed tissue-intensive PBPK model and patient-specific Doc plasma concentrations were then used as the input to a semi-mechanistic neutrophil model developed by Friberg *et al.* Neutrophil model parameter alterations were necessary to describe neutrophil count progression from the two evaluated clinical studies [6, 195] for patients administered 50-75 $\frac{\text{mg}}{\text{m}^2}$ Doc q3w over a 1-hour infusion. This neutrophil model was then used to simulate patient neutrophil progression over alternative Doc treatment schedules (“weekly” and every other week) as literature results indicate decreased occurrence of grade 3 and 4 neutropenia for these treatment schedules. Initial simulation results indicated decreased toxicity for “weekly” Doc treatment, however, this reduction in neutropenia was found to be infusion duration dependent and could not be achieved if Doc for the “weekly” schedule was administered over 30-minutes as implemented clinically. Neither alterations to the PD effect term nor simultaneous parameter estimation for patients dosed q3w and “weekly” resulted in parameters capable of describing both Doc treatment regimens. However, the inclusion of an effect-compartment with either a log-linear or sigmoidal PD effect term allowed for population predictions of grade 3/4 neutropenia consistent with results from the literature.

An NMPC algorithm was used to develop Doc administration schedules for three separate model structures: (i) Friberg model with updated parameters; (ii) effect-compartment with log-linear drug effect; and (iii) effect-compartment with sigmoidal drug effect. For each of these models, three separate Doc schedules were developed based upon model parameters

consistent with median, low risk, and high risk patients. State constraints on ANC were relaxed and incorporated within the system objective function to avoid infeasible controller formulations. Predictions for low risk patients for all three evaluated models, while increasing Doc delivery, are likely artifacts of limited patient neutrophil count samples and should not imply that such an amount of Doc could be delivered to any patient over a 12 week interval. Dose schedule predictions for the median patient using each of the three models increased administration of Doc over a 12 week period compared to a q3w 70 $\frac{\text{mg}}{\text{m}^2}$ regimen and may allow for improved treatment efficacy without an increase in accompanying toxicity. Doc delivery schedules for high risk patients, while delivering 38-62% less total Doc than the schedule for the median patient and 18-52% less total Doc than q3w 70 $\frac{\text{mg}}{\text{m}^2}$, allowed the high risk patient group to avoid grade 3 occurrences of neutropenia.

7.2 FUTURE WORK

Throughout the course of these studies, a number of methodologies regarding the modeling and interpretation of experimental data have been encountered. Some have been applied in the above model development, while many were uncovered after the fact during reflection. What follows are a number of items to consider during model development for increasing the downstream relevance of dose schedule design.

7.2.1 Tumor Models

When modeling tumor data, parameters should not be estimated based upon the average data obtained at individual points. Assuming the PK is identical for each mouse, a necessary assumption in model development, it is immediately recognizable that the PD term is nonlinear and the perturbed treatment progression should depend on the initial volume of the tumor (current models, however, display initial condition independence). Clinical and preclinical evidence support the premise that treating a smaller tumor is more likely to result in treatment success. From a modeling standpoint, these would be the tumors

that displayed a slower overall growth rate, hence, they are less likely to recover following initial treatment cycles. Developing PD parameters based upon the average tumor volumes obtained at individual time points over a distributed initial tumor volume range will be preferentially biased towards under-predicting the actual tumor treatment effect. Taking this concept one step further, individual tumor growth models should also be developed for each individual xenograft.

7.2.1.1 Untreated Tumor Growth Evaluation The evolving tumor growth profiles are dependent upon two system variables: (i) initial condition effects stemming from implantation of the xenograft fragment, vascularization, and subsequent growth; and (ii) growth rate defined by the cycling fraction of the tumor (often viewed as S -phase fraction) that is dependent on a number of environmental factors and ultimately defines the xenograft doubling time. For initial condition effects, these can be viewed as time-shifted xenografts with identical tumor progression trajectories; identical tumor progression parameters should be sufficient for describing the progression of each of these tumors. For trajectories which do not appear as time-shifted, these would be categorized as xenografts displaying altered tumor progression dynamics and require individual parameter identification. While this would at first seem to be data limited, the identification of models, even for the age-structured PBEs described above, can be formulated using the following framework: (i) assume a standard transition rate within both S -phase and M -phase compartments; (ii) evaluate G -phase transition using tumor progression data from implantation to the start of treatment, or if this short term progression agrees with that of a control xenograft, the duration of the study. For the 4-phase saturating model, restrict G -phase to S -phase progression to literature values, then evaluate parameters for k_{GQ} and k_{QG} , which can not be guaranteed as unique. Finally, (iii) base the system θ upon the entire set of data. It should be noted that this approach is non-ideal for G -phase active agents and would require additional information regarding the G - and Q -phase transition relationship to ensure model accuracy.

7.2.1.2 Inclusion of Natural Apoptosis Another concern is the failure to include non-drug induced cell apoptosis within the tumor growth model, or, when it is included,

to ground the function based on experimental observations as opposed to estimating values which fit the data. As already discussed, the evaluation of individual cell-cycle progression rates based upon a bulk measure of tumor growth will return multiple solutions, a problem only compounded by the addition of an overall rate of apoptosis within the model, or worse, cell-phase dependent rates of apoptosis. Depending on the rate of apoptosis within a solid tumor, the estimated parameters for tumor growth dynamics may significantly under-predict the actual rate of proliferation and provide inaccurate tumor progression predictions during the course of treatment. There have been some modeling attempts to selectively limit apoptosis to individual phases (*i.e.*, probabilistically most likely during cell division) [196, 197], however, other authors have had more success in model development by including equivalent apoptotic rates in every progressing model phase [65]. One may observe apoptotic rates from proliferating cells *in vitro*, however, this rate is dependent on the degree of confluence within the culture and increases as cells form a complete monolayer. Further, these observations would likely serve as a lower bound on apoptotic rates for solid tumors, which have additional apoptotic influences due to environmental conditions (*i.e.*, hypoxic environment, low pH conditions) and the immune system of the host. Whether apoptosis is a significant factor during unperturbed tumor progression remains unconfirmed, however, apoptosis following treatment (*i.e.*, PD effect) requires further evaluation to improve both the model accuracy and applicability to dose schedule development.

7.2.1.3 Accurate PD Terms/Kernels Following treatment, susceptible cells have their growth trajectory altered, leading to either prolonged phase residence time while the cell recovers or, if unsuccessful in repairing cellular damage, due to apoptosis. However, almost all tumor treatment models have an immediate death effect, eliminating the contributions of affected cells from the overall volume. There is a tendency in these models, however, to over predict the degree and onset of drug effect, and other authors have investigated additional model compartments for representing cells undergoing apoptosis [147, 198]. Some models have included transition rates back and forth between affected and unaffected cellular compartments [65, 117], though, these multiple state representations encounter the same difficulties regarding multiple solutions as those discussed in estimating cell-cycle parameters,

with the additional disadvantage that there is little biological insight for grounding parameter values within specific bounds. Basse and coauthors included an apoptotic compartment within a DNA-structured cell-cycle PBE, tracking apoptotic cells based on DNA degradation, a novel approach for developing a PD effect relationship [198]. Flask experiments involving cultures of a melanoma cell line (NZM13) exposed to paclitaxel for 72 hours were performed, with cells collected at 0, 18, 48, 72, and 96 hours and subsequent cell-cycle fraction evaluation using flow cytometry. Similar approaches can be utilized in constructing more accurate PD dynamics with different tumor lines and drugs, taking into account the need to titrate exposure levels (*e.g.*, more accurate representation of PK profile) in addition to exploring alternative dosing levels.

7.2.1.4 Bulk Tumor Measurement Errors It is important to consider possible errors when validating a PD effect model based on bulk tumor volume measurements. Previously in this dissertation (Chapter 2), it has already demonstrated that progression can be represented by including phase-specific effect within any phase, implying that the current representations of PD effect are already under-defined. An additional concern is the reliability of a bulk tumor measurement for gauging the degree of anti-tumor effect following treatment. For the untreated case, the measurement device, typically digital calipers, have an accuracy of $\pm 5\%$ in the measured directions. These errors may result in a 16% error based on tumor volume calculations using the longest tumor dimension, l , and the second longest dimension, w , as follows:

$$V = \frac{lw^2}{2}$$

This bound on error neglects skin and hair contributions to the measurement, which have a decreasing effect on measurement error as the overall size of the xenograft increases. Additionally, caliper measurements can not distinguish necrotic portions of a xenograft which may have arisen during tumor progression. Following treatment, volume measurement errors can be compounded due to inflammation and edema resulting from cell apoptosis and necrosis within a tumor. While apoptotic events are observed rapidly *in vitro* following treatment (0-4 hours), regression of the bulk tumor mass may not occur until >4 days following the

start of treatment. This mismatch of timescale dynamics between PK profile and PD onset is often neglected during model development or approximated using indirect response models. Furthermore, preclinical regimens with repeating cycles may display more rapid xenograft regression during initial or subsequent cycles. Possible explanations of this phenomena are an increased localization of macrophages, responding to apoptotic cells from the initial cycle, or acclimation of the tumor mass on follow-up treatments (*e.g.*, decreased inflammation). Better understanding and inclusion of these bulk tumor altering effects would improve both treated and untreated tumor growth model quality, allowing for increased accuracy of downstream schedule development.

7.2.2 Neutrophil Toxicity Model

The neutrophil model investigated herein utilized a structure developed and validated by Friberg *et al.* across a number of different chemotherapeutics [3]. Alterations to the model structure, however, were necessary when evaluating alternative Doc dosing regimens in order to accurately describe observed clinical neutrophil progression. A number of items remain to be addressed regarding the validation and clinical relevance of this model structure.

7.2.2.1 Low Dose Model Validation The model developed by Friberg *et al.* [3] was adapted with both a Hill function effect term, indicating a threshold drug concentration level necessary for manifestation of the PD effect, and a filter constant to reduce the effect of Doc plasma concentration during the infusion on model predictions. However, data from only a few patients were available for developing this model, and typical baseline neutrophil counts from these patients were two or more fold greater than typical population baselines. As such, additional patient data would aid in the validation of both the parameter values and the model structure. Also, while a comprehensive PBPK model was developed for predicting human Doc tissue concentrations, the PD effect on hematopoietic stem cells was based on a filtered circulating Doc plasma concentration. Ideally, the model would be updated with an additional compartment depicting bone marrow Doc concentrations to provide a more accurate representation of hematopoietic stem cell exposure to Doc. Alternatively,

the current structure could be updated to relate the unbound fraction of Doc, based on the predicted PK profile and patient-specific measures, to downstream PD effect. Karlsson *et al.* have explored using a number of metrics for generating a population PD model for predicting the toxicity effects from Doc treatment, noting only a correlation between patient AAG and the bilinear effect constant in their PD model [106]. Baker *et al.* have also found a significant correlation between the free fraction of Doc to AAG (decreasing free fraction with increasing AAG levels) and the unbound AUC of Doc in plasma to worst grade of neutropenia (increased unbound AUC leads to increased toxicity, a correlation not observed based on total Doc AUC) [8]. As additional patient characteristics (*e.g.*, albumin) also affect the unbound fraction of Doc without altering AAG levels, unbound fraction may serve as a more reliable and appropriate metric for predicting patient toxicity.

7.2.2.2 GCS-F Neutrophil Models Therapeutic regimens often include other drugs, either for increasing the efficacy of treatment or aiding in patient recovery. With Doc treatments, it is common to have concurrent GCS-F administered to aid in neutrophil recovery following Doc administration. While the present model did not include an explicit representation for GCS-F within the model structure, other more involved structures from the literature can relate administration of GCS-F to increases in neutrophil production [51]. Using such a model, the multi-input problem (Doc and GCS-F administration) could be evaluated using a NMPC algorithm to determine if the efficacy and patient quality of life could be improved under different treatment regimens.

7.2.2.3 Objective Function Formulation Objective functions during these studies were limited to either following a desired tumor trajectory or maximizing the total amount of Doc delivered subject to toxicity constraints. As illustrated earlier, attempting to follow a prespecified tumor regression trajectory raises numerous ethical and practical questions, leaving us no better off than previous solutions generated using optimal control or open-loop systems analysis. Likewise, maximizing dose subject to toxicity constraints neglects the repercussions of prolonged neutrophil counts beneath homeostatic levels. Future objective function formulations can investigate the inclusion of an integrated neutrophil metric or

time above additional thresholds. Also, the objective function can be extended to include both tumor regression and toxicity aspects with a weighting preference towards toxicity constraints as these manifest at earlier points during treatment and may cause the premature discontinuation of a regimen.

APPENDIX A

NOMENCLATURE

Abbreviations

ANC	absolute neutrophil count
ALB	albumin
AAG	α_1 -acid glycoprotein
AIC	Akaike's information criterion
ALT	alanine aminotransferase
AST	asparatate aminotransferase
AUC	area under the curve
BSA	body surface area
CHOP	cyclophosphamide/doxorubicin/vincristine/prednisone
CL	clearance
Doc	docetaxel
ER+	estrogen receptor positive
GCS-F	granulocyte colony stimulating factor
GM	Gompertz model
GMC	Gompertz model controller
GMCS-F	granulocyte macrophage colony stimulating factor
HSV	Hankel singular value

HTM	4-hydroxytamoxifen
IV	intravenous
9NC	9-nitrocamptothecin
PE	performance error
PD	pharmacodynamic
PK	pharmacokinetic
PBPK	physiologically-based pharmacokinetic
MAPE	median absolute performance error
MILP	mixed-integer linear programming problem
MINLP	mixed-integer nonlinear programming problem
MSKCC	Memorial Sloan-Kettering Cancer Center
MTT	mean transit time
NONMEM	nonlinear mixed-effects modeling
NS	normalized sensitivity
ODE	ordinary differential equation
PBE	population balance equation
PET	positron emission topography
q3w	drug dosing once every three weeks
QCM	quiescent cell model
QCMC	quiescent cell model controller
RS	relative sensitivity
RMSPE	root mean squared performance error
SCID	severe combined immunodeficient
SCM	saturating-rate cell model
SCMC	saturating-rate cell model controller
SERM	selective estrogen receptor modulator
SSE	sum squared error

UPCI	University of Pittsburgh Cancer Institute
WSSE	weighted sum squared error

Notation

a_{ci}	minimum transition age during i -phase
$a_{ci_{up}}$	value after which a constant i -phase transition occurs
B_i	toxicity bounds for the neutrophil model
C_i	concentration in compartment i
C_{i_e}	extravascular concentration of compartment i
C_{i_v}	vascular concentration of compartment i
$[Doc]$	plasma docetaxel concentration
D_i	generic drug concentration for drug i
E_{drug}	drug effect
E_i	filtered generic drug concentration for drug i
E_{max}	maximum drug effect
EC_{50}	drug concentration necessary for 50% of E_{max}
F	filtered docetaxel concentration
F_i	tissue blood flow rate in compartment i
$G(j\omega)$	n -state original model
$G_r(j\omega)$	reduced k -state model
f_{hem}	hematocrit fraction
f_{unb}	unbound plasma fraction
i	index variable
j	index variable
k	time step
k_{cl_i}	metabolic elimination rates in compartment i
k_D	cell-kill rate

k_f	filter rate
k_i & k_{ij}	transition rate constants
k_{iev}	extravascular to vascular transition rate in compartment i
k_{iv}	vascular to extravascular transition rate in compartment i
k_M	M -phase cell-kill rate
k_S	S -phase cell-kill rate
k_{tr}	neutrophil transition rate
ℓ	length of a tumor during measurement
m	manipulated variable moves used in model predictive control algorithms
m_{ci}	minimum transition mass during i -phase
$m_{ci_{up}}$	value after which a constant i -phase transition occurs
M_i	big-M constraints
N_0	initial tumor volume; initial neutrophil count
N	tumor size; circulating neutrophil count
N_i	tumor volume in i -phase (deterministic)
$N_i(a, t)$	cell density in i -phase (age-structured)
$N_i(m, t)$	cell density in i -phase (mass-structured)
N_t	total tumor volume (all phases)
n	scaling parameter for the linear E_{drug} formulation
p	prediction horizon used in model predictive control algorithms
P	proliferating neutrophil compartment
P_i	partition coefficient in compartment i
R	reference trajectory
$\dot{R}(m)$	mass accumulation rate
t	time
T_i	neutrophil transition compartment i

$t_{\frac{1}{2}}$	half-life
u	input to a system
u_{min}	lower bound on the input
u_{max}	upper bound on the input
V_i	compartment volume
V_{ie}	extravascular compartment volume
V_{iv}	vascular compartment volume
w	width of a tumor during measurement or week in which a measurement is taken
W_1	output weighting vector for parameter estimation
x	internal state variable
X_G	number of cells in the lumped G -phase of the cell-cycle
X_{G_1}	number of cells in the G_1 -phase of the cell-cycle
X_M	number of cells in the lumped M -phase of the cell-cycle
X_Q	number of cells in the Q -phase of the cell-cycle
X_S	number of cells in the S -phase of the cell-cycle
X_i	drug mass in compartment i
y	outputs
Y_{act}	observed output value
Y_{pred}	model predicted output value

Greek Letters

α	scaling parameter for the log-linear E_{drug} formulation
β	exponent for the log-linear E_{drug} formulation
β_i	parameter governing the rate of transition through cell phase i
β_i	ultimate transition rate through i -phase
Δu	change in the input
η	binary vector of week-to-week toxicity constraint violations

Γ_i	weight of the importance of i in the objective function
$\Gamma_i(a)$	phase transition rate (age-structured)
$\Gamma_i(m)$	phase transition rate (mass-structured)
γ_1	rebound effect within the neutrophil model
γ_2	Hill coefficient in the sigmoidal drug effect model
κ	binary vector of weekly toxicity constraint violations
μ	mean
ϕ	binary vector of weekly toxicity constraint violations
ρ	parameter vector
σ	standard deviation
σ_i^H	i th Hankel singular value of the original model
θ	plateau population in tumor growth
τ_i	sharpness of the i -phase transition function
τ_{ij}	system time constant, unless specified otherwise
τ	pseudo-doubling time for tumor volumes governed by Gompertzian growth

APPENDIX B

PBPK MODEL EQUATIONS

The complete set of equations for the Doc mouse PBPK model are shown below.

Venous Blood

$$\begin{aligned}\frac{dC_{ven}}{dt} &= \frac{\sum_j F_j C_{j_e} - F_{tot} C_{ven}}{V_{ven}(1 - f_{hem})} + \frac{u(t)}{V_{ven}(1 - f_{hem})} \\ &\quad + \frac{f_{hem}}{(1 - f_{hem})} k_{rbcp\text{las}} C_{rbcv} - k_{pl\text{as}rbc} f_{unb} C_{ven} \\ \frac{dC_{rbcv}}{dt} &= -k_{rbcp\text{las}} C_{rbcv} + \frac{(1 - f_{hem})}{f_{hem}} k_{pl\text{as}rbc} f_{unb} C_{ven}\end{aligned}$$

Lung

$$\begin{aligned}\frac{dC_{l_v}}{dt} &= \frac{F_l}{V_{l_v}} (C_{ven} - C_{l_v}) - k_{l_{ve}} f_{unb} C_{l_v} + \frac{V_{l_e}}{V_{l_v}} k_{l_{ev}} C_{l_e} \\ \frac{dC_{l_e}}{dt} &= \frac{V_{l_v}}{V_{l_e}} k_{l_{ve}} f_{unb} C_{l_v} - k_{l_{ev}} C_{l_e} + k_{bind_{out}} C_{l_b} - k_{bind_{in}} C_{l_e} \\ \frac{dC_{l_b}}{dt} &= -k_{bind_{out}} C_{l_b} + k_{bind_{in}} C_{l_e}\end{aligned}$$

Arterial Blood

$$\begin{aligned}\frac{dC_{art}}{dt} &= \frac{1}{V_{art}(1 - f_{hem})} (F_l C_{l_v} - F_{tot} C_{art}) + \frac{f_{hem}}{(1 - f_{hem})} k_{rbcp\text{las}} C_{rbca} \\ &\quad - k_{pl\text{as}rbc} f_{unb} C_{art} \\ \frac{dC_{rbca}}{dt} &= -k_{rbcp\text{las}} C_{rbca} + \frac{(1 - f_{hem})}{f_{hem}} k_{rbcp\text{las}} f_{unb} C_{art}\end{aligned}$$

Gut

$$\frac{dC_{g_v}}{dt} = \frac{F_g}{V_{g_v}} (C_{art} - C_{g_v})$$

Brain

$$\begin{aligned}\frac{dC_{b_v}}{dt} &= \frac{F_b}{V_{b_v}} (C_{art} - C_{b_v}) - k_{b_{ve}} f_{unb} C_{b_v} + \frac{V_{b_e}}{V_{b_v}} k_{b_{ev}} C_{b_e} \\ \frac{dC_{b_e}}{dt} &= \frac{V_{b_v}}{V_{b_e}} k_{b_{ve}} f_{unb} C_{b_v} - k_{b_{ev}} C_{b_e} + k_{bind_{out}} C_{b_b} - k_{bind_{in}} C_{b_e} \\ \frac{dC_{b_b}}{dt} &= -k_{bind_{out}} C_{b_b} + k_{bind_{in}} C_{b_e}\end{aligned}$$

Spleen

$$\begin{aligned}\frac{dC_{s_v}}{dt} &= \frac{F_s}{V_{s_v}} (C_{art} - C_{s_v}) - k_{s_{ve}} f_{unb} C_{s_v} + \frac{V_{s_e}}{V_{s_v}} k_{s_{ev}} C_{s_e} \\ \frac{dC_{s_e}}{dt} &= \frac{V_{s_v}}{V_{s_e}} k_{s_{ve}} f_{unb} C_{s_v} - k_{s_{ev}} C_{s_e} + k_{bind_{out}} C_{s_b} - k_{bind_{in}} C_{s_e} \\ \frac{dC_{s_b}}{dt} &= -k_{bind_{out}} C_{s_b} + k_{bind_{in}} C_{s_e}\end{aligned}$$

Liver

$$\begin{aligned}\frac{dC_{li_v}}{dt} &= \frac{1}{V_{li_v}} (F_{li} C_{ab} + F_g C_g + F_s C_{s_v} - (F_g + F_s + F_{li}) C_{li_v}) - k_{li_{ve}} f_{unb} C_{li_v} \\ &\quad + \frac{V_{li_e}}{V_{li_v}} k_{li_{ev}} C_{li_e} \\ \frac{dC_{li_e}}{dt} &= \frac{V_{li_v}}{V_{li_e}} k_{li_{ve}} f_{unb} C_{li_v} - k_{li_{ev}} C_{li_e} + k_{bind_{out}} C_{li_b} - k_{bind_{in}} C_{li_e} - k_{cli} C_{li_e} \\ \frac{dC_{li_b}}{dt} &= -k_{bind_{out}} C_{li_b} + k_{bind_{in}} C_{li_e} - k_{cli} C_{li_b}\end{aligned}$$

Heart

$$\begin{aligned}\frac{dC_{h_v}}{dt} &= \frac{F_h}{V_{h_v}} (C_{art} - C_{h_v}) - k_{h_{ve}} f_{unb} C_{h_v} + \frac{V_{h_e}}{V_{h_v}} k_{h_{ev}} C_{h_e} \\ \frac{dC_{h_e}}{dt} &= \frac{V_{h_v}}{V_{h_e}} k_{h_{ve}} f_{unb} C_{h_v} - k_{h_{ev}} C_{h_e} + k_{bind_{out}} C_{h_b} - k_{bind_{in}} C_{h_e} \\ \frac{dC_{h_b}}{dt} &= -k_{bind_{out}} C_{h_b} + k_{bind_{in}} C_{h_e}\end{aligned}$$

Kidney

$$\begin{aligned}\frac{dC_{k_v}}{dt} &= \frac{F_k}{V_{k_v}} (C_{art} - C_{k_v}) - k_{k_{ve}} f_{unb} C_{k_v} + \frac{V_{k_e}}{V_{k_v}} k_{k_{ev}} C_{k_e} \\ \frac{dC_{k_e}}{dt} &= \frac{V_{k_v}}{V_{k_e}} k_{k_{ve}} f_{unb} C_{k_v} - k_{k_{ev}} C_{k_e} + k_{bind_{out}} C_{k_b} - k_{bind_{in}} C_{k_e} \\ \frac{dC_{k_b}}{dt} &= -k_{bind_{out}} C_{k_b} + k_{bind_{in}} C_{k_e}\end{aligned}$$

Muscle

$$\frac{dC_{m_v}}{dt} = \frac{F_m}{V_{m_v}} (C_{art} - C_{m_v}) - k_{m_{ve}} f_{unb} C_{m_v} + \frac{V_{m_e}}{V_{m_v}} k_{m_{ev}} C_{m_e}$$

$$\frac{dC_{m_e}}{dt} = \frac{V_{m_v}}{V_{m_e}} k_{m_{ve}} f_{unb} C_{m_v} - k_{m_{ev}} C_{m_e} + k_{bind_{out}} C_{m_b} - k_{bind_{in}} C_{m_e}$$

$$\frac{dC_{m_b}}{dt} = -k_{bind_{out}} C_{m_b} + k_{bind_{in}} C_{m_e}$$

Fat

$$\frac{dC_{f_v}}{dt} = \frac{F_f}{V_{f_v}} (C_{art} - C_{f_v}) - k_{f_{ve}} f_{unb} C_{f_v} + \frac{V_{f_e}}{V_{f_v}} k_{f_{ev}} C_{f_e}$$

$$\frac{dC_{f_e}}{dt} = \frac{V_{f_v}}{V_{f_e}} k_{f_{ve}} f_{unb} C_{f_v} - k_{f_{ev}} C_{f_e} + k_{bind_{out}} C_{f_b} - k_{bind_{in}} C_{f_e}$$

$$\frac{dC_{f_b}}{dt} = -k_{bind_{out}} C_{f_b} + k_{bind_{in}} C_{f_e}$$

Tumor

$$\frac{dC_{t_v}}{dt} = \frac{F_t}{V_{t_v}} (C_{art} - C_{t_v}) - k_{t_{ve}} f_{unb} C_{t_v} + \frac{V_{t_e}}{V_{t_v}} k_{t_{ev}} C_{t_e}$$

$$\frac{dC_{t_e}}{dt} = \frac{V_{t_v}}{V_{t_e}} k_{t_{ve}} f_{unb} C_{t_v} - k_{t_{ev}} C_{t_e} + k_{bind_{out}} C_{t_b} - k_{bind_{in}} C_{t_e}$$

$$\frac{dC_{t_b}}{dt} = -k_{bind_{out}} C_{t_b} + k_{bind_{in}} C_{t_e}$$

Other

$$\frac{dC_{o_v}}{dt} = \frac{F_o}{V_{o_v}} (C_{art} - C_{o_v}) - k_{o_{ve}} f_{unb} C_{o_v} + \frac{V_{o_e}}{V_{o_v}} k_{o_{ev}} C_{o_e}$$

$$\frac{dC_{o_e}}{dt} = \frac{V_{o_v}}{V_{o_e}} k_{o_{ve}} f_{unb} C_{o_v} - k_{o_{ev}} C_{o_e} + k_{bind_{out}} C_{o_b} - k_{bind_{in}} C_{o_e}$$

$$\frac{dC_{o_b}}{dt} = -k_{bind_{out}} C_{o_b} + k_{bind_{in}} C_{o_e}$$

APPENDIX C

ACTUAL AND MODEL PREDICTED HUMAN DOC PLASMA CONCENTRATION VERSUS TIME PLOTS

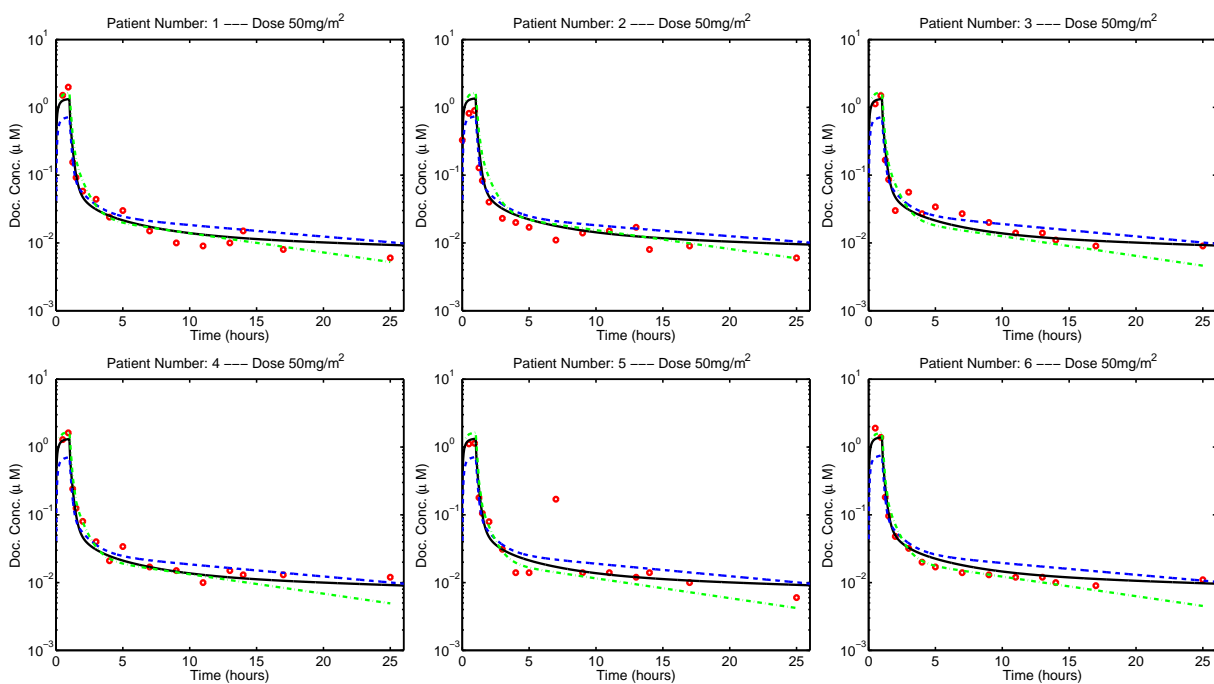


Figure C1: Measured Doc plasma concentration data in humans from UPCI protocol 01-150 dosed at $50 \frac{\text{mg}}{\text{m}^2}$ vs. human PBPK model predictions from the tissue-intensive PBPK (solid), the Bradshaw-Pierce PBPK (dashed), and the population PK Bruno (dash-dot) model.

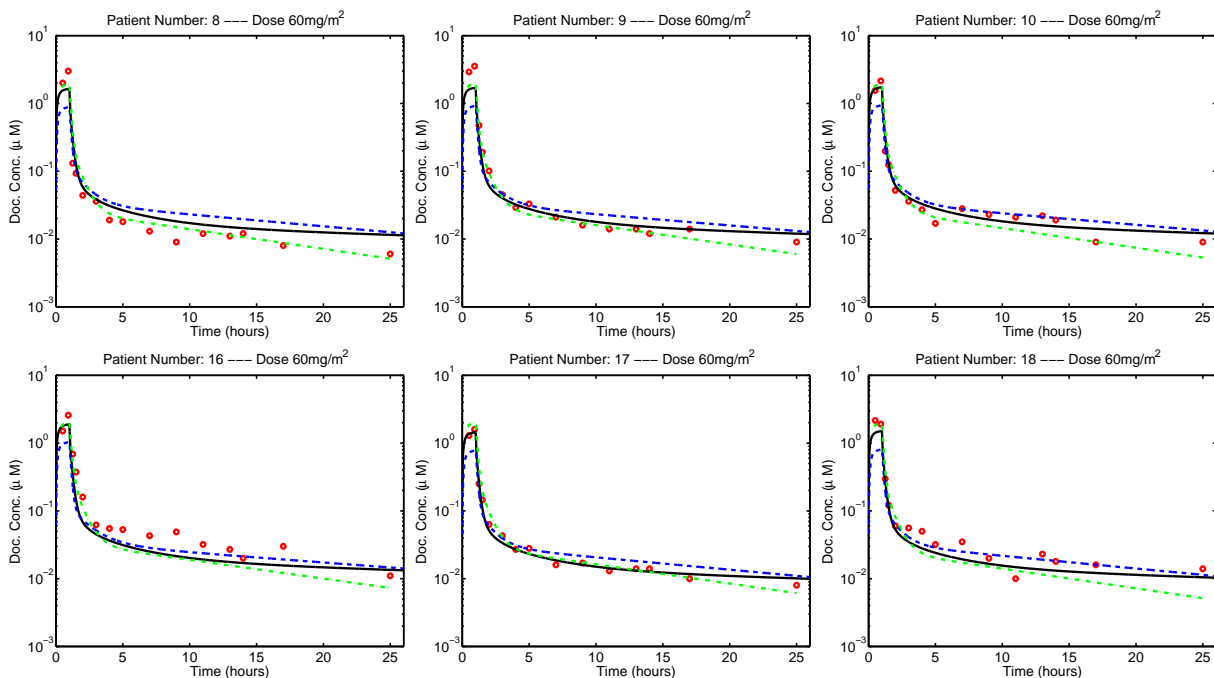


Figure C2: Measured Doc plasma concentration data in humans from UPCI protocol 01-150 dosed at $60 \frac{\text{mg}}{\text{m}^2}$ vs. human PBPK model predictions from the tissue-intensive PBPK (solid), the Bradshaw-Pierce PBPK (dashed), and the population PK Bruno (dash-dot) model.

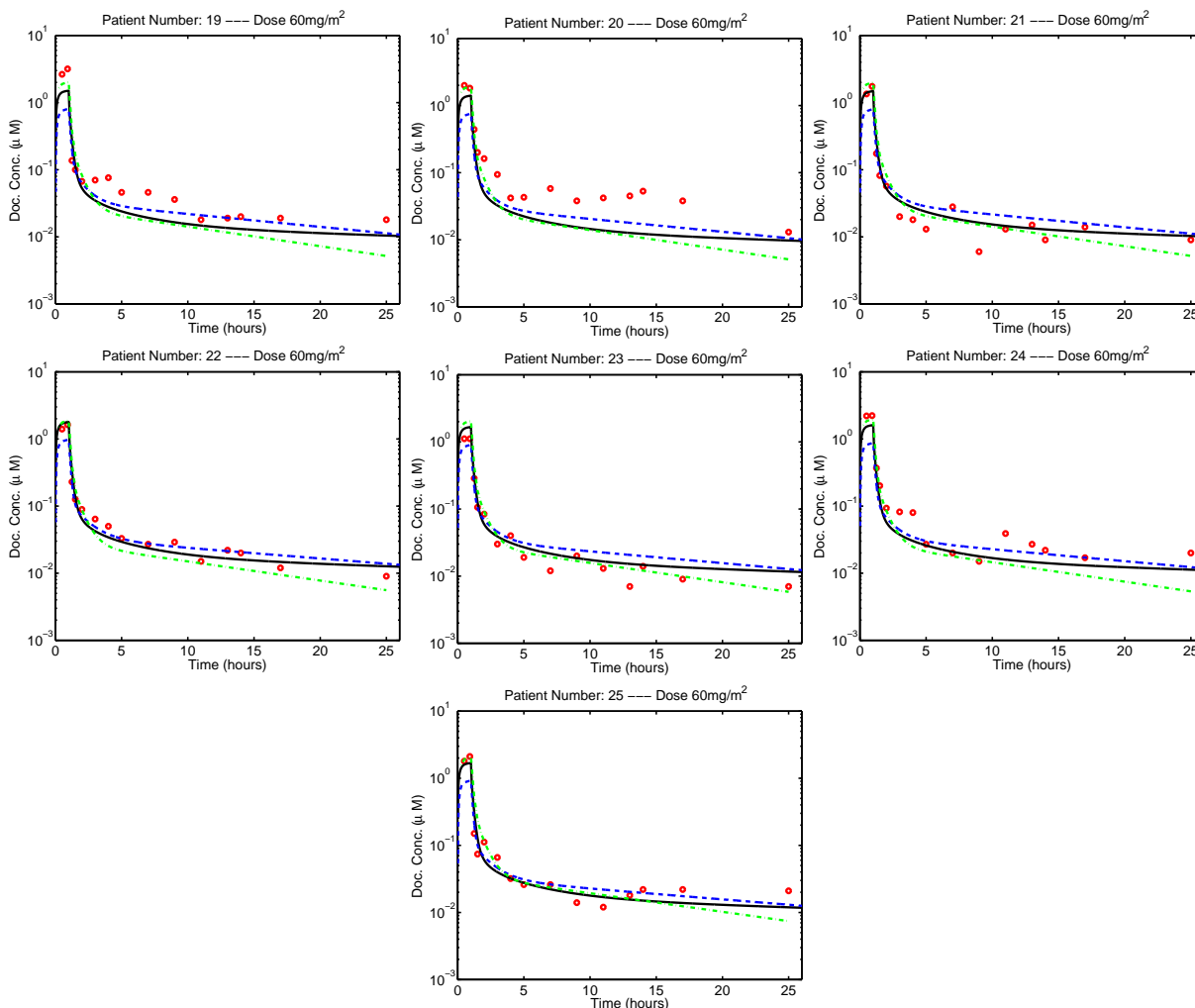


Figure C3: Measured Doc plasma concentration data in humans from UPCI protocol 01-150 dosed at $60 \frac{\text{mg}}{\text{m}^2}$ vs. human PBPK model predictions from the tissue-intensive PBPK (solid), the Bradshaw-Pierce PBPK (dashed), and the population PK Bruno (dash-dot) model.

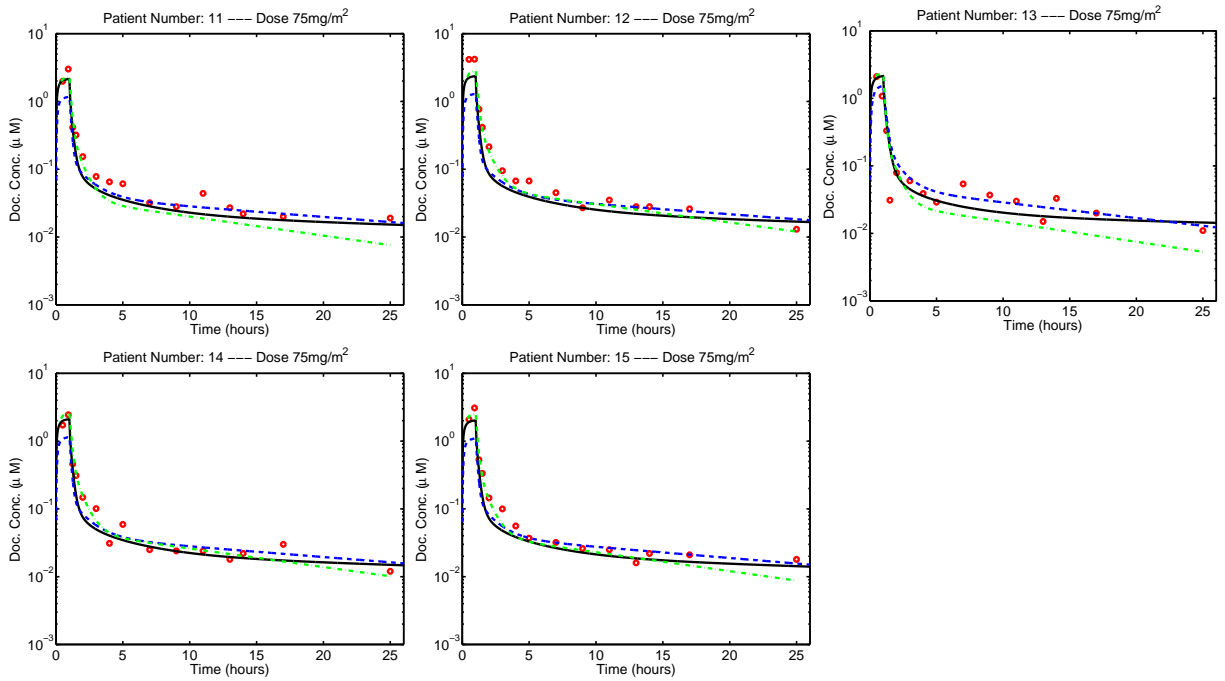


Figure C4: Measured Doc plasma concentration data in humans from UPCI protocol 01-150 dosed at $75 \frac{\text{mg}}{\text{m}^2}$ vs. human PBPK model predictions from the tissue-intensive PBPK (solid), the Bradshaw-Pierce PBPK (dashed), and the population PK Bruno (dash-dot) model.

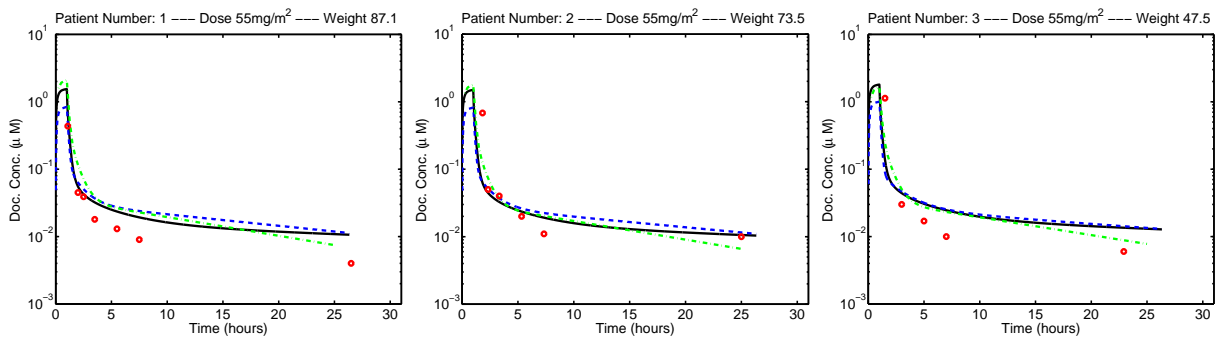


Figure C5: Measured Doc plasma concentration data in humans from a Phase 1 clinical trial at MSKCC [6] dosed at $55 \frac{\text{mg}}{\text{m}^2}$ vs. human PBPK model predictions from the tissue-intensive PBPK (solid), the Bradshaw-Pierce PBPK (dashed), and the population PK Bruno (dash-dot) model.

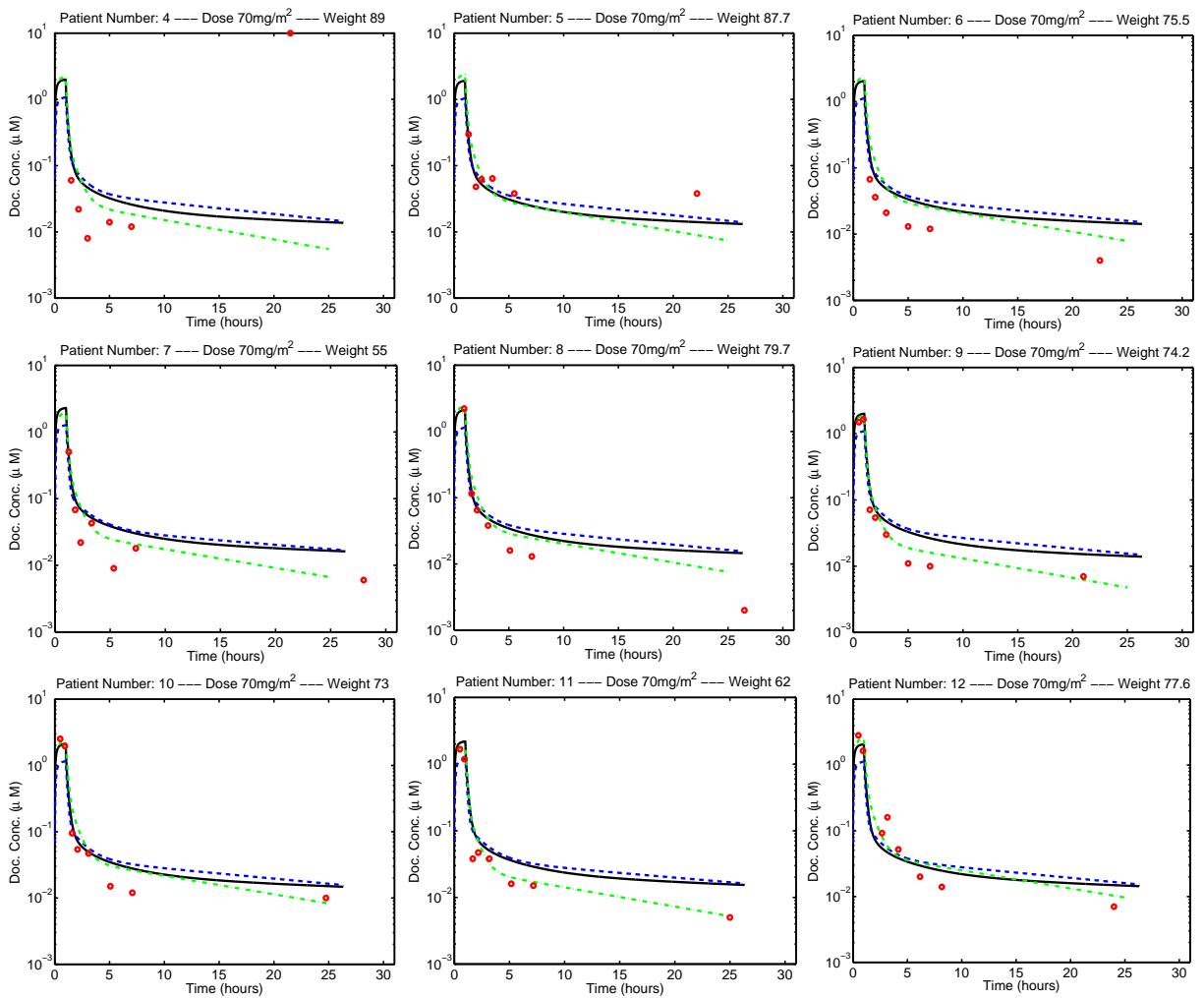


Figure C6: Measured Doc plasma concentration data in humans from a Phase 1 clinical trial at MSKCC [6] dosed at $70 \frac{\text{mg}}{\text{m}^2}$ vs. human PBPK model predictions from the tissue-intensive PBPK (solid), the Bradshaw-Pierce PBPK (dashed), and the population PK Bruno (dash-dot) model.

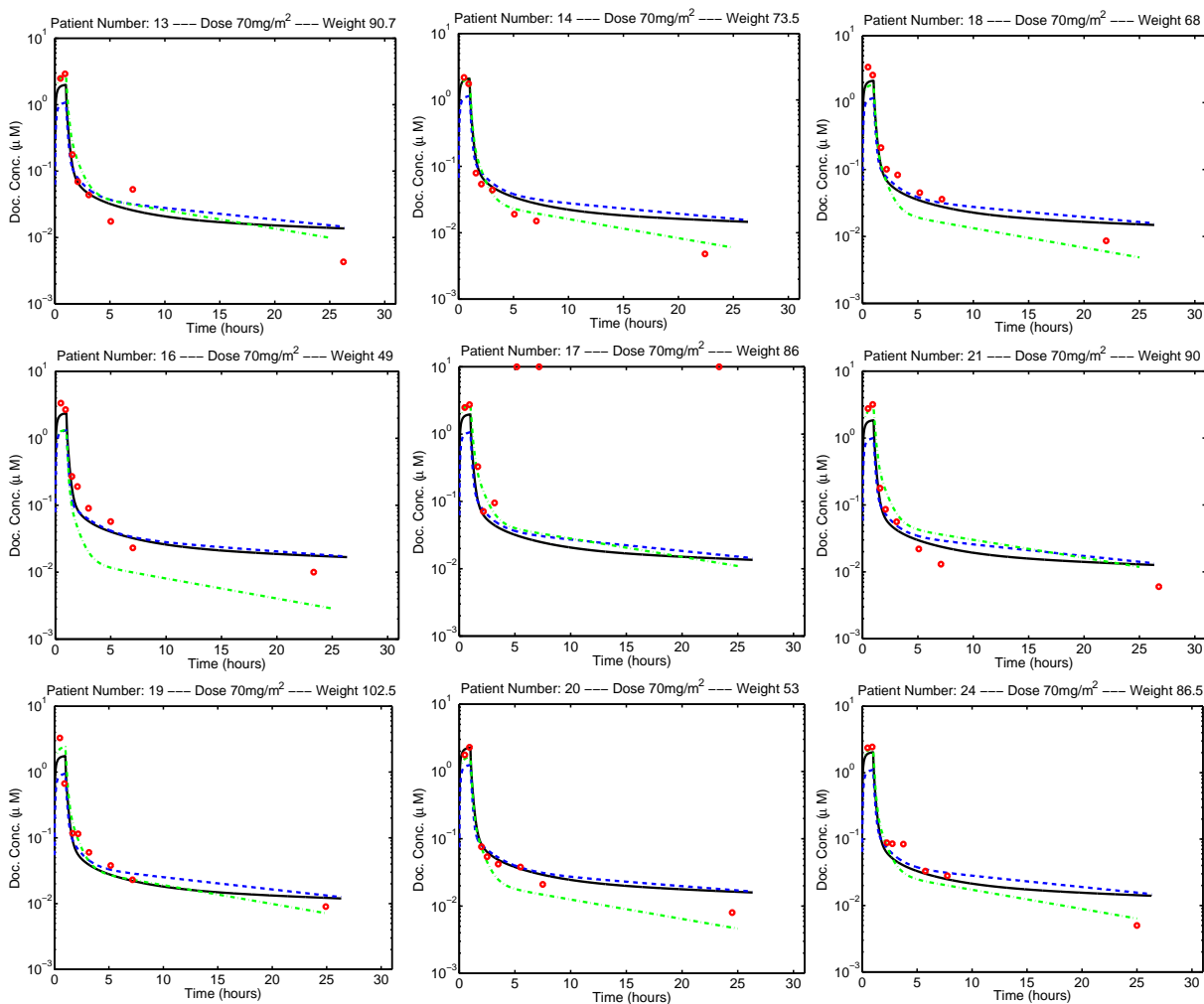


Figure C7: Measured Doc plasma concentration data in humans from a Phase 1 clinical trial at MSKCC [6] dosed at $70 \frac{\text{mg}}{\text{m}^2}$ vs. human PBPK model predictions from the tissue-intensive PBPK (solid), the Bradshaw-Pierce PBPK (dashed), and the population PK Bruno (dash-dot) model.

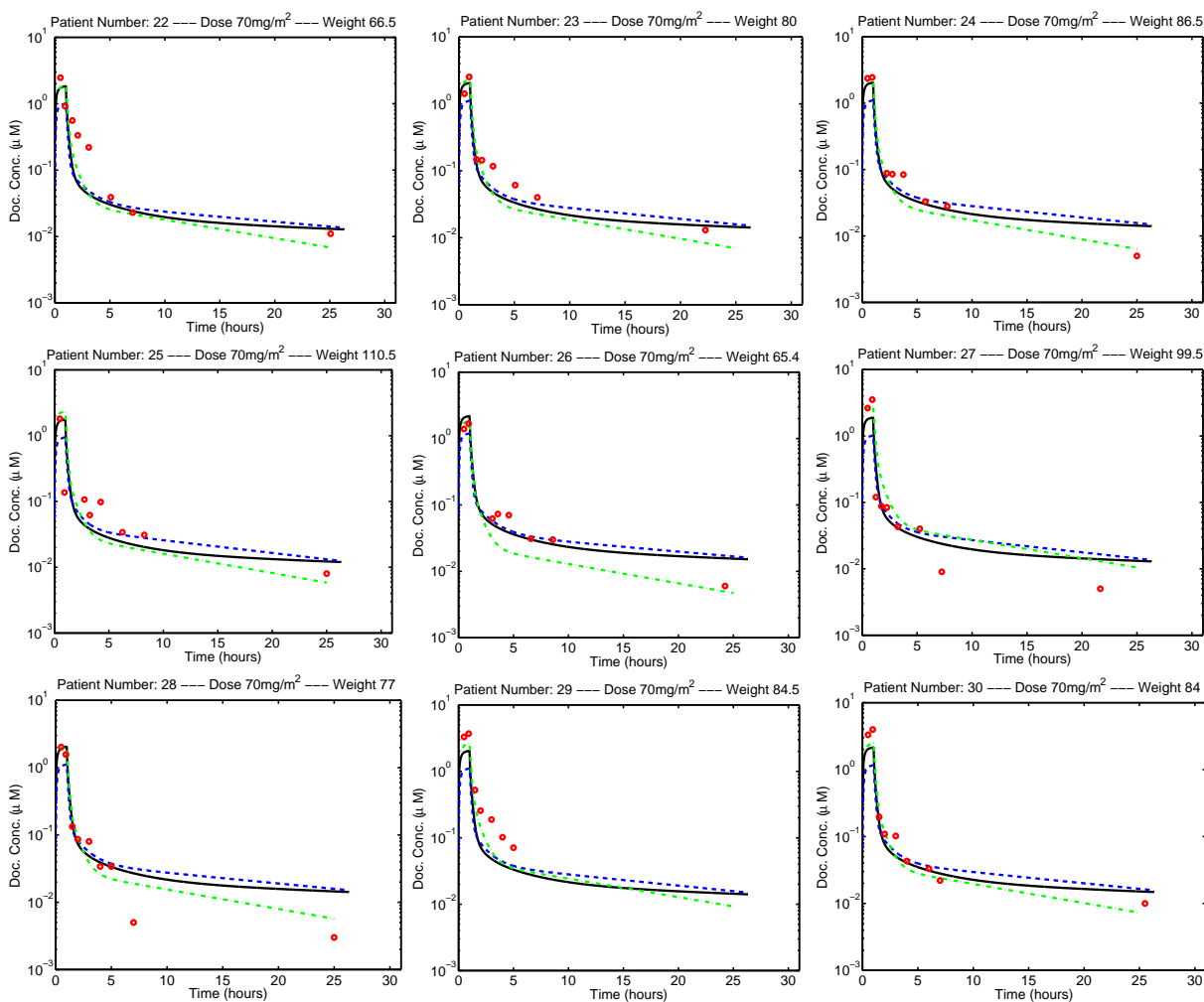


Figure C8: Measured Doc plasma concentration data in humans from a Phase 1 clinical trial at MSKCC [6] dosed at $70 \frac{\text{mg}}{\text{m}^2}$ vs. human PBPK model predictions from the tissue-intensive PBPK (solid), the Bradshaw-Pierce PBPK (dashed), and the population PK Bruno (dash-dot) model.

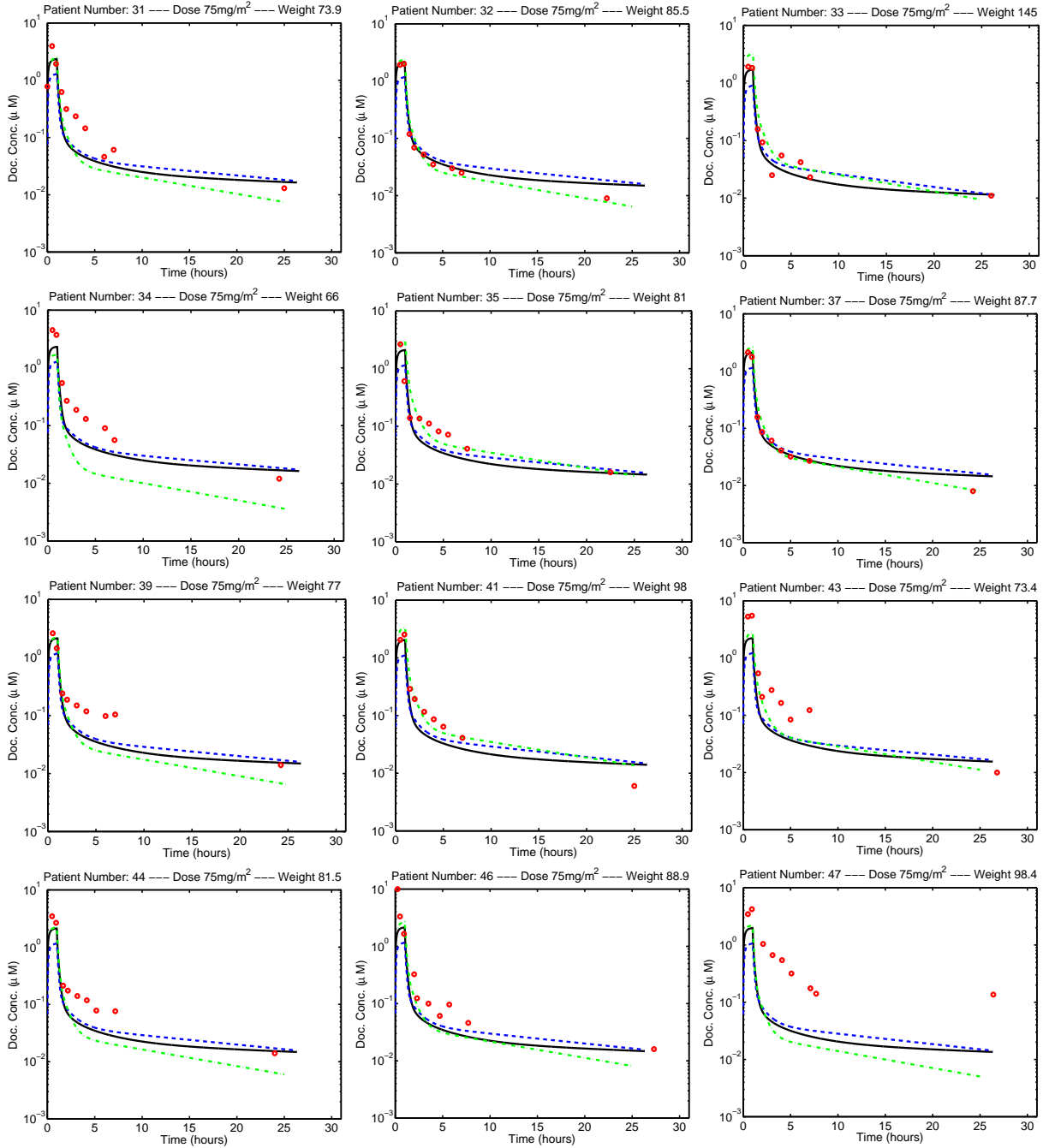


Figure C9: Measured Doc plasma concentration data in humans from a Phase 1 clinical trial at MSKCC [6] dosed at $75 \frac{\text{mg}}{\text{m}^2}$ vs. human PBPK model predictions from the tissue-intensive PBPK (solid), the Bradshaw-Pierce PBPK (dashed), and the population PK Bruno (dash-dot) model.

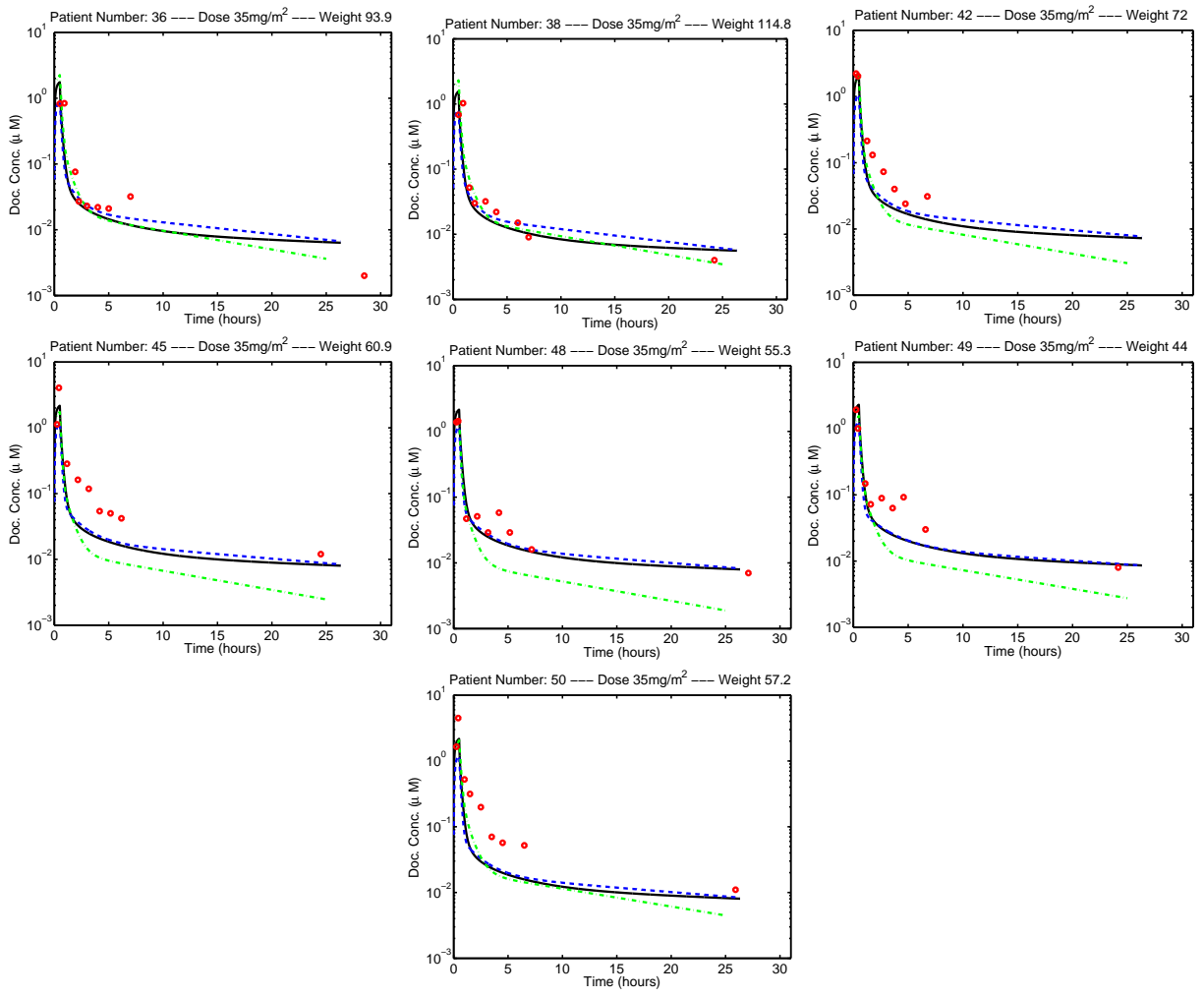


Figure C10: Measured Doc plasma concentration data in humans from a Phase 1 clinical trial at MSKCC [6] dosed at $35 \frac{\text{mg}}{\text{m}^2}$ vs. human PBPK model predictions from the tissue-intensive PBPK (solid), the Bradshaw-Pierce PBPK (dashed), and the population PK Bruno (dash-dot) model.

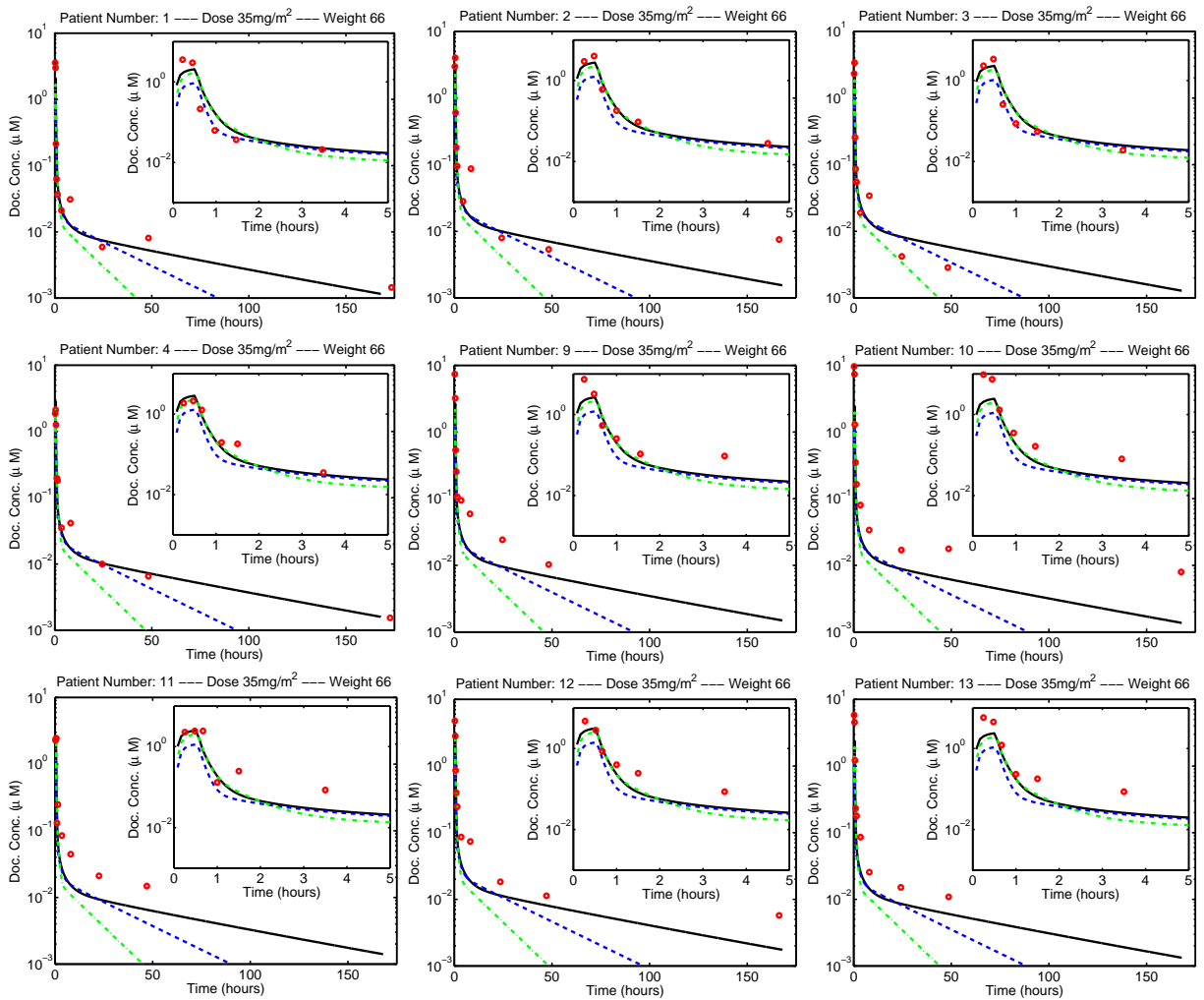


Figure C11: Measured Doc plasma concentration data in humans from a Phase 1 clinical trial at MSKCC in elderly patients dosed at $35 \frac{\text{mg}}{\text{m}^2}$ vs. human PBPK model predictions from the tissue-intensive PBPK (solid), the Bradshaw-Pierce PBPK (dashed), and the population PK Bruno (dash-dot) model.

APPENDIX D

ACTUAL AND MODEL PREDICTED HUMAN DOC PLASMA CONCENTRATION VERSUS TIME PLOTS (UNBOUND FRACTION)

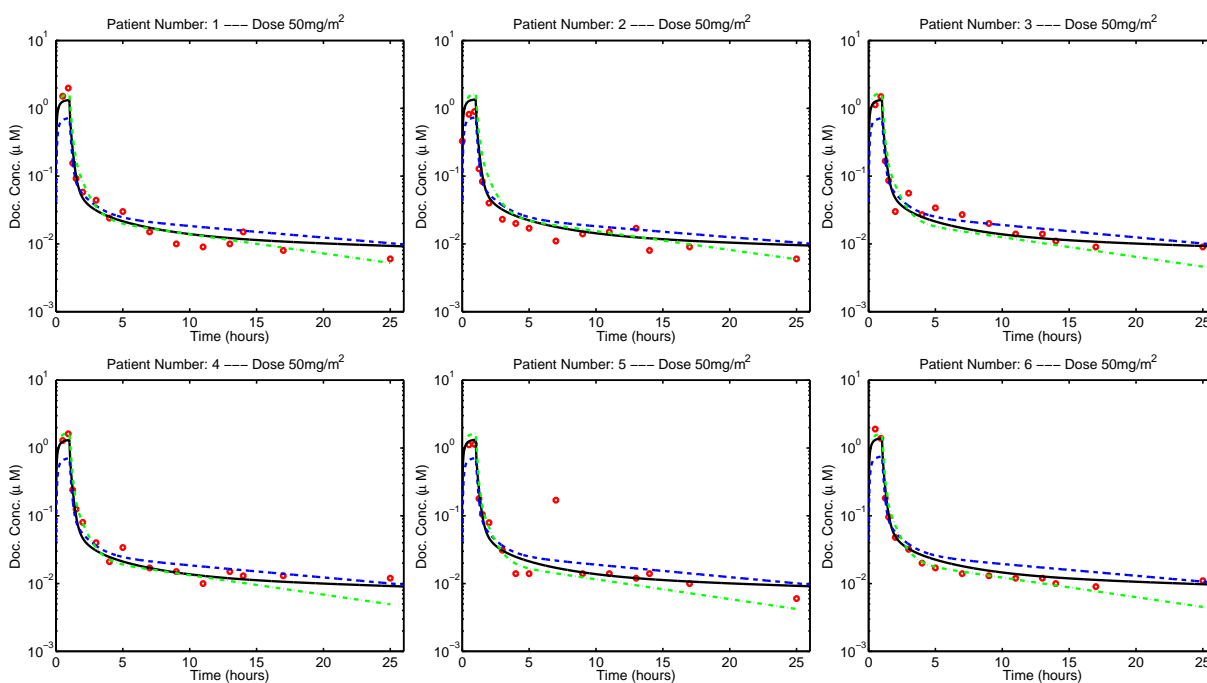


Figure D1: Measured Doc plasma concentration data in humans from UPCI protocol 01-150 dosed at $50 \frac{\text{mg}}{\text{m}^2}$ vs. human PBPK model predictions from the tissue-intensive PBPK (solid), the Bradshaw-Pierce PBPK (dashed), and the population PK Bruno (dash-dot) model.

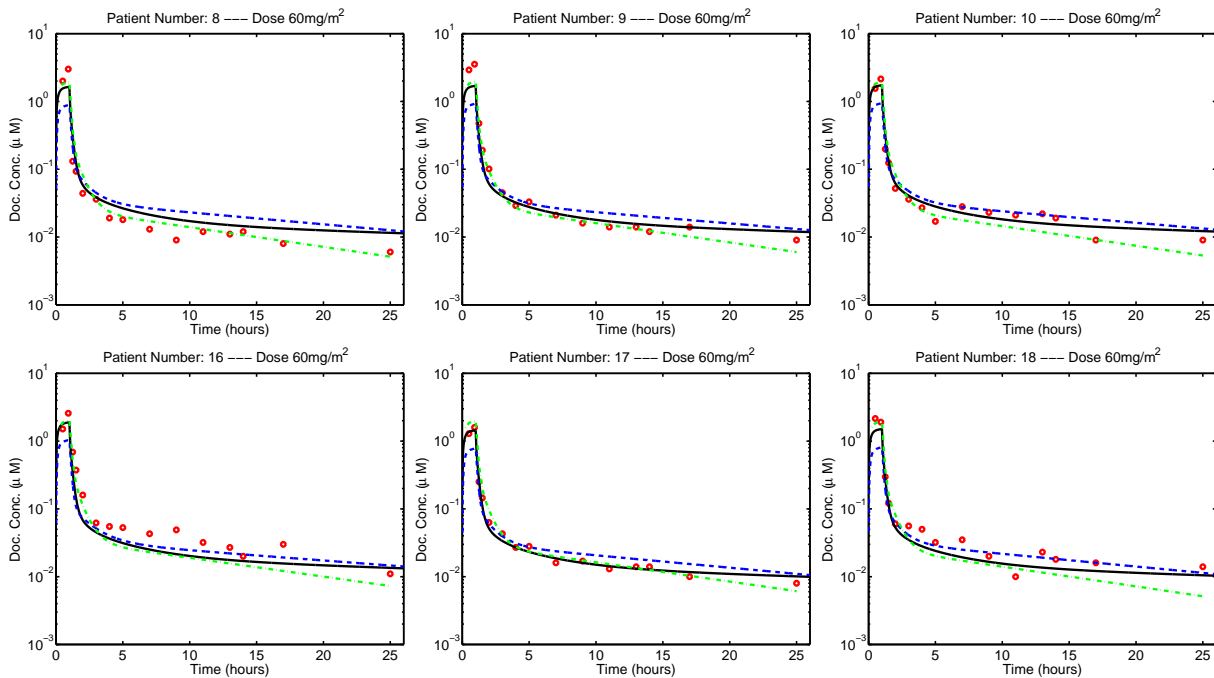


Figure D2: Measured Doc plasma concentration data in humans from UPCI protocol 01-150 dosed at $60 \frac{\text{mg}}{\text{m}^2}$ vs. human PBPK model predictions from the tissue-intensive PBPK (solid), the Bradshaw-Pierce PBPK (dashed), and the population PK Bruno (dash-dot) model.

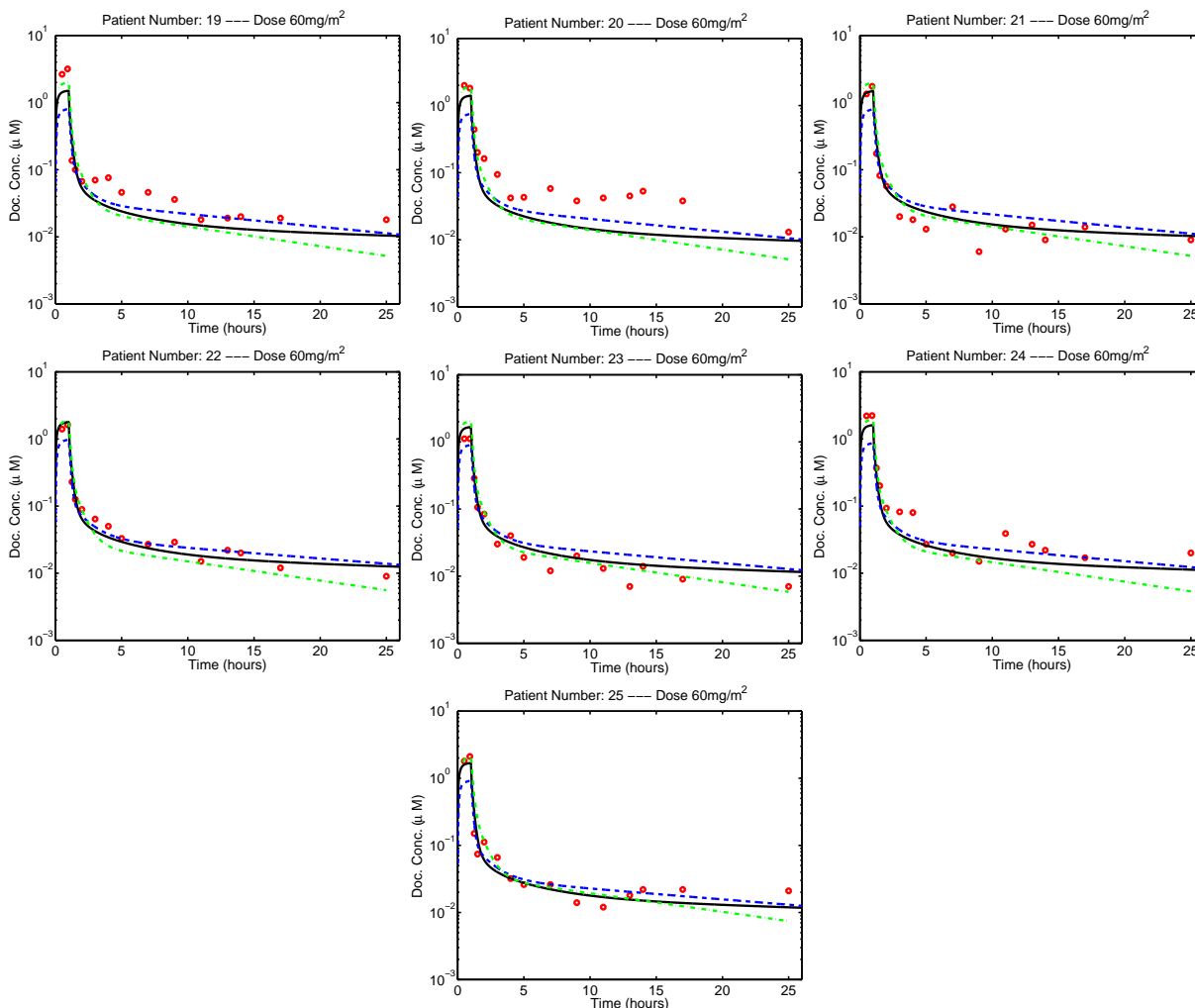


Figure D3: Measured Doc plasma concentration data in humans from UPCI protocol 01-150 dosed at $60 \frac{\text{mg}}{\text{m}^2}$ vs. human PBPK model predictions from the tissue-intensive PBPK (solid), the Bradshaw-Pierce PBPK (dashed), and the population PK Bruno (dash-dot) model.

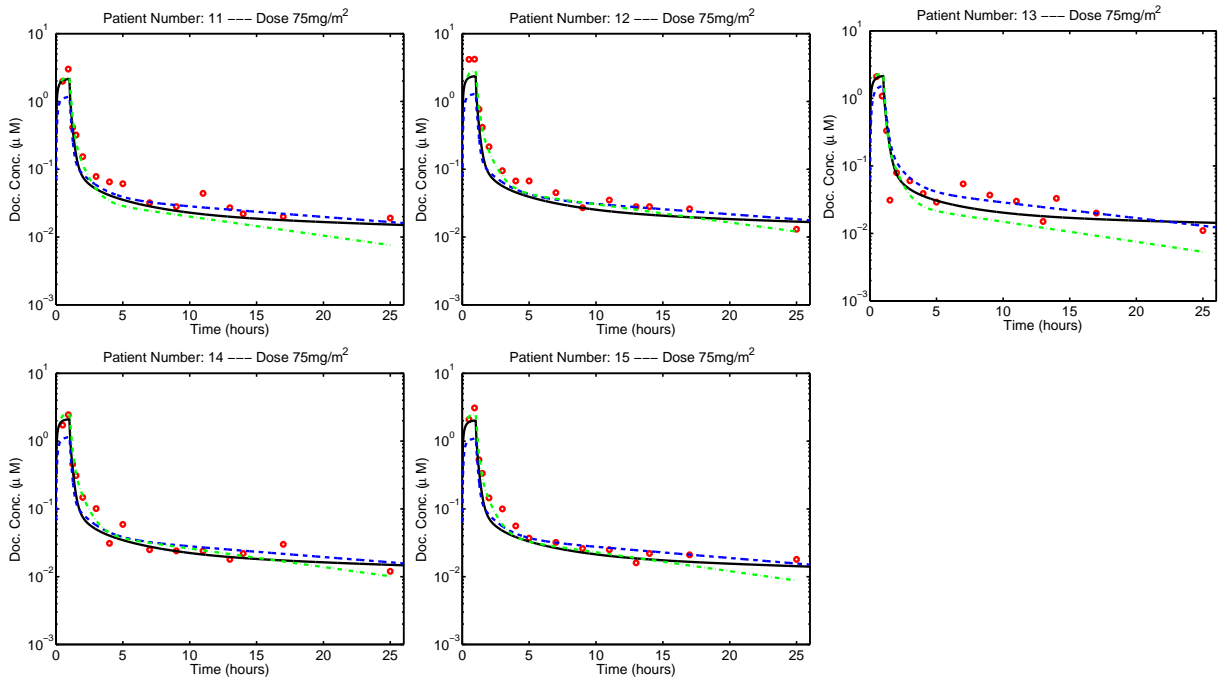


Figure D4: Measured Doc plasma concentration data in humans from UPCI protocol 01-150 dosed at $75 \frac{\text{mg}}{\text{m}^2}$ vs. human PBPK model predictions from the tissue-intensive PBPK (solid), the Bradshaw-Pierce PBPK (dashed), and the population PK Bruno (dash-dot) model.

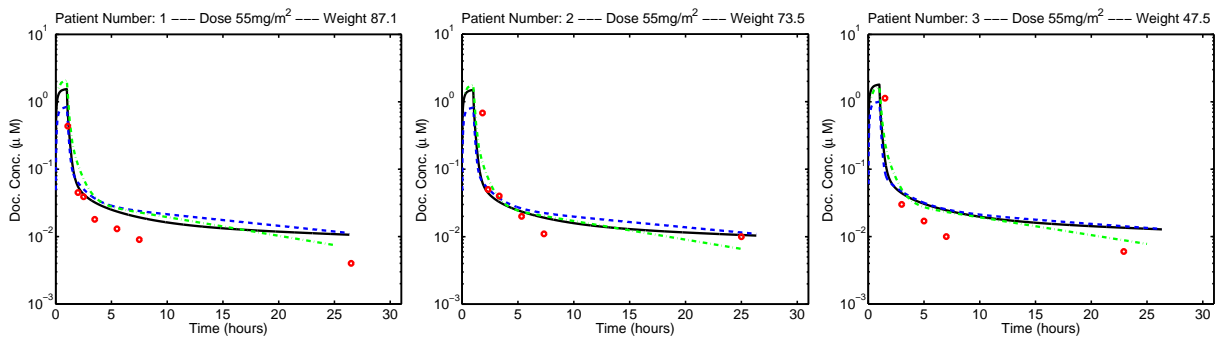


Figure D5: Measured Doc plasma concentration data in humans from a Phase 1 clinical trial at MSKCC [6] dosed at $55 \frac{\text{mg}}{\text{m}^2}$ vs. human PBPK model predictions from the tissue-intensive PBPK (solid), the Bradshaw-Pierce PBPK (dashed), and the population PK Bruno (dash-dot) model.

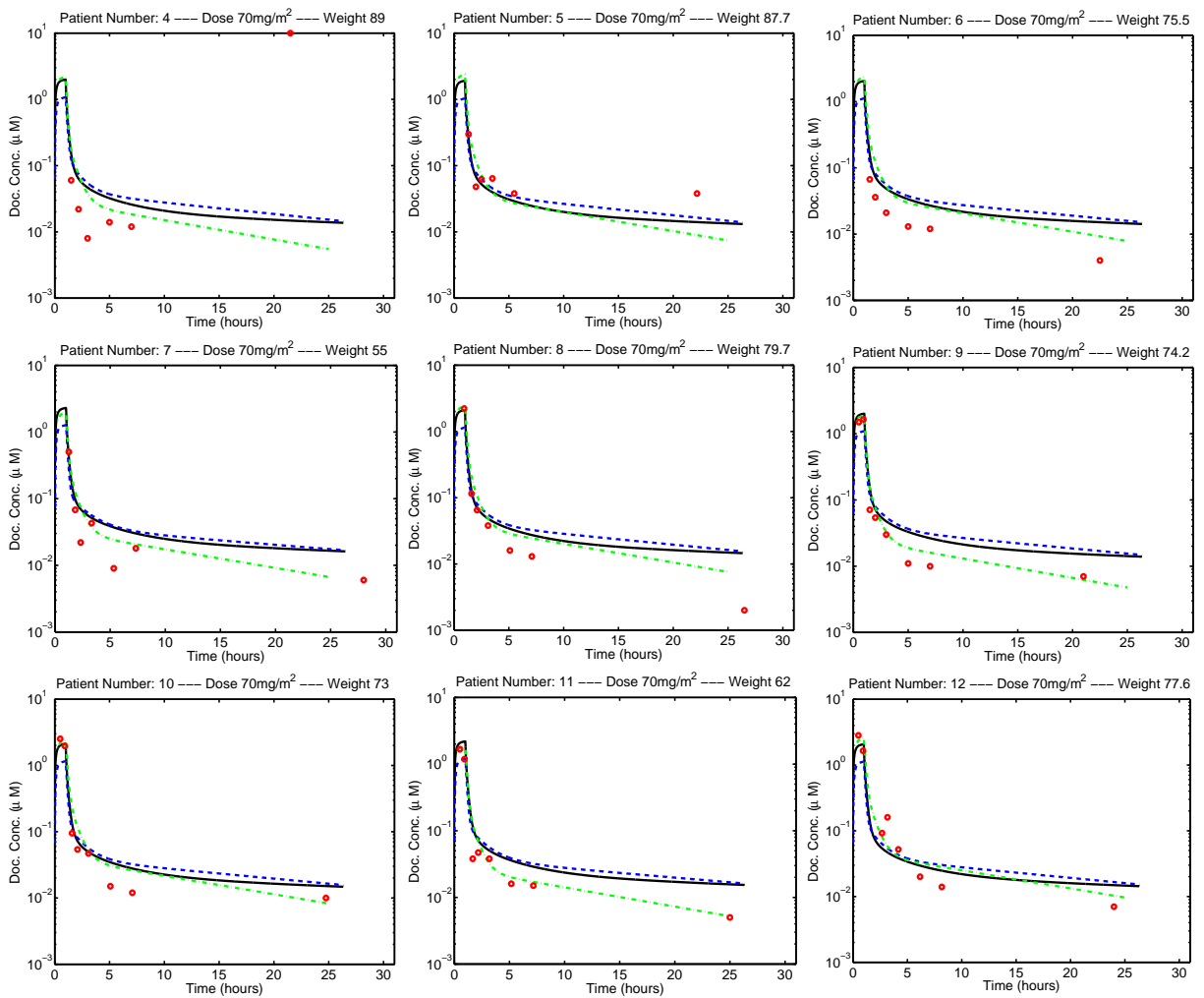


Figure D6: Measured Doc plasma concentration data in humans from a Phase 1 clinical trial at MSKCC [6] dosed at $70 \frac{\text{mg}}{\text{m}^2}$ vs. human PBPK model predictions from the tissue-intensive PBPK (solid), the Bradshaw-Pierce PBPK (dashed), and the population PK Bruno (dash-dot) model.

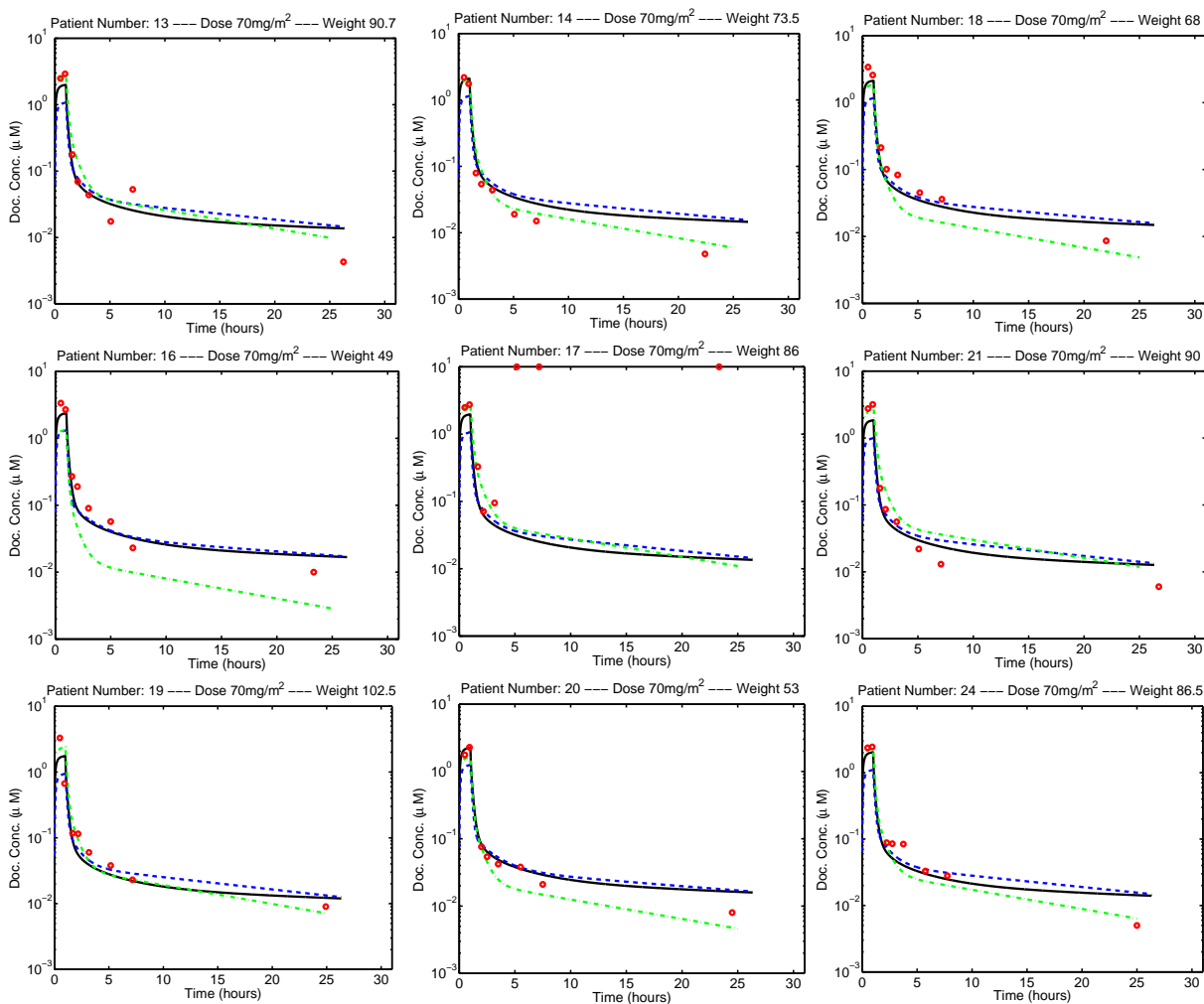


Figure D7: Measured Doc plasma concentration data in humans from a Phase 1 clinical trial at MSKCC [6] dosed at $70 \frac{\text{mg}}{\text{m}^2}$ vs. human PBPK model predictions from the tissue-intensive PBPK (solid), the Bradshaw-Pierce PBPK (dashed), and the population PK Bruno (dash-dot) model.

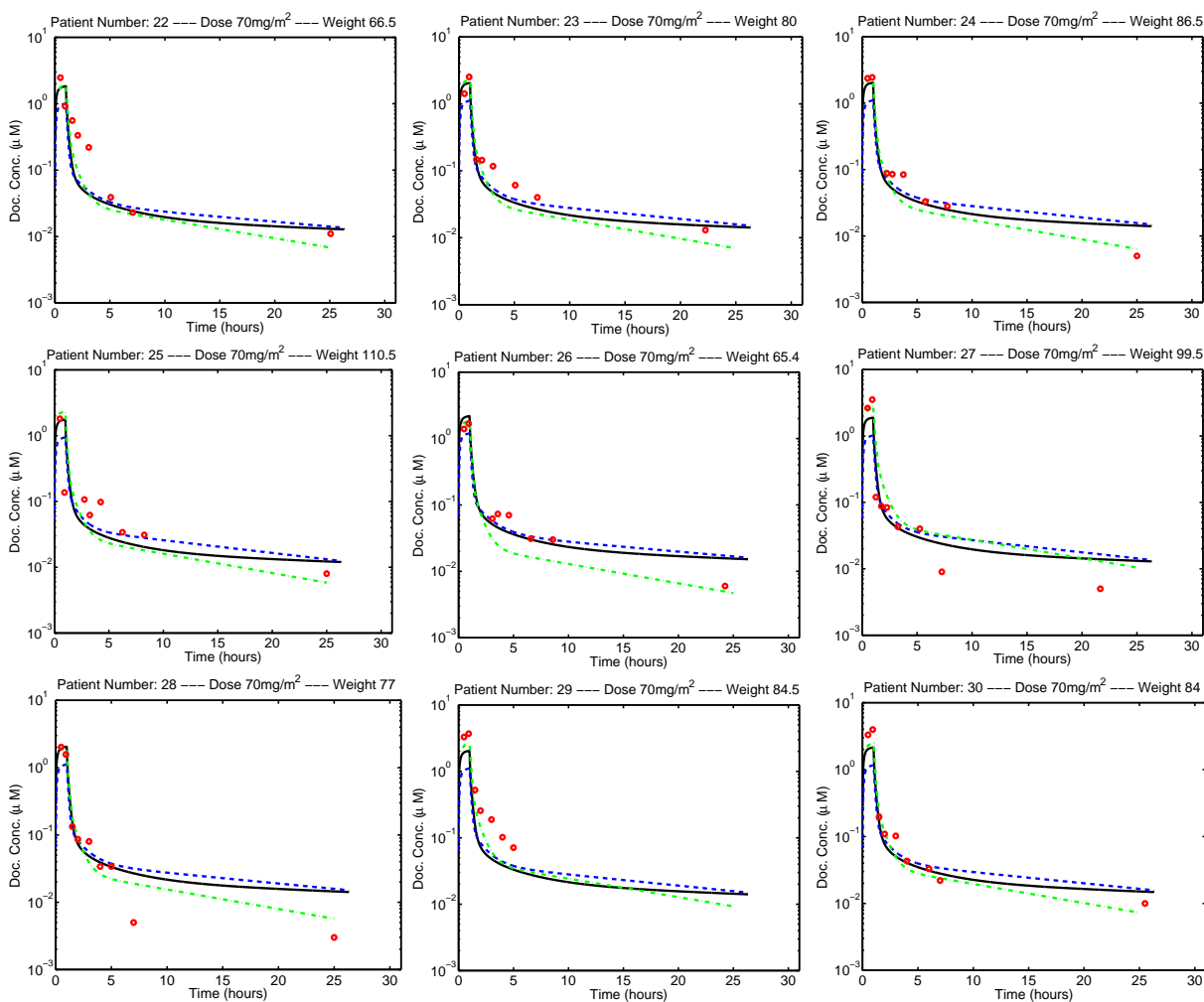


Figure D8: Measured Doc plasma concentration data in humans from a Phase 1 clinical trial at MSKCC [6] dosed at $70 \frac{\text{mg}}{\text{m}^2}$ vs. human PBPK model predictions from the tissue-intensive PBPK (solid), the Bradshaw-Pierce PBPK (dashed), and the population PK Bruno (dash-dot) model.

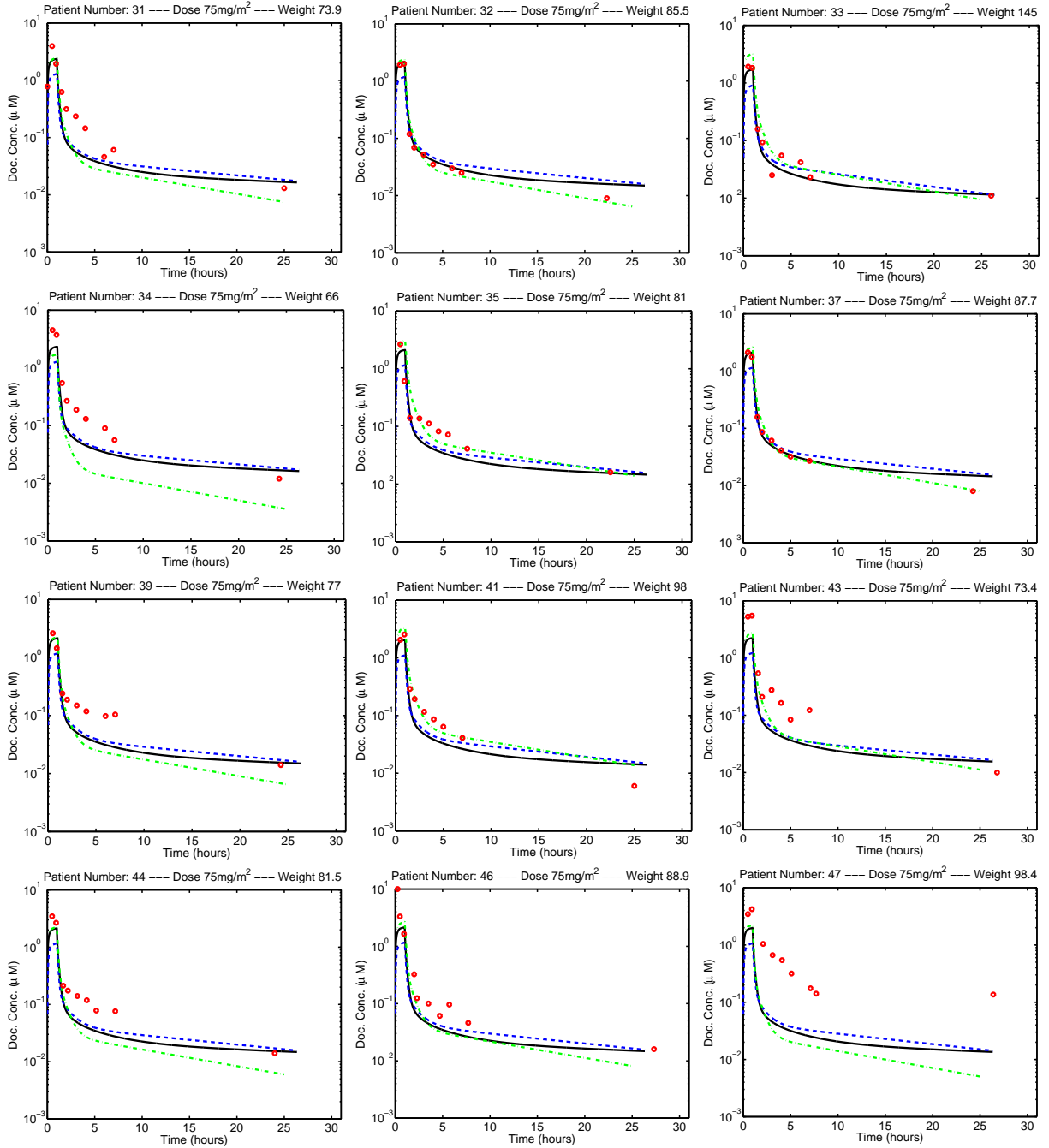


Figure D9: Measured Doc plasma concentration data in humans from a Phase 1 clinical trial at MSKCC [6] dosed at $75 \frac{\text{mg}}{\text{m}^2}$ vs. human PBPK model predictions from the tissue-intensive PBPK (solid), the Bradshaw-Pierce PBPK (dashed), and the population PK Bruno (dash-dot) model.

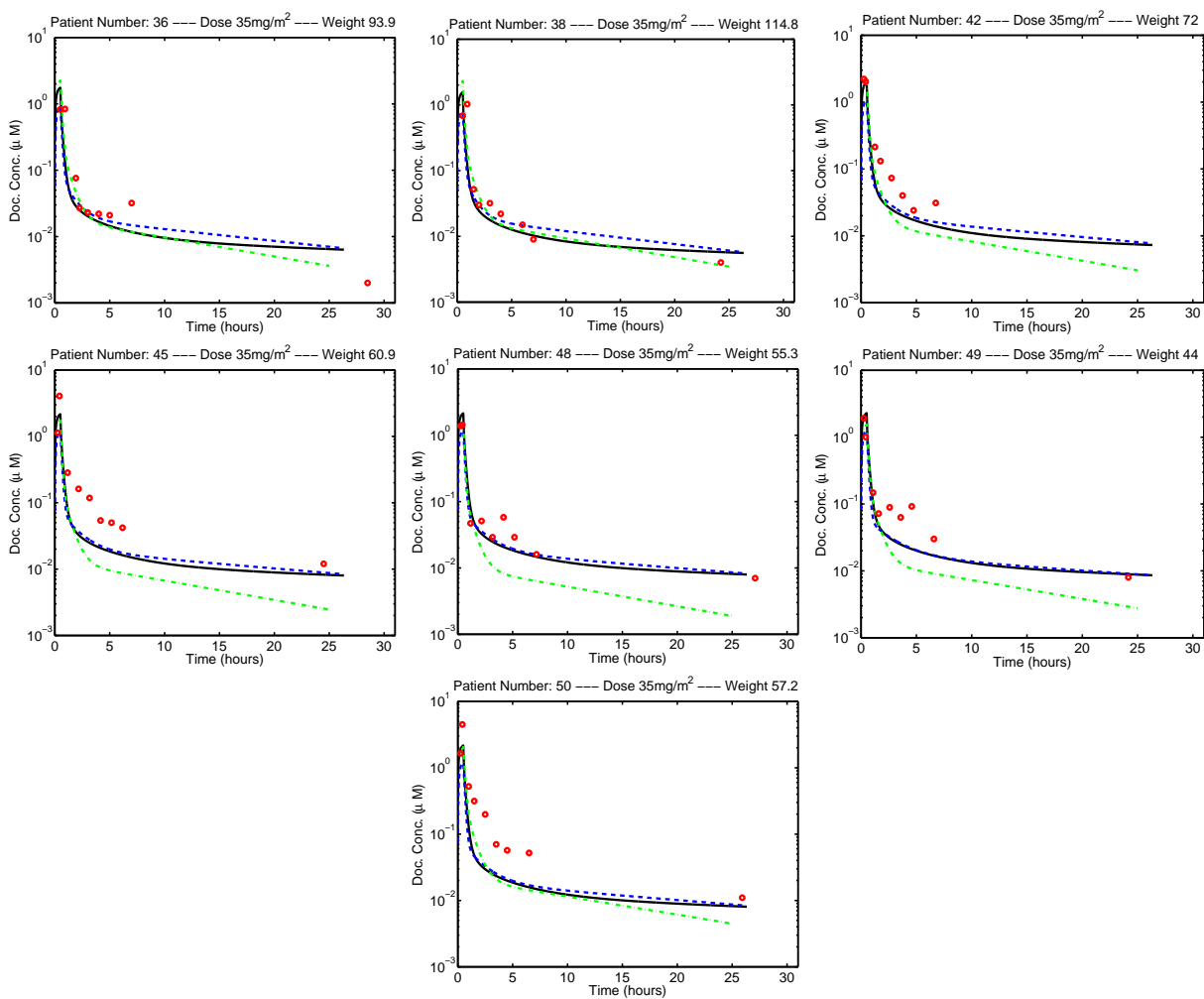


Figure D10: Measured Doc plasma concentration data in humans from a Phase 1 clinical trial at MSKCC [6] dosed at $35 \frac{\text{mg}}{\text{m}^2}$ vs. human PBPK model predictions from the tissue-intensive PBPK (solid), the Bradshaw-Pierce PBPK (dashed), and the population PK Bruno (dash-dot) model.

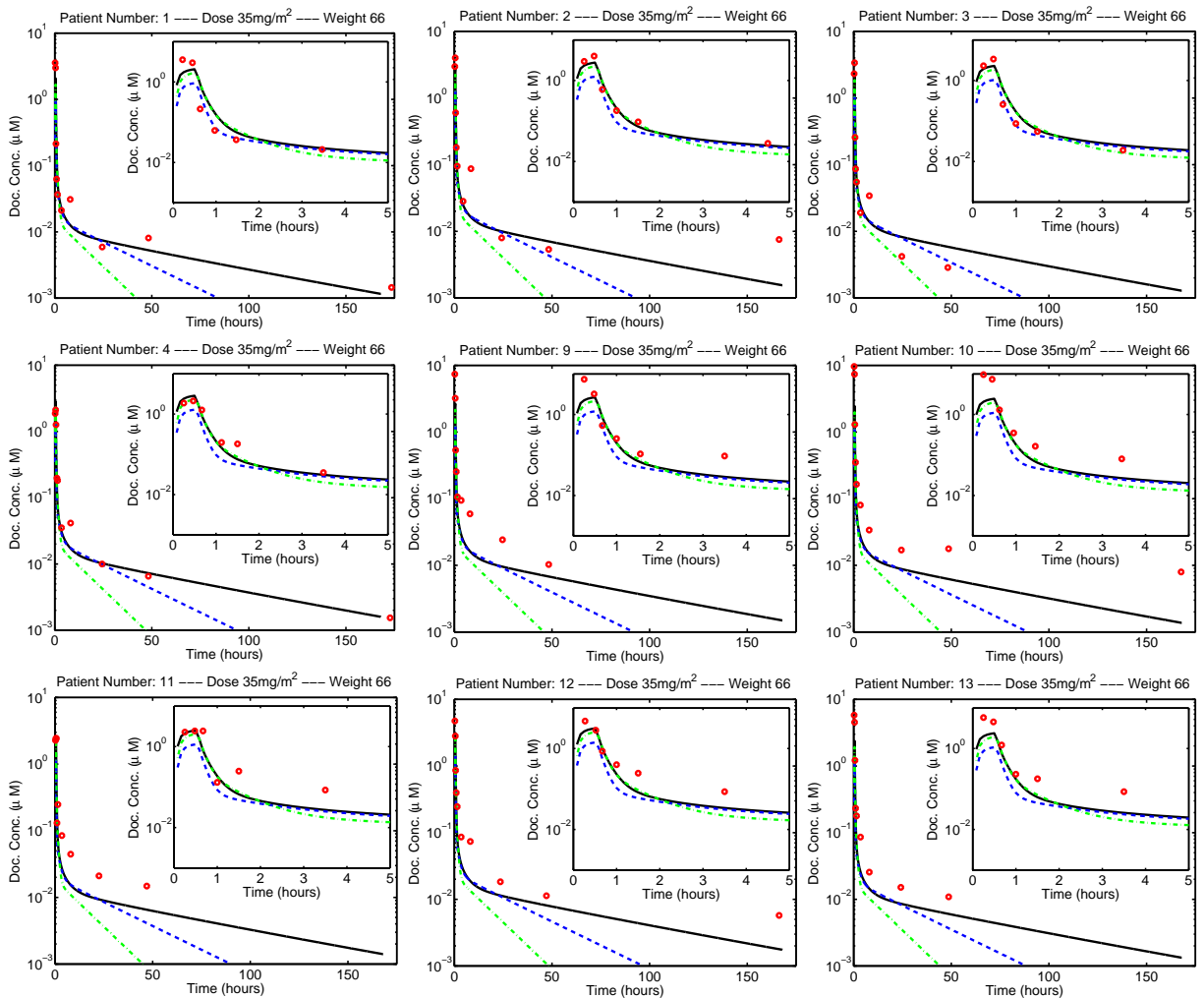


Figure D11: Measured Doc plasma concentration data in humans from a Phase 1 clinical trial at MSKCC in elderly patients dosed at $35 \frac{\text{mg}}{\text{m}^2}$ vs. human PBPK model predictions from the tissue-intensive PBPK (solid), the Bradshaw-Pierce PBPK (dashed), and the population PK Bruno (dash-dot) model.

BIBLIOGRAPHY

- [1] R. P. Brown, M. D. Delp, S. L. Lindstedt, L. R. Rhomberg, and R. P. Beliles. Physiological parameter values for physiologically based pharmacokinetic models. *Toxicol Ind Health*, 13(4):407–84, Jul-Aug 1997.
- [2] R. Bruno, N. Vivier, C. Veyrat-Follet, G. Montay, and G. R. Rhodes. Population pharmacokinetics and pharmacokinetic-pharmacodynamic relationships for docetaxel. *Invest. New Drug*, 19:163–9, 2001.
- [3] Friedman HS, Keir S, Pegg AE, Houghton PJ, Colvin OM, Moschel RC, Bigner DD, and Dolan ME. O6-BG mediated enhancement of chemotherapy. *Molecular Cancer Therapeutics*, 1:943–8, September 2002.
- [4] H. M. Shapiro. *Practical Flow Cytometry*. Wiley-Liss, Hoboken, New Jersey, 4th edition, 2003.
- [5] E. L. Bradshaw-Pierce, S. G. Eckhardt, and D. L. Gustafson. A physiologically based pharmacokinetic model of docetaxel disposition: from mouse to man. *Clin. Cancer Res.*, 13(9):2768–76, May 2007.
- [6] D. B. Solit, C. Egorin, M. Kopil, A. Delacruz, D. Shaffer, S. Slovin, M. Morris, W. K. Kelly, N. Rosen, and H. Scher. Phase I pharmacokinetic and pharmacodynamic trial of docetaxel and 17-AAG (17-allylamino-17-demthoxygeldanamycin). In *Proc. Amer. Assoc. Cancer Res.*, volume 23, page 3051, 2005.
- [7] A. Hurria, M. T. Flemin, S. D. Baker, W. K. Kelly, K. Cutchall, K. Panageas, J. Caravelli, H. Yeung, M. G. Kris, J. Gomez, V. A. Miller, G. D’Andrea, H. I. Scher, L. Norton, and C. Hudis. Pharmacokinetics and toxicity of weekly docetaxel in older patients. *Clin. Cancer Res.*, 12(20):6100–5, Oct 2006.
- [8] S. D. Baker, J. Li, A. J. ten Tije, W. D. Figg, W. Graveland, J. Verweij, and A. Sparreboom. Relationship of systemic exposure to unbound docetaxel and neutropenia. *Clin. Pharmacol. Ther.*, 77(1):43–53, 2005.
- [9] J. M. Slingerland and I. F. Tannock. *Cell Proliferation and Cell Death*, chapter 7, pages 134–165. The Basic Science of Oncology. McGraw-Hill, third edition, 1998.

- [10] The American Cancer Society. Cancer facts & figures: 2008. URL: <http://www.cancer.org/downloads/STT/2008CAFFfinalsecured.pdf>, 2008.
- [11] B. A. Ogunnaike and W.H. Ray. *Process Dynamics, Modeling, and Control*. Oxford University Press, New York, NY, 1994.
- [12] T. Teorell. Kinetics of distribution of substances administered to the body I. *Arch. Int. Pharma. Ther.*, 57:202–225, 1937.
- [13] T. Teorell. Kinetics of distribution of substances administered to the body II. *Arch. Int. Pharma. Ther.*, 57:226–240, 1937.
- [14] Federal Drug Administration. Gemzar (gemcitabine hcl) for injection. URL: <http://www.fda.gov/cder/foi/label/2006/020509s039lbl.pdf>, 2006.
- [15] M. J. Moore and C. Erlichman. *Pharmacology of Anticancer Drugs*, chapter 16, pages 370–391. *The BASIC SCIENCE of ONCOLOGY*. McGraw-Hill, third edition, 1998.
- [16] P. Macheras and A. Iliadis. *Modeling in Biopharmaceutics, Pharmacokinetics, and Pharmacodynamics*, volume 30. Springer, New York, New York, 2006.
- [17] J. M. Gallo, J. Brennan, T. C. Hamilton, T. Halbherr, P. B. Laub, and R. F. Ozols. Time-dependent pharmacodynamic models in cancer chemotherapy: Population pharmacodynamic model for glutathione depletion following modulation by buthionine sulfoximine BSO in a phase I trial of melphalan and BSO. *Cancer Research*, 55:4507–11, Oct 1995.
- [18] P. Magni, R. Bellazzi, G. Sparacino, and C. Cobelli. Bayesian identification of a population compartmental model of C-peptide kinetics. *Annals Biomed. Eng.*, 28:812–23, 2000.
- [19] A. Henningsson, M. Karlsson, L. Viganó, L. Gianni, J. Verweij, and A. Sparreboom. Mechanism-based pharmacokinetic model for paclitaxel. *J. Clin. Oncol.*, 19(20):4065–73, Oct 2001.
- [20] D. R. Stanski and P. O. Maltre. Population pharmacokinetics and pharmacodynamics of thipental: The effect of age revisited. *Anesthesiology*, 72:412–22, 1990.
- [21] L. Nguyen, E. Chatelut, C. Chevreau, B. Tranchand, I. Lochon, J. Bachaud, A. Pujol, G. Houin, R. Bugat, and P. Canal. Population pharmacokinetics of total and unbound etoposide. *Cancer Chemother. Pharmacol.*, 41:125–32, 1998.
- [22] Wu. H. and A. A. Ding. Population HIV-1 dynamics *in vivo*: Applicable models and inferential tools for virological data from AIDS clinical trials. *Biometrics*, 55:410–8, 1999.

- [23] J. M. Gallo, P. B. Laub, E. K. Rowinsky, L. B. Grochow, and S. D. Baker. Population pharmacokinetic model for topotecan derived from phase I clinical trials. *J. Clin. Oncol.*, 18(12):2459–67, June 2000.
- [24] J. F. Jen, D. L. Cutler, M. P. Sudhakar, V. K. Batra, M. B. Affrime, D. N. Zambas, S. Heft, and G. Hajian. Population pharmacokinetics of temozolomide in cancer patients. *Pharmaceut. Research*, 17(10):1284–9, 2000.
- [25] B. B. Goh, Lee. S., L. Wang, L. Fan, J. Guo, J. Lamba, E. Schuetz, R. Lim, H. Lim, A. Ong, and H. Lee. Explaining interindividual variability of docetaxel pharmacokinetics and pharmacodynamics in asians through phenotyping and genotyping strategies. *J. Clin. Oncol.*, 20(17):3683–90, Sept 2002.
- [26] A. Henningsson, A. Sparreboom, M. Sandstrom, A. Freijis, R. Larsson, J. Bergh, P. Nygren, and M. O. Karlsson. Population pharmacokinetic modelling of unbound and total plasma concentrations of paclitaxel in cancer patients. *Eur. J. Cancer.*, 39(8):1105–14, May 2003.
- [27] K. A. Slaviero, S. J. Clarke, A. J. McLachlan, E. Y. Blair, and L. P. Rivory. Population pharmacokinetics of weekly docetaxel in patients with advanced cancer. *BJ Clin. Pharmacol.*, 57(1):44–53, 2003.
- [28] M. Sandstrom, H. Lindman, P. Nygren, M. Johansson, J. Bergh, and M. O. Karlsson. Population analysis of the pharmacokinetics and the haematological toxicity of the fluorouracil-epirubicin-cyclophosphamide regimen in breast cancer patients. *Can. Chemother. Pharmacol.*, 58:143–56, 2006.
- [29] S. L. Beal and L. B. Sheiner. *NONMEM User's Guide*. NONMEM Project Group, University of California, San Francisco, 1992.
- [30] D. Z. D'Argenio and A. Schumitzky. *ADAPT II Users Guide: Pharmacokinetic and Pharmacodynamic Systems Analysis Software*. Biomedical Simulations Resource, University of Southern California, Los Angeles, CA, 1997.
- [31] J. Gabrielsson and D. Weiner. In The Swedish Pharmaceutical Press, editor, *Pharmacokinetic and Pharmacodynamic Data Analysis: Concepts and Applications*. 2nd edition, 1997.
- [32] Iftexhar Mahmood. Prediction of clearance, volume of distribution, and half-life by allometric scaling and by use of plasma concentration predicted from pharmacokinetic constants: A comparative study. *J. Pharm. Pharmacol.*, 51:905–10, 1999.
- [33] R. Gomeni, C. Falcoz, C. D'Angeli, and A. Bye. In-silico prediction of drug properties in man using preclinical data and computer assisted drug development. *Drug Information Journal*, 35:1047–63, 2001.

- [34] F. Jonsson and G. Johanson. Physiologically based modeling of the inhalation kinetics of styrene in humans using a bayesian population approach. *Toxicol. App. Pharmacol.*, 179:35–49, 2002.
- [35] P. R. Gentry, T. R. Covington, H. J. Clewell III, and M. E. Anderson. Application of a physiologically based pharmacokinetic model for reference dose and reference concentration estimation for acetone. *J. Toxicol. Environ. Health*, 66:2209–2225, 2003.
- [36] H. Chen, X. Wang, and X. Chen. A novel PBPK/PD model with automatic nervous system in anesthesia. *Eng. Med. Biol.*, pages 66–9, 2005.
- [37] D. G. Levitt and T. W. Schnider. Human physiologically based pharmacokinetic model for propofol. *BMC Anesthesiology*, 5(4):1–29, 2005.
- [38] R. N. Upton and G. Ludbrook. A physiologically based, recirculatory model of the kinetics and dynamics of propofol in man. *Anesthesiology*, 103:344–52, 2005.
- [39] J.T. Sorensen, C.K. Colton, R.S. Hillman, and J.S. Soeldner. Use of a physiological pharmacokinetic model of glucose homeostasis for assessment of performance requirements for improved insulin therapies. *Diabetes Care*, 5:148–157, 1982.
- [40] R. S. Parker, E. P. Gatzke, and F. J. Doyle III. Advanced model predictive control (MPC) for type I diabetic patient blood glucose control. In *Proc. American Control Conf.*, volume 5, pages 3483–3487, 2000.
- [41] L. Xu. Physiologically-based pharmacokinetics and mechanistically-based pharmacodynamics of geldanamycin derivatives and their application in clinical trials. Master’s thesis, University of Southern California, 2003.
- [42] C. R. Kirman, M. L. Gargas, G. M. Marsh, D. E. Strother, J. E. Klaunig, J. J. Collins, and R. Deskin. Cancer dose response assessment for acrylonitrile based upon rodent brain tumor incidence: Use of epidemiologic, mechanistic, and pharmacokinetic support for nonlinearity. *Reg. Toxicol. Pharmacol.*, 43:85–103, 2005.
- [43] J. A. Florian, Jr., M. J. Egorin, W. C. Zamboni, J. L. Eiseman, T. F. Lagattuta, C. P. Belani, G. S. Chatta, H. I. Scher and D. B. Solit, and R. S. Parker. A physiologically-based pharmacokinetic (PBPK) and pharmacodynamic model of docetaxel (Doc) and neutropenia in humans. In *American Society of Clinical Oncology Annual Meeting*.
- [44] Donghan Yu. A physiologically based pharmacokinetic model of inorganic arsenic. *Reg. Toxicol. Pharmacol.*, 29:128–41, 1999.
- [45] L. Hu, J. Au, and M. G. Wientjes. Computational modeling to predict effect of treatment schedule on drug delivery to prostate in humans. *Clin. Cancer Res.*, 13(4):1278–87, Feb 2007.
- [46] A. Asachenkov, G. Marchuk, R. Mohler, and S. Zuev. *Disease Dynamics*. Birkhäuser, Boston, 1994.

- [47] N. L. Dayneka, V. Gard, and W. J. Jusko. Comparison of four basic models of indirect pharmacodynamic responses. *Journal of Pharmacokinetics and Biopharmaceutics*, 21(4):457–78, Aug 1993.
- [48] J. C. Panetta and J. Adam. A mathematical model of cycle-specific chemotherapy. *Math. Comput. Model.*, 22(2):67–82, 1995.
- [49] M. Simeoni, P. Magni, C. Cammia, G. De Nicolao, V. Croci, E. Pesenti, M. Germani, I. Poggese, and M. Rocchetti. Predictive pharmacokinetic-pharmacodynamic modeling of tumor growth kinetics in xenograft models after administration of anticancer agents. *Cancer Res.*, 64:1094–1101, 2004.
- [50] W.C. Zamboni, L.L. Jung, R. Jin, M.J. Egorin, M.K.K. Wong, C.P. Belani, D.M. Potter, J.S. Tauch, S. Strychor, S.L. Sun, D.L. Trump, and R.K. Ramanathan. Phase I and pharmacokinetic (PK) study of intermittently administered 9-nitrocamptothecin (9NC, rubitecan) in patients with advanced malignancies. volume 20 (#411) of *Proceedings of ASCO*, 2001.
- [51] C. Engel, M. Scholz, and M. Loeffler. A computational model of human granulopoiesis to simulate the hematotoxic effects of multicycle polychemotherapy. *Hematopoiesis*, 104(8):2323–31, Oct 2004.
- [52] R. Hovorka, V. Canonico, L. J. Chassin, U. Haueter, M. Massi-Benedetti, M. O. Federici, T. R. Pieber, H. C. Schaller, L. Schaupp, T. Vering, and M. E. Wilinska. Nonlinear model predictive control of glucose concentration in subjects with type 1 diabetes. *Physiological Measurement*, 25:905–920, 2004.
- [53] A. Roy and R.S. Parker. Dynamic modeling of free fatty acids, glucose, and insulin: An extended minimal model. *Diabetes Tech. Therapeut.*, 8:617–626, 2006.
- [54] A. Roy and R.S. Parker. Dynamic modeling of exercise effects on plasma glucose and insulin levels. *J. Diabetes Sci. Tech.*, (in press).
- [55] A. S. Perelson and P. W. Nelson. Mathematical analysis of HIV-1 dynamics *in vivo*. *SIAM Review*, 41:3–44, 1999.
- [56] M. Bachar and A. Dorfmayr. HIV treatment models with time delay. *C. R. Biol.*, 327(11):983–94, 2004.
- [57] M. Joly and J. M. Pinto. Role of mathematical modeling on the optimal control of HIV-1. *Process Systems Engineering*, 52(3):856–84, 2006.
- [58] C.W. Frei, M. Derighetti, M. Morari, A.H. Glattfelder, and A. Zbinden. Improved regulation of mean arterial blood pressure during anesthesia through estimates of surgery effects. *IEEE Trans. Biomed. Eng.*, 47:1456–1464, 2000.

- [59] A. Morley, J. Derrick, P. Mainland, B. B. Lee, and T. G. Short. Closed-loop control of anaesthesia: An assessment of the bispectral index as the target of control. *Anaesthesia*, 55:953–59, 2000.
- [60] A. Gentilini, C. Schaniel, M. Morari, C. Bieniok, R. Wymann, and T. W. Schnider. Multitasked closed-loop control in anesthesia. *IEEE Trans. Biomed. Eng.*, 49(4):289–99, Apr 2002.
- [61] H. E. Skipper, F. M. Schabel Jr., and W. S. Wilcox. Experimental evaluation of potential anticancer agents. XIII. On the criteria and kinetics associated with “curability” of experimental leukemia. *Can. Chemother. Rep.*, 61:1307–1317, 1964.
- [62] J. W. Jusko and H. C. Ko. Physiologic indirect response models characterize diverse types of pharmacodynamic effects. *Clin. Pharmacol. Ther.*, 56(4):406–419, 1994.
- [63] R. Martin and K. L. Teo. *Optimal Control of Drug Administration in Cancer Chemotherapy*. World Scientific, River Edge, NJ, 1994.
- [64] J.M. Harrold, J. L. Eiseman, E. Joseph, S. Strychor, W. C. Zamboni, and R. S. Parker. Control-relevant modeling of the antitumor effects of 9-nitrocamptothecin in SCID mice bearing ht29 human colon xenografts. *J. Pharmacokinet. Pharmacodyn.*, 32:65–83, 2005.
- [65] K. R. Fister and J. C. Panetta. Optimal control applied to cell-cycle specific cancer chemotherapy. *SIAM J. Appl. Math.*, 60(3):1059–72, 2000.
- [66] M. Scholz, C. Engel, and M. Loeffler. Model-based design of chemotherapeutic regimens that account for heterogeneity in leucopenia. *Br. J. Haematol.*, 132(6):723–35, Mar 2006.
- [67] R. B. Martin, M. E. Fisher, R. F. Minchin, and K. L. Teo. A mathematical model of cancer chemotherapy with an optimal selection of parameters. *Math. Biosci.*, 99:205–230, 1990.
- [68] G. F. Brunton and T. E. Wheldon. The gompertz equation and the construction of tumor growth curves. *Cell Tissue Kinet.*, 13:455–60, 1980.
- [69] L. Norton. A Gompertzian model of human breast cancer growth. *Cancer Res.*, 48:7067–7071, 1988.
- [70] M. Fornier and L. Norton. Dose-dense adjuvant chemotherapy for primary breast cancer. *Breast Cancer Res*, 7(2):64–9, 2005.
- [71] S. N. Gardner. A mechanistic, predictive model of dose-response curves for cell cycle phase-specific and -nonspecific drugs. *Cancer Res.*, 60:1417–1425, March 2000.

- [72] Michael B. Kastan and Stephen X. Skapek. *Molecular Biology of Cancer: The Cell Cycle*, chapter 6, pages 91–109. *Cancer: principles & practice of oncology*. Lippincott, Williams & Wilkins, 2001.
- [73] J. Smith and L. Martin. Do cells cycle? *Proc. Natl. Acad. Sci. USA*, 70:1263–67, 1973.
- [74] N. M. Lopes, E. G. Adams, and B. K. Bhuyan. Cell kill kinetics and cell cycle effects of Taxol on human and hamster ovarian cell lines. *Cancer Chemoth. Pharm.*, 32(3):235–242, 1993.
- [75] J. C. Panetta. A mathematical model of breast and ovarian cancer treated with paclitaxel. *Math. Biosci.*, 146(2):89–113, 1997.
- [76] F. Kozusko, P. Chen, S. G. Grant, B. W. Day, and J. C. Panetta. A mathematical model of *in vitro* cancer cell growth and treatment with the antimitotic agent curacin A. *Math. Biosci.*, 170:1–16, 2001.
- [77] J. C. Panetta, W. E. Evans, and M. H. Cheok. Mechanistic mathematical modelling of mercaptopurine effects on cell cycle of human acute lymphoblastic leukaemia cells. *Br. J. Cancer*, 94(1):93–100, 2006.
- [78] F. L. Pereira, C. E. Pedreira, M. R. Pinho, M. H. Fernandes, and J. B. Sousa. An optimal control algorithm for multidrug cancer chemotherapy design. In *Proc. IEEE EMBS Ann. Conf.*, volume 12, pages 1021–1022, 1990.
- [79] J. A. Florian, Jr., J. L. Eiseman, and R. S. Parker. A nonlinear model predictive control algorithm for breast cancer treatment. In *Proc. DYCOPS 7*, Boston, MA, 2004.
- [80] J. A. Florian Jr., J. L. Eiseman, and R. S. Parker. A population balance model of cell cycle-specific tumor growth. In *Proc. 2005 IFAC World Congress*, volume (accepted), Prague, Czech Republic, 2005.
- [81] G. Webb. Resonance phenomena in cell population chemotherapy models. *Rocky Mountain J. Math.*, 20:1195–1216, 1990.
- [82] L. Cojocararu and Z. Agus. Theoretical analysis of interval drug dosing for cell-cycle phase-specific drugs. *Random and Computational Dynamics*, 109:85–97, 1992.
- [83] A. Bertuzzi, A. Fasano, A. Gandolfi, and D. Marangi. Cell kinetics in tumor cords studied by a model with variable cell cycle length. *Math. Biosci.*, 177&178:103–125, 2002.
- [84] L. Cojocararu and Z. Agus. Asynchronous exponential growth in an age structured population of proliferating and quiescent cells. *Math. Biosci.*, 177-178:73–78, 2002.
- [85] E. A. Gaffney. The application of mathematical modelling to aspects of adjuvant chemotherapy scheduling. *J. Math. Biol.*, 48:375–422, 2004.

- [86] E. Sherer, R. E. Hannemann, A. Rundell, and D. Ramkrishna. Analysis of resonance chemotherapy in leukemia treatment via multi-staged population balance models. *J. Theor. Biol.*, 240, Jan 2006.
- [87] B. A. Ogunnaike. Elucidating the digital control mechanism for DNA damage repair with the p53-Mdm2 system: Single cell data analysis and ensemble. *J. R. Soc. Interface.*, 3:175–184, 2006.
- [88] M. A. Chaplain, M. Ganesh, and I. G. Graham. Spatio-temporal pattern formation on spherical surfaces: Numerical simulation and application to solid tumor growth. *J. Math. Biol.*, 42:387–423, 2001.
- [89] L. M. Wein, J. T. Wu, A. G. Ianculescu, and R. K. Puri. A mathematical model of the impact of infused targeted cytotoxic agents on brain tumours: Implications for detection, design and delivery. *Cell Prolif*, 35(6):343–61, Dec 2002.
- [90] T. L. Jackson. Intracellular accumulation and mechanism of action of doxorubicin in a Spatio-temporal tumor model. *J. Theor. Biol.*, 220(2):201–13, Jan 2003.
- [91] V. P. Antipas, G. S. Stamatakis, N. K. Uzunoglu, D. D. Dionysiou, and R. G. Dale. A Spatio-temporal simulation model of the response of solid tumours to radiotherapy *in vivo*: Parametric validation concerning oxygen enhancement ratio and cell cycle duration. *Phys. Med. Biol.*, 49(8):1485–504, Apr 2004.
- [92] R. Venkatasubramanian, M. A. Henson, and N. S. Forbes. Incorporating cellular metabolism into growth models of multicellular tumor spheroids. *J. Theor. Biol.*, 242:440–53, 2006.
- [93] R. Venkatasubramanian, M. A. Henson, and N. S. Forbes. Integrating cell cycle progression, drug penetration, and metabolic tumor growth to identify optimal therapeutic strategies. (submitted).
- [94] A. R. Kansal, S. Torquato, G. R. Harsh IV, E. A. Chiocca, and T. S. Deisboeck. Simulated brain tumor growth dynamics using a three-dimensional cellular automaton. *J. Theo. Biol.*, 203:367–382, January 2000.
- [95] A. A. Patel, E. T. Gawlinski, S. K. Lemieux, and R. A. Gatenby. A cellular automaton model of early tumor growth and invasion: The effects of native tissue vascularity and increased anaerobic metabolism. *J. Theor. Biol.*, 213:315–31, 2001.
- [96] S. Turner and J. A. Sherrat. Intercellular adhesion and cancer invasion: A discrete simulation using the extended potts model. *J. Theor. Biol.*, 216:85–100, 2002.
- [97] R. Bruno, R. Olivares, J. Berille, P. Chaikin, N. Vivier, L. Hammershaimb, G. R. Rhodes, and J. R. Rigas. α -1-acid glycoprotein as an independent predictor for treatment effects and a prognostic factor of survival in patients with non-small cell lung cancer treated with docetaxel. *Clin. Cancer Res.*, 9:1077–82, March 2003.

- [98] T. Alarcón, H. M. Byrne, and P. K. Maini. Towards whole-organ modelling of tumour growth. *Prog. Biophys. Mol. Biol.*, 85:451–72, 2004.
- [99] R. B. Martin, M. E. Fisher, R. F. Minchin, and K. L. Teo. Optimal control of tumor size used to maximize survival time when cells are resistant to chemotherapy. *Math. Biosci.*, 110:221–252, 1992.
- [100] J. Lange. A rational approach to the selection and sequencing of nucleoside/nucleotide analogues: A new paradigm. *Antivir. Ther.*, 6(Suppl 3):45–54, 2001.
- [101] S. Cui. Analysis of a mathematical model for the growth of tumors under the action of external inhibitors. *J. Math. Biol.*, 44(5):395–426, 2002.
- [102] B. Novak and J. J. Tyson. Modelling the controls of the eukaryotic cell cycle. *Biochem. Soc. Trans.*, 3(Pt 6):1526–9, Dec 2003.
- [103] B. Novak and J. J. Tyson. A model for restriction point control of the mammalian cell cycle. *J. Theor. Biol.*, 230(4):563–79, Oct 2004.
- [104] Cancer Therapy Evaluation Program. Common terminology criteria for adverse events v3.0 (CTCAE). URL: <http://ctep.cancer.gov/forms/CTCAEv3.pdf>, 2003.
- [105] H. Saito and H. Mizoguchi. Treatment of elderly patients with hematological malignancies. *Gan To Kagaku Ryoho*, 19(11):1801–7, Sep 1992.
- [106] C. Kloft, J. Wallin, A. Henningsson, E. Chatelut, and M. O. Karlsson. Population pharmacokinetic and pharmacodynamic model for neutropenia with patient subgroup identification: Comparison across anticancer drugs. *Clin. Cancer Res.*, 12(18):5481–90, Sept 2006.
- [107] M. T. Huizing, G. Giaccone, H. M. Pinedo, C. H. Veenhaf, and J. H. Beijnen. Pharmacokinetics of paclitaxel and carboplatin in a dose-escalating and dose-sequencing study in patients with non-small-cell lung cancer. *J. Clin. Oncology*, 15(1):317–29, Jan 1997.
- [108] H. Zhou, L. Choi, H. Lau, U. Brunsch, E. E. Vries, G. Eckhardt, A. T. Oosterom, J. Verweij, H. Schran, N. Barbet, R. Linnartz, and R. Capdeville. Population pharmacokinetics/toxicodynamics (PK/TD) relationship of SAM486A in phase I studies in patients with advanced cancers. *J. Clin. Pharmacol.*, 40:275–83, 2000.
- [109] H. Minami, K. Kawada, Y. Sasaki, T. Igarashi, T. Saeki, M. Tahara, K. Itoh, and H. Fujii. Pharmacokinetics and pharmacodynamics of protein-unbound docetaxel in cancer patients. *Cancer Sci*, 97(3):235–41, March 2006.
- [110] C. Segura, E. Bandres, I. F. Troconiz, O. Saya, M. J. Renedo, and M. J. Garrido. Hematological response of topotecan in tumor bearing rats: Modeling of the time course of different cell populations. *Pharmaceut. Research*, 21(4):567–73, Apr 2004.

- [111] M. Sandstrom, H. Lindman, P. Nygen, E. Lidbrink, J. Bergh, and M.O. Karlsson. Model describing the relationship between pharmacokinetics and hematologic toxicity of the epirubicin-docetaxel regimen in breast cancer patients. *J Clin Oncol.*, 23(3):413–21, January 2005.
- [112] J. E. Latz, M. O. Karlsson, J. J. Rusthoven, A. Ghosh, and R. D. Johnson. A semimechanistic-physiologic population pharmacokinetic/pharmacodynamic model for neutropenia following pemetrexed therapy. *Can. Chemother. Pharmacol.*, 57:412–26, 2006.
- [113] E. K. Afenya. Recovery of normal hemopoiesis in disseminated cancer therapy – a model. *Math. Biosci.*, 172:15–32, 2001.
- [114] W. Krzyzanski and W. J. Jusko. Multiple pool cell lifespan model of hematological effects of anticancer agents. *J. Pharmacokin. Pharmacodynam.*, 29(4):311–37, Aug 2002.
- [115] C. Ane and D. Concordet. Population pharmacokinetics/pharmacodynamics relationships of an anticancer drug. *Statist. Med.*, 22:833–46, 2003.
- [116] L. E. Friberg, F. Agneta, M. Sandstrom, and M. O. Karlsson. Semiphysiological model for the time course of leukocytes after varying schedules of 5-Fluorouracil in rats. *J. Pharmacol. Exp. Ther.*, 2005(2):734–40, Nov 2000.
- [117] M. I. S. Costa, J. L. Boldrini, and R. C. Bassanezi. Drug kinetics and drug resistance in optimal chemotherapy. *Math. Biosci.*, 125:191–209, 1995.
- [118] A. Swierniak and J. Smieja. Cancer chemotherapy optimization under evolving drug resistance. *Nonlinear Analysis*, 47:375–386, 2001.
- [119] D. Barbolosi and A. Iliadis. Optimizing drug regimens in cancer chemotherapy: A simulation study using a PK-PD model. *Comput. Biol. Med.*, pages 157–172, 2001.
- [120] A. Świerniak, U. Ledzewicz, and H. Schattler. Optimal control for a class of compartmental models in cancer chemotherapy. *Int. J. Appl. Math. Comput. Sci.*, 13(3):357–68, 2003.
- [121] R. S. Parker, J. W. Fisher, A. P. Venook, M. J. Ratain, and M. J. Egorin. Development of a pharmacokinetically-guided gemcitabine (dFdC) dosing schedule to reduce potentially excessive plasma dFdC concentrations. In *Am. Soc. Clinical Oncology Annual Meeting*, Orlando, FL, 2005.
- [122] A. Swierniak, A. Polanski, and M. Kimmel. Optimal control problems arising in cell-cycle-specific cancer chemotherapy. *Cell Prolif.*, 29:117–39, 1996.
- [123] G. Arcangeli, M. Benassi, L. Nieddu, C. Passi, G. Patrizi, and M. T. Russo. Optimal adaptive control of treatment planning in radiation therapy. *Eur. J. Operat. Research*, 140:399–412, 2002.

- [124] J. M. Harrold. *Model-Based Design of Cancer Chemotherapy Treatment Schedules*. PhD thesis, University of Pittsburgh, Pittsburgh, PA, 2005.
- [125] U. Ledzewicz and H. Schättler. Optimal bang-bang controls for a two-compartment model in cancer chemotherapy. *J. Optimization Theory Appl.*, 114(3):609–637, 2002.
- [126] E. A. Gaffney. The mathematical modelling of adjuvant chemotherapy scheduling: Incorporating the effects of protocol rest phases and pharmacokinetics. *Bull. Math. Biol.*, 67(3):563–611, May 2005.
- [127] E. Sherer, R. E. Hannemann, A. Rundell, and D. Ramkrishna. Estimation of likely cancer cure using first- and second-order product densities of population balance models. *Ann. Biomed. Eng.*, 35(6):903–15, June 2007.
- [128] M. J. Ellis and S. M. Swain. Steroid hormone therapies for cancer. In B. A. Chabner and D. L. Longo, editors, *Cancer Chemotherapy and Biotherapy: Principles and Practice*, pages 103–13. Lippincott Williams and Wilkins, 3rd edition, 2001.
- [129] S. P. Robinson, S. M. Langan-Fahey, A. J. Delinda, and V. C. Jordan. Metabolites, pharmacodynamics, and pharmacokinetics of tamoxifen in rats and mice compared to the breast cancer patient. *Drug Metabolism and Disposition*, 19(1):36–43, 1991.
- [130] B. A. Conley, T. S. Ramsland, D. L. Sentz, S. Wu, D. M. Rosen, M. Wollman, and J. L. Eiseman. Antitumor activity, distribution, and metabolism of 13-*cis*-retinoic acid as a single agent or in combination with tamoxifen in established human MCF-7 xenografts in mice. *Cancer Chemother. Pharmacol.*, 43:183–197, 1999.
- [131] C. H. Takimoto and S. G. Arbuck. *Topoisomerase I Targeting Agents: The Camptothecins*, chapter 20, pages 579–646. *Cancer Chemotherapy & Biology*. Lippincott Williams & Wilkins, 3rd edition, 2001.
- [132] G. S. Lee, K. S. Ryu, S. P. Kim, S. E. Namkoong, and K. T. Han. Multiparametric flow cytometric analysis in a breast cancer cell line (MCF-7). *J. Obstet. Gynaecol. Res.*, 28(3):141–8, June 2002.
- [133] M. Riesberg, C. Kasper, K. F. Reardon, and T. Scheper. Flow cytometry in biotechnology. *Appl. Microbiol. Biotechnol.*, 56:350–60, 2001.
- [134] H. Akaike. A Bayesian extension of the minimal AIC procedures of autoregressive model fitting. *Biometrika*, 66:237, 1979.
- [135] M. Morari and E. Zafiriou. *Robust Process Control*. Prentice-Hall, Englewood Cliffs, NJ, 1989.
- [136] E. A. Martin, P. Carthew, I. N. White, R. T. Heydon, M. Gaskell, R. J. Mauthe, K. W. Turteltaub, and L. L. Smith. Investigation of the formation and accumulation of liver DNA adducts in mice chronically exposed to tamoxifen. *Carcinogenesis*, 18(11):2209–15, 1997.

- [137] F. Allgöwer, T. A. Badgwell, J. S. Qin, J. B. Rawlings, and S. J. Wright. *Nonlinear Predictive Control and Moving Horizon Estimation – An Introductory Overview*, pages 391–449. *Advances in Control – Highlights of ECC '99*. Springer, London, 1999.
- [138] M. Morari and N. L. Ricker. *Model Predictive Control Toolbox*. The MathWorks, Inc., Natick, MA, 1994.
- [139] J. M. Brown and A. J. Giaccia. The unique physiology of solid tumors: Opportunities (and problems) for cancer therapy. *Cancer Res.*, 58:1408–16, April 1998.
- [140] C. N. Coleman and J. B. Mitchell. *Radiation Modifiers*, pages 708–20. *Cancer Chemotherapy and Biotherapy: Principles and Practice*. Lippincott Williams and Wilkins, 3rd edition, 2001.
- [141] A. G. Fredrickson, D. Ramkrishna, and H. M. Tsuchiya. Statistics and dynamics of procaryotic cell populations. *Math. Biosci.*, 1:327–74, 1967.
- [142] D. Ramkrishna. *Population Balances: Theory and Applications to Particulate Systems in Engineering*. Academic Press, San Diego, CA, 2000.
- [143] G.-Y. Zhu, A. Zamamiri, M. A. Henson, and M. A. Hjortsø. Model predictive control of continuous yeast bioreactors using cell population balance models. *Chem. Eng. Sci.*, 55:6155–6167, 2000.
- [144] P. Daoutidis and M. A. Henson. Dynamics and control of cell populations in continuous bioreactors. In *Proceedings of CPC VI*, AIChE Symposia Series. CACHE Corporation, 2002.
- [145] N. V. Mantzaris, F. Srienc, and P. Daoutidis. Nonlinear productivity control using a multi-staged cell population balance model. *Chem. Eng. Sci.*, 57:1–14, 2002.
- [146] A. M. Zamamiri, Y. Zhang, M. A. Henson, and M. A. Hjortsø. Dynamics analysis of an age distribution model of oscillating yeast cultures. *Chem. Eng. Sci.*, 57:2169–2181, 2002.
- [147] B. Basse and P. Ubezio. A generalised age- and phase-structured model of human tumour cell populations both unperturbed and exposed to a range of cancer therapies. *Bull. Math. Biol.*, 69:1673–90, 2007.
- [148] M. Derenzini, D. Tere, A. Pession, M. Govoni, S. Valentina, and P. Chieco. Nucleolar size indicates the rapidity of cell proliferation in cancer tissues. *Journal of Pathology*, 191:181–86, 2000.
- [149] R. B. Martin. Optimal control drug scheduling of cancer chemotherapy. *Automatica*, 28:1113–1123, 1992.
- [150] W. C. Zamboni, S. Strychor, E. Joseph, R. A. Parise, M. J. Egorin, and J. L. Eiseman. Tumor, tissue, and plasma pharmacokinetics studies and antitumor response studies of

- docetaxel in combination with 9-nitrocamptothecin in mice bearing SKOV-3 human ovarian xenografts. *Cancer Chemother. Pharmacol.*, page submitted, 2007.
- [151] S. D. Baker, A. Sparreboom, and J. Verweij. Clinical pharmacokinetics of docetaxel. *Clin. Pharmacokinet.*, 45(3):232–52, 2006.
- [152] M. Shou, M. Martinet, K. R. Korzekwa, K. W. Krausz, F. J. Gonzalez, and H. V. Gelboin. Role of human cytochrome p450 3A4 and 3A5 in the metabolism of taxotere and its derivatives: Enzyme specificity, interindividual distribution and metabolic contribution in the human liver. *Pharmacogenetics*, 8(5):391–401, Oct 1998.
- [153] T. Walle, U. K. Walle, G. N. Kumar, and K. N. Bhalla. Taxol metabolism and disposition in cancer patients. *Drug Metab Dispos*, 23(11):1286–90, Nov 1995.
- [154] S. J. Clarke and L. P. Rivory. Clinical pharmacokinetics of docetaxel. *Drug Disposition*, 36(2):99–114, 1999.
- [155] S. D. Baker, M. Zhao, C. K. K. Lee, J. Verweij, Y. Zabelina, J. R. Brahmer, A. C. Wolff, A. Sparreboom, and M. A. Carducci. Comparative pharmacokinetics of weekly and every-three-weeks docetaxel. *Clinical Cancer Research*, 10:1976–1983, Mar 2004.
- [156] I. F. Tannock, R. de Wit, W. R. Berry, J. Horti, A. Pluzanska, K. N. Chi, S. Oudard, C. Théodore, N. D. James, I. Turesson, M. A. Rosenthal, and M. A. Eisenberger. Docetaxel plus prednisone or mitoxantrone plus prednisone for advanced prostate cancer. *N Engl J Med*, 1(15):1502–12, Oct 2004.
- [157] R. Gervais, A. Doculone, J. L. Breton, D. Braun, B. Lebeau, F. Vaylet, D. Debieuvre, J. L. Pujol, J. Tredaniel, P. Clouet, and E. Quoix. Phase II randomised trial comparing docetaxel given every 3 weeks with weekly schedule as second-line therapy in patients with advanced non-small-cell lung cancer. *Annals Oncol.*, 16:90–6, 2005.
- [158] S. Vazquez, C. Grande, M. Amenedo, J. L. Firvida, M. Lazaro, G. Alonso, T. Curiel, G. Huidobro, J. R. Mel, and M. Ramos. Biweekly docetaxel as second-line chemotherapy of patients with advanced non-small-cell lung cancer: A phase II study of the galician lung cancer group GGCP 006-00. *Anticancer Drugs*, 15:489–94, 2004.
- [159] J. D. Hainsworth. Practical aspects of weekly docetaxel administration schedules. *Oncologist*, 9:538–45, 2004.
- [160] M. Marland, C. Gaillard, G. Sanderin, S. Roberts, P. Jaonnou, V. Facchini, P. Chapelle, and A. Frydman. Kinetics, distribution, metabolism, and excretion of radiolabelled taxotere (14C-RP 56976) in mice and dogs. In *Proc. Am. Assoc. Cancer Res.*, volume 34, page 393, 1993.
- [161] H. L. McLeod, C. M. Kearns, J. G. Kuhn, and R. Bruno. Evaluation of linearity of docetaxel pharmacokinetics. *Cancer Chemother. Pharmacol.*, 142:155–9, 1998.

- [162] D. L. Gustafson, M. E. Long, J. A. Zirrolli, M. W. Duncan, S. N. Holden, A. S. Pierson, and S. G. Eckhardt. Analysis of docetaxel pharmacokinetics in humans with the inclusion of later sampling time-points afforded by the use of a sensitive tandem LCMS assay. *Cancer Chemother. Pharmacol.*, 52:159–66, 2003.
- [163] R. S. Parker, J. H. Ward, N. A. Peppas, and F. J. Doyle III. Robust H_∞ glucose control in diabetes using a physiological model. *AIChE Journal*, 46:2537–2549, 2000.
- [164] S. Strychor, J. L. Eiseman, R. A. Parise, M. J. Egorin, E. Joseph, and W. C. Zamboni. Plasma, tumor, and tissue disposition of docetaxel in SCID mice bearing SKOV-3 human ovarian xenografts. In *Proc. Amer. Assoc. Cancer Res.*, volume 46, page 983, 2005.
- [165] R. A. Parise, R. K. Ramanathan, W. C. Zamboni, and M. J. Egorin. Sensitive liquid chromatography-mass spectrometry assay for quantitation of docetaxel and paclitaxel in human plasma. *J. Chromatogr. B. Analyt. Technol. Biomed. Life Sci.*, 783(1):231–6, Jan 2003.
- [166] F. Kallinowski, K. H. Schlenger, S. Runkel, M. Kloes, M. Stohrer, P. Okunieff, and P. Vaupel. Blood flow, metabolism, cellular microenvironment, and growth rate of human tumor xenografts. *Cancer Research*, 49:3759–64, July 1989.
- [167] J. F. Diaz, R. Strobe, Y. Engelborghs, A. A. Souto, and J. M. Andreu. Molecular recognition of taxol by microtubules. *J. Biol. Chem.*, 275(34):26265–76, Aug 2000.
- [168] F. A. Shepard, J. Dancey, R. Ramlau, K. Mattson, R. Gralla, M. O’Rourke, N. Levitan, L. Gressot, M. Vincent, R. Burkes, S. Coughlin, Y. Kim, and J. Berille. Prospective randomized trial of docetaxel versus best supportive care in patients with non-small-cell lung cancer previously treated with platinum-based chemotherapy. *J. Clin. Oncol.*, 18(10):2095–103, May 2000.
- [169] J. Tabernero, M. A. Climent, A. Lluch, J. Albanell, J. Vermorken, A. Barnadas, A. Anton, C. Laurent, J. I. Mayordomo, N. Estaun, I. Losa, V. Guillem, J. Garcia-Conde, J. L. Tisaire, and J. Baselga. A multicentre, randomised phase II study of weekly or 3-weekly docetaxel in patients with metastatic breast cancer. *Ann. Oncol.*, 15(9):1358–65, Sep 2004.
- [170] V. Georgoulas, A. Ardavanis, A. Agelidou, M. Agelidou, V. Chandrinos, E. Tsaroucha, M. Toumbis, C. Kouroussis, K. Syrigos, A. Polyzos, N. Samaras, P. Papakotoulas, C. Christofilakis, N. Ziras, and A. Alegakis. Docetaxel versus docetaxel plus cisplatin as front-line treatment of patients with advanced non-small cell lung cancer: A randomized, multicenter phase III trial. *J. Clin. Oncol.*, 22(13):2602–2609, July 2004.
- [171] K. A. Charles, L. P. Rivory, M. R. Stockler, P. Beale, J. Beith, M. Boyer, and S. J. Clarke. Predicting the toxicity of weekly docetaxel in advanced cancer. *Clin. Pharmacokinet.*, 45(6):611–22, 2006.

- [172] F. K. Engels and J. Verweij. Docetaxel administration schedule: From fever to tears? *Eur J Cancer*, 41:1117–26, 2005.
- [173] M. Shouche, H. Genceli, P. Vuthandam, and M. Nikolaou. Simultaneous constrained model predictive control and identification of DARX processes. *Automatica*, 34:1521–2530, 1998.
- [174] A. J. ten Tije, J. Verweij, M. A. Carducci, W. Graveland, T. Rogers, T. Pronk, M. P. Verbruggen, F. Dawkins, and S. D. Baker. Prospective evaluation of the pharmacokinetics and toxicity profile of docetaxel in the elderly. *J. Clin. Oncol.*, 23(6):1070–77, February 2005.
- [175] N. Yamamoto, T. Tamura, H. Murakami, H. Shimoyama, T. Nokihara, Y. Ueda, I. Sekine, H. Kunitoh, Y. Ohe, T. Kodama, M. Shimizu, K. Nishio, N. Ishizuka, and N. Saijo. Randomized pharmacokinetic and pharmacodynamic study of docetaxel: Dosing based on body surface area compared with individualized dosing based on cytochrome P450 activity estimated using a urinary metabolite cortisol. *J. Clin. Oncol.*, 23(6):1061–69, February 2005.
- [176] K. A. Mortier and W. E. Lambert. Determination of unbound docetaxel and paclitaxel in plasma by ultrafiltration and liquid chromatography-tandem mass spectrometry. *J. Chromatogr. A*, 1108(2):195–201, March 2005.
- [177] W. J. Loos, S. D. Baker, J. Verweij, J. G. Boonstra, and A. Sparreboom. Clinical pharmacokinetics of unbound docetaxel: Role of polysorbate 80 and serum proteins. *Clin. Pharmacol. Ther.*, 74:364–71, 2003.
- [178] R. Bruno, D. Hille, A. Riva, N. Vivier, S. B. Kaye, J. Verweij, F. V. Fossella, V. Valero, J. R. Rigas, A. D. Seidman, B. Chevallier, P. Fumoleau, H. A. Burris, P. M. Ravdin, and L. B. Sheiner. Population pharmacokinetics/pharmacodynamics of docetaxel in phase II studies in patients with cancer. *J. Clin. Oncol.*, 16(1):187–96, Jan 1998.
- [179] G. S. Chatta, M. Fakhri, C. P. Belani, S. Ramlingam, R. K. Ramanathan, W. Zamboni, R. Parise, S. Fiedland, S. Tutchko, and M. J. Egorin. Phase I pharmacokinetic (PK) study of daily imatinib in combination with docetaxel for patients with advanced solid tumors. In *Proc. Amer. Assoc. Cancer Res.*, volume 22, page 577, 2003.
- [180] L. D. Lewis, A. A. Miller, G. L. Rosner, J. E. Dowell, M. Valdivieso, M. V. Relling, M. J. Egorin, R. R. Bies, D. R. Hollis, E. G. Levine, G. A. Otterson, F. Millard, and M. J. Ratain. A comparison of the pharmacokinetics and pharmacodynamics of docetaxel between african-american and caucasian cancer patients. *Clin. Cancer Research*, 13(11):3302–11, Jun 2007.
- [181] H. Dumez, G. Guetens, G. D. Boeck, M. S. Highley, E. A. de Bruijn, A. T. van Oosterom, and R. A. Maes. *In Vitro* partition of docetaxel and gemcitabine in human volunteer blood: The influence of concentration and gender. *Anticancer Drugs*, 16:885–91, 2005.

- [182] F. Leger, W. Loos, R. Bugat, R. Mathijssen, M. Goffinet, J. Verweij, A. Sparreboom, and E. Chatelut. Mechanism-based models for topotecan-induced neutropenia. *Clin. Pharmacol. Ther.*, 76:567–78, 2004.
- [183] J. Hing, J. J. Perez-Ruixo, K. Stuyckens, A. Soto-Matos, L. Lopez-Lazaro, and P. Zannikos. Mechanism-based pharmacokinetic/pharmacodynamic meta-analysis of trabectedin (ET-743) induced neutropenia. *Clin. Pharmacol. Ther.*, 83(1):130–43, Jan 2008.
- [184] Y. M. Chen, J. F. Shih, R. P. Perng, C. M. Tsai, and J. Whang-Peng. A randomized trial of different docetaxel schedules in non-small-cell lung cancer patients who failed previous platinum-based chemotherapy. *Chest*, 129(4):1031–8, Apr 2006.
- [185] J. A. Florian, Jr. and R. S. Parker. Empirical modeling for glucose control in diabetes and critical care. *Eur. J. Control*, 11:601–616, 2005.
- [186] R. P. Hoogma, A. J. Spijker, M. van Doorn-Scheele, T. T. van Doorn, R. P. Michels, R. G. van Doorn, M. Levi, and J. B. Hoekstra. Quality of life and metabolic control in patients with diabetes mellitus type I treated by continuous subcutaneous insulin infusion or multiple daily insulin injections. *Neth. J. Med*, 62(10):383–7, Nov 2004.
- [187] C. L. Yu, R. J. Roy, H. Kaufman, and B. W. Bequette. Multiple-model adaptive predictive control of mean arterial blood pressure. *IEEE Trans. Biomed. Eng.*, 39:765–778, 1992.
- [188] R. Zurakowski and A. R. Teel. A model predictive control based scheduling method for HIV. *J. Theor. Biol.*, 238:368–82, 2006.
- [189] J. A. Florian Jr., J. L. Eiseman, and R. S. Parker. Modeling quiescent cells in tumor growth and cancer treatment. In *Proc. Foundations of Systems Biology in Engineering*, volume (submitted), Santa Barbara, CA, 2005.
- [190] C. Veyrat-Follet, R. Bruno, R. Olivares, G. R. Rhodes, and P. Chaikin. Clinical trial simulation of docetaxel in patients with cancer as a tool for dosage optimization. *Clinical Pharmacology & Therapeutics*, 68:677–687, 2000.
- [191] T. Thigpen. Maybe more is better. *J. Clin. Oncol.*, 21(13):2454–2456, 2003.
- [192] J. Chen, Y. Lo, C. Yu, C. Hsu, J. Shih, and C. Yang. Predictors of toxicity of weekly docetaxel in chemotherapy treated non-small cell lung cancers. *Lung Cancer*, page epub, 2007.
- [193] F. B. Stehman. Is more always better? *Gynecologic Oncology*, 61:1–2, 1996.
- [194] I. J. Fidler and L. M. Ellis. Chemotherapeutic drugs: More really is not better. *Nature Medicine*, 6(5):500–2, May 2000.

- [195] E. Chatelut, J. Delord, and P. Canal. Toxicity patterns of cytotoxic drugs. *Invest. New Drugs*, 21:141–8, 2003.
- [196] Y. A. Lazebnik, S. Cole, C. A. Cooke, W. G. Nelson, and W. C. Earnshaw. Nuclear events of apoptosis in vitro in cell-free mitotic extracts: A model system for analysis of the active phase of apoptosis. *Journal of Cell Biology*, 123(1):7–22, Oct 1993.
- [197] M. R. Wilson, T. W. Close, and J. E. Trosko. Cell population dynamics (apoptosis, mitosis, and cell-cell communication) during disruption of homeostasis. *Experimental Cell Research*, 254:257–68, 2000.
- [198] B. Basse, B. C. Baguley, E. S. Marshall, W. R. Joseph, B. van Brunt, G. Wake, and D. J. Wall. Modelling cell death in human tumour cell lines exposed to the anticancer drug paclitaxel. *J. Math. Biol.*, 49:329–57, 2004.